Title
Spatially Resolving Dynamics and Nanoscale Migration of Excitons in Organic Semiconductors Using Transient Absorption Imaging and STED Microscopy

Author
Penwell, Samuel

Publication Date
2016

Peer reviewed|Thesis/dissertation

Spatially Resolving Dynamics and Nanoscale Migration of Excitons in Organic Semiconductors Using Transient Absorption Imaging and STED Microscopy

by

Samuel B. Penwell

A dissertation submitted in partial satisfaction of the

requirements for the degree of

Doctor of Philosophy

in

Chemistry

in the

Graduate Division

of the

University of California, Berkeley

Committee in charge:

Associate Professor Naomi S. Ginsberg, Chair
Professor Stephen R. Leone
Professor Alex Zettl

Summer 2016

Spatially Resolving Dynamics and Nanoscale Migration of Excitons in Organic Semiconductors Using Transient Absorption Imaging and STED Microscopy

Abstract

Spatially Resolving Dynamics and Nanoscale Migration of Excitons in Organic Semiconductors Using Transient Absorption Imaging and STED Microscopy

by

Samuel B. Penwell

Doctor of Philosophy in Chemistry

University of California, Berkeley

Associate Professor Naomi S. Ginsberg, Chair

This thesis focuses on the development and application of new methods for spatially and temporally resolving measurements of exciton dynamics and migration in organic semiconducting thin films, which are commonly used in organic field effect transistors (OFETs), organic light emitting diode (OLEDs), and organic photovoltaics (OPVs). Three methods of probing exciton dynamics and migration on length scales better matched to the structural heterogeneity in organic semiconductors are presented. First, the benefits of spatially resolving ultrafast dynamics are explored, by employing transient absorption microscopy on single domains of polycrystalline films of 6,13-bis-(triisopropylsilylethynyl)-pentacene (TIPS-Pn), revealing a polarization dependence that significantly aids the assignment of the excited state dynamics. A full kinetic model of population dynamics, as a function of both polarization and time, is developed and fit to the experimental data, where the polarization dependence provides a several fold increase in the number of constraints for the fitting routine. The global fitting analysis successfully reproduces the experimental data, and the observed dynamics are determined to include ultrafast thermalization of the initially hot exciton in $\sim$ 50 fs, followed by singlet fission in the first few picoseconds, and then internal conversion over several hundred picoseconds. The success of the kinetic model and the assignment of the dynamics are direct results of the polarization dependence, which is only revealed at the single domain level.

Second, stimulated emission depletion (STED) fluorescence microscopy, originally developed for super-resolution fluorescence imaging of isolated, robust, fluorescent dye labels in biological imaging applications, is adapted to image conjugated polymer solids using their endogenous, densely packed, non-ideal chromophores. Notably, the challenge posed by the strong two photon absorption of the so called "STED pulse", which depletes the initially diffraction-limited excited state population to yield a sub-diffraction resolution excitation volume, in conjugated polymers is successfully mitigated through careful control of the STED pulse parameters in combination with the pile-up correction and excitation modulation. This technique is demonstrated on nanoparticles of the conjugated polymer poly(2,5-

di(hexyloxy)cyanoterephthalylidene) (CN-PPV), where an imaging resolution of better than 90 nm is achieved.

Finally, a new method to measure exciton migration on its native nanometer and picosecond scales is presented, based on a further adaptation of STED microscopy, which provides ultrafast time resolution of spatial migration dynamics. This technique of time-resolved ultrafast stimulated emission depletion (TRUSTED) is achieved by adding a second STED pulse, with a controlled time delay, to define an optical quenching boundary that preferentially quenches excitation that has migrated beyond a critical radius. The theoretical and experimental sensitivity of this technique to migration processes is demonstrated, through kinetic simulations and experimental studies. The application of TRUSTED to CN-PPV thin films, in combination with a custom fitting routine, reveals the exciton migration length to be $L_d = 16 \pm 2$ nm. Additionally, Monte Carlo simulations of incoherent exciton hopping are performed for a variety of possible spatioenergetic landscapes, revealing the migration process in CN-PPV to be approximately diffusive in nature, where the 5 ns lifetime capitalizes on the diffusive motion, resulting in the relatively long observed migration length. The simulations also reveal more generally how the energetic and spectral parameters of a material combine to determine the extent and nature of exciton migration.

The results presented here, and the future experiments enabled by this work, will reveal the importance of matching the scale of the experimental resolution to the natural scale of the process or heterogeneity of the material. The insight that stands to be gained through the continued pursuit of these research goals will elucidate the nature of the structure/function relationship in organic semiconductors, informing the rational design of the next generation of semiconducting materials for applications in displays, computing, lighting, and light harvesting.

To my Parents, who taught me the value of curiosity, education, and critical thinking.

And to my wife Nikki, without whose understanding and constant support this work would not have been possible.

Contents

List of Figures

List of Tables

List of Abbreviations

Below are the abbreviations used in this thesis. Additional variables are defined as needed in text.

Abbreviation	Definition
2H	second harmonic
2PA	two photon absorption
3H	third harmonic
CN-PPV	poly(2,5-di(hexyloxy)cyanoterephthalylidene)
D	diffusivity
DAQ	data acquisition card
ΔT	change in transmission
$\Delta T/T$	change in transmission/transmission
diF-TES-ADT	2,8-difluoro-5,11- bis(triethylsilylethynyl)anthradithiophene
ESA	excited state absorption
FRET	Förster resonant energy transfer
FWHM	full width half maximum
GSB	ground state bleach
IHB	inhomogeneous broadening
L_d	diffusion length
MSD	mean squared displacement
NA	numerical aperture
NOPA	non-colinear optical parametric amplifier
OFET	organic field effect transistor
OLED	organic light emitting diode
OPA	optical parametric amplifier
OPV	organic photovoltaic
PAINT	point accumulation for imaging in nanoscale topography
PALM	photoactivated localization microscopy
PLQ	photoluminescence quenching
PMT	photomultiplier tube
PSF	point spread function

RMSD	root mean square displacement
RMSE	root mean square error
SIM	structured illumination microscopy
SPAD	single photon counting avalanche photodiode
SSB	site specific broadening
STED	stimulated emission depletion
STORM	stochastic optical reconstruction microscopy
SE	stimulated emission
SS	Stokes shift
TA	transient absorption
TAM	transient absorption microscopy
TCSPC	time correlated single photon counting
TIPS-Pn	6,13-bis-(triisopropylsilylethynyl)- pentacene
TRUSTED	time-resolved ultrafast stimulated emission depletion

Acknowledgments

I would like to acknowledge the contributions of Dr. Cathy Wong and Ben Cotts, who coauthored the work resented in Chapter 2, and Lucas Ginsberg who coauthored the work presented in Chapters 3 and 4, contributing to the design and implementation of the STED microscope, to running the experiments, and to the development of the interpretation. I would also like to acknowledge Dr. Rodrigo Noriega for his contributions to and guidance in the development of the simulations of the experimental data in Chapter 4. Additionally, I would like to thank my thesis adviser, Dr. Naomi Ginsberg, and the rest of the Ginsberg group for many insightful conversations that helped guide the direction of these projects.

Chapter 1

Introduction and Background on Organic Semiconductors

1.1 Introduction

Semiconducting materials are found in almost every piece of modern technology including computers, cellphones, displays, light bulbs, and solar cells. They have altered the way we interact with each other, perform business, light our homes, and power our devices. Organic semiconductors, made from small organic molecules or polymers, have emerged as potential replacements for high performance inorganic materials, which can be toxic and expensive to produce.[1, 2] Organic materials have the advantage of chemical tunability in their molecular structure to customize their performance to specific applications; many can be solution processed by roll to roll printing for inexpensive mass production, and they offer a range of other benefits, such as enabling flexible electronics.[3–7]

Most applications of organic semicondutors fall into one of a few categories, organic field effect transistors (OFETs), organic light emitting diodes (OLEDs), and organic photovoltaics (OPVs).[3, 8–10] The utility of these devices derives from the excited state dynamics of the organic semiconducting material. Optical excitations in organic semiconductors form bound electron-hole pairs called "exitons" that can undergo many dynamical processes, such as singlet-triplet interconversion and spatial migration, which determine the functionality of the material in a device.[4] The observed dynamics are the result of both the intramolecular properties of the molecular units and their intermolecular interaction in the densely packed thin films used in devices.[11, 12] This relationship between the structure of the material and its function is of fundamental importance to the performance of organic semiconductors in devices and to enabling the rational design of new materials for specific applications.

Solution processing, which is a key benefit of organic semiconductors, often produces kinetically trapped heterogeneous substructures that depend on the preparation conditions, leading to a large array of morphologies and device performances for a given material.[13] Typical measurements of exciton dynamics and migration, however, are made in bulk, av-

eraging over any heterogeneous substructures present, precluding any correlation with the underlying morphology.[14]

To better inform the structure/function relation in organic semiconductors, we have developed three methods of probing their exciton dynamic and migration on length scales better matched to their structural heterogeneity. First, we employ transient absorption microscopy on single domains of polycrystalline films of 6,13-bis-(triisopropylsilylethynyl)-pentacene (TIPS-Pn) (Chapter 2), revealing a polarization dependence that significantly aids the assignment of the excited state dynamics. Second, we adapt stimulated emission depletion (STED) fluorescence microscopy to image conjugated polymer nanoparticles (Chapter 3), demonstrating the ability to define sub-diffraction excitation volumes. Finally, we further adapt this technique to measure exciton migration in poly(2,5-di(hexyloxy)cyanoterephthalylidene) (CN-PPV) on its native nanometer and picosecond scales (Chapter 4), opening the door for correlative mapping of exciton migration with the local substructure, and revealing fundamental properties of the exciton migration process in conjugated polymers.

The results presented here, and the future experiments enabled by this work, will reveal the importance of matching the scale of the experimental resolution to the natural scale of the process or heterogeneity of the material. The insights that stand to be gained through the continued pursuit of these research goals will elucidate the nature of the structure/function relationship in organic semiconductors, enhancing our fundamental understanding of exciton dynamics and migration, and informing the rational design of the next generation of semiconducting materials for applications in displays, computing, lighting, and light harvesting. These technologies continue to improve the quality of our lives and the efficiency and sustainability of our society.

1.2 Background on Exciton Dynamics and Migration in Organic Semiconductors

The goals of the research presented here, as outlined above, are to combine high spatial and temporal resolution methods to construct new techniques to measure exciton migration and dynamics in organic semiconductors, on the native scales of the processes and material heterogeneity. This chapter will introduce the relevant properties of organic semiconductors, and the fundamental physics and methods on which the presented work relies. Subjects to be covered include the definition of semiconducting materials (Section 1.2.1), the properties and advantages of organic semiconductors (Section 1.2.2), the nature of optical excitations in organic semiconductors (Section 1.2.3), including fundamentals of optical processes and the nature of excitons, a review of the excited state dynamics typically found in organic materials (Section 1.2.4), including an brief overview of transient absorption, which is typically used to study these dynamics, the definition of a chromophore in molecular solids and a discussion of the types of energetic disorder in the energy of chromophores (Section 1.2.5), an overview

of theories of exciton migration with a brief introduction to Dexter transfer, Förester theory, and diffusion (Section 1.2.6), an overview of the types and scales of structural heterogeneity (Section 1.2.7), and an overview of current methods to resolve this heterogeneity (Section 1.2.8), including a review of microscopy and the diffraction limit. The successful demonstration of the methods developed herein will lay the foundation for correlative studies of material properties and substructure, elucidating the critical structure/function relationship that underpins rational material design and device performance.

1.2.1 Semiconducting Materials

This work will focus on the photophysics of semiconductors. Traditional semiconducting materials are crystalline materials, which have bandgaps (between the valence and conduction bands) on the scale of optical excitation energies for photons in the visible and infrared spectrum, with the Fermi level in the gap, resulting in carrier densities (electrons in the conduction band or holes in the valence band) typically less than 10^{20} cm^{-3}.[15] As a result, they are insulating in the ground state, but can be conductive under illumination. Common uses of semiconducting materials include transistors, light emitting diodes, and photovoltaics.[3, 8–10]

Semiconductors are often categorized as n-type or p-type, based on the dominant type of charge carrier. If the Fermi level is close to the conduction band, some electrons may be thermally promoted to the conduction band (n-type), while if the Fermi level is close to the valence band electrons may again be thermally promoted, this time leaving holes in the valence band (p-type). In classical crystalline inorganic semiconductors, this is achieved by doping the material with a small concentration of atoms one group above (n-type) or below (p-type) the atomic group of the host.[16]

1.2.2 Organic Semiconductors

Specifically, this work will investigate the optical properties of organic semiconductors. An organic semiconductor is a solid film composed of either small π-conjugated organic molecules or π-conjugated organic polymers, in contrast to the atomic lattices in inorganic materials. The organic, molecular, nature of organic semiconductors allows the material properties to be tuned through the chemistry of the molecular constituents, yielding a diverse zoology of potential materials that can be customized to specific applications.[3–5] Some of these organic materials can also be solution-processed into materials, via roll to roll printing, reducing production costs compared to vapor deposition.[1, 2] Additionally, some organic semiconductors have other desirable properties, such as flexibility for the production of flexible electronics.[6, 7] The molecular nature of organic semiconductors also results in various degrees of disorder in the material structure. For disordered, non-periodic, materials, the band picture does not apply, however, the molecular or locally delocalized occupied and unoccupied energy levels are still separated by an energy gap and the terminology that

stems from the traditional band picture, such as the "band gap", is often still applied to these systems.

Small molecule organic semiconductors often exhibit a high degree of order, forming molecular crystals, where the small molecules self-assemble to form large crystalline domains with specific unit cells. These molecular crystals are analogous to the atomic lattices in inorganic semiconductors, however, the coupling between sites in the lattice are governed by Van der Waals interactions of the molecular constituents. As such, there are much weaker interactions between lattice sites, and much less delocalization of the excited states between lattice sites, so the nature of the excited states is somewhere between the molecular orbital picture of the individual molecules and the full band picture for inorganic crystalline solids. The relevant molecular orbitals, which determine the electronic structure of π-conjugated small molecule materials, are formed by the delocalization of the p-orbitals that participate in the conjugation. Most conjugated organic systems have just enough electrons to fill the bonding orbitals, such that the band gap originates from the π to $\pi*$ molecular transitions. The size of this gap is also generally related to the extent of conjugation, with longer conjugated systems exhibiting lower transition energies, in analogy to the transitions for a particle in a box.[3, 4, 17]

The coupling of two such molecules results in an energy splitting, producing new delocalized states with perturbed energies, where the splitting is proportional to the strength of the coupling. The Hamiltonian for the dimerization of two molecular monomers can be expressed as,[4, 18]

$$H = H_1 + H_2 + V \tag{1.1}$$

where H_1 and H_2 are the Hamiltonians of the respective molecules and V is the coupling. The ground state wavefunction can then be expressed as the product of the monomer wavefunctions (ψ_1, ψ_2):

$$\Psi = \psi_1\psi_2. \tag{1.2}$$

The energy of the ground state is then found in the typical way.

$$\begin{aligned} H\left|\Psi\right\rangle &= E_g\left|\Psi\right\rangle \\ E_g &= \left\langle\Psi\right| H\left|\Psi\right\rangle \\ E_g &= \left\langle\psi_1\psi_2\right| H_1\left|\psi_1\psi_2\right\rangle + \left\langle\psi_1\psi_2\right| H_2\left|\psi_1\psi_2\right\rangle + \left\langle\psi_1\psi_2\right| V\left|\psi_1\psi_2\right\rangle \\ E_g &= E_1 + E_2 + \left\langle\psi_1\psi_2\right| V\left|\psi_1\psi_2\right\rangle \\ E_g &= E_1 + E_2 + W \end{aligned} \tag{1.3}$$

Where the coupling energy, $W = \left\langle\psi_1\psi_2\right| V\left|\psi_1\psi_2\right\rangle$, is typically negative for dimers. The excited state wave function will then be a linear combination of monomer 1 or monomer 2 in the excited state, with equal weighting for identical monomers. There are two possible

linear combinations:

$$\Psi^+ = \frac{1}{\sqrt{2}}\left(\psi_1^*\psi_2 + \psi_1\psi_2^*\right) \tag{1.4}$$

$$\Psi^- = \frac{1}{\sqrt{2}}\left(\psi_1^*\psi_2 - \psi_1\psi_2^*\right) \tag{1.5}$$

where the star denotes an excited state. The Hamiltonian can then be written in matrix form in this basis:

$$\begin{bmatrix} H_{++} & H_{+-} \\ H_{-+} & H_{--} \end{bmatrix}. \tag{1.6}$$

The terms for identical monomers with ground state monomer energy, E, and excited state monomer energy, E^*, are,

$$\begin{aligned} H_{++} =& \left\langle \frac{1}{\sqrt{2}}\left(\psi_1^*\psi_2 + \psi_1\psi_2^*\right) \right| H_1 + H_2 + V \left| \frac{1}{\sqrt{2}}\left(\psi_1^*\psi_2 + \psi_1\psi_2^*\right) \right\rangle \\ =& \frac{1}{2}\left[E_1^* + E_1 + E_2 + E_2^* + \langle\psi_1^*\psi_2| V |\psi_1^*\psi_2\rangle + \langle\psi_1\psi_2^*| V |\psi_1\psi_2^*\rangle \right. \\ & \left. + \langle\psi_1^*\psi_2| V |\psi_1\psi_2^*\rangle + \langle\psi_1\psi_2^*| V |\psi_1^*\psi_2\rangle\right] \\ =& E + E^* + \langle\psi_1^*\psi_2| V |\psi_1^*\psi_2\rangle + \langle\psi_1^*\psi_2| V |\psi_1\psi_2^*\rangle \\ =& E + E^* + W^* + \beta \end{aligned}$$

where $W^* = \langle\psi_1^*\psi_2| V |\psi_1^*\psi_2\rangle$ is the coupling of one excited state and one ground state monomer, and $\beta = \langle\psi_1^*\psi_2| V |\psi_1\psi_2^*\rangle$. The remaining terms are,

$$\begin{aligned} H_{+-} =& \left\langle \frac{1}{\sqrt{2}}\left(\psi_1^*\psi_2 + \psi_1\psi_2^*\right) \right| H_1 + H_2 + V \left| \frac{1}{\sqrt{2}}\left(\psi_1^*\psi_2 - \psi_1\psi_2^*\right) \right\rangle \\ =& \frac{1}{2}\left[E_1^* - E_1 + E_2 - E_2^* + \langle\psi_1^*\psi_2| V |\psi_1^*\psi_2\rangle - \langle\psi_1\psi_2^*| V |\psi_1\psi_2^*\rangle \right. \\ & \left. \langle\psi_1^*\psi_2| V |\psi_1\psi_2^*\rangle - \langle\psi_1\psi_2^*| V |\psi_1^*\psi_2\rangle\right] \\ =& 0 \end{aligned}$$

$$\begin{aligned} H_{-+} =& \left\langle \frac{1}{\sqrt{2}}\left(\psi_1^*\psi_2 - \psi_1\psi_2^*\right) \right| H_1 + H_2 + V \left| \frac{1}{\sqrt{2}}\left(\psi_1^*\psi_2 + \psi_1\psi_2^*\right) \right\rangle \\ =& \frac{1}{2}\left[E_1^* - E_1 + E_2 - E_2^* + \langle\psi_1^*\psi_2| V |\psi_1^*\psi_2\rangle - \langle\psi_1\psi_2^*| V |\psi_1\psi_2^*\rangle \right. \\ & \left. \langle\psi_1^*\psi_2| V |\psi_1\psi_2^*\rangle - \langle\psi_1\psi_2^*| V |\psi_1^*\psi_2\rangle\right] \\ =& 0 \end{aligned}$$

$$\begin{aligned} H_{--} =& \left\langle \frac{1}{\sqrt{2}} \left(\psi_1^* \psi_2 - \psi_1 \psi_2^*\right) \right| H_1 + H_2 + V \left| \frac{1}{\sqrt{2}} \left(\psi_1^* \psi_2 - \psi_1 \psi_2^*\right) \right\rangle \\ =& \frac{1}{2} \left[E_1^* + E_1 + E_2 + E_2^* + \langle \psi_1^* \psi_2 | \, V \, | \psi_1^* \psi_2 \rangle + \langle \psi_1 \psi_2^* | \, V \, | \psi_1 \psi_2^* \rangle \right. \\ & \left. - \langle \psi_1^* \psi_2 | \, V \, | \psi_1 \psi_2^* \rangle - \langle \psi_1 \psi_2^* | \, V \, | \psi_1^* \psi_2 \rangle \right] \\ =& E + E^* + \langle \psi_1^* \psi_2 | \, V \, | \psi_1^* \psi_2 \rangle - \langle \psi_1^* \psi_2 | \, V \, | \psi_1 \psi_2^* \rangle \\ =& E + E^* + W^* - \beta \end{aligned}$$

Thus the energies of the Ψ^+ and Ψ^- states are,

$$E_+ = E + E^* + W^* + \beta \tag{1.7}$$

$$E_- = E + E^* + W^* - \beta \tag{1.8}$$

and the resulting level diagram is shown in Figure 1.1.

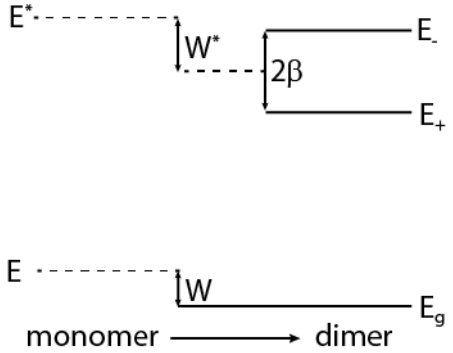

Figure 1.1: Schematic of the energy level splitting that results from dimerization of identical monomers.

In the case of a molecular crystal with N molecules, the ground state wavefunction becomes[4]

$$\Psi = \sum_{n=1}^{N} \psi_n^0 \tag{1.9}$$

where ψ_n^0 is the ground state of the nth molecule. The Hamiltonian is,

$$H = \sum_{n=1}^{N} H_n + \sum_{m \neq n}^{N} V_{mn} = H_o + V. \tag{1.10}$$

For simplicity, assume a one dimensional crystal with periodic boundary conditions and lattice spacing l. In this case, there are N degenerate excited states,

$$\Psi_i' = \psi_i^1 \sum_{n \neq i}^{N} \psi_n^0. \tag{1.11}$$

The first excited state will be a linear combination of these levels,

$$\Psi' = \sum_{n=1}^{N} a_n \Psi'_n. \tag{1.12}$$

For nearest neighbor interactions and periodic boundary conditions, the solutions are,

$$\Psi'_k = \frac{1}{\sqrt{N}} \sum_{n=1}^{N} e^{inkl} \Psi'_n \tag{1.13}$$

where k is a wavevector for the excited state with allowed values of $0 \pm 2\pi/Nl \pm 4\pi/Nl, ..., \pi/l$. The corresponding transition energies are,

$$E_k = (E^* - E) + (W^* - W) + 2\beta \cos(kl) \tag{1.14}$$

where β is the nearest neighbor interaction energy,

$$\beta = \left\langle \psi_i^o(r_1)\psi_{i+1}^1(r_2) \mid V_{12} \mid \psi_i^1(r_1)\psi_{i+1}^0(r_2) \right\rangle. \tag{1.15}$$

The result is a band of N states of width 4β. Since the coupling is generally weak for molecular materials, the observed absorption spectrum of the solid is similar to the solution spectra of the molecular units, however, the spectrum in solid state is typically red shifted due to the delocalization of the excited state and the energy splitting induced by the inter-molecular coupling.

Conjugated polymers can also be considered as molecular materials,[19] but tend to form disordered solids, where the backbone of the polymer largely adopts random configurations. These disordered configurations cause some disruptions in the conjugation along the length of the polymer, resulting in a series of connected conjugated systems which act as chromophores in the film. Some polymers can, however, exhibit some ordered packing over short length scales.[20] In regions with a high degree of local order, the electronic structure is similar to the molecular crystals discussed above, while more disordered regions, with less periodicity, have smaller inter-molecular couplings with more variations depending on the specific local configuration and tend to have more solution like, localized, states with some dimerization or aggregates.[11, 21] This heterogeneous morphology results in a spatially heterogeneous manifold of states, where the local electronic structure is determined by the underlying local morphology.

In either case, the performance of the material depends strongly on its optical properties and photophysics. The experimental methods used to investigate the properties are also largely based optical probes. Thus, we now turn to the nature of optical excitations in organic semiconductors.

1.2.3 Optical Excitations in Organic Semiconductors: Excitons

Before discussing the specific optical properties of organic semiconducting systems, we will briefly review the the physics of the linear optical response of a simple two-level system and the effects of the introducing vibrational levels within the ground and excited electronic states.

1.2.3.1 Background on Absorption and Emission

To begin we will consider the linear interaction of a simple two-level optical system with a field. We will subsequently increase the complexity to account for the possibility of degenerate states and the effect of the vibrational modes found in real molecular systems. The kinetics of a simple two-level optical system interacting with a light field can be expressed using the Einstein coefficients for stimulated absorption (B_{12}), stimulated emission (B_{21}), and spontaneous emission (A_{21}), depicted in Figure 1.2.[22] These Einstein coefficients deter-

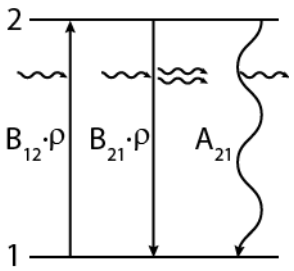

Figure 1.2: The Einstein coefficients for stimulated absorption, stimulated emission, and spontaneous emission.

mine the rate constants for the corresponding processes. The rate constant for spontaneous emission is simply the A_{21} coefficient, while the rate constants for the simulated processes are found by multiplying the Einstein B coefficients by the spectral energy density in the field (ρ). The system of equations, governing the kinetics of the system can then be expressed as follows,

$$\frac{dN_1}{dt} = -B_{12}\rho N_1 + B_{21}\rho N_2 + A_{21}N_2 \tag{1.16}$$

$$\frac{dN_2}{dt} = +B_{12}\rho N_1 - B_{21}\rho N_2 - A_{21}N_2 \tag{1.17}$$

where N_1 and N_2 are the populations in levels 1 and 2. In more complex systems, where there may be degeneracy in the states, but still two primary energy levels, the Einstein B coefficients are related by the degeneracy of the states,

$$B_{12} = \frac{g_2}{g_1}B_{21} \tag{1.18}$$

where g_1 and g_2 are the degeneracies of states 1 and 2 respectively. The kinetics can then be simplified to

$$\frac{dN_1}{dt} = B_{12}\rho\left(\frac{g_1}{g_2}N_2 - N_1\right) + A_{21}N_2 \tag{1.19}$$

$$\frac{dN_2}{dt} = -B_{12}\rho\left(\frac{g_1}{g_2}N_2 - N_1\right) - A_{21}N_2. \tag{1.20}$$

Note that the response of the system to the driving field ρ depends on the difference between the populations in the two states. As a result, a strong field will produce an equilibrium condition between the two states, where the relative population at equilibrium depends on the relative degeneracy of the levels. This treatment assumes "π pulses" cannot be used to achieve full population inversion, due either to rapid dephasing or to the presents of multiple transitions with a distribution of transition strengths in real molecules, as discussed below. There are some theories, however, concerning the possible implementation of such "π pulses" in electronic transitions in molecular systems.[23]

The Einstein A_{21} coefficient can also be related to the B coefficients by,

$$A_{21} = \frac{8\pi h\nu^3}{c^3}B_{21} \tag{1.21}$$

where h is Planck's constant and c is the speed of light. Since the number of photons in the field at frequency ν is $n(\nu) = 8\pi\nu^2/c^3$, the rate of spontaneous emission into a given mode of the field is equal to the rate of stimulated emission induced by a single photon in that mode:

$$\frac{A_{21}}{n(\nu)} = B_{21}h\nu. \tag{1.22}$$

R.C. Hilborn gives an excellent overview of the relations between the Einstein coefficients and other measures of transition strength, such as the absorption cross-section, oscillator strength, and transition dipole.[24]

Real molecular systems, however, are more complex than the simple two level systems discussed above. In particular, molecular systems have vibrational levels in both the ground and excited electronic states. The probability of transitioning between any two of these "vibronic" levels during absorption or emission depends on the vibrational wavefunction overlap, as described by the Franck-Condon factors in the Born-Oppenheimer approximation. This approximation assumes that the electronic motions are fast compared to the nuclear (vibrational) motion, so that the wavefunction can be factored into electronic and vibrational components, and the electronic portion of the wavefunction can be solved assuming a series of fixed nuclear arrangements. The resulting dependence of the energy of the electronic state on the nuclear coordinate acts as a potential surface for the nuclear vibrational motion. Typically, the dominant nuclear vibrational mode is treated as a harmonic oscillator. In this case, the electronic potential is quadratic and the energy of the vibrational levels are given by,

$$E_v = \hbar\omega(v + \frac{1}{2}) \tag{1.23}$$

where $\hbar$ is the reduced Planck's constant, ω is the angular vibrational frequency, and v is the vibrational quantum number. The transition probability, P, between vibronic levels in the ground and excited state can then be expressed as,

$$P = |\langle \Psi_1 \psi_v \mid \mu \mid \Psi_2 \psi_{v'} \rangle|^2 \tag{1.24}$$

where Ψ_1 and Ψ_2 are the ground and excited electronic wavefunctions, ψ_v and $\psi_{v'}$ are the vibrational wavefunctions in the ground and excited electronic state respectively, and μ is the dipole operator. The dipole operator acts only on the electronic portion of the wavefunction, and the vibrational overlap becomes a scaling factor (Frank-Condon factor).[16, 25–27] The transition probability is then,

$$P = |\langle \psi_v \mid \psi_{v'} \rangle|^2 \, |\langle \Psi_1 \mid \mu \mid \Psi_2 \rangle|^2 \tag{1.25}$$

where the Franck-Condon factor, $|\langle \psi_v \mid \psi_{v'} \rangle|^2$, modulates the electronic dipole coupling, and predicts the relative amplitudes of the vibronic transitions. The distribution of vibronic transitions that are accessible for absorption from the ground state, or emission from the excited state, contributes to the observed width of the absorption and emission profiles, respectively.

Additionally, the two quadratic electronic potential curves are typically offset along the nuclear coordinate, as in Figure 1.3, because the nuclear coordinate has a different equilibrium position depending on the electronic state. For example, if the electronic excitation promotes an electron from a bonding orbital to an anti-bonding orbital the nuclear coordinate will be less tightly bound, resulting in a larger equilibrium nuclear separation. The most likely transition from the ground state ($v = 0$ in electronic state 1) will then be to a vibrationally excited level. The excited state subsequently vibrationally relaxes, however, to the $v' = 0$ level. This energy loss represents the excited state reorganization energy, and corresponds to the nuclear coordinates relaxing to a new configuration after the electronic excitation. The emission from the $v' = 0$ level is also most likely to occur to a vibrationally excited level in the ground electronic state, where there is again a reoganization energy associated with the subsequent vibrational relaxation to $v = 0$. The net effect is that the most probable photon energy for emission is less than the most probable energy for absorption, by $\sim 2\times$ the reorganizational energy. This effect is called the "Stokes shift".

1.2.3.2 Excitons

The absorption of a photon by a semiconducting material or molecule generates a Coulombically bound electron-hole pair called an exciton. In the traditional picture of crystalline semiconductors, the electron, which is promoted to the conduction band by the absorption of a photon, leaves a positively charged vacancy or "hole" in the valence band. The electron and hole have a Coulombic attraction that couples them with a binding energy that is dependent on the dielectric of the semiconductor. Inorganic semiconductors generally have high dielectric constants, which corresponds to large charge screening, producing weakly bound

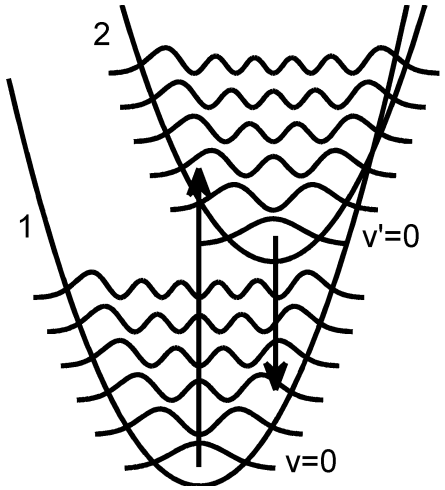

Figure 1.3: Schematic of the Frank-Condon principle and the origin of the Stokes shift.

excitons. These so called "Wannier-Mott" excitons typically have binding energies on the order of 0.01 eV and delocalize over large areas (an exciton with a binding energy of 0.01 eV in a material with a dielectric constant of 10 has a radius of ∼7 nm), (see Figure 1.4a). This low binding energy can often be overcome by thermal fluctuations to rapidly produce free carriers. Organic semiconductors generally have lower dielectric constants, and thus much less charge screening, which results in a much higher exciton binding energy. These "Frenkel" type excitons typically have binding energies on the order of 0.1-1 eV and are therefore much more localized, typically to a few chromophores (see Figure 1.4b).[4, 16] Due to their high binding energies, Frenkel excitons are much longer lived, typically surviving in their bound state until they decay by fluorescence or internal conversion, with a lifetime on the order of 1 ns. Efficient charge separation only occurs at donor-acceptor interfaces where matching of the Fermi levels provides a driving force to overcome the binding energy.[28] It is important then to understand the processes that an exciton can undergo in its lifetime to better elucidate the limiting factors on overall device performance.

1.2.4 Exciton Dynamics

The primary excited state processes available to an exciton are charge separation, thermalization, fluorescence, intersystem crossing, phosphorescence, and internal conversion. In addition, if the triplet state, T_1, is close to half the energy of the singlet state, S_1^0, then singlet fission can also occur, where a singlet exciton is converted to a correlated pair of triplet excitons (TT). These processes are all illustrated in Figure 1.5 and they will be important in the analysis of the work presented in Chapter 2.

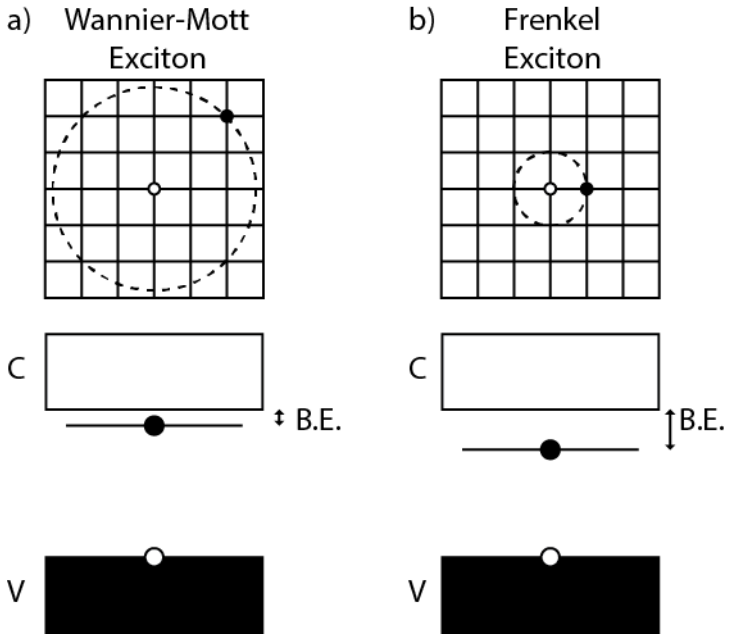

Figure 1.4: Schematic of the delocalization and energy levels of a) Wannier-Mott and b) Frenkel type excitons on a periodic lattice.

Charge Separation

$$S_1^n \xrightarrow{k_{cs}} CS$$
$$\text{exciton} \xrightarrow{k_{cs}} e^- + h^+$$

The separation of the exciton into free charges (k_{cs} in Figure 1.5) is the desired outcome in a OPV device, but is unlikely to occur from the thermalized excitonic S_1^0 state due to the large binding energy of the Frenkel type exciton (see Figure 1.4b). If a photon is absorbed with energy above the bandgap or first excited state energy, however, it may produce a "hot", vibrationally excited, exciton in a state S_1^n, which could in principle undergo direct charge separation, although this process must compete with the ultrafast (∼100 fs) thermalization (k_{th} in Figure 1.5) to S_1^0. Once the exciton has thermalized, the only efficient pathway for charge separation is through exciton migration to a donor-acceptor interface, which produces a driving force to overcome the exciton binding energy.[29, 30]

Radiative Relaxation

$$S_1^0 \xrightarrow{k_{fl}} S_0 + h\nu$$
$$T_1 \xrightarrow{k_{ph}} S_0 + h\nu$$

Another decay pathway for the exciton is radiative relaxation (k_{fl} and k_{ph} in Figure 1.5) through spontaneous emission, where the charges recombine and emit a photon. Radiative relaxation from the singlet state, S_1, (fluorescence) occurs on the order of 1 ns, while radiative

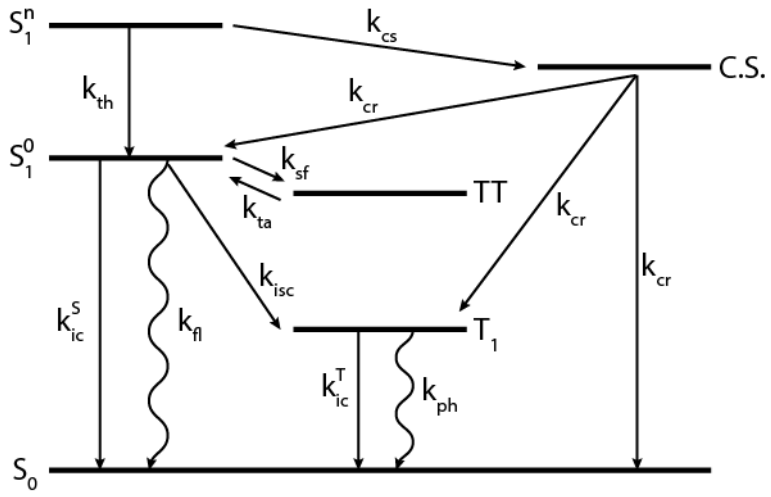

Figure 1.5: Schematic of the typical energy levels, including: the ground state (S_0), the singlet excited state (S_1^0), thermally excited singlet state (S_1^n), the triplet state (T_1), correlated triplet pair (TT), and the charge separated state ($C.S.$), as well as the common excited state processes found in organic semiconductors, including: thermalization (k_{th}), fluorescence (k_{fl}), intersystem crossing (k_{isc}), phosphorescence (k_{ph}), internal conversion from the singlet (k_{ic}^S) and triplet (k_{ic}^T), singlet fission (k_{sf}), triplet annihilation (k_{ta}), charge separation (k_{cs}), and charge recombination (k_{cr}).

relaxation from the triplet state, T_1, (phosphorescence) occurs on the order of 1 μs - 1 ms. Emission of a photon is the desired outcome in an OLED device. Organic semiconductors can have a large range of quantum yields for fluorescence emission, depending on the details of local environment.[9, 31–33]

Internal Conversion

$$S_1^0 \xrightarrow{k_{ic}^S} S_0$$
$$T_1 \xrightarrow{k_{ic}^T} S_0$$

Internal conversion, or non-radiative relaxation, (k_{ic} in Figure 1.5) is a process of excited state relaxation in which the energy of the electronic excitation is redistributed among vibrational and phonon modes, rather than being lost through the emission of a photon. The rate of internal conversion generally depends on access to particular configurations for the chromophore that facilitate the redistribution of the excited state energy. Thus, chromophores that are more "floppy" tend to have faster rates of internal conversion, since they have access to larger portions of configuration space, while more rigid chromophrores tend to have slower rates.[34]

Intersystem Crossing and Reverse Intersystem Crossing

$$S_1^0 \underset{k_{risc}}{\overset{k_{isc}}{\rightleftharpoons}} T_1$$

Intersystem crossing is the conversion of excited singlet states to triplet states by an electron spin flip, and reverse intersystem crossing is the conversion of triplets back to the excited singlet state. Singlets and triplets do not differ significantly in their charge separation characteristics in an OPV device, but their differences in lifetime and migration length can still impact the overall performance of an OPV.[35] In recent OLEDs, reverse intersystem crossing is critical to device performance, since uncorrelated charges combine to form triplets and singlets in a 3:1 ratio due to spin statistics, and phosphorescence from the triplet state is generally slow due to symmetry. The rate of intersystem crossing can be accelerated by increasing the spin-orbit coupling in the system, typically by the inclusions of a heavy element, whose core electrons move at relativistic speeds, introducing a significant spin-orbit coupling.[36] Alternatively, the energy of the singlet and triplet can be tuned to near resonance, through the chemical structure of the molecule, thereby mixing the singlet and triplet states.[37, 38]

Singlet Fission

$$S_1^0 \xrightarrow{k_{sf}} TT$$

Singlet fission occurs where the singlet energy is close to twice the triplet energy, allowing for a resonant conversion of the singlet to a correlated pair of triplets (TT) that together form an over all singlet, resulting in two excitons generated from a single photon absorption event. This multi-exciton generation pathway is of particular interest in the OPV community as a method to boost the efficiency of devices and potentially break the Shockley-Queisser barrier.[39–42]

Triplet Annihilation

$$T_1 + T_1 \xrightarrow{k_{ta}} S_0 + S_1^0$$

Triplet annihilation is the reverse of singlet fission, which is usually the only pathway to recover singlet excitons from the triplet state, due to the large energy gap between the singlet and triplet limiting the rate of reverse intersystem crossing, unless there is exceptionally strong spin-orbit coupling. This process is bi-molecular and diffusion limited from the T_1 state, and thus generally slow and inefficient, creating only a small singlet population that decays quickly through internal conversion and/or fluorescence.[43] An exception is the case of a correlated triplet pair ($TT \xrightarrow{k_{ta}} S_0 + S_1^0$), which is an overall singlet in spin and can readily convert back to the singlet state while the spin correlation persists.[44]

Charge Recombination

$$CS \xrightarrow{k_{cr}} S_1 \quad \text{or}$$
$$CS \xrightarrow{k_{cr}} T_1$$

Charge recombination occurs when free charges recombine to form an exciton, as in an OLED. The recombination is typically diffusion limited, and due to spin statistics, produces triplets and singlets in a 3:1 ratio.[9]

1.2.4.1 Background on Transient Absorption

Transient absorption (TA), also known as pump-probe spectroscopy, is a third order non-linear spectroscopic technique, commonly used to study ultrafast dynamics, such as those discussed above.[12, 41, 45–48] We will build on this method in the work presented in Chapter 2. The fundamental concept is to study the response of a system to the absorption of light, by pumping the system with an ultrafast "pump" pulse and then examining the differential change in the transmission of a second ultrafast "probe" pulse at a controlled time delay. This is achieved by cofocusing the beams on a sample and modulating the pump at a known frequency, as shown in Figure 1.6. When the pump is on (unblocked) it creates an optical excitation in the sample that the probe can then interact with. The change in the probe transmission (ΔT) between the pump on and off phases is recorded as a function of the delay time, and typically reported normalized to the pump-off probe transmission as $\Delta T/T$, which can be universally compared, as it is proportional to the change in optical density induced by the pump excitation.

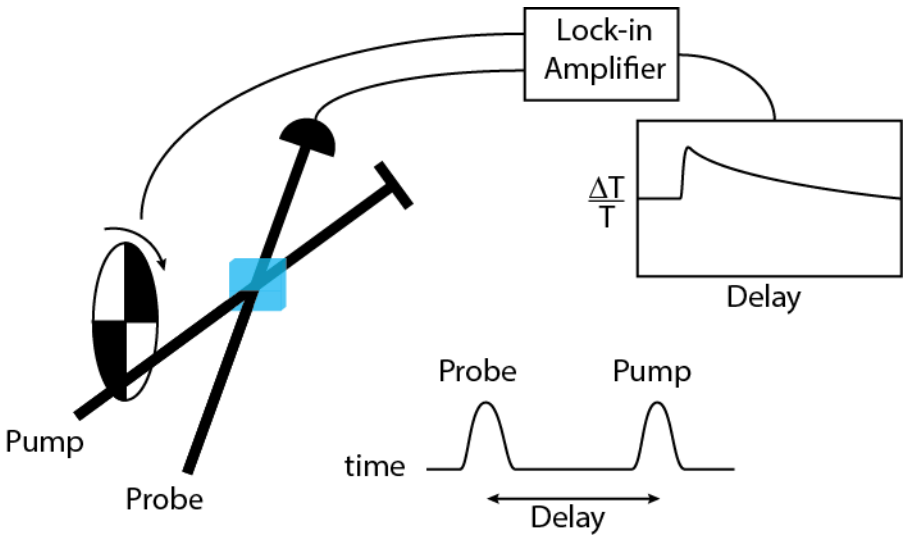

Figure 1.6: Schematic of a typical pump-probe experiment, including beam geometry, pump modulation, pulse time delay, and data.

There are three basic processes that produce $\Delta T/T$ signals: ground state bleach, stimulated emission, and excited state absorption (see Figure 1.7). Ground state bleach (GSB) occurs due to the vacancies in the ground state caused by the absorption of the pump pulse. When the probe pulse passes through the sample, these vacancies reduce the optical density of the sample causing an increased transmission of the probe, which corresponds to a positive $\Delta T/T$ signal. Stimulated emission (SE) occurs when the probe stimulates the excitations created by the pump to emit additional photons. These emission events add photons to the probe field producing a positive $\Delta T/T$ signal. Excited state absorption (ESA) occurs when an excitation created by the pump absorbs a photon from the probe and is promoted from the first excited state S_1 to a higher excited state S_n, or from T_1 to T_n yielding sensitivity to the population in triplet state. These absorption events reduce the intensity of the probe, creating a negative $\Delta T/T$ signal. These signals combine to form the net response of the sample, which evolves as a function of the pump-probe delay time as the excited state dynamics proceed, eventually trending to zero when all the pump-induced excitation has returned to the ground state.[49]

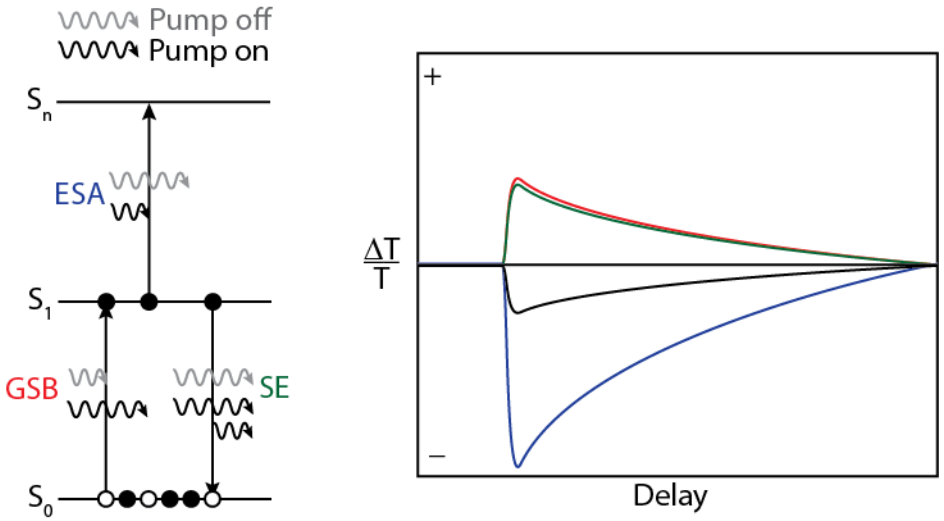

Figure 1.7: Schematic of the probe interactions that generate transient absorption signals with the "pump off" condition in gray and the "pump" on condition in black. The processes shown are GSB (red), SE (green), and ESA (blue), with corresponding transients on the right and the net signal transient shown in black.

1.2.5 Energetic Disorder in Site Energies

Organic semiconductors, especially those formed of conjugated polymers, can be disordered systems, where the differences in local configuration can produce an inhomogeneous

distribution of exciton energies over distinct sites in the material. For example, in conjugated polymer solids, the chromophores that define the sites available for excitons are often treated as originating due to kinks in the polymer backbone that interrupt the conjugation as the polymer is packed to condensed phase densities, although there are higher level treatments.[50] The statistical variations in the backbone persistence length generates a distribution of chromophores of various sizes and corresponding transition energies. This effect results in a static, spatially dependent, distribution of the individual site energies.[51] Other effects that contribute to this inhomogeneous broadening (σ_{IHB}) of the site energies include variation in the local electrostatic environment and the particular nature of the interchromophore interactions produced by the local configuration. Additionally, there are also homogeneous effects, which in this context are those that produce an intrinsic spectral width to all sites, or those that cause fluctuations in the site energy that are fast compared to the time an exciton occupies an individual sites (ps - ns). These effects include the Franck-Condon progression of the chromophores and fast thermal fluctuations in the site energy, and are collectively referred to in Chapter 4 as "site specific broadening" (σ_{SSB}). These energetic parameters combine to produce a spatioenergetic landscape, where chromophores are distributed in both space and energy. The observed width of the absorption profile of a material is the convolution of the inhomoeneous and site specific broadening effects, which is $\sigma_{tot}^2 = \sigma_{IHB}^2 + \sigma_{SSB}^2$ for Gaussian distributions, which makes distinguishing the contributions of the underlying inhomogeneous and site specific effects challenging. These energetic parameters and there impact on exciton migration will be discussed in more detail in Chapter 4.

1.2.6 Exciton Migration

Excitons in electronically coupled materials, such as organic semiconductors, can also undergo spatial migration. This migration process occurs through a series of consecutive pairwise transfer events, "hops", between chromophore sites over the lifetime of an exciton, resulting in extended exciton migration length. Exciton migration is critical to the function of many semiconducting devices, especially organic solar cells, where the exciton must migrate to a junction for the exciton binding energy to be overcome in order to generate free charge carriers.[28] The limited length scale of migration observed in organic semiconductors, especially conjugated polymers (5-20 nm),[14] is a limiting factor in the overall efficiency of organic photovoltaics.[52] Exciton migration in conjugated polymers will be discussed in detail in Chapter 4.

Due to the importance of this process, there has been a lot of research into the underlying mechanism of migration and the cause of the limited length scale of migration in organic materials.[14, 53, 54] There are several possible pathways for migration to proceed. The dipole-dipole coupling of two sites, at short distances ($\lesssim$ 10 nm), can result in Förster resonant energy transfer (FRET), described by Förster theory, where the excitation is non-

radiatively transferred between chromophores. The rate of FRET transfer is,

$$\begin{aligned} k_{FRET}(r) &= \frac{1}{\tau}\left(\frac{R_o}{r}\right)^6 \\ R_o &= \left[\frac{9c^4\hbar^4\eta\kappa^2}{8\pi n^4}\int \frac{A_{abs}(\epsilon)D_{ems}(\epsilon)}{\epsilon^4}d\epsilon\right]^{1/6} \end{aligned} \tag{1.26}$$

where r is the distance between the sites, τ is the fluorescence lifetime, R_o is the "FRET radius", c is the speed of light, $\hbar$ is the reduced Planck's constant, η is the quantum yield of fluorescence, κ is a dipole orientation faction ($\kappa = 2/3$ for isotropic orientational averaging), n is the index of refraction, ϵ is energy, A_{abs} is the absorption profile of the acceptor, and D_{ems} is the normalized emission profile of the donor.[26]

When sites are in very close proximity, as in a molecular crystal, there can be orbital overlap between adjacent sites that facilitates the exchange of electrons between sites (Dexter transfer).[55] The rate of this process depends on the degree of orbital overlap of sites and is thus very short range, occurring for separations on the order of 1 nm and decaying exponentially with increasing separation. The rate of Dexter transfer can be expressed as,

$$k_{Dexter} = AJ\exp(-2r/l) \tag{1.27}$$

where A is an experimentally determined constant, J is the spectral overlap integral, r is the site separation, and l is the sum of the Van der Waals radii for the donor and acceptor. This regime also opens the possibility for coherent transfer.[56, 57] In this case, it is important to consider the role of dynamical thermal fluctuations in the positions of the sites, which can have a large impact on the inter-molecular coupling strength.[58] In more disordered systems, systems with weak coupling, or in the presence of large thermal fluctuations, exciton migration is typically considered to consist of a series of incoherent hoping events, driven by FRET.

The spatial migration is also coupled to an energy relaxation of the exciton across the inhomogeously broadened distribution of site energies. As the exciton explores the spatioenergetic landscape it tends to migrate to successively lower energy sites until it reaches the band edge. The exciton can then become trapped, exhibit further thermally activated migration, or continue to migrate isoenergetically by diffusion, depending on the specifics of the spatioenergetic landscape at the band edge. This energy loss during migration adds to the intrinsic Stokes shift of the sites, resulting in a larger apparent Stokes shift in electronically coupled films than in isolated molecules in solution.[14, 59–61]

The extent of exciton migration is typically characterized by the "diffusion length", L_d, which describes the average root mean squared displacement of the exciton over its lifetime, under the assumption that the migration can be treated as a diffusive process, or described as a deviation from diffusive motion (sub-diffusive or super-diffusive). We will thus take some time to review the basic principles of diffusion.

1.2.6.1 Background on Diffusion

Diffusive motion is the description of the movement of particles when the momentum of the particles is frequently randomized, typically by collisions with other particles or the environment, on a bias-free energy landscape.[62] The prevalence of diffusive motion makes it an important process to understand and indicates that there is a commonality between the disparate physical phenomena to which diffusive motion applies. The reason for this prevalence is that diffusive motion is the statistical description of a random walk, which can be described by considering discrete time steps on a lattice of sites, where the probability of the particle moving to a given site is equal for all nearest neighbors. In this case, we will consider excitons to act as diffusing particles, since the "momentum" of the exciton is randomized between each hopping event, in the incoherent hopping regime. In this section, we will thus treat the diffusion of a generalized "particle".

The equation that governs the diffusive motion that results from a random walk can be derived by examining how the probability of a particular site being occupied evolves over a time step. Consider a one dimensional lattice with a particle at site x_o at time t_o. At time $t_o + \Delta t$ there is 50% chance the particle is at site $x_o + \Delta l$ and 50% chance it is on site $x_o - \Delta l$. This illustrates how the occupation probability on a give site redistributes in one time step, but what is the final occupation probability on the site x_o? All of the original probability density has been redistributed to the surrounding sites, but the site at x_o also gained probability density from those neighboring sites. Specifically site x_o will gain 50% of the probability density, P, from site $x_o + \Delta l$ and 50% of the probability density, P, from the site $x_o - \Delta l$:[63]

$$P(x_o, t_o + \Delta t) = \frac{1}{2}P(x_o + \Delta l, t_o) + \frac{1}{2}P(x_o - \Delta l, t_o). \tag{1.28}$$

If we then expand the left side of Equation 1.28 in Δt and the terms on the right in Δl, the three individual resulting terms are:

$$P(x_o, t_o + \Delta t) = P(x_o, t_o) + \frac{\partial P}{\partial t}(t_o, x_o)(\Delta t) + \frac{1}{2}\frac{\partial^2 P}{\partial t^2}(t_o, x_o)(\Delta t)^2, \tag{1.29}$$

$$\frac{1}{2}P(x_o + \Delta l, t_o) = \frac{1}{2}P(x_o, t_o) + \frac{1}{2}\frac{\partial P}{\partial x}(t_o, x_o)(+\Delta l) + \frac{1}{4}\frac{\partial^2 P}{\partial x^2}(t_o, x_o)(+\Delta l)^2, \text{ and} \tag{1.30}$$

$$\frac{1}{2}P(x_o - \Delta l, t_o) = \frac{1}{2}P(x_o, t_o) + \frac{1}{2}\frac{\partial P}{\partial x}(t_o, x_o)(-\Delta l) + \frac{1}{4}\frac{\partial^2 P}{\partial x^2}(t_o, x_o)(-\Delta l)^2. \tag{1.31}$$

After substituting these terms into Equation 1.28, the zero order terms on the left and right side cancel, the first order term in (Δt) survives so the second order term is dropped, and the first order terms for $(+\Delta l)$ and $(-\Delta l)$ cancel. The remaining terms yield

$$\frac{\partial P}{\partial t}(t_o, x_o)(\Delta t) = \frac{1}{2}\frac{\partial^2 P}{\partial x^2}(t_o, x_o)(\Delta l)^2, \tag{1.32}$$

which can be rewritten as

$$\begin{aligned}\frac{\partial P}{\partial t} &= \frac{\Delta l^2}{2\Delta t}\frac{\partial^2 P}{\partial x^2} \\ &= D\frac{\partial^2 P}{\partial x^2},\end{aligned} \tag{1.33}$$

for a constant $D = \frac{\Delta l^2}{2\Delta t}$. The same procedure can be used for higher spatial dimensions. Cross terms will show up in the expansion in these cases, but they will all cancel. The final express can be written as:

$$\frac{\partial P}{\partial t} = D\,\nabla^2 P. \tag{1.34}$$

It is important to note that this analysis assumes that D, the so-called diffusivity or diffusion constant, is constant with respect to the spatial coordinates.

This diffusion equation can be solved very generally by Fourier transforming both sides. We will demonstrate the derivation for a single spatial dimension, x, with the corresponding spatial frequency dimension, k, in Fourier space for simplicity. Applying the Fourier transform to Equation 1.34 yields,

$$\mathcal{F}\left[\frac{\partial P}{\partial t}\right] = \mathcal{F}\left[D\,\nabla^2 P\right] \tag{1.35}$$

where on the left, the Fourier transform, $\mathcal{F}$, commutes with the time derivative, and on the right side, the spatial derivative brings out a factor of ik for each order. The result,

$$\frac{\partial \mathcal{F}[P]}{\partial t} = -k^2 D\mathcal{F}[P] \tag{1.36}$$

and its integral,

$$\mathcal{F}[P] = \mathcal{F}[P_o]\,e^{-k^2 Dt} \tag{1.37}$$

all us to recover P:

$$P = \mathcal{F}^{-1}\left[\mathcal{F}[P_o]\,e^{-k^2 Dt}\right] \tag{1.38}$$

a general expression, where $\mathcal{F}^{-1}$ denotes the inverse Fourier transform and P_o is the initial condition. Consider the special case of an initial delta function at the origin. The Fourier transform of a delta function is a constant in Fourier space,

$$\begin{aligned}P &= \mathcal{F}^{-1}\left[A\,e^{-k^2 Dt}\right] \\ &= \frac{A}{\sqrt{4\pi Dt}}e^{-\frac{x^2}{4Dt}}.\end{aligned} \tag{1.39}$$

This solution is a Gaussian with a standard deviation of $\sigma = \sqrt{2Dt}$. It is then easily shown that if the initial condition is a Gaussian with a standard deviation of σ_o the solution is:

$$P(x,t) = \frac{A}{\sqrt{2\pi(2Dt+\sigma_o^2)}}e^{-\frac{x^2}{2(2Dt+\sigma_o^2)}} \tag{1.40}$$

by a change of variable in t. In this case we can write the standard deviation as follows:

$$\sigma^2 = \sigma_o^2 + 2Dt. \tag{1.41}$$

This linear dependence of the variance of the distribution with time is characteristic of diffusive motion. This derivation was shown for one dimension, but as long as the initial condition is separable the solution is also separable. So for a symmetric Gaussian initial condition in n-dimensional Cartesian space the solution is,

$$P(x_1, ..., x_n, t) = \prod_{i=1}^{n} P(x_i, t) = \frac{\prod_{i=1}^{n} A_i}{(2\pi\sigma^2)^{n/2}} e^{-\frac{\sum_{i=1}^{n} x_i^2}{2\sigma^2}} \tag{1.42}$$

and the radius, r, is defined as $r^2 = \sum_{i=1}^{n} x_i^2$, which yields

$$P(r, t) = \frac{A}{(2\pi\sigma^2)^{n/2}} e^{-\frac{r^2}{2\sigma^2}}. \tag{1.43}$$

The above solution to the diffusion equation assumes that the diffusivity, D, is constant with respect to both space and time. There are, however, some interesting physical cases where the rate of diffusion changes over time, such that $D = D(t)$, such as the super-diffusive ($D(t)$ increases with time) and sub-diffusive ($D(t)$ decreases with time) cases mentioned above. Inserting $D(t)$ into Equation 1.34 yields,

$$\frac{\partial P(r, \theta, t)}{\partial t} = D(t)\, \nabla^2 P(r, \theta, t). \tag{1.44}$$

This case can be solved by a convenient substitution of the following form:[64]

$$\gamma(t) = \int_0^t D(t')dt', \tag{1.45}$$

which yields,

$$\frac{\partial P(r, \gamma)}{\partial \gamma} \frac{\partial \gamma}{\partial t} = D(t)\, \nabla^2 P(r, \gamma). \tag{1.46}$$

Since γ is the inverse derivative of $D(t)$,

$$\frac{\partial \gamma}{\partial t} = D(t). \tag{1.47}$$

Therefore, Equation 1.46 simplifies to

$$\frac{\partial P(r, \gamma)}{\partial \gamma} = \nabla^2 P(r, \gamma), \tag{1.48}$$

which is a simple diffusion equation, like Equation 1.34, in terms of γ and has a known solution as outlined above:

$$P(r, \gamma) = \frac{1}{(2\pi\sigma^2)^{n/2}} e^{-\frac{r^2}{2\sigma^2}}, \tag{1.49}$$

where the standard deviation is

$$\begin{aligned}\sigma^2 &= \sigma_o^2 + 2\gamma \\ &= \sigma_o^2 + 2\int_0^t D(t')dt',\end{aligned} \tag{1.50}$$

and the solution may be expressed as

$$P(r,t) = \frac{e^{-\frac{r^2}{2\left(\sigma_o^2+2\int_0^t D(t')dt'\right)}}}{\left(2\pi\left(\sigma_o^2+2\int_0^t D(t')dt'\right)\right)^{n/2}}. \tag{1.51}$$

The diffusion length, L_d, is the length scale for the migration of particles with finite lifetimes. To derive its form, first consider the mean squared displacement (MSD) of an n-dimensional distribution centered at the origin:

$$\begin{aligned}MSD = \left\langle r^2\right\rangle &= \sum_{i=1}^{n}\left\langle x_i^2\right\rangle \\ &= \sum_{i=1}^{n}\left[\frac{\int_{-\infty}^{\infty} x_i^2 P(x_i,t)dx_i}{\int_{-\infty}^{\infty} P(x_i,t)dx_i}\right] \\ &= \sum_{i=1}^{n}\sigma^2 \\ &= n\,\sigma^2 \\ &= 2nDt + n\sigma_o^2.\end{aligned} \tag{1.52}$$

Since σ_o is the initial variance, the change in the MSD is

$$\begin{aligned}\Delta MSD &= n\,\sigma^2 - n\,\sigma_o^2 \\ &= 2nDt.\end{aligned} \tag{1.53}$$

The square of the diffusion length is then the time average of this quantity over the lifetime of the particles:

$$\begin{aligned}L_d^2 &= \left\langle 2nDt\right\rangle_t \\ L_d^2 &= \frac{\int_0^\infty 2nDt\,N(t)dt}{\int_0^\infty N(t)dt},\end{aligned} \tag{1.54}$$

where $N(t)$ describes the particle decay. In the special case where $N(t) = e^{-t/\tau}$, the integral has a simple solution:

$$L_d = \sqrt{2nD\tau}. \tag{1.55}$$

This quantity represents the average displacement of the particles from the origin over their lifetime, τ. Another possible definition of L_d is the average displacement in a particular direction x_i, which does not depend on dimensionality and is useful in describing the diffusion of particles towards a boundary along a given dimension:

$$L_d = \sqrt{2D\tau}. \tag{1.56}$$

A lot of the literature, related exciton diffusion in particular, drops both the dimensionality and the factor of two and defines the diffusion length as:[4, 14]

$$L_d = \sqrt{D\tau}. \tag{1.57}$$

Care must be taken to understand which definition is in use in a particular work. Although Equations 1.55 and 1.56 are more physically relevant, we will adhere to the commonly cited form in Equation 1.57, which implies that our reported values underestimate the typical micration distances by a factor of $\sqrt{2}$. In the case of time dependent diffusivity, Equation 1.54 becomes:

$$L_d^2 = \frac{\int_0^\infty 2n \left(\int_0^t D(t')dt' \right) N(t)dt}{\int_0^\infty N(t)dt}, \tag{1.58}$$

and must be evaluated for the particular form of $D(t)$.

1.2.6.2 Methods of Measuring Exciton Migration

Several methods have been developed to measure the extent of exciton migration in organic semiconductors.[14] The most popular is photoluminescence quenching (PLQ), where thin films (on the scale of the diffusion length, typically 5-10 nm) of a sample are grown over an exciton quenching substrate like TiO_2.[65–79] Excitons that migrate to the interface are quenched, so by studying the photoluminesence as function of film thickness the exciton migration length can be extracted. There can be complications, however, due to the stringent requirements of the sample preparation for smooth thin films and possible FRET of the excitons to the interface.[80]

As an alternative to measuring the photoluminescence of the semiconductor, it is also possible to measure the conductivity of the TiO_2 that is induced by the charge transfer events at the interface, by monitoring the change in the microwave reflectivity.[81–84] This method has the added advantage of sensitivity to non-emissive exciton states, such as triplets, but does not resolve the other issues of PLQ.

Thicker samples can be used (on the scale of microns) in spectrally resolved photoluminescence quenching, where the sample is excited by a series of monochromatic wavelengths. The diffusion length can then be extracted by comparing to a single other sample without the quenching layer, however, this method is only compatible with materials with long diffusion lengths, such as molecular crystals.[85–90]

The quenching material may also be distributed within the semiconductor as a dopant, and the photoluminescence quenching studied as a function of the concentration of the

quencher, as long as the dopant remains well distributed and does not phase separate.[91–97] In each of these cases, there are also questions of how the presence of the quenching material perturbs the electronic structure and dynamics in the semiconductor.

Exciton annihilation can also be used to determine the exciton diffusion length, where the excitons act as their own quenchers. Since the efficiency of annihilation depends on the diffusivity of the material, the diffusion length can be extracted from fitting the photoluminescent decay profile at multiple excitation densities.[71, 87, 98–107] This method can be performed on a single sample, but requires robust materials that can withstand the intense laser fields used to create high excitation densities.

An elegant alternative to using quenching to measure exciton migration is to directly observe the evolution of an initially diffraction limited exciton distribution by imaging its photoluminescence.[59, 60] It has been used on quantum dot solids and molecular films with long triplet diffusion lengths. This method circumvents the need for a quenching site, while also avoiding the high excitation densities required for exciton-exciton annihilation, and can be performed on a diffraction limited area within a single film. It does still, however, face the challenge of measuring the small change cause by exciton migration, $L_d \sim 5 - 10$ nm in conjugated polymer films, in the relatively large, ∼200 nm, initial distribution, and the diffraction limited resolution is still insufficient to resolve the spatial heterogeneity in most conjugated polymers, as outlined below.

1.2.7 Spatial Heterogeneity in Organic Semiconductors

One of the major advantages of organic semiconductors is that many of them are solution processable, which can reduce the cost of device production. This processing method, however, produces kinetically trapped heterogeneous morphologies. Since the functionality of these materials is inherently tied to their structure, these heterogeneous local microstructures could have very different performance characteristics.[108–113] In order to fully understand the structure/function relationship of organic semiconductors in devices, it is critical to have a clear understanding of how their function varies over the microstructures present and how the boundaries between domains impact performance.

The length scale of this morphological heterogeneity varies with the material and preparation method. Polymers tend to produce disordered films with very short length scales for heterogeneity on the order of 10-100 nm.[114–119] Small molecules tend to form more highly ordered crystalline domains, which can have much longer characteristic length scales on the order of 1-100 μm.[111, 120–123]

The techniques used to study migration and dynamics, however, lack sufficient resolution to resolve this spatial heterogeneity. For example, traditional transient absorption measurements, typically used to study exciton dynamics, use long focal length lenses or mirrors to focus on the sample, creating beam waists on the order of 100-1000 μm. In most organic semiconductors these beam diameters will average the response of many heterogeneous microstructural domains, convolving their individual responses and obscuring the underlying structure/function relationship.

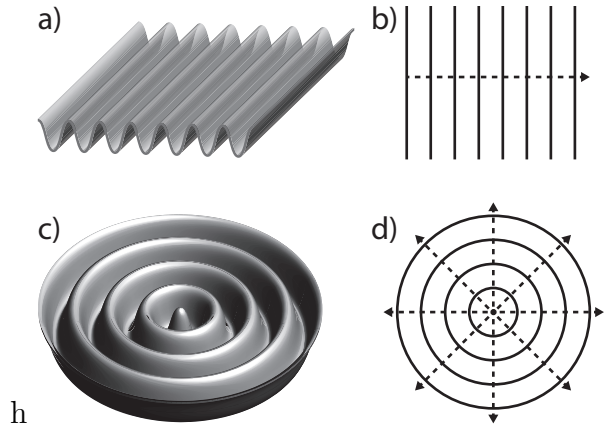

Figure 1.8: Illustration of waves, wavefronts, and rays: a) a plane wave, b) the wavefront for a plane wave, c) a spherical wave from a point source, d) the wavefront for a spherical wave. Some example rays are shown as dashed lines.

Additionally, most methods of measuring exciton migration, discussed above, excite bulk areas of the sample, and many require several physical samples for a single measurement. The best methods provide diffraction-limited resolution, which may be sufficient for some small molecule organic semiconductors, but will not be able to resolve the sub-diffraction heterogeneity in conjugated polymers.

1.2.8 Methods for Enhancing Spatial Resolution

Enhancing spatial resolution in optical measurements, a theme in Chapters 2, 3, and 4, typically involves some form of optical microscopy. To review, we will begin with a brief introduction to the basic concepts of microscopy and the diffraction limit and then discuss some methods of improving the spatial resolution of measurements.

1.2.8.1 Background on Microscopy

Wavefronts and Snell's Law: In optics and microscopy, light can treated as a wave, as illustrated in Figure 1.8, with the mathematical form:[124–126]

$$E = Eo\, e^{i(kz-\omega t+\phi)}, \tag{1.59}$$

for Figure 1.8a, where $k = \frac{2\pi}{\lambda}$ is the wavevector, $\omega = 2\pi\nu$ is the angular frequency, λ is the wavelength, ν is the frequency, z is the direction of propagation, t is time, and ϕ is the phase. For simplicity, rays and/or wavefronts are commonly used to depict the shape of the field. The wavefront can be thought of as an isosurface of phase, shown in Figure 1.8 b) and d) as solid curves, and will be an important concept in Chapters 3 and 4. For a perfectly collimated laser beam, the phase is uniform in each plane perpendicular to the ray, so the

wavefront is a flat plane, giving rise to the phrase "plane wave" to describe well-collimated light. Rays are drawn in the direction of propagation, shown in Figure 1.8 as dashed lines. The propagation direction is always perpendicular to the wavefront, so one way to change the direction of propagation is to intentionally tilt the wavefront. This can be achieved by an angled interface with a material of a different index of refraction.

As the wave enters the higher index material it slows down. The speed of light in a material, c' is

$$c' = \frac{c}{n}, \tag{1.60}$$

where c is the speed of light in vacuum and n is the index of refraction in the material. With this reduction in speed, there is a corresponding reduction in the wavelength,

$$\lambda' = \frac{\lambda}{n}. \tag{1.61}$$

This occurs because the energy of a photon is related to the frequency of the electromagnetic wave. Thus, when the speed changes the wavelength must also change to conserve energy:

$$E = h\nu = \frac{hc}{\lambda} = \frac{hc'}{\lambda'}. \tag{1.62}$$

Now we can construct a picture of a refracting wave as shown in Figure 1.9. If we know the

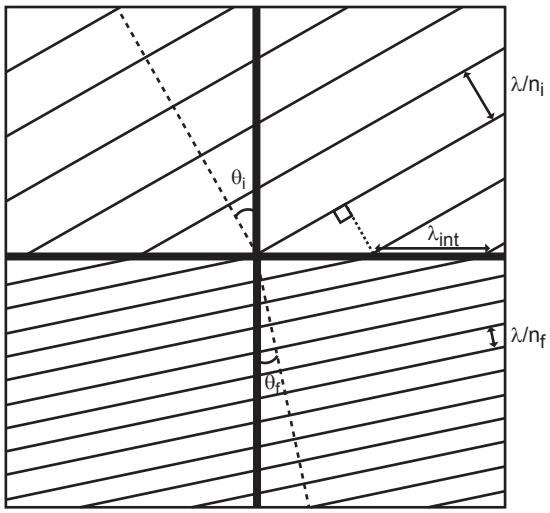

Figure 1.9: Illustration of Snell's Law

angle, θ_i, of the incoming wave relative the surface normal and the index of the materials, n_i and n_f, we can calculate the refracted angle. We start by considering the phase of the incoming wave along the interface. The phase of the field along the interface can be described by a sine wave with $\lambda_{int} = \frac{\lambda}{n_i \sin\theta_i}$. To maintain continuity of the phase, the phase of the

field in the material must match the phase of the field at the interface. The wavelength in the material, however, has changed so the angle must also change,

$$\lambda_{int} = \frac{\lambda}{n_i \sin\theta_i} = \frac{\lambda}{n_f \sin\theta_f}, \tag{1.63}$$

which yields Snell's Law:

$$n_i \sin\theta_i = n_f \sin\theta_f. \tag{1.64}$$

Lenses: The change in speed and wavelength at an interface of two materials with different indices of refraction acts to tilt the wavefront and correspondingly change the direction of propagation. If the interface is curved, as in Figure 1.10, then the angle of refraction increases as the angle of incidence increases. So for a convex surface there is more deflection near the edges than at the center, and the field is focused. Equivalently, the phase is delayed more in the center than at the edges and the wavefront gains a concave curvature, which corresponds to a focusing field. The same principles can also be utilized to collimate light from a point

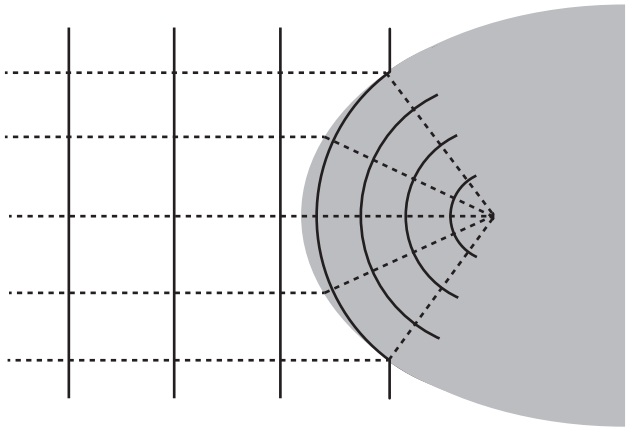

Figure 1.10: A plane wave is focused by a convex interface with a material of higher index (grey).

source, as shown in Figure 1.11. One important note is that a curved interface is not actually required. The focusing is achieved by modifying the wavefront, so the same effect can be produced by any means of imparting the correct pattern of phase delay transverse to the propagation direction. For instance, a flat interface with a index gradient will also act as a lens, as shown in Figure 1.12.

Imaging systems One or more lenses can be combined to form an imaging system. The action of a lens, in the "thin lens" approximation, is to focus collimated light (parallel rays) to a point at a distance f from the lens, where f is called the focal length of the lens. Conversely, the lens will also act to collimate light originating from the focal point. Based on these simple principles it is possible derive the location (d_i) and size (h_i) of the image for

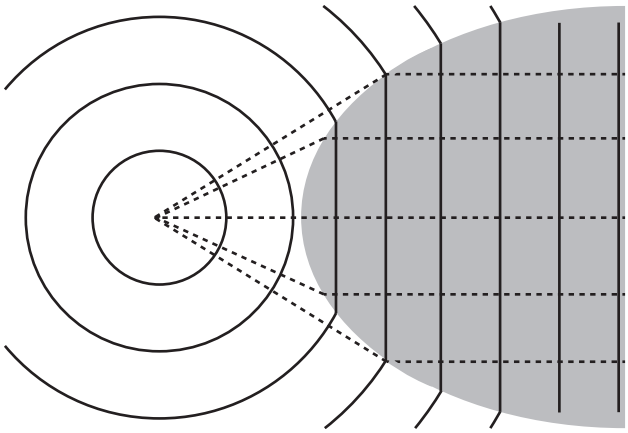

Figure 1.11: A spherical wavefront is collimated by a convex interface with a material of higher index (grey).

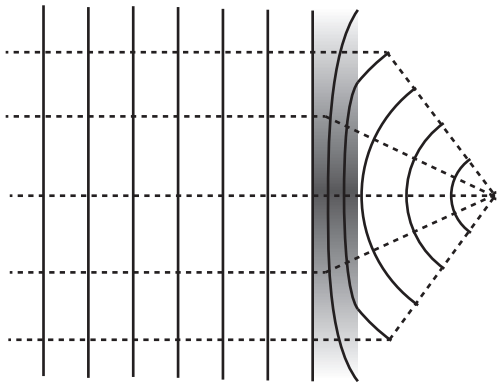

Figure 1.12: Illustration of an index gradient lens. Higher index is shown as a darker shade of grey.

an object of height (h_o) placed at a given distance (d_o) from a lens, as shown in Figure 1.13. The magnification is given by,

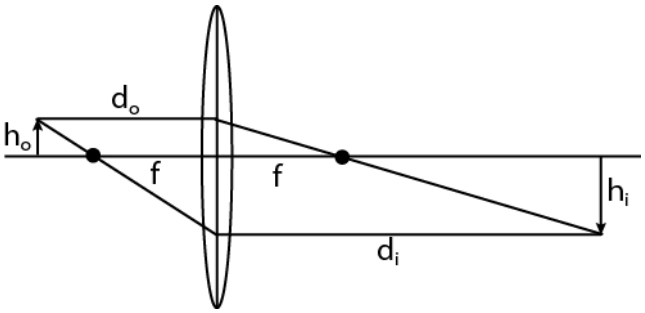

Figure 1.13: An illustration of the image (i) produced for an object (o) placed at distance (d_o) from a thin lens.

$$\begin{aligned} M &= \frac{h_i}{h_o} \\ &= -\frac{d_i}{d_o} \\ &= \frac{f}{f - d_o} \end{aligned} \tag{1.65}$$

where the negative value of M denotes the inversion of the image. More control of the image can be achieved by combining two lenses, as shown in Figure 1.14. The magnification of this

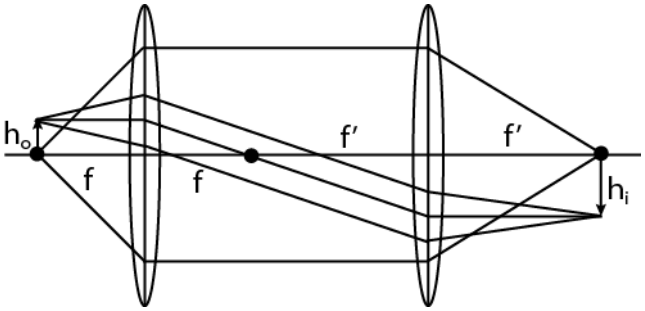

Figure 1.14: An illustration of a two lens imaging system with lenses of focal lengths f and f'.

system is $\sim f'/f$. The plane of the object and image are referred to as conjugate planes. In more complex, multi-lens, systems there are two sets of conjugate planes, one set in which the object is in focus, and one set in which the object is Fourier transformed. This plane, one focal length on the opposite side of a lens from an object placed in the focus, is called the back focal plane. Sets of these conjugate planes are illustrated in Figure 1.15. To see that the field in the back focal plane corresponds to the Fourier transform of the image, we briefly review Abbé theory.[127, 128]

Abbé theory relies on an understanding of how an object diffracts an incident plane wave. When a plane wave passes through an object with slits, close to the size of the wavelength in

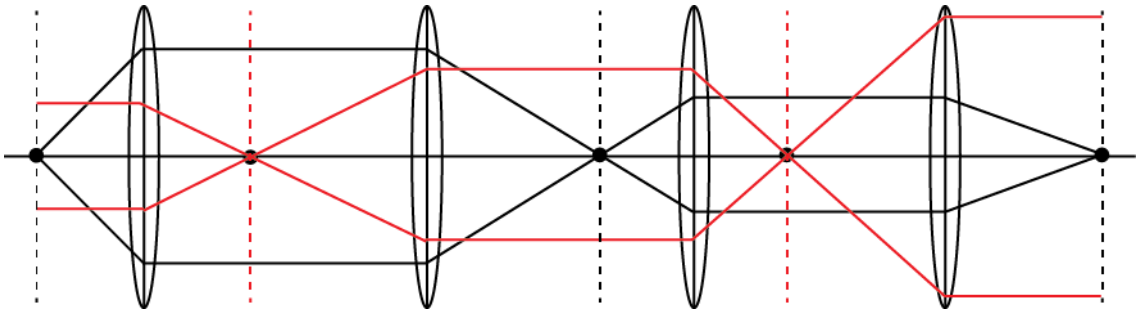

Figure 1.15: An illustration of the concept of conjugate planes in an imaging system. The two sets of conjugate planes are indicated by red and black dashed lines. The set of planes in which the object is in focus simply depends on where the object is placed.

the medium (λ') equally distributed with a separation (d), each slit in the plane of the object acts an individual point source. The constructive interference of the resulting spherical waves emitted from each slit will have a maximum for angles at which the path length difference for the interfering waves corresponds to an integer multiple (m) of the wavelength. This angle (θ_m) is given by,

$$\sin\theta_m = \frac{m\lambda'}{d}. \tag{1.66}$$

If the pattern is a sinusoidal gradient of transparency in the object plane, with a spatial frequency $k_o = 2\pi/\lambda_o$, rather than the square wave that would describe the slits in the case above, then only the zero and first diffraction order ($m = 0$ and $m = 1$) will be observed. An arbitrary object can then be conceptualized as a superposition of a large number of such spatial frequencies. The higher orders (m values) in the case of the slits originate from the need to superimpose many spatial frequencies to construct the square wave that describes the slits.

Abbé theory states that the light diffracted from an object corresponds to the light waves that would interfere to form its image. Two waves, both incident on an image plane with angle θ, interfere to create a spatial frequency, sine wave in the image plane, with a wavelength λ_o predicted by

$$\lambda_o = \frac{\lambda}{n\sin(\theta)}, \tag{1.67}$$

in analogy to Equation 1.63. Therefore, if the object has a spatial frequency $k_o = 2\pi/\lambda_o$, light will diffract from it at an angle determined by

$$\theta = \sin^{-1}\left(\frac{\lambda'}{\lambda_o}\right). \tag{1.68}$$

Features in the object plane with higher spatial frequencies, smaller objects, diffract light at larger angles, while features with lower spatial frequencies, large objects, will diffract light

at smaller angles. A lens placed one focal length from the object plane will then collimate these rays in the back focal plane of the objective, such that light diffracted from low spatial frequencies (small angles) corresponds to small radii from optical axis (axis through the center of all lenses), while light diffracted from higher spatial frequencies corresponds to larger radii. This concept is illustrated in Figure 1.16, which shows a high spatial frequency (red) and low spatial frequency (black) in the object plane (the slight offset is just for visualization). The rays diffracted from the higher spatial frequency appear at larger radii in the back focal plane. Also shown in Figure 1.16, is the concept of image manipulation by control of the back focal plane. Since the red rays are blocked, by an aperture in this example, they do not contribute to the image formation and the high spatial frequency information is lost in the image, while the lower spatial frequencies are reproduced in the image plane.

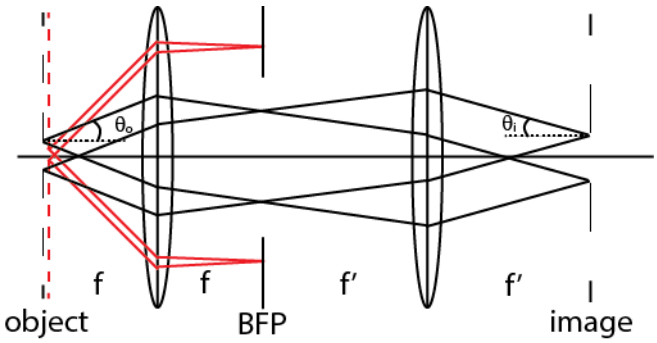

Figure 1.16: An illustration of how a Fourier transform of an object is created in the back focal plane (BFP) of a lens.

The magnification of the imaging system is ultimately determined by how the spatial frequencies in the sample are transformed in the image. For example, in Figure 1.16, the black rays are diffracted at a certain angle (θ_o) and interfered to form the image at a different angle (θ_i) creating a different spatial frequency in the image than was present in the object. Thus the magnification can more generally be written

$$M = \frac{n_o \sin(\theta_o)}{n_i \sin(\theta_i)}, \tag{1.69}$$

where the important quantity, $n \sin(\theta)$, is called the numerical aperture (NA), and

$$M = \frac{NA_o}{NA_i} \tag{1.70}$$

The resolving power of a lens is better characterized by its numerical aperture than by its focal length, because the highest spatial frequency that can be created in an image depends on the largest angle of diffracted light that can be captured by the lens.

The Diffraction Limit The size of the smallest feature that can be created by interference is referred to as the diffraction limit. As shown in Equation 1.67, the wavelength of the spatial frequency produced by interfering waves is $\lambda_i = \frac{\lambda}{n \sin\theta}$, where θ is the angle of incidence of the waves on the image plane. The size, d, of the feature created by this interference is taken to be half the wavelength,

$$d = \frac{\lambda}{2n \sin\theta} \tag{1.71}$$

$$= \frac{\lambda}{2NA}. \tag{1.72}$$

Thus the smallest feature that can be created in an imaging system depends on the wavelength of light used and the NA of the system. For a lens with an infinite diameter, $\theta \to \pi/2$ and $d \to \frac{\lambda}{2n}$, so the diffraction limit is $\sim \lambda/2$ or ~ 200 nm for visible wavelengths.[127, 128]

1.2.8.2 Super-Resolution Fluorescence Microscopy

Since many interesting biological and materials systems have features on length scales below the diffraction limit, extensive research has been performed on methods to achieve sub-diffraction-limited resolution fluorescence imaging, culminating in the 2014 Nobel prize in Chemistry being awarded from the development of super-resolution fluorescence microscopy.[129–137] These techniques are collectively referred to as super-resolution fluorescence microscopy. Many of these methods rely on collecting many photons from a single molecule emitter, creating a diffraction limited Gaussian distribution in the image, and then identifying the peak of the distribution to locate the emitter. These forms of localization microscopy, such as STORM,[131] PALM,[132, 133] and PAINT, can achieve nm-scale resolutions, but require many photon detection events from isolated emitter molecules. Structured illumination microscopy (SIM) images a grating onto the sample, where the spatial frequencies in the sample beat against the spatial frequency of the grating, creating Moiré patterns of low spatial frequencies that encode the information of much higher spatial frequencies in the sample.[134] This effectively translates a region of the Fourier space that normally falls outside of the aperture of the lens, to the region of the Fourier space that the imaging system can capture. By recording the pattern in the back focal plane for different angles of rotation of the gradient, a super-resolution image can be reconstructed. Finally, stimulated emission depletion (STED) microscopy uses structured beam modes to drive stimulated emission from the periphery of an initially diffraction-limited excitation volume. This method will be discussed in detail in Chapter 3, and forms the basis of the work in both Chapters 3 and 4. [135–137]

1.2.9 Contributions of the Presented Work

The work presented here explores the benefits of combining high spatial and temporal resolution methods to study exciton migration and dynamics in organic semiconductors at

the length scale of the underlying processes and the material heterogeneity. Chapter 2 will discuss the application of transient absorption microscopy to polycrystaline thin films of TIPS-Pn, revealing a polarization dependence that significantly aids the assignment of the excited state dynamics. In Chapter 3, we demonstrate the extension of STED microscopy to conjugated polymer solids, using their endogenous chromophores to create sub-diffraction images. Finally, Chapter 4 will present a new method of measuring exciton migration, on its native picosecond and nanometer scales, though a further adaptation of STED microscopy, and its application to CN-PPV, where the diffusion length is found to be $L_d = 16 \pm 2$ nm. This method of measuring exciton migration opens the door for correlative mapping of exciton migration length with the local substructure in conjugated polymers. The results presented herein, and the future experiments enabled by this work, will reveal the importance of matching the scale of the experimental resolution to the natural scale of the process or heterogeneity of the material, and enable high resolution studies of the structure/function relationship of exciton dynamics and migration in organic semiconductors, which will inform the rational design of next generation semiconducting materials.

Chapter 2

Transient Absorption Microscopy of TIPS-Pentacene Thin Films

2.1 Introduction to Ultrafast Dynamics in Small Molecule Organic Semiconductors

The exciton dynamics introduced in the previous chapter generally fall into two categories, spatial migration dynamics, and energetic population dynamics. While both are fundamentally important to the behavior of an organic semiconductor, the length scale of exciton migration is typically small, $\sim$ 10 nm for conjugated polymers and up to $\sim$ 1 μm for small molecules,[14] while the scale of heterogeneity in the population dynamics depends on the structural heterogeneity, $\sim$ 100 nm in conjugated polymers[114–119] and $\sim 1 - 100$ μm in small molecule films.[111, 120–123] This chapter will focus on improving the spatial resolution of measurements of the energetic population dynamics in a small molecule organic semiconductor, where the relatively large length scale of heterogeneity found in small molecule polycrystalline thin films allows individual domains to be addressed with diffraction limited optics.

Small molecule organic semiconductors, such as polyacenes, have a long history of study as model molecular systems.[4, 138–141] Many of these molecular materials can be solution processed to form thin films that exhibit well ordered crystalline domains, strong π-stacking, large carrier mobilities, optical absorption of visible wavelengths, and singlet fission. Additionally, their organic nature means that their material properties can be tuned by changing the chemistry of the molecular monomers, yielding a diverse and adaptable zoology of potential materials. These properties have recently garnered a resurgence of research on their potential application to organic electronics, such as organic photovoltaics (OPVs), organic light emitting diodes (OLEDs), and organic field effect transistors (OFETs).[1, 5, 45, 120, 142–147]

Exciton population dynamics (referred to as exciton dynamics in this chapter), are typically studied with transient absorption, also known as pump-probe spectroscopy, which uses

short laser pulses to resolve the response of a system to optical excitation with $\sim$ 100 fs temporal resolution (see Section 1.2.4.1). Transient absorption is a powerful tool in the study of photophysics, and has a long history of application to organic semiconductors and dyes, where the ultrafast time resolution enables detailed studies of excited state dynamics on their natural time scales.[12, 41, 45–49] Traditional transient absorption measurements, however, are performed with large spot sizes, on the order of 100 - 1000 μm, and thus average over the heterogeneous structures and responses present in most organic semiconducting materials.

The potential benefits of adding enhanced spatial resolution to transient absorption measurements have recently begun to be recognized in the growing field of transient absorption microscopy.[148–169] The results in this chapter, which were previously published in the Journal of Physical Chemistry C,[170] present further evidence of the importance of matching the resolution of measurements of dynamics to the scale of the material heterogeneity, by probing the domain specific photophysics of the small molecule organic semiconductor 6,13-bis-(triisopropylsilylethynyl)-pentacene (TIPS-Pn) in a home-built transient absorption microscope. With the enhanced spatial resolution of transient absorption microscopy, a probe polarization dependence in the dynamics within crystalline domains is revealed, which significantly aids the assignment of the observed dynamics, and would be obscured in traditional bulk measurements. A full kinetic model of the system is then constructed that successfully models both the temporal and polarization dependence of the signal, enabling a single fitting routine to account of all observed data trends.

This work represents an important first step to the enhancement of the spatial resolution of exciton dynamics in organic semiconductors. The lessons learned from the challenges presented by reducing the probed volume in these experiments provide valuable insight to the best methods to further improve the spatial resolution to match the sub-diffraction length scales of heterogeneity and exciton migration commonly found in organic semiconductors.

2.2 Conceptual Overview of Transient Absorption Microscopy

In order to resolve the dynamics from individual microstructural domains, it is necessary to increase the spatial resolution of transient absorption measurements so that the probed volume is smaller than the characteristic length scale of heterogeneity. For small molecule organic semiconductors, this can be achieved by performing transient absorption microscopy, where the pump and probe beams are coupled into an optical microscope and focused on the sample by an objective to a spot on the order of a few hundred nanometers to a few microns. Similar methods have been previously used to provide molecular specific contrast in biological imaging[148, 157–159, 169] and to reveal and understand the spatial heterogeneity of the excited state dynamics of inorganic nanostructures,[150, 153, 154, 171–175] graphene,[151, 155, 163, 176] perylene microcrystals,[166, 177, 178] and OPV polymer blends.[48, 152, 161,

167, 168]

Transient absorption microscopy operates on the same principles as traditional transient absorption, described in Section 1.2.4.1, but with increased spatial resolution. The improved resolution corresponds to a reduction in the sampled volume, which has several effects on the signal production that should be considered. First, the tighter focusing conditions mean lower beam powers are required in order to achieve the intensities needed to drive the third order non-linear response. This can be a benefit if the available power is limited, but care must also be taken to avoid sample damage due to thermal build up. This can be achieved by raster scanning the sample over several spatial locations, allowing a given sample location to rest and return to thermal equilibrium between measurements. Secondly, since the intensity on a given region of the sample needs to be approximately the same as in traditional transient absorption, the reduced sample volume in transient absorption microscopy causes a reduction in the observed signal level, since fewer chromophores are being probed. This is an important consideration, as the probed volume in transient absorption microscopy can be on the order of 1,000x - 10,000x smaller than in traditional transient absorption. Therefore, care must be taken to minimize any sources of noise.

2.3 Background on TIPS-Pn

One small molecule organic semiconductor that has received a lot of recent attention is 6,13-bis-(triisopropylsilylethynyl)-pentacene (TIPS-Pn), shown in Figure 2.1a.[1, 5, 120, 142–145] Pentacene, the core of TIPS-Pn, has been extensively studied and demonstrated to have efficient singlet fission, but can only be prepared by vapor deposition. TIPS-Pn shares the basic pentacene structure, but its bulky side groups increase its solubility in organic solvents, which makes it solution processable.[179] When cast in the proper conditions, TIPS-Pn forms polycrystalline thin films with $\sim$100 μm wide domains, as shown in Figure 2.1b. The side groups also have a dramatic effect on the packing structure of these domains. While pentacene has a herringbone structure, TIPS-Pn takes on a brick-layer conformation to accommodate the side groups. This conformational change increases the π-stacking leading to larger carrier mobilities and air stability, but the fundamental properties that make pentacene attractive for organic electronics are preserved.[180, 181] Additionally, both pentacene and TIPS-Pn are known to exhibit singlet fission, which may enhance the performance of these materials in OPV devices by potentially doubling the yield of excitons produced.[142, 146, 147, 182] The dynamics of singlet fission feature prominently in our transient absorption measurements.

The crystal structure of thin films of TIPS-Pn differs from that of a single crystal grown in solution.[179, 183] The orientation of the crystal relative to the substrate, as reported from X-ray diffraction,[183] is illustrated in Figure 2.1d, where the substrate is in the plane of the page, as is the $a-b$ plane of the crystal. Note, that the $S_0 \rightarrow S_1$ transition dipole is aligned with the short (transverse) axis of the pentacene core.[184]

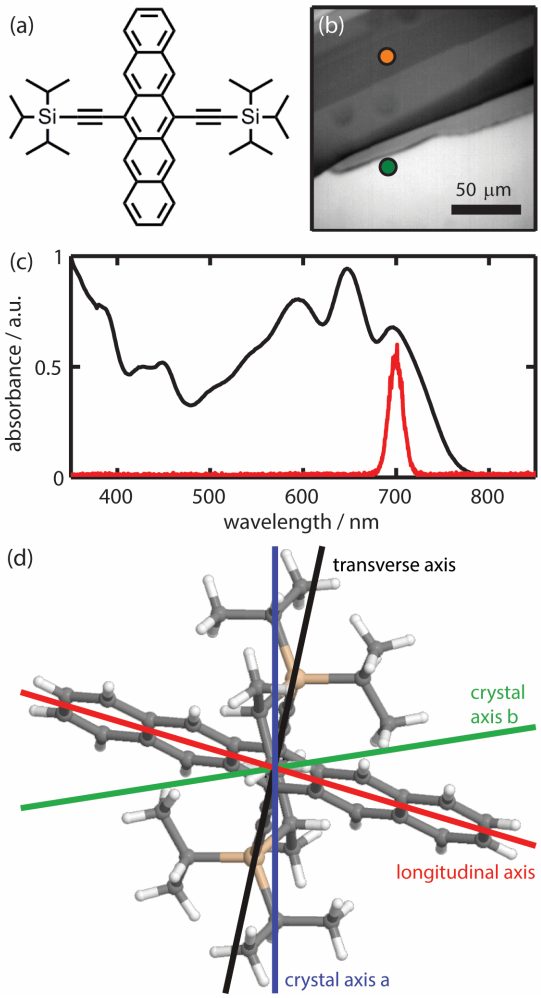

Figure 2.1: Important properties of TIPS-pn including: a) the chemical structure of TIPS-Pn, b) a polarized optical microscopy image of a TIPS-Pn film, c) the TIPS-Pn optical absorption spectra with our pump laser spectrum in red, d) the crystal axes of thin film TIPS-Pn with the substrate, and the crystal $a-b$ plane, in the plane of the page with the transverse and longitudinal axes shown in black and red respectively.

Next we will describe the methods for film preparation and transient absorption microscopy measurements, then present the results and analysis, including kinetic modeling.

2.4 Transient Absorption Microscopy Experimental Methods

2.4.1 TIPS-Pn Sample Preparation and Characterization

Glass substrates were sonicated for 10 min in acetone, soapy water, and then isopropyl alcohol with rinses of that solvent between each step. During deposition, the substrates were placed onto an aluminum block on top of a hot plate held between 60 and 70 °C. Approximately 40 μL of filtered (0.2 μm pore size) 5 mg/mL TIPS-Pn in toluene solution was drop cast onto the substrates and immediately covered with a 100 mm Petri dish to control the evaporation rate. This yielded 600 nm thick films with finger-like domains 50-150 μm wide and multiple millimeters long (Figure 2.1b).

Optical profilometry measurements were taken on an ADE MicroXAM-100 optical profilometer. Crosses were scribed into the sample to delineate regions of interest and to provide a zero for the thickness measurements. Linear absorption measurements were taken on a Cary 100 UVvis spectrophotometer (Figure 2.1c). Samples were then mounted face down onto large rectangular coverslips for TA microscopy measurements.

2.4.2 Transient Absorption Microscopy Setup

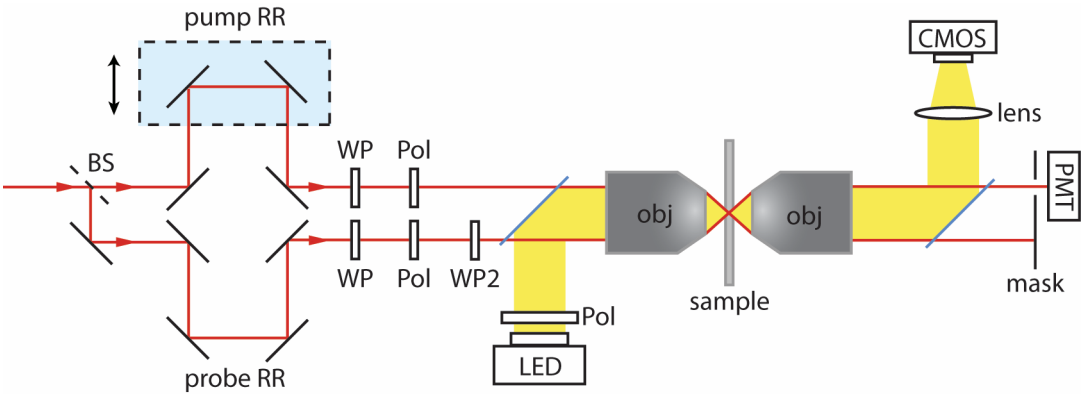

Figure 2.2: Schematic of the experimental setup for transient absorption microscopy.

Transient absorption microscopy measurements were conducted in a home-built optical microscope (Figure 2.2). Briefly, an 80 MHz mode-locked Ti:sapphire Coherent Mantis oscillator was used to seed a 5 kHz Coherent Legend-Elite regenerative amplifier, which was used to pump an optical parametric amplifier (Coherent OPerA Solo), producing laser light centered at 700 nm (Figure 2.1c), pumping the $S_0 \rightarrow S_1$ transition of TIPS-Pn. This beam was split into degenerate pump and probe pulses in a 4:1 intensity ratio that were fed into a 0.4 NA 10X Plan Apo Leica objective to yield sub-10-μm-diameter spot sizes (fit

to $1/e^2$) with pulse duration of ∼35 fs (FWHM). As shown in Figure 2.2, the collinearly propagating pulses were offset equidistant from the optical axis of the objective so that they would focus to the same spot in the sample plane. Energy fluences were set relatively low to avoid sample photodamage (400 μJ/cm^2 for pump; 100 μJ/cm^2 for probe) as confirmed by a power dependence study (Figure 2.7). The power was set for the pump and probe beams through separate waveplate and polarizer combinations. Additionally, probe polarizations were varied in steps of 15 degrees from 0° - 180° by rotating a second waveplate (Figure 2.2). After passing through the sample, the transmitted beams were collected using an identical objective to the first, and the pump beam was removed via spatial filtering while the probe beam was focused onto a Hamamatsu H9306-03 photomultiplier tube (PMT). The output from the PMT was split and coupled to two lock-in amplifiers, with one locked to the pump chopping frequency (500 Hz) to collect the unnormalized TA signal, ΔT, and the other locked to the laser pulse repetition rate to collect the probe transmission signal, T. By rastering the sample position using a computer-controlled Physik Instrumente piezostage, spatial maps of $\Delta T/T$ were generated. Additionally, by toggling the kinematically mounted mirrors shown in blue in Figure 2.2, the beam path could be modified to focus onto a CMOS camera (Thorlabs DCC1545M) for imaging the beams or sample.

2.5 Transient Absorption Microscopy of TIPS-Pn

2.5.1 Results for TA Microscopy on TIPS-Pn Thin Films

We performed transient absorption microscopy of TIPS-Pn films with 8 μm spot sizes, which can easily fit within single domains, allowing us to study and compare domain specific dynamics. Additionally, the crystalline nature of the domains in TIPS-Pn results in a probe polarization dependence (see Figures 2.3 and 2.4), which significantly aids in our assignment of the three observed excited state time scales in TIPS-Pn to ultrafast exciton thermalization, singlet fission, and exciton recombination. These probe polarization effects were obscured in previous studies, whose spot sizes were on the order of 200 μm, or ∼1000x greater than those used here, producing bulk measurements averaging over multiple domains and their respective orientations.[46, 142, 185, 186] The insights we gained through domain-specific studies of organic semiconductors will significantly enhance our understanding of the relationship between physical structure and device performance.

The strong polarization dependence of our signals illustrates that areas within our 8 μm spots have a high degree of crystallinity. In our measurement of these crystalline domains, the pump polarization is held in a fixed orientation, as it only serves to modulate the overall signal intensity by changing the coupling to the $S_0 \rightarrow S_1$ transition dipole and thus the magnitude of the initial excited state population. When the probe pulse interacts with the sample at time τ, however, it can couple to both the $S_0 \rightarrow S_1$ transition dipole, generating GSB and SE ($+\Delta T/T$ signals), and any resonant ESA transition dipoles ($-\Delta T/T$ signals), such as $S_1 \rightarrow S_n$, which can have their own distinct orientations. The projection of the

probe polarization onto each of these transition dipoles determines the contribution of the corresponding process to the observed transient signal, providing a means to better decouple the contribution of distinct excited state processes. While the spot size could be further reduced by increasing the NA of the objective or expanding our beams to overfill the back aperture, it is unlikely this would reveal additional significant heterogeneity in this sample and would reduce the observed signal.

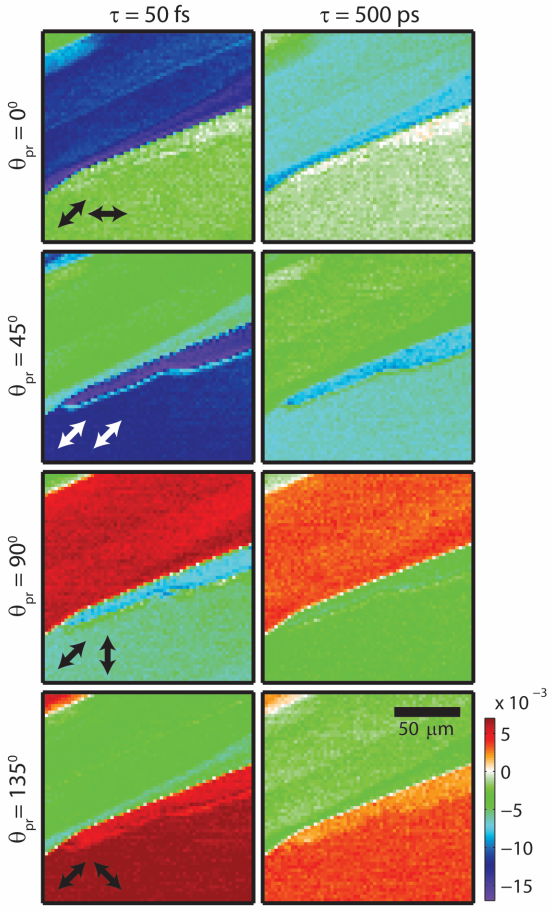

Figure 2.3: TA microscopy images of a TIPS-Pn film, in the same region of interest shown in Figure 2.1b, for probe polarizations (θ_{pr}) of 0°, 45°, 90°, and 135° and delay times of 50 fs and 500 ps. Positive $\Delta T/T$ signals are shown in orange and red while negative $\Delta T/T$ signals are shown in green and blue.

Transient absorption microscopy data can be collected in multiple modalities. The spatial variation of the transient absorption signal can be examined by fixing the laser polarization and pump-probe time delay, while scanning the sample over a dense lattice of spatial locations to build a transient absorption image of the sample. As shown in Figure 2.3, these images may then be taken at a few discrete time delays and probe polarizations to reveal trends.

In Figure 2.3, two primary domains are observed with a domain boundary near the center of the image. The upper domain yields strongly negative, slightly negative, positive, and slightly negative signals at $\theta_{pr} = 0°$, 45°, 90°, and 135° respectively, while the lower domain yields slightly negative, strongly negative, slightly negative, and positive signals for the same probe polarizations. In all cases, the amplitude of the signal at $\tau = 500$ ps has decreased, but not changed sign, relative to $\tau = 50$ fs.

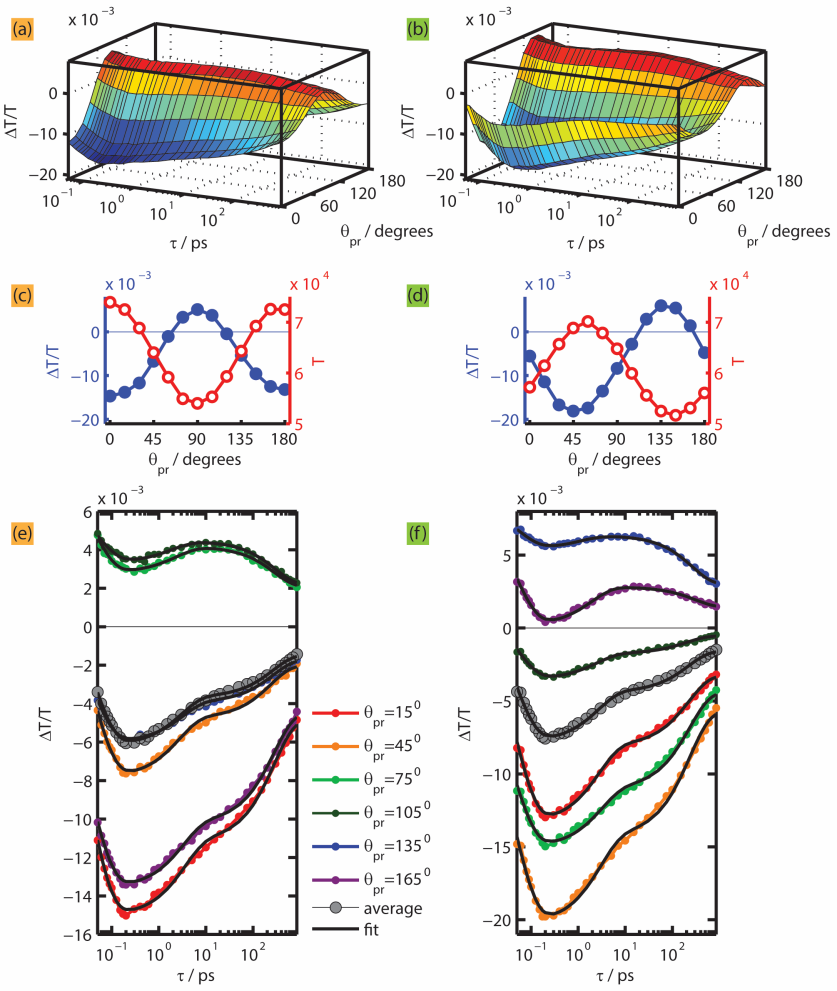

Figure 2.4: The transient absorption microscopy data for the orange (a,c,e) and green (b,d,f) spots in Figure 2.1b. a,b) Full $\Delta T/T$ vs probe polarization (θ_{pr}) and time delay (τ) data sets, where positive signals are red and negative signals are green/blue. c,d) The polarization dependence of the linear transmission (T) in red, with a polarization dependent slice of the $\Delta T/T$ data at $\tau = 1$ ps in blue. e,f) The evolution of the $\Delta T/T$ signal over the delay time for select probe polarizations, with the average of all probe polarizations shown in gray to approximate the signal from a traditional TA measurement.

It is clear from these images that transient absorption signal can be used as a contrast agent to identify distinct domains in TIPS-Pn films. The primary source of this contrast is the distinct and well defined orientation of each domain's transition dipoles, which produce clear differences in the transient signal for a given probe polarization and time delay. Thus the enhanced resolution of TA microscopy elucidates the relationship between the TA signal

and the relative molecular orientation within each domain.

The domain-specific, polarization-dependent, transient absorption signal may be studied in more detail by selecting only a few spatial locations (the two we chose are indicated in Figure 2.1b as orange and green spots) and increasing the number of polarizations and time delays for data collection. The resulting data are shown in Figure 2.4, where the left column (parts a,c,e) shows data from the upper domain (orange spot in Figure 2.1b) and the right column (parts b,d,f) shows data from the lower domain (green spot in Figure 2.1b). The surfaces in panels a and b show the full polarization and time delay dependence of the TA microscopy signal for the corresponding locations. Both spots have a periodic polarization dependence with positive and negative signals, where the negative component strongly outweighs the positive.

The primary difference between the domains is in the phase of the polarization dependence, as the transients in panels e and f show very similar dynamics. This phase difference is highlighted in panels c and d, which show the polarization dependence of the linear transmission T (red) and $\Delta T/T$ at $\tau = 1$ ps (blue). The phase offset between the two domains indicates their relative orientations. Additionally, the overall weighting of the $\Delta T/T$ signal towards negative values indicates that the probe interaction with ESA dipoles is stronger than its interaction with the GSB/SE dipole, by a factor of $\sim$2.5:1. Furthermore, the most positive $\Delta T/T$ signals are achieved for polarizations that correspond to the minimum in the linear transmission, indicating the orientation of the $S_0 \rightarrow S_1$ dipole for GSB and SE. This agreement, and the fact that the most negative $\Delta T/T$ signals are observed $\sim 90°$ from the $S_0 \rightarrow S_1$ dipole, indicate the the $S_1 \rightarrow S_n$ ESA dipole is oriented orthogonal to the $S_0 \rightarrow S_1$ dipole. Since the $S_0 \rightarrow S_1$ dipole is known to be oriented along the transverse (short) axis of the pentacene backbone, and projections of the transverse and longitudinal axis of the TIPS-Pn molecule are close to orthogonal in the sample plane (see Figure 2.1d), it follows that the $S_1 \rightarrow S_n$ dipole is oriented along the molecular longitudinal axis. Our ability to resolve these polarization dependent effects and assign dipole orientations is a direct result of the enhanced spatial resolution of TA microscopy, where bulk measurements would average over domain orientations obscuring the rich polarization dependence of the transient absorption signals. To illustrate the benefit of the polarization dependence, we have averaged our data over polarization to approximate the signal that would be obtained in traditional transient absorption and plotted it in gray in Figures 2.4e,f. This single trace would be the only accessible information in a traditional transient absorption measurement.

2.5.2 Assignment of the Observed Dynamics to Underlying Physical Process

To assign the observed dynamics to physical processes, it is most convincing to construct a kinetic model of the system based on the proposed photophysical processes and verify that the model can simultaneously reproduce all observed trends in the data in a global fit. To achieve this, a set of proposed physical processes must first be identified. We therefore, begin

by performing a simpler analysis with exponential fits to the data at individual polarizations, to identify trends and elucidate which physical processes could theoretically produce these dynamics. We return later on to a treatment based on a kinetic model.

2.5.2.1 Exponential Fits to the Observed Dynamics

The dynamics in Figure 2.4e,f, show that regardless of whether the $\Delta T/T$ signal is initially positive or negative at a given polarization, the signal first trends towards more negative values, then towards more positive values, before decaying towards zero. The time scales of these population dynamics can be revealed by fitting the individual polarization transients to a tri-exponential function with an offset,

$$\frac{\Delta T}{T} = a_1 e^{\tau/t_1} + a_2 e^{\tau/t_2} + a_3 e^{\tau/t_3} + c, \tag{2.1}$$

shown as black lines in Figure 2.4e,f. The full set of collected transients and their fits are shown in Figure 2.5. Plots of the fit parameters as a function of polarization (see Figures 2.6) reveal that the time scales are ∼50 fs, ∼3 ps, and ∼250 ps and do not vary with probe polarization or between the domains, as they describe the material-specific evolution of the excited state population. The amplitudes, however, have a strong dependence on the probe polarization and a phase shift between domains because the contribution of each process to the observed signal depends on the coupling of the probe to the respective transition dipole moment.

An additional advantage to resolving the probe polarization dependence via TA microscopy is the ability to clearly distinguish excited state population transfer from exciton relaxation. Exciton relaxation reduces the excited state population causing the signal to trend towards zero regardless of its sign, so the amplitude of the corresponding exponential in the fit changes with the sign of the signal to create a decay in the signal for all transients. We see this behavior in the third (∼250 ps) timescale and its amplitude (a_3). Excited state population transfer changes the relative contributions of the corresponding dipoles to the signal, causing the signal to trend toward more positive or negative $\Delta T/T$ values regardless of the sign of the signal, so the amplitude of the corresponding exponential in the fit has a constant sign for all polarizations. We see this behavior for the first two timescales ($\sim$ 50 fs and $\sim$ 3 ps) and their corresponding amplitudes (a_2 and a_3). A typical bulk measurement would average over the polarization dependence and return only a single transient signal, which we have estimated by averaging our polarization dependent data and shown in Figure 2.4e,f in gray. If these traces were taken independently, the second, ∼3 ps, timescale would likely be assigned as a fast component in the exciton relaxation, as is appears to act identically to the third, ∼250 ps, timescale. It is only through the polarization dependence that the second component can clearly be assigned to an excited state population transfer, since the signal increases for positive signals on this timescale, which can not be explained by exciton relaxation. Based on this analysis we assign the ∼250 ps timescale to exciton relaxation through internal conversion and/or spontaneous emission. The first two timescales

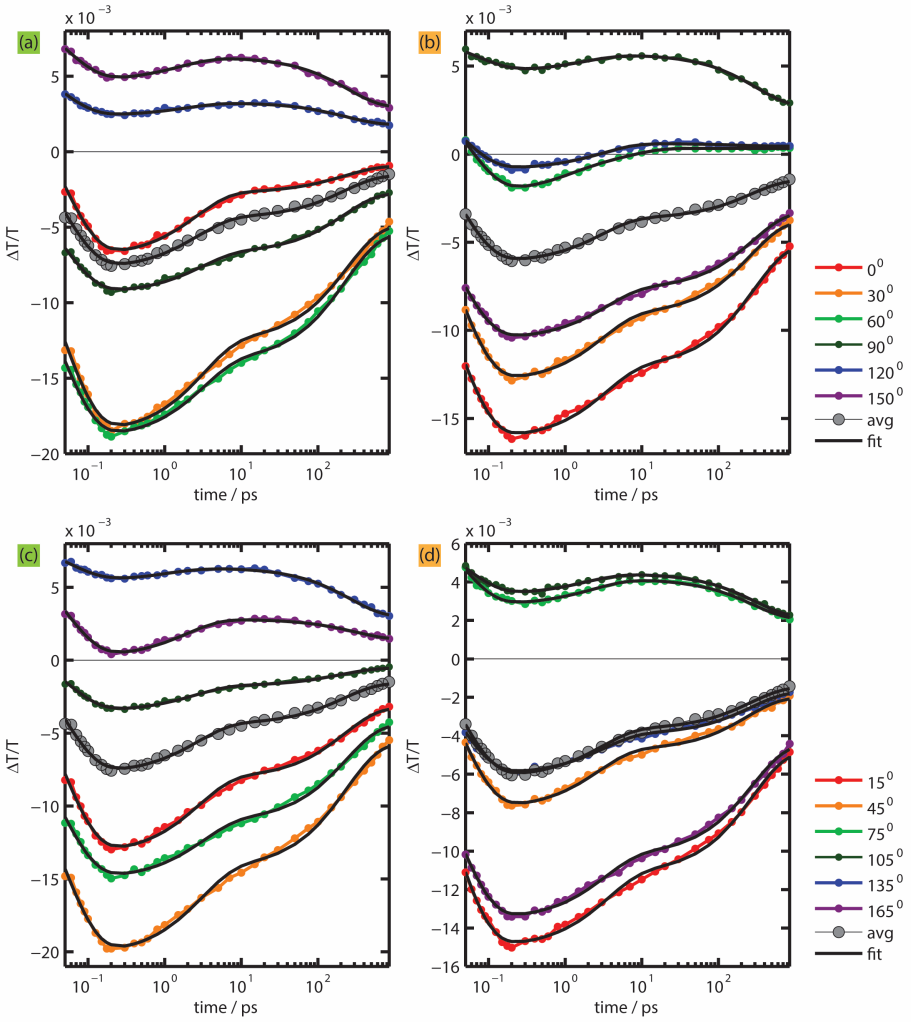

Figure 2.5: The transient $\Delta T/T$ data for all probe polarization for the green (a,c) and orange (b,d) spots, with the corresponding tri-exponential fits overlaid in black. Parts a and b shown the transients for $\theta_{pr} = 0°$, 30°, 60°, 90°, 120°, and 150°. Parts c and d shown the transients for $\theta_{pr} = 15°$, 45°, 75°, 105°, 135°, and 165°.

must correspond to excited state population transfer processes and their assignments are addressed below.

2.5.2.2 Assignment of Physical Processes

The fastest, ∼50 fs, timescale could correspond to a number of ultrafast processes, such as vibrational relaxation, charge separation, singlet fission or singlet-singlet annihilation.[187, 188] The power dependence, shown in Figure 2.7, demonstrates that the experiments are

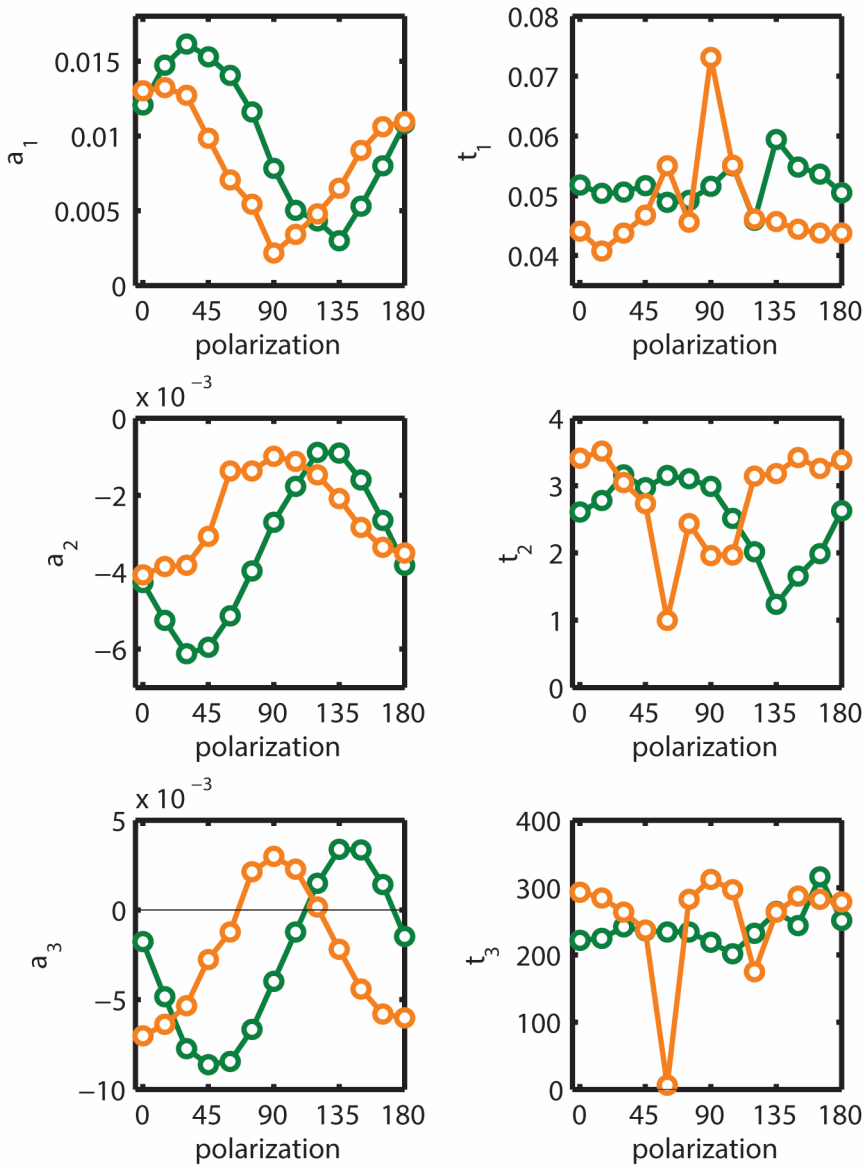

Figure 2.6: Variation of the tri-exponential fit parameters with probe polarization for the orange and green spots indicated in Figure 2.1b.

in a linear regime and thus annihilation does not contribute significantly to the signal. We must consider how the remaining processes would impact the $\Delta T/T$ signal to identify which could produce a trend towards more negative values.

To relate the change in the $\Delta T/T$ signal to the underlying population dynamics, recall that the ΔT component is just the change in the transmission of the probe, with the pump on and off, which in turn is related to the change in the probe intensity as it passes through the sample, due to the net stimulated absorption and emission from each level. The signal

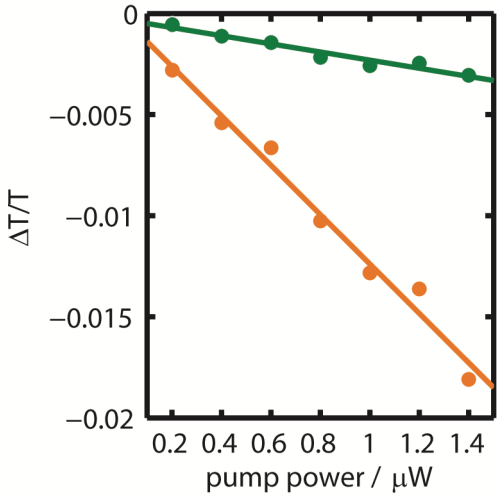

Figure 2.7: Power dependence of the TAM signal in the orange and green locations.

will depend on the occupation of each excited state, the strength of the transition dipoles for each process, and how strongly they couple to the probe field. Thus, we can build an understanding of how the redistribution of excited state population effects the generated signal, by considering the following approximation:

$$\Delta T/T \approx (\mu_{01} \cdot \rho_{pr})S_1 + (\mu_{01} \cdot \rho_{pr})S_0^v - (\mu_{1n} \cdot \rho_{pr})S_1 \tag{2.2}$$

where μ_{01} is the ground state dipole and ρ_{pr} is the probe field. Then $(\mu_{01} \cdot \rho_{pr})S_1$ describes the SE from the first excited state, $(\mu_{01} \cdot \rho_{pr})S_0^v$ describes the GSB due to the ground state vacancies (S_0^v), and $-(\mu_{1n} \cdot \rho_{pr})S_1$ describes the ESA from the first excited state to a higher level.

Since the ∼50 fs timescale process produces a more negative signal, it must correspond to some combination of an increase in ESA, decrease in GSB, or decrease in SE. Also the amplitude of the process, a_1 in Figure 2.6, is smallest for positive signals and largest for negative signals, indicating the dominant dipole for this process is roughly orthogonal to the linear absorption dipole, which is also the GSB/SE dipole. Thus, the increasing negative signal on this timescale is most likely due to an increase in the amount or strength of ESA.

Singlet fission, which is the conversion of a singlet into two triplets, would reduce the S_1 population, but increase the S_0^v population proportionally, canceling both effects. So the primary difference would be in the ESA, where the transfer from $S_1 \rightarrow TT$ would either increase or decrease the ESA depending on the relative strength of the probe's interaction with the $S_1 \rightarrow S_n$ and $T_1 \rightarrow T_n$ transition dipoles. Therefore, singlet fission is only consistent with the ∼50 fs timescale if ESA from the triplet state is strong. At the time we performed

this work the triplet ESA at our probe wavelength (700 nm) had previously been reported to be negligible in TIPS-Pn.[142] We concluded, therefore, that singlet fission is not likely to be responsible for this timescale. Ongoing work in our lab[189] has demonstrated that triplet absorption does in fact occur, however, it is not strong enough to produce the observed drop in signal on this timescale.

Charge separation would likely remove the contribution of stimulated emission, while also changing the ESA. The ESA on the original $S_1 \rightarrow S_n$ dipole would be lost, and an additional ESA from the free charges might be introduced. This dipole would, however, likely be aligned with the crystal lattice, specifically in the direction of the highest charge mobility. To determine if this effect is represented in the data, we fit the polarization dependence at several time delays to the sinusoidal function:

$$\frac{\Delta T}{T} = A\ \cos^2(x + \theta) + c \tag{2.3}$$

The evolution of these parameters over the delay time is shown in Figure 2.8. While the amplitude and offset change as the signal decays, the orientation (θ) only varies by a likely negligible 2°. The consistent orientation of the polarization dependence indicates that the ESA from the states populated by the excited state dynamics has very similar dipole orientations as the initially pumped state.

We conclude from this analysis that the simplest explanation for the ultrafast ∼50 fs timescale is vibrational relaxation from an initially pumped hot state, $S_1^n \rightarrow S_1^0$. This relaxation would shift the stimulated emission out of resonance with the probe, removing its contribution to the signal. Additionally, the ESA from S_1^n and S_1 would likely have the same orientation, differing only in a vibrational term. The strength of the ESA could either increase or decrease depending on the Franck-Condon overlap of each level with the higher lying state.

Now we must consider the second, ∼3 ps, timescale, over which the signal trends towards more positive $\Delta T/T$ values at all polarizations, regardless of the sign of the signal. This trend indicates an increase in GSB/SE or a decrease in ESA. The amplitude of this process (a_2 in Figure 2.6) also indicates that the dominant dipole is orthogonal to the linear absorption dipole, so the increasingly positive signal is likely due to a loss of ESA. This could be achieved by charge separation, migration to trap states, or singlet fission. Charge separation is unlikely to occur from the thermalized S_1^0 state due to the large binding energy of the Frenkel type exciton. The potential effect of trap states on the signal is unknown as it would depend on the ESA spectrum and absorption dipole orientation of the traps. Singlet fission, however, is known to occur in TIPS-Pn.[142] The effect of singlet fission would be the loss of SE from the singlet, if the SE has not already been lost due to thermalization, an increase in GSB due to the promotion of a second triplet, and the loss of the singlet ESA. So if the SE had already been lost due to thermalization, the gain in GSB and loss of the singlet ESA would cause the signal to trend upwards. The net effect would again depend on the difference in ESA between the singlet and triplet states. As indicated above, at the time we performed this work the triplet ESA at our probe wavelength (700 nm) had previously been

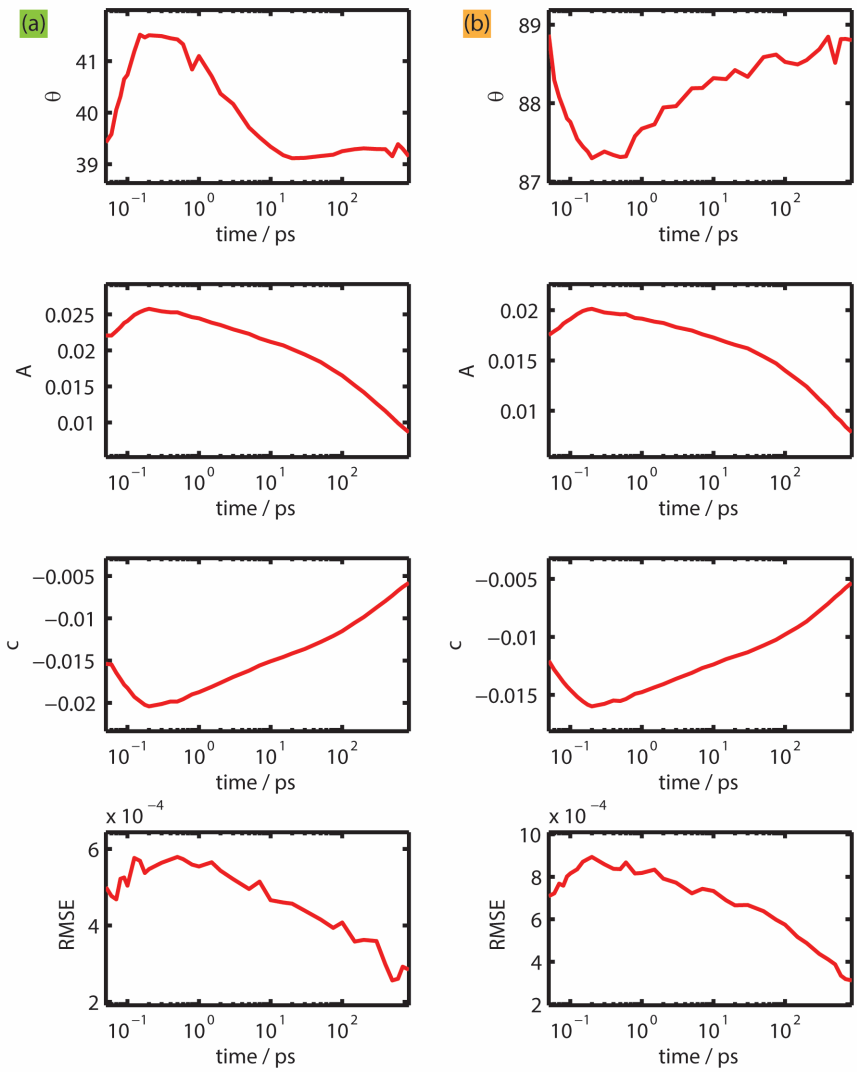

Figure 2.8: Time dependence of the parameters of the fit of the polarization dependence to a sinusoidal function for the green (a) and orange (b) spots. The plots correspond to the orientation (θ), amplitude (A), offset (c), and root mean square error of the fit (RMSE).

reported to be negligible in TIPS-Pn.[142] We concluded, therefore, that the net effect of singlet fission would be an increasingly positive $\Delta T/T$, as observed. Ongoing further work in our lab, with the introduction of multiple probe wavelengths,[189] has demonstrated that triplet absorption does in fact occur. Including this process in the analysis, however, did not change the assignments reported herein.

From the above analysis, we assign our observed dynamics to an ultrafast ∼50 fs thermalization in the singlet state, followed by singlet fission on a ∼3 ps timescale, with exciton

recombination at longer times. To check the validity of these assignments, we construct a kinetic model of the process to fit the data.

2.5.3 Kinetic Modeling and Fit to Experimental Data

We can now proceed with the construction of a kinetic model to simulate and fit the data based on the proposed assignments from the above analysis. The benefit of a kinetic model is that it can fully account for the interplay of the dynamic processes in the system, removing our dependence on intuitive arguments to support our assignments, verifying that the observed dynamics in the data can in fact be reproduced by the proposed kinetics. The kinetic model also allows the full data set to be fit simultaneously in a single global fitting routine, providing a higher degree of confidence in the result.

Based on the above analysis, we have constructed a four-level kinetic model (Figure 2.9b) to fit the data. The model includes the ground state (S_0), initially excited hot singlet state (S_1^n), thermalized singlet state (S_1^0), and the correlated triplet pair (TT). The kinetics included are thermalization ($S_1^n \rightarrow S_1^0$) with rate k_{th}, singlet fission ($S_1^0 \rightarrow TT$) with rate k_{sf}, triplet annihilation of the correlated pair ($TT \rightarrow S_1^0$) with rate k_{ta}, and singlet relaxation ($S_1^0 \rightarrow S_0$) with rate k_r.

In order to produce simulated data for the fit, we must first solve the coupled differential equations that describe the evolution of the population of the excited states. The system of equations is:

$$\begin{aligned} \frac{dS_1^n}{dt} &= -k_{th}S_1^n \\ \frac{dS_1^0}{dt} &= k_{th}S_1^n - k_r S_1^0 - k_{sf}S_1^0 + k_{ta}TT \\ \frac{dTT}{dt} &= k_{sf}S_1^0 - k_{ta}TT. \end{aligned} \tag{2.4}$$

Numerically propagating these kinetics in a fit, which tests many combinations of rates, would be computationally prohibitive. An analytic solution can be found, however, for a system of coupled first order linear differential equations. We begin by writing the equation in matrix form.

$$\frac{d\mathbf{S}}{dt} = \mathbf{K}\mathbf{S} \tag{2.5}$$

$$\mathbf{S} = \mathbf{S}(t) = \begin{bmatrix} S_1^n(t) \\ S_1^0(t) \\ TT(t) \end{bmatrix} \quad \mathbf{K} = \begin{bmatrix} -k_{th} & 0 & 0 \\ k_{th} & -(k_{sf}+k_r) & k_{ta} \\ 0 & k_{sf} & -k_{ta} \end{bmatrix} \tag{2.6}$$

The solution to this system of equations can be found by first solving for the eigenvectors and eigenvalues of the rate constant matrix, $\mathbf{K}$. Let $\mathbf{P}$ be a matrix where the columns of $\mathbf{P}$ are the eigenvectors, and $\mathbf{\Lambda}$ be the matrix of negative eigenvalues, where the diagonal holds the negative eigenvalues and there are no off diagonal terms. Then equation 2.6 can

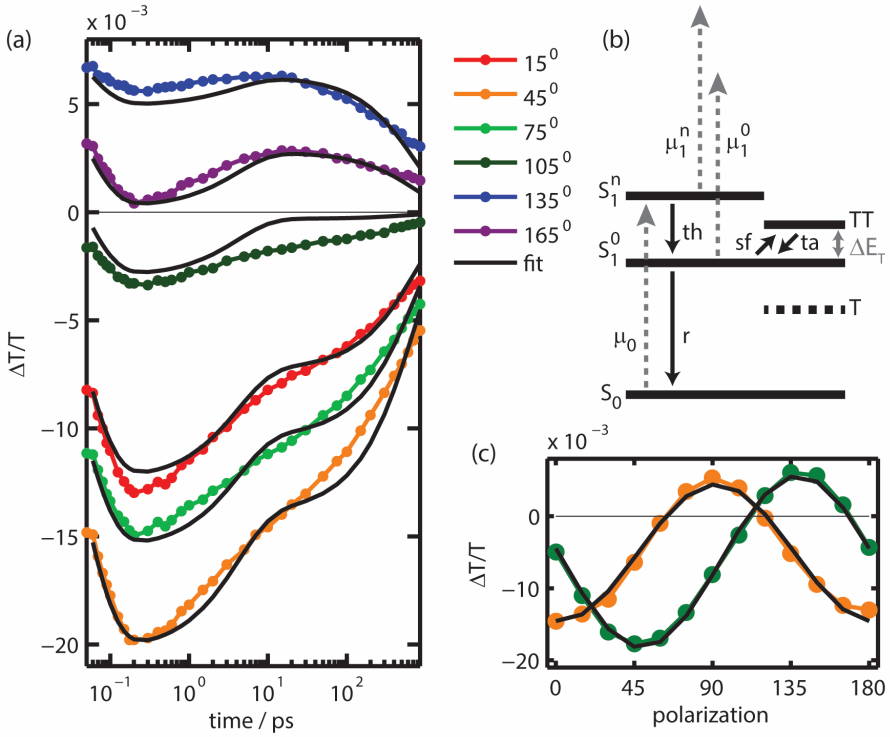

Figure 2.9: Kinetic model and fit to experimental data. a) Selected transients from the green spot with the fit overlaid in black. b) The levels, rates, and transition dipoles included in the kinetic model. c) The polarization dependence of the data from the green and orange spots with the results from the fit overlaid in black.

be solved using the following expression:[190]

$$\mathbf{S} = \mathbf{P}e^{\mathbf{\Lambda}t}\mathbf{P}^{-1}\mathbf{S_i} \tag{2.7}$$

Where $\mathbf{S_i} = [1; 0; 0]$ is the initial condition.

It is important to verify that $\mathbf{P}^{-1}\mathbf{K}\mathbf{P} = \mathbf{\Lambda}$. One thing to note about this expression is that the quantity $e^{\mathbf{\Lambda}t}$ needs to be a diagonal matrix with zeros in the off diagonal elements. If using MatLab's "eig()" function to find the eigenvectors and eigenvalues, $\mathbf{\Lambda}$ is reported as a 2D matrix with zeros for the off diagonal terms. If the exponential is then applied to this 2D $\mathbf{\Lambda}$ matrix the off diagonal terms will be ones, not zeros. The "diag" function can be used to correct for this with the expression:

$$\text{diag}(\exp(\text{diag}(\mathbf{\Lambda})t)).$$

This method efficiently calculates the predicted population dynamics for a given set of test rate constants by composing the rate matrix ($\mathbf{K}$) in Equation 2.6, finding its eigenvalues

and eigenvectors, and using Equation 2.7 to calculate the resulting population dynamics. In order to compare the fit to the data, however, the $\Delta T/T$ signal and probe polarization dependence produced by these dynamics must also be determined. Thus we use Equation 2.8,

$$\frac{\Delta T}{T}(t,\theta) = A_o(\theta)S_v(t) - A_1^0(\theta)S_1^0(t) + \left[A_0(\theta) - A_1^n(\theta)\right] S_1^n(t), \tag{2.8}$$

to calculate the $\Delta T/T$ signal and its probe polarization dependence from the predicted population dynamics in analogy to Equation 2.2. Here we include the GSB/SE dipole (μ_0) and separate ESA dipoles from S_1^n (μ_1^n) and S_1^0 (μ_1^0), shown in gray in Figure 2.9b. SE from S_1^0 is neglected, as it will be out of resonance with the probe. Absorption from the triplet state is also neglected, as it is assumed herein that there is no transition from this level that is resonant with our 700 nm laser pulse.[142] As mentioned above, on going further work has found that while triplet absorption does occur, it's inclusion in the model does not change the assignments reported here. The $S_v(t) = S_0(0) - S_0(t)$ term is the number of ground-state vacancies and accounts for GSB, the S_0^1 term contributes to the ESA, and the two terms for S_1^n account for its ESA and the SE. The amplitudes A_0, A_1^0, and A_1^n include the couplings of the probe field with the transition dipoles μ_0, μ_1^0, and μ_1^n, respectively, and are assumed to obey the following functional form:

$$A(\theta) = a + b\,\cos^2(\theta + c) \tag{2.9}$$

where c is the dipole orientation, b is the strength of the anisotropy in the dipole-probe interaction, and a is an offset to account for any disorder in the dipole orientation.

To perform the fit, we use MatLab's "lnsqcurvefit()" function with a trust-region-reflective algorithm. The fit uses a custom function to calculate the $\Delta T/T(\theta,\tau)$ data from an input guess for rate constants and the variables that define the amplitudes A_0, A_1^0, and A_1^n, based on Equations 2.6, 2.7, 2.8, and 2.9. To enable the fit to address the most physical parameters, the rate constant for the approach to singlet/triplet equilibrium, $k_T = k_{sf} + k_{ta}$, and the energy gap between level TT and S_1^0, $E_T = E_{TT} - E_{S_1^0}$, are used as inputs. The model then calculates k_{sf} and k_{ta} from k_T and ΔE_T via the Arrhenius relation[190]

$$\frac{k_{ta}}{k_{sf}} = e^{-\Delta E_T/k_b T}. \tag{2.10}$$

The fit of this simulated $\Delta T/T$ signal to the experimental data was performed simultaneously for all time points, all 13 probe polarizations, and both the green and orange spots, in a single global fitting routine. The fit parameters include $[k_{th}, k_T, \Delta E_T, k_r, A_0, A_1^0, A_1^n]$ at each location, where each amplitude is described by the three parameters in Equation 2.9. All fit parameters were allowed to vary independently between locations, with the only constraints being that the A_0 dipole orientation for each location was taken as constant from the polarization dependence of the linear transmission (T) in Figure 2.4c,d, and the ratio of the A_0 dipole strengths between the domains was inferred from the relative modulation of the these linear transmission curves.

The resulting fit for selected transients at the green spot is shown in Figure 2.9a, with additional fits to the full set of polarization traces for the green and orange spots in Figure 2.10. The rate constants and other fit parameters are summarized in Table 2.1 and the polarization dependent amplitudes A_0, A_1^0, and A_1^n are plotted in Figure 2.11.

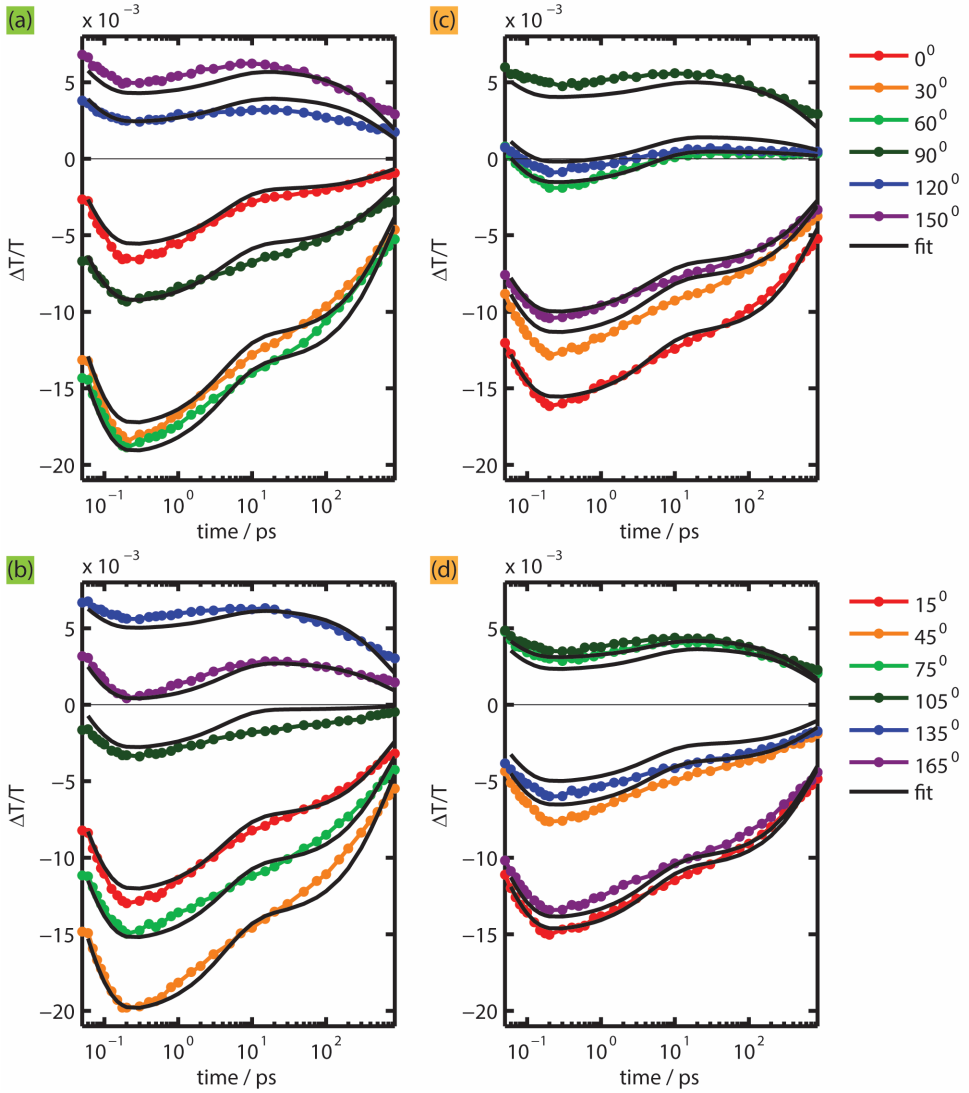

Figure 2.10: The transient $\Delta T/T$ data for all probe polarization for the green (a,c) and orange (b,d) spots, with the kinetic model fit overlaid in black. Parts a and b shown the transients for $\theta_{pr} = 0°$, 30°, 60°, 90°, 120°, and 150°. Parts c and d shown the transients for $\theta_{pr} = 15°$, 45°, 75°, 105°, 135°, and 165°.

The kinetic model fits the data well and the rates in the green and orange spots are in good agreement, even though the transients for a given polarization appear very different

	$1/k_{th}$ (fs)	$1/k_T$ (ps)	ΔE_T (meV)	$1/k_r$ (ps)
green spot	45	4.2	26	555
orange spot	43	4.7	26	665

Table 2.1: Table of parameters returned by the full kinetic model fit.

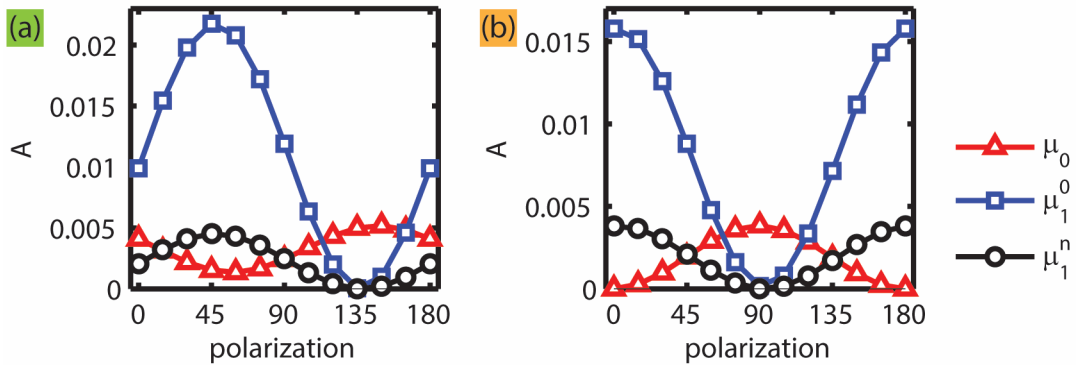

Figure 2.11: The polarization dependence of the amplitudes A_0, A_1^0, and A_1^n for the corresponding dipoles μ_0, μ_1^0, and μ_1^n, in red, blue, and black respectively, for the green (a) and orange (b) locations.

from each other. The kinetic model finds that the fastest rate is thermalization (k_{th}) of hot excitons, with a time constant of ∼44 fs, in excellent agreement with the fastest timescale in the empirical tri-exponential fit of 50 fs. The second fastest rate in the kinetic model is found to be the rise time of triplets due to singlet fission (k_T), with a time constant of ∼4.4 ps, in good agreement with the second time constant in the empirical fit of ∼3 ps. The slow component in the kinetic model is found to be the relaxation of the singlet state (k_r), with a time constant of ∼605 ps. The discrepancy here with the slowest time constant in the empirical fit of ∼250 ps is likely due to the fact that the tri-exponential fit includes an offset, while the kinetic model does not. The fit also accurately captures the polarization dependence of both data sets, as seen in Figure 2.9c. Additionally, the orientation of the transition dipoles μ_1^0 and μ_1^n were unconstrained in the fit, yet they are found to be perpendicular to the orientation of μ_0 in each domain (Figure 2.11), as predicted. The agreement in timescales between the two locations and the dipole orientations returned by the fit are further evidence that these domains differ only in an azimuthal rotation, and are likely oriented similarly with respect the substrate.

Finally, the fit to the kinetic model finds that the energetic splitting between the S_1^0 and TT states is 26 meV, with the TT state slightly higher in energy. While the model fitting places the TT state higher in energy than the S_1^0 state, Ramanan et al.[142] find a large singlet fission yield that would likely require the TT state to be lower in energy than S_1^0. This difference could be because of different sample morphologies probed. It is also possible that we have underestimated the triplet yield in our simple model by not

including the subsequent correlated triplet separation, TT $\rightarrow$ T + T, which would provide a greater driving force for the singlet fission process. Ongoing further work with the same TA microscope in our lab, now with multiple probe wavelengths and the inclusion of triplet absorption and the separation of the correlated triplet pair, has enabled us to further confirm the assignment that we provide in this thesis.[189] The minimal energy difference that we obtain indicates that the S_1^0 and TT states are effectively resonant with one another when thermal effects are taken into account and may provide some insight into the degree of resonance between the singlet and triplet pair energies, a property which could be tuned through molecular functionalization and design.

2.6 Conclusions and Outlook for Transient Absorption Microscopy

We successfully investigated the ultrafast photophyscis of individual domains in a polycrystalline thin film of TIPS-Pn, by focusing our lasers to spots $\sim$3 orders of magnitude smaller than is typical for bulk transient absorption measurements. This form of transient absorption microscopy can produce images using $\Delta T/T$ as a contrast agent, revealing regions with differing dynamics or orientations. In this case, we image two domains with distinct crystalline orientations producing clear contrast in their $\Delta T/T$ signals. We also observe a strong probe polarization dependence in the measured transient absorption signals, indicating a high degree of crystallinity and anisotropy in the regions within our $\sim$8 μm diameter focal volumes. This polarization dependence allows us to build a clear picture of the excited state dynamics and dipole orientations within each domain. Our analysis determines the primary ESA dipole to be roughly orthogonal to $S_0 \rightarrow S_1$ dipole. Furthermore, by fitting the experimental data to both an empirical tri-exponential and a full global kinetic model, we are able to determine that the excited state dynamics include the ultrafast thermalization of the initially excited hot singlet exciton in $\sim$50 fs, followed by singlet fission in the first few picoseconds, and finally internal conversion back to the ground state in several hundred picoseconds. The kinetic model also produces an estimate of the energy gap between the singlet and the correlated triplet pair of $\sim$26 meV, implying near resonance in singlet fission. The rapid rate of singlet fission in TIPS-Pn makes it a good model system for studying the effect of singlet fission on the efficiency of solar cells. These results from the fit to the kinetic model are aided by the additional constraints provided by multiple polarizations, which would be inaccessible in a traditional bulk transient absorption measurement.

The initially distinct response of different domains to polarized transient absorption microscopy can be reconciled by careful analysis of the polarization dependence and is revealed to be dominated by the domain orientation. The domains studied here are demonstrated to have consistent kinetics and likely adopt similar orientations relative to the substrate, differing only in their azimuthal orientation. After the domain-specific dynamics were characterized by this work, further transient absorption microscopy studies in out

research group revealed the structure and dynamics at domain boundaries in TIPS-Pn films[191] and that the variability in the individual domain dynamics in 2,8-difluoro-5,11-bis(triethylsilylethynyl)anthradithiophene (diF-TES-ADT) films is much greater than those in TIPS-Pn.[192]

We envision transient absorption microscopy as a powerful tool to examine more complex microstructures in more disordered materials, potentially decreasing the focal volume beyond the diffraction limit. The transient absorption signals from such excitation volumes would be extremely small, however, and the realization of sub-diffraction limit transient absorption microscopy on organic semiconductors will require significant advances. Fluorescence microscopy, on the other hand, has the capability to measure extremely small signals, down to the single molecule/photon regimes, with many advanced methods for sub-diffraction imaging, but at the expense of the ability to resolve the various GSB, SE, and ESA signals available in transient absorption, which inform studies of population dynamics. To further our study of the spatial resolution of exciton dynamics in organic semiconductors, we therefore turn our attention to super-resolution fluorescence microscopy and the extent of exciton migration in conjugated polymers.

Chapter 3

Extending STED Microscopy to Electronically Coupled Materials with Endogenous Chromophores

3.1 Motivation for STED on Conjugated Polymers

As demonstrated by the results in the previous chapter, there are substantial benefits to spatially resolving studies of exciton dynamics in heterogeneous materials. The diffraction limited transient absorption method presented above, however, is only suitable for use in materials with relatively large scales of heterogeneity. Many complex, naturally luminescent materials possess much smaller, nanoscale, structural heterogeneity. The effect of this heterogeneity on the materials' optical properties has been difficult to determine because of the challenges of imaging naturally luminescent materials below the optical diffraction limit. In many cases, these materials are composed of organic molecular chromophores that are packed so densely that they are electronically coupled; their Coulomb interactions rediagonalize their electronic quantum mechanical states, leading to optical properties of the resulting material that differ significantly from those of the individual molecular components.[4] These properties range from static spectral characteristics and oscillator strengths to the ultrafast dynamics of charge carrier or excitation energy transport.[53, 193–196]

For example, the solution-processing of modern printable organic-electronics creates kinetically trapped solid structures, which must be understood in the context of their local and macroscopic effects on the functional electronic and optical properties of these materials.[170, 191, 197–201] When the morphology of these materials is critical to their function, fluorescent labeling, as is performed in bioimaging, is impractical because it disrupts the very structure whose effects are meant to be studied. Furthermore, the luminescence of the endogenous chromophores can overwhelm that of the dilute labels, and the labels may also electronically couple to the material, perturbing the function of both. These challenges exist for organic semiconducting solids composed of small π-conjugated molecules and polymers

used in optoelectronic applications, and they are equally problematic in luminescent biomaterials with endogenous chromophores, as found in photosynthesis,[202] circadian rhythm regulation,[203] and other forms of bioluminescence.[204] A common challenge in characterizing heterogeneous, naturally luminescent materials is that there are no straightforward means to obtain their optical properties on the characteristic length scale over which they vary.

The work presented in this chapter, previously published in the Journal of Physical Chemistry Letters,[205] will demonstrate a method to adapt stimulated emission depletion (STED) microscopy, a form of super-resolution fluorescence microscopy, to naturally luminescent materials, using their endogenous chromophores. An introduction and background information on STED microscopy is first presented (Section 3.2), along with practical experimental concerns for its application to arbitrary systems (Section 3.3), and a scheme for overcoming two photon absorption (2PA) of the STED pulse (Section 3.4). The experimental setup (Section 3.5) and results (Section 3.6) are then discussed for super-resolution imaging of conjugated polymer nanoparticles of poly(2,5-di(hexyloxy)cyanoterephthalylidene) (CN-PPV). The successful demonstration of this method of preparing sub-diffraction excitation volumes in naturally luminescent systems lays the foundation for local measurements of exciton dynamics and migration, on their native scales. In particular, the extension of this method to perform direct and local measurements of exciton migration in conjugated polymers will be explored in Chapter 4.

3.2 Background on STED Microscopy

3.2.1 Introduction to Stimulated Emission Depletion Microscopy

Stimulated emission depletion (STED) microscopy is a super-resolution fluorescence imaging technique developed by Stefan Hell.[135] STED is typically performed in a confocal microscope and achieves super-resolution by first exciting a diffraction limited distribution of chromophores with an excitation (pump) pulse, then driving stimulated emission with an annular depletion pulse (see Figure 3.1). This depletion pulse (or STED pulse) is sufficiently intense to drive the stimulated emission in the sample to saturation everywhere except near the center of the annulus, where the field goes to zero. The remaining excitation volume, after depletion, is confined to an area that can be vanishingly small and depends on the intensity of the STED pulse used.[137] This method of creating sub-diffraction excitation volumes in fluorescent materials has been predominately applied to biological imaging applications, by dye labeling samples with one of the chromophores demonstrated to work with STED.[206–208] The resolution enhancement achieved by STED, and other super-resolution methods, has enabled a revolution in biological imaging and garnered a Noble prize in chemistry in 2014.[129, 130]

Below we will consider the theory and practical considerations of STED microscopy in more detail including the kinetics of stimulated emission depletion (Section 3.2.2), the

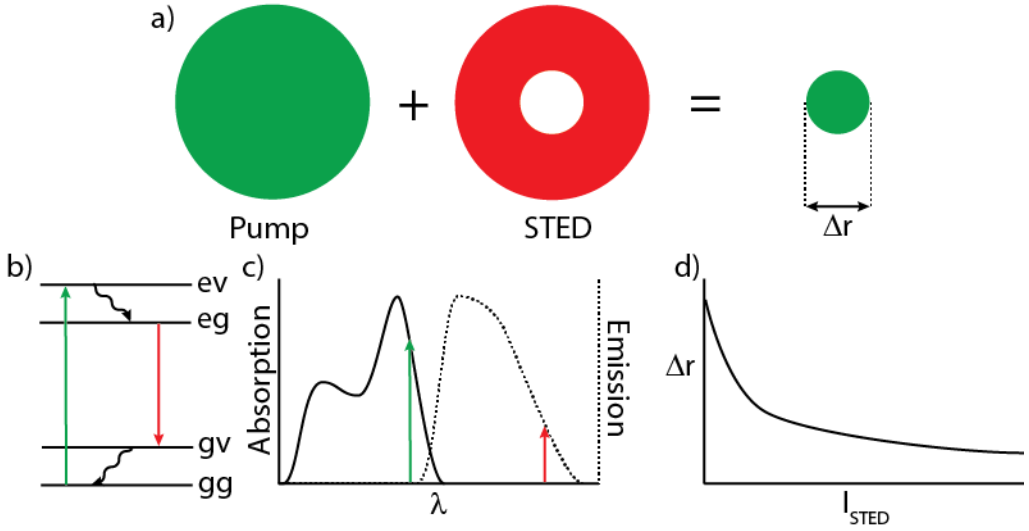

Figure 3.1: Schematics of important concepts in STED microscopy including: a) the beam modes and confined volume, b) energy levels for stimulated emission, c) typical wavelength of the pump and STED pulses relative to the sample absorption and emission, d) the resolution of the confined volume vs STED intensity.

creation and characterization of the annular STED beam mode (Section 3.2.3), the effects of the STED polarization (Section 3.2.3.3), the theoretical resolution of STED microscopy (Section 3.2.4), and a brief overview of the practical limitations (Section 3.2.5) which are discussed in more detail in Section 3.3.

3.2.2 The Kinetics of Stimulated Emission Depletion

The kinetics of the stimulated emission depletion process are essentially the same as those in a laser. The system can be modeled with 4 levels, a ground and vibrational excited state in each of the ground and excited electronic levels, as shown in Figure 3.2a. An impulsive excitation drives the gg-ev transition creating a population in the excited state. This population then undergoes rapid vibrational relaxation in the excited state to eg. The stimulated emission field then strongly drives the eg-gv transition, creating an equilibrium between these levels. The field is left on long enough for the eg-gv equilibruim population to decay to level gg through the ground state vibrational relaxation. If the excited state vibrational relaxation is fast, the system can be simplified to a three level picture as in Figure 3.2b.

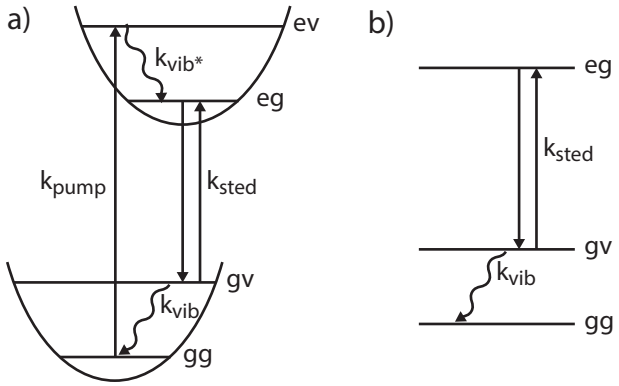

Figure 3.2: Level diagrams for STED: a) Full 4-level system, b) simplified 3-level system for impulsive excitation and fast excited state vibrational relaxation

To visualize the kinetics, we can write the rate equations for the 4-level system:

$$\begin{aligned}
\frac{dN_{ev}}{dt} &= k_{pump}N_{gg} - k_{vib*}N_{ev} \\
\frac{dN_{eg}}{dt} &= -k_{sted}N_{eg} + k_{sted}N_{gv} + k_{vib*}N_{ev} \\
\frac{dN_{gv}}{dt} &= k_{sted}N_{eg} - k_{sted}N_{gv} - k_{vib}N_{gv} \\
\frac{dN_{gg}}{dt} &= -k_{pump}N_{gg} - k_{vib}N_{gv}.
\end{aligned} \tag{3.1}$$

The time dependence of the field is encapsulated in the rate of the stimulated processes, k_{pump} and k_{sted} as[22]

$$k_i = B_i\rho_i(t), \quad i = pump \text{ or } sted, \tag{3.2}$$

where B is the Einstein coefficient and ρ describes the field. Now we can numerically propagate the kinetics with small time steps, δt:

$$\begin{aligned}
N_{ev}(t+\Delta t) &= N_{ev}(t) + [k_{pump}N_{gg} - k_{vib*}N_{ev}]\,\Delta t \\
N_{eg}(t+\Delta t) &= N_{eg}(t) + [-k_{sted}N_{eg} + k_{sted}N_{gv} + k_{vib*}N_{ev}]\,\Delta t \\
N_{gv}(t+\Delta t) &= N_{gv}(t) + [k_{sted}N_{eg} - k_{sted}N_{gv} - k_{vib}N_{gv}]\,\Delta t \\
N_{gg}(t+\Delta t) &= N_{gg}(t) + [-k_{pump}N_{gg} - k_{vib}N_{gv}]\,\Delta t
\end{aligned} \tag{3.3}$$

The results are summarized in Figure 3.3. Note that the STED pulse is typically delayed from the pump to allow for the excited state vibrational relaxation and that the eg and gv populations are forced to equilibrium by the STED field and decay together on the time scale of the ground state vibrational relaxation, so that the STED pulse must be long compared to the ground state vibrational relaxation to optimize the quenching of the excited state. This effect implies a practical limitation on the time resolution of an experiment, due to

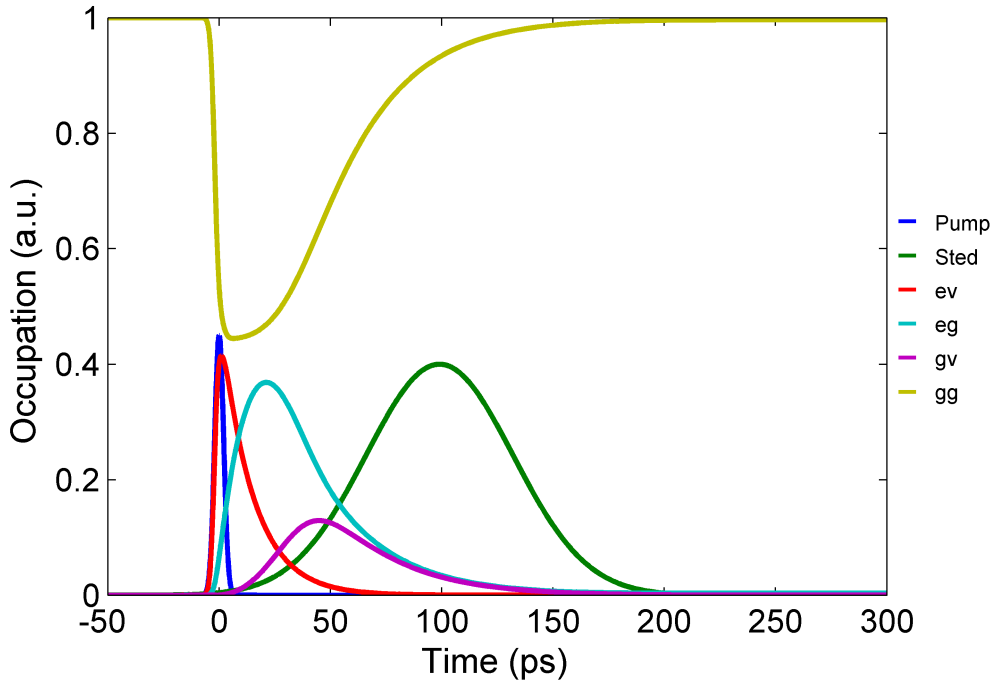

Figure 3.3: Kinetics of STED in a 4-level system

the required duration of the STED pulse. Since vibrational relaxation in solids is on the order of picoseconds,[25] an effective STED pulse can not typically be shorter than 10's of picoseconds, and is usually close to nanoseconds in duration.[206]

Now we will assume that the first two steps are impulsive and that the system starts in level eg, so that we can simplify our picture to the 3-level system in Figure 3.2b. Then if we approximate the STED pulse as a square wave, we can solve the system analytically for the duration of the pulse to find the excited state population remaining after the application of the STED pulse. First, the kinetic equations are written in matrix form,

$$\begin{bmatrix} \frac{dN_{eg}}{dt} \\ \frac{dN_{gv}}{dt} \\ \frac{dN_{gg}}{dt} \end{bmatrix} = \begin{bmatrix} -k_{sted} & k_{sted} & 0 \\ k_{sted} & -k_{sted} - k_{vib} & 0 \\ 0 & k_{vib} & 0 \end{bmatrix} \begin{bmatrix} N_{eg} \\ N_{gv} \\ N_{gg} \end{bmatrix}. \tag{3.4}$$

Then we can define

$$\mathbf{A} = \begin{bmatrix} N_{eg} \\ N_{gv} \\ N_{gg} \end{bmatrix} \quad \mathbf{K} = \begin{bmatrix} -k_{sted} & k_{sted} & 0 \\ k_{sted} & -k_{sted} - k_{vib} & 0 \\ 0 & k_{vib} & 0 \end{bmatrix} \quad \mathbf{A_i} = \begin{bmatrix} N_{eg}(0) \\ N_{gv}(0) \\ N_{gg}(0) \end{bmatrix} \tag{3.5}$$

and write the equation in a simple differential form.

$$\frac{d\mathbf{A}}{dt} = \mathbf{KA} \tag{3.6}$$

The solution to this system of equations can be found by first solving for the eigenvectors and eigenvalues of the rate constant matrix, $\mathbf{K}$. Let $\mathbf{P}$ be the matrix of eigenvectors, where the columns of $\mathbf{P}$ are the eigenvectors, and $\mathbf{\Lambda}$ be the matrix of negative eigenvalues, where the diagonal holds the negative eigenvalues and there are no off-diagonal terms. Then equation 3.6 can be solved using the following expression:[190]

$$\mathbf{A} = \mathbf{P}e^{\mathbf{\Lambda}t}\mathbf{P}^{-1}\mathbf{A_i}. \tag{3.7}$$

It is important to verify that $\mathbf{P}^{-1}\mathbf{KP} = \mathbf{\Lambda}$. One thing to note about this expression is that the quantity $e^{\mathbf{\Lambda}t}$ needs to be a diagonal matrix with zeros in the off diagonal elements. If using MatLab's "eig" function to find the eigenvectors and eigenvalues, $\mathbf{\Lambda}$ is reported as a 2D matrix with zeros for the off diagonal terms. If the exponential is then applied to this 2D $\mathbf{\Lambda}$ matrix the off diagonal terms will be ones, not zeros. The "diag" function can be used to correct for this with the following expression:

$$\text{diag}(\exp(\text{diag}(\mathbf{\Lambda})t)).$$

Equation 3.7 can be solved analytically in a program like Mathematica or numerically in MatLab. The main result we are interested in is the final population in the excited state level eg, which is,

$$N_{eg}(t_{on}) = N_{eg}(0)\frac{e^{-\frac{1}{2}(K_{eff}+2k_{sted}+k_{vib})t_{on}}((1+e^{K_{eff}t_{on}})K_{eff} + (e^{K_{eff}t_{on}}-1)k_{vib})}{2K_{eff}} \tag{3.8}$$

where $K_{eff} = \sqrt{4k_{sted}^2 + k_{vib}^2}$, t_{on} is the duration of the STED pulse square wave, and $N_{eg}(t_{on})$ is the population remaining in the excited state after the STED pulse finishes. Since we have assumed in this analysis that the STED pulse is a square wave, the rate k_{sted} is now a constant that is proportional to the intensity of the field. We can therefore plot $N_{eg}(t_{on})$ vs k_{sted} to see how the system responds to different STED intensities, shown if Figure 3.4. As you can see, there is a saturation in the response of the excited state population to increasing intensity for a given pulse duration, and that saturation occurs at different excited state populations for the various pulse durations. It is this non-linear saturation in the sample that allows STED to achieve sub-diffraction resolution. To see why, we will have to examine the spatial variation of the STED intensity and how it combines with this saturation effect to determine the resolution of a STED image.

3.2.3 The Phase Mask and STED Beam Mode

The transverse spatial mode of the STED pulse plays a critical role in determining the final resolution of the image, and the formation of the correct mode is one of the most

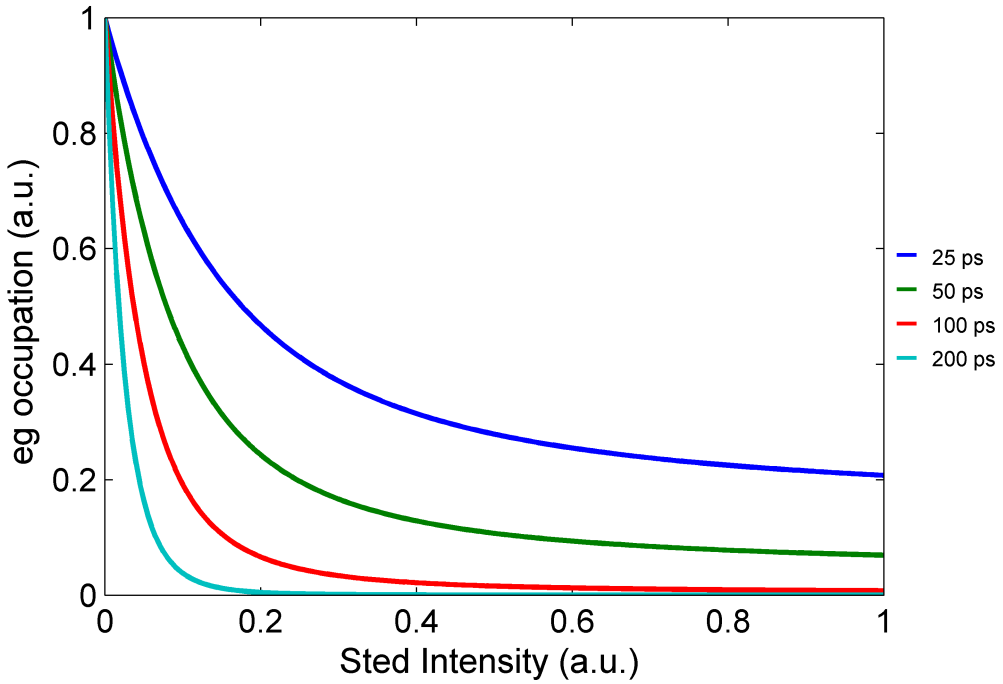

Figure 3.4: Excited state (eg) population vs STED intensity for several STED pulse durations, assuming a square wave STED pulse. The rate of vibrational relaxation was chosen to be 0.1 ps^{-1} for this plot.

challenging experimental aspects of STED microscopy. As such, care should be taken to understand the principles that determine the shape and quality of the STED point spread function (PSF).

3.2.3.1 The Phase Mask

The shape of the STED PSF depends not only on the mode of the beam, but also on the wavefront, which is a surface depicting the phase of the field as a function of location in the beam mode. The shape of the STED pulse PSF is essentially an intentional aberration. It is formed by using a phase mask to impart a specific wavefront (phase pattern), onto the beam. Since the STED PSF is formed by a particular wavefront pattern, it is easily distorted by additional wavefront errors, which are introduced by imperfection in optical surfaces, over-tightening of optics mounts, misalignment of imaging systems, and non-ideal lenses. To form a high quality STED PSF the beam incident on the mask should, therefore, start with as flat a wavefront as possible (constant phase across the mode), any optics in the beam line should be as smooth as possible (preferably $\frac{\lambda}{10}$ wavefront error), and the microscope must be well aligned. The phase mask used to produce the STED PSF is a helical phase ramp from 0 to 2π phase delay, as shown in Figure 3.5. When this wavefront is imprinted on the

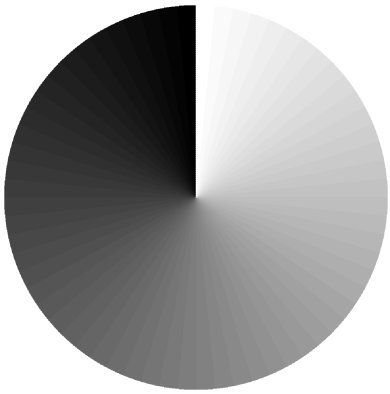

Figure 3.5: Vortex phase mask with phase delay varying from 0 (white) to 2π (black).

beam the center has all phases simultaneously, so the only solution to Maxwell's equations is for there to be zero amplitude at this position. In addition, points in opposing positions relative to the central null are out of phase and thus destructively interfere when the beam is focused, maintaining the central null. The desired phase delay is achieved by carefully depositing a polymer with different thicknesses for the different phase delays desired.

3.2.3.2 The STED Beam Mode

If we start with a Gaussian beam with a flat wavefront and imprint the wavefront described by the phase mask in Figure 3.5, we can calculate the resulting far field beam mode, as shown in Figure 3.6. The central zero shows up very quickly, with a set of surrounding fringes. Also note that the beam is not collimated after the phase mask. This is because it diffracts off the phase anomaly in the center of the phase mask.

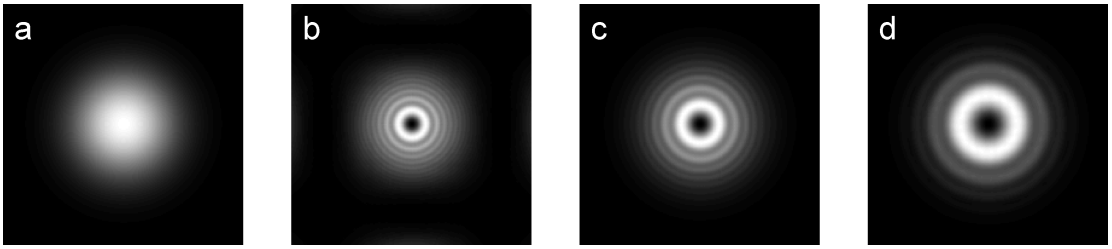

Figure 3.6: The simulated beam mode of an initial Gaussian beam passing through the vortex phase mask. Positions shown are (a) in the plane of the phase mask, (b) 0.5 m after the phase mask, (c) 1 m after phase mask, and (d) 2.5 m after phase mask. Each plot corresponds to 1 cm per side. For reference, the distance between the phase mask and sample in our experiment is ~ 2 m.

Additionally, the actual phase delay imparted to the beam depends on the thickness of the polymer, its index of refraction, and the wavelength of light used. Thus the phase mask is only a true 0 to 2π phase ramp for a particular wavelength. If there is a mismatch between the design wavelength and the wavelength used, the phase will not be stitched together properly at the thickness discontinuity and the beam will diffract off this edge. This can be seen in the far field as a dark line extending from the center of the STED pulse in a given direction. Usually a few diffraction fringes will also be visible. A simulation of this effect is shown in Figure 3.7.

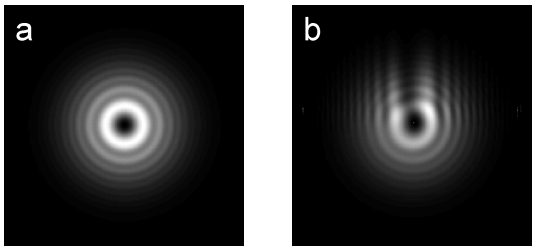

Figure 3.7: The simulated beam mode 1 m after the phase mask for (a) a phase mask match to the wavelength of the field and (b) a phase mask that only achieves a 0 to 1.6π phase ramp due to a mismatch between the design wavelength and the field. Plots correspond to 1 cm per side.

The fringes surrounding the main ring of intensity merge at sufficient distance from the phase mask, as shown in Figure 3.8, or if the beam is focused, as shown in Figure 3.9.

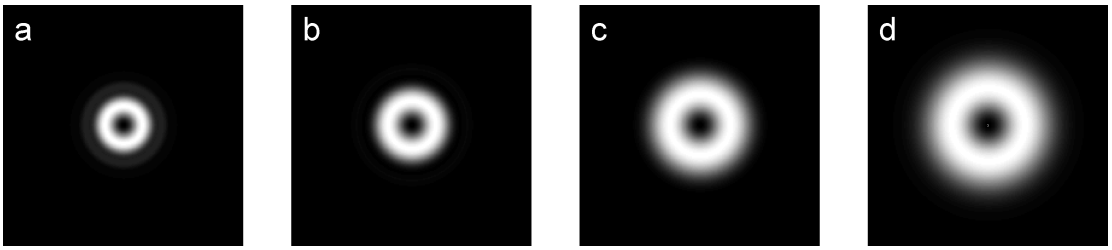

Figure 3.8: The simulated beam mode of an initial Gaussian beam passing through the vortex phase mask. Positions shown are, a) 5 m after the phase mask, b) 10 m after the phase mask, c) 20 m after phase mask, d) 30 m after phase mask. Each plot corresponds to 2 cm per side. For reference, the distance between the phase mask and sample in our experiment is ~ 2 m.

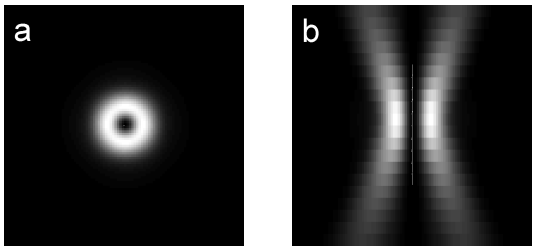

Figure 3.9: The simulated PSF of a focused STED beam with a 50 mm lens placed 1 m after the phase mask. Showing slices of a) xy for a 25×25 μm area and b) xz for a 25×500 μm area.

The far field, or focused, beam mode created by the proper phase mask, when properly centered on the Gaussian mode, is typically considered to be a Laguerre-Guassian distribution for $l = 1, p = 0$:[209]

$$\begin{aligned} E_{l,p}(r,\phi,z) =& \frac{C_{lp}^{LG}}{\mathrm{w}(z)} \left(\frac{r\sqrt{2}}{\mathrm{w}(z)}\right)^{|l|} \exp\left(-\frac{r^2}{\mathrm{w}^2(z)}\right) L_p^{|l|}\left[\frac{2r^2}{\mathrm{w}^2(z)}\right] \\ & \exp\left(-ik\frac{r^2}{2R(z)}\right) \exp(il\phi)\, \exp(-ikz)\, \exp(i\Phi(z)). \end{aligned} \tag{3.9}$$

C_{lp}^{LG} is a normalization constant and

$$\mathrm{w}(z) = \mathrm{w}_o \sqrt{1 + \left(\frac{z}{z_R}\right)^2} \tag{3.10}$$

is the beam waist. In the focus, $z = 0$ so $\mathrm{w}(0) = \mathrm{w}_o$. Here, z_R is the Rayleigh range,

$$z_R = \frac{\pi \mathrm{w}_o^2}{\lambda}, \tag{3.11}$$

$R(z)$ is the radius of curvature, which goes to infinity in the focus,

$$R(z) = z\left[1 + \left(\frac{z_R}{z}\right)^2\right], \tag{3.12}$$

and $\Phi(z)$ is the Gouy phase shift,

$$\Phi(z) = (|l| + 2p + 1)\arctan\left(\frac{z}{z_R}\right) \tag{3.13}$$

which is zero in the focus. Finally L_p^l are the generalized Laguerre polynomials. The STED pulse corresponds to $l = 1, p = 0$, so we only need to know the corresponding term,

$$L_0^\alpha(x) = 1. \tag{3.14}$$

Now substituting everything back in, we find an expression for the field:

$$E_{1,0}(r,\phi,0) = A\,r\,\exp\left(-\frac{r^2}{\mathrm{w}_o^2}\right)\exp(i\phi). \tag{3.15}$$

The corresponding intensity distribution is the square of the field:

$$I(r,\phi)\;\alpha\;r^2\,\exp\left(-\frac{2r^2}{\mathrm{w}_o^2}\right). \tag{3.16}$$

Comparisons of this functional form to the calculated far field beam mode and focused PSF are shown in Figure 3.10.

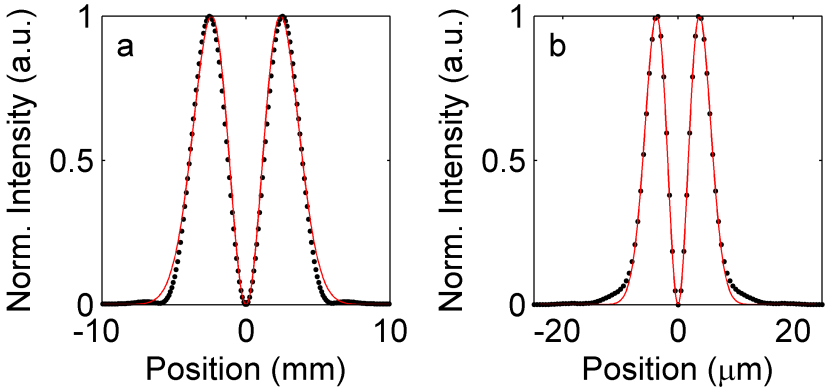

Figure 3.10: Comparison of the Laguerre-Gaussian distribution (red) to a) the calculated STED beam mode at 10 m after the phase mask, and b) the calculated PSF in the focal plane of a 50 mm lens places 1 m after the phase mask.

3.2.3.3 Polarization Effects

While the phase mask alone will produce a central null in the beam in the far field, it isn't enough to guarantee there will be near zero central intensity in the focus of the microscope. This is because of how the microscope objectives distort polarized light. When a ray of light passes through a lens, it is bent toward the optical axis. Since the polarization vector is orthogonal to the ray it gains a tilt in (x, y, z). This effect is most dramatic for high NA lenses like objectives, where the rays are bent at steep angles. This means that for a linearly polarized beam, the z component of the polarization will not cancel perfectly in the center of the STED pulse. In order for the z component of the field to cancel the beam must be circularly polarized with the same handedness as the phase mask, as shown in Figure 3.11.

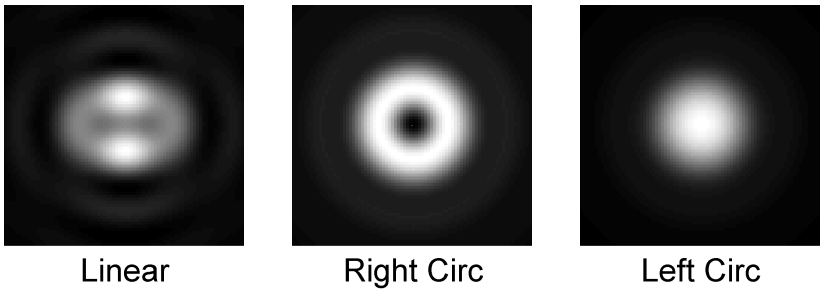

Figure 3.11: Simulations of the focus of a STED pulse with linear, right hand circular, and left hand circular polarization through a 2 mm focal length ideal lens. This simulation is based on simple geometric rays and interference.

This effect is more completely described by the electric field vector in the focal plane in the case of a high NA lens, which can be expressed as[210]

$$E(R,\psi,z) = \frac{i}{\lambda}\iint_{\Omega} A_1(\theta,\phi)\, A_2(\theta)\, A_3(\theta,\phi)\, \exp(it\phi)\, \exp\left[-ikR\sin\theta\cos(\phi-\psi)\right] \exp(-ikz\cos\theta)\, a(\theta,\phi)\sin\theta d\theta d\phi \tag{3.17}$$

where $E(R,\psi,z)$ is the electric field in the focal plane, λ is the wavelength in the medium, $k = 2\pi/\lambda$, θ is the angle between the optical axis and a given ray, and ϕ is the azimuth angle. The integral is over the solid angle Ω defined by $\phi\,\epsilon[0-2\pi]$ and $\theta\,\epsilon[0-\theta_{max}]$, such that $NA = n\sin(\theta_{max})$. A_1 is the amplitude distribution in the back aperture of the objective, for a first order Laguerre-Gaussian beam,

$$A_1(\theta,\phi) = r(\theta)\, \exp\left(-\frac{r^2(\theta)}{\omega_o^2}\right). \tag{3.18}$$

A_2 is called the apodization factor, which for an aplanatic objective is:

$$A_2(\theta) = \sqrt{\cos(\theta)}. \tag{3.19}$$

A_3 is a function that describes the aberrations in the imaging system, which we will neglect to see the ideal case. Finally $a(\theta,\phi)$ is the polarization vector for a given ray propagating towards the focus. Recombining these terms yield,

$$E(R,\psi,0) = \frac{i}{\lambda}\iint_{\Omega} r(\theta)\, \exp\left(-\frac{r^2(\theta)}{\mathrm{w}_o^2}\right) \sqrt{\cos(\theta)}\, \exp(i\phi)\, \exp\left[-ikR\sin\theta\cos(\phi-\psi)\right] a(\theta,\phi)\sin\theta d\theta d\phi, \tag{3.20}$$

for the field in the focal plane. Now consider the central point in the focal plane, where the null should be:

$$E(0,0,0) = \frac{i}{\lambda}\iint_{\Omega} r(\theta)\, \exp\left(-\frac{r^2(\theta)}{\mathrm{w}_o^2}\right) \sqrt{\cos(\theta)}\, \exp(i\phi)\, a(\theta,\phi)\sin\theta d\theta d\phi. \tag{3.21}$$

If we could neglect the polarization $a(\theta, \phi)$, the integral over ϕ would vanish. So we will need to carefully consider the polarization to determine the quality of the null. The polarization vectors in the collimated STED beam are summarized in Figure 3.12 under different polarization conditions.

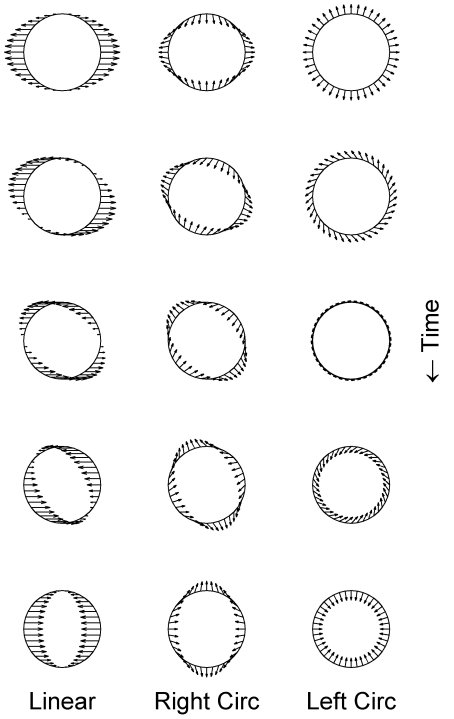

Figure 3.12: Polarization vectors for a collimated STED beam after passing through a right handed phase mask.

When the STED beam is focused through the objective, polarization vectors that point inwards will gain a $-z$ component, while vectors that point outwards will gain a $+z$ component. The cases that have symmetric polarization vectors where all vectors point either inwards or outwards will produce strong fields in z. In order to preserve the central null in the STED pulse, there needs to be a balance between the positive and negative z components. This is achieved for circularly polarized light with the same handedness as the phase mask (in this case right handed). Figure 3.13 shows the $x-z$ projections of the polarization vectors after passing through an objective with $NA = 1.4$. It is therefore important to ensure that the polarization of the STED field is as close to perfectly circularly polarized in the back focal plane of the objective as possible. This can be achieved by mounting a high quality achromatic $\lambda/4$ waveplate behind the objective on a kinematic (x, y) rotation stage. The orientation of this waveplate can then be set by monitoring the power transmitted by a rotating polarizer (driven by a small motor) placed down stream. The fluctuations in

transmitted intensity should be minimized by adjusting the rotation and (x, y) tilt of the waveplate to ensure circular polarization of the STED field.

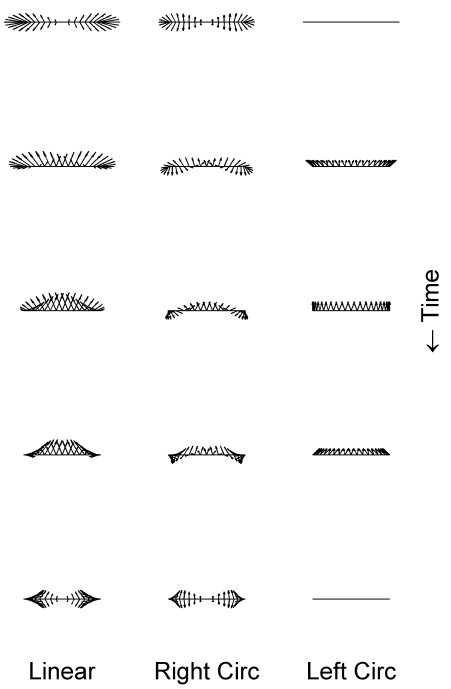

Figure 3.13: Polarization vectors for a focusing STED beam after passing through a right handed phase mask and a NA=1.4 objective.

3.2.4 Theoretic Resolution of STED Microscopy

Now that we have defined the shape and kinetics of the STED pulse we can determine the resolution that can be achieved. The spatial distribution of excitations remaining after the STED pulse can be calculated by combining the kinetics in Equation 3.3 with the spatial variation of the field we derived in Equation 3.16 to describe the spatial component of k_{sted} and assuming a Gaussian in time. The pump can be treated as a Gaussian in both space and time. The shape of the distribution depends on both the intensity of the STED pulse and its duration. When the duration of the STED pulse is large compared to $\frac{1}{k_{vib}}$ the distribution can be reasonably approximated as a Gaussian whose full width half max (FWHM) is a function of the STED intensity. This relationship has the following functional form:[137]

$$\text{FWHM} = \frac{\lambda}{2n \sin\theta \sqrt{1 + \frac{I_{STED}}{I_{sat}}}}. \tag{3.22}$$

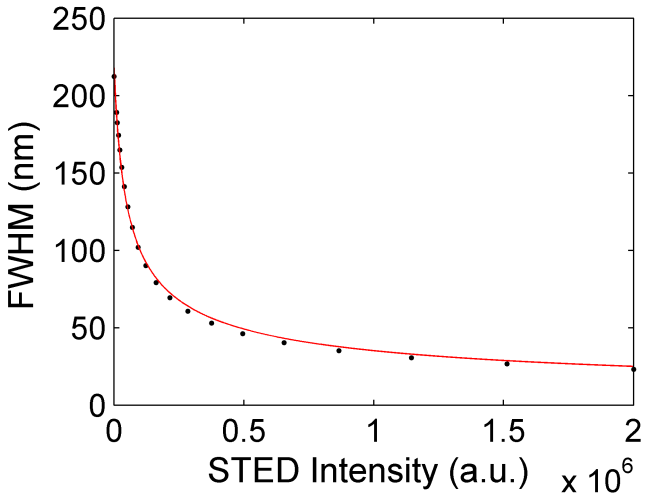

Figure 3.14: Simulation (black) of the FWHM of the final excited state population distribution as a function of the intensity of the STED pulse with a fit to the functional form in Equation 3.22 (red). The intensity axis is in the arbitrary units of the simulation.

Figure 3.14 shows a plot of the simulated FWHM of the final distribution as a function of the STED intensity (black) with an overlay of a fit to the functional form in Equation 3.22 (red).

3.2.5 Practical Limitation

In practice, the actual resolution of a STED image is limited by several factors. The central null or "zero" in the center of the STED pulse is never perfect and the field intensity in this region is typically on the order of ∼1-2% of the maximum intensity. The imperfection in the "zero" results in some quenching of the excitation in the center of the pulse, which limits the maximum STED intensity that can be used before sacrificing signal/noise. An additional limitation on the STED intensity is the damage threshold of the sample. The STED intensity can not be arbitrarily increased without causing thermal damage or even ablating the sample. There are also spectral considerations, such as the wavelength of the STED pulse. Any overlap with the absorption profile will prevent quenching and likely cause damage. However, the STED pulse must also have significant overlap with the emission profile to efficiently drive stimulated emission. As a result, STED is most effective on samples with large Stokes shifts. Finally, the excitation must remain in a bright state with a reasonable transition dipole for emission. If, for example, triplets were formed, then stimulated emission would no longer be efficient. The need to satisfy all these requirements has resulted in a limited number of STED compatible fluorescent dyes.[206]. These effects will be further explored in the

following section.

3.3 Limitations of Traditional STED for Arbitrary Chromophores

Far-field super-resolution fluorescence imaging has become very prominent, in particular in bioimaging, where molecules of interest are fluorescently labeled so that their nanoscale organization can be determined. Whether employing structured illumination microscopy,[134] stochastic photoactivated approaches,[131–133, 211] or stimulated emission depletion (STED) imaging,[137] care is generally taken in selecting the fluorescent labels used. In particular, in STED microscopy, though some efforts employ luminescent inorganic nanoparticles,[212–216] the fluorescent labels are typically small and rigid π-conjugated dye molecules that are comparatively resistant to photobleaching and that have been selected based on whether their photophysical properties are empirically found to be compatible with stimulated emission depletion.[206, 217] Fluorophores with high triplet, photoisomerization, or other photochemistry yields, fluorophores prone to photodamage, and especially fluorophores that permit absorption of the annular STED quenching laser wavelength on account of a limited Stokes shift or lingering red absorption tail are generally incompatible with STED microscopy. In addition to linear absorption of the STED laser pulse, two-photon absorption (2PA), which is a prominent second-order process in π-conjugated organic molecules[218, 219] and solid materials,[220] can also prevent appropriate levels of stimulated emission depletion. Moreover, the inflexibility of working with endogenous chromophores in naturally luminescent materials and the requirements for well-behaved fluorescent labels in super-resolution imaging together present severe challenges toward optically characterizing naturally luminescent materials on the nanoscale.

3.3.1 Damage Thresholds

The method for achieving high resolution described in Section 3.2 relies on the use of strong fields to drive the sample even at the inner regions of the STED pulse, where the field is weak, to saturation. This means that the peak intensities need to be very high in order to achieve the best resolution. For this reason, the record STED resolutions of < 3 nm, have been reported for materials like N-V diamond centers,[221] which are extremely robust to high electric fields. Most materials, however, will be damaged by the field intensities required to make such small spots. So in practice the resolution is limited by the damage threshold of the sample. Most STED images of organic materials have been limited to resolutions around 40-80 nm for this reason.[206]

There are many pathways for a material to be damaged by a focused laser beam.[222] The three most relevant mechanisms for this work are photo-bleaching, thermal build-up, and ablation. Many organic materials are easily oxidized after excitation, which causes photobleaching of the chromophores in the sample.[223] This can be mostly avoided by keeping

the sample under N_2 or another inert atmosphere. Thermal damage is most common for high repetition rate (100 kHz or MHz) laser systems, or for materials with poor thermal conductivity. If the time delay between pulses is on the same order as or faster than thermal diffusion, even very low pulse energies will cause a build up in thermal energy near the focus, until an equilibrium with thermal diffusion is reached.[224] These thermal effects can be mitigated by raster scanning the sample between several points of interest, allowing each one enough time for the thermal energy to dissipate before returning to a given location. Finally, if the pulse energy is extremely high the sample may be ablated.[225] The intense electric field can ionize electrons from the material and then accelerate them to speeds where their collisions cause additional ionization events. This process forms a plasma on the sample, which will rapidly expand, removing material.[226] This phenomena is commonly utilized in industry to perform laser milling of fine features.[227, 228] The only way to mitigate this effect is to reduce the peak pulse power by either reducing the pulse energy, or by stretching the pulse in time.

3.3.2 Spectral Requirements

The wavelength and bandwidth of the STED pulse, relative to the absorption and emission profiles of the material, also impact the efficiency of stimulated emission deletion. The biggest spectral concern is direct absorption of the STED pulse.[216] If the STED pulse has any overlap with the absorption profile, the intense field will cause a lot of excitation and heating. These additional excitations could outcompete any stimulated emission, and the heat load resulting could damage the sample. There must also, however, be some spectral overlap with the emission profile. The STED pulse works by stimulating emission through a normal fluorescent pathway, and requires sufficient oscillator strength at the frequency of the STED pulse. As a result, STED requires a large Stokes shift in the fluorescence, so there can be good STED bandwidth overlap with the emission profile while simultaneously avoiding spectral overlap with the absorption profile.[229] Another spectral concern is strong excited state absorption features at the STED frequency. Just like overlap with the ground state absorption profile, overlap with the excited state absorption profile should also be minimized to avoid sample heating and competition with the STED transition. The magnitude of this contribution is, however, unclear. We do in fact see some excited state absorption in our samples at the STED wavelength, but it does not significantly hinder the stimulated emission process.

3.3.3 Excited State Dynamics

Since STED relies on the ability to stimulate emission from the sample, any excited state dynamics that prevent access to this pathway will interfere with STED. For example, if there is fast intersystem crossing to a triplet state the STED beam will not be able to drive stimulated emission because the transition to the ground state is forbidden. There are some workarounds for this problem, such as T-rex STED.[230] The excited state vibrational

relaxation should also be fast, since this is the pathway that populates the level that the STED pulse is stimulating. If this relaxation is slow the STED pulse will be ineffective at early times and will either need to be stretched or delayed in time until the majority of the excited state population has vibrationally relaxed. The ground state vibrational relaxation rate is also critical and should be as fast as possible. Recall from Section 3.2.2 that the STED pulse drives an equilibrium between the ground and exited states, and it is the ground state vibrational relaxation that causes this equilibrium population to subsequently decay. If the ground state vibrational relaxation is slow, the STED pulse will remove only ∼50% of the population from the excited state, because the strong field drives an equilibrium between stimulated emission and absorption on the driven transition. For this reason, the STED pulse duration must be long compared to the ground state vibrational relaxation lifetime. In combination with the advantages in avoiding damage, this has led to the common use of very long e.g, 1 ns duration STED pulses.[206]

3.3.4 Two Photon Absorption

Another potential problem with the strong fields used in STED is two photon absorption (2PA). 2PA is a non-linear process that depends on the square of the intensity and occurs for wavelengths below the band edge. STED microscopy employs considerable laser intensities to induce adequate stimulated emission, yet it is precisely at these high intensities that 2PA can become a competing factor that may dominate the stimulated emission process.[231, 232] Since the STED pulse provides very strong fields below the band edge, 2PA is a pathway for the STED pulse to create excitations in the material even when there is no direct overlap with the absorption profile. This can pose a significant hurdle to achieving sub-diffraction resolution.

3.3.5 Labeling Density

Due to the effects mentioned above, there is typically some STED-induced fluorescent background in the image.[216] This reduces the contrast that can be achieved and is related to the number of additional chromophores overlapped with the STED pulse when a given chromophore, in the center of the pulse, is being imaged. This effect is commonly mitigated by limiting the labeling density in the sample, so that there aren't too many chromophores in a given area. This effect must also be balanced with the need for sufficient labeling density to resolve the image features to be studied.

3.3.6 Typical Characteristics of STED Samples

For all of these reasons, STED has most commonly and successfully been applied to samples that can be sparsely labeled with a dye from the growing, but limited, list of those shown to work with STED.[206] This has largely included biological samples, where much effort has been put into labeling techniques. It also means that the possible application of

STED to more complex systems with densely packed endogenous chromophores has remained largely unexplored.

3.3.7 Consequences for STED in Conjugated Polymers

In the context of the above limitations, the densely packed endogenous chromophores in a conjugated polymer solid would not appear to be well suited for STED microscopy. Conjugated polymers are oxygen sensitive and will quickly photo-bleach under excitation in air. Samples must therefore be encapsulated in a nitrogen glove box to seal out any oxygen. As with all dielectric materials, conjugated polymers are also sensitive to high intensity fields and can be damaged by thermal buildup and/or ablation. To avoid these effects, samples must be raster scanned to allow individual locations to rest and thermally equilibrate between measurements, and the STED pulse must be stretched to a sufficient duration to avoid overly high peak intensities. The large Stokes shift in conjugated polymers is beneficial, but care must still be taken to select the wavelength and bandwidth of the STED pulse to simultaneously minimize spectral overlap with the absorption profile, minimize the typically strong 2PA in conjugated polymers, and maximize the spectral overlap with the emission profile. The strong 2PA and the photobleaching of the sample can both be mitigated, at the expense of time resolution, by extending the duration of the STED pulse. If time resolution is desired, as will become important in Chapter 4, care must be taken to find a pulse duration that balances these effects. In spite of these challenges, we will show in Section 3.6 that STED microscopy can be successfully extended to conjugated polymer solids. This advance is largely due to a carefully considered modulation scheme which eliminates the contribution of 2PA from the signal, as outlined in the following section.

3.4 Overcoming 2PA in STED Microscopy

The strong effect of 2PA in conjugated polymers presents a significant challenge to achieving super-resolution. The large STED-induced fluorescent background must be removed from the signal to isolate the pump-induced contribution. This process is similar to the case of transient absorption, where the small change in the probe transmission induced by the pump must be isolated from the large linear transmission of the sample. In the case of transient absorption, as outlined in Chapter 2, an optical chopper is used to modulate the pump pulse and a lock-in amplifier isolates the change in the probe intensity at the corresponding frequency. This approach fails here due to the pile-up effect in single photon counting detectors, as outlined below. A correction can, however, be applied to regain an analogous signal to a lock-in output, through post processing.

3.4.1 The Pile-up Effect in Single Photon Detectors

To collect sample fluorescence, we use a one of a kind single photon counting avalanche photodiode (SPAD) that can be gated on in < 200 ps for reasons that will become evident in Chapter 4. Single photon detectors, like the SPAD that we use, have a "dead time" after a detection event.[233] When a photon is detected by our SPAD it triggers an avalanche of charge that needs to be replenished before the detector regains sensitivity. This time scale is $\sim$50 ns for most detectors. We actually program our detector to be held in an off state for 300 ns after a detection event to avoid some signal artifacts that can show up for short hold off times, such as after-pulses. This creates a 300 ns window after a detection event in which the detector is off. Since typical fluorescent lifetimes are on the order of 1 ns, there will be at most one photon detected per excitation laser pulse. If multiple fluorescent photons hit the detector due to sample excitation by a given excitation pulse, at most one will be recorded. This means it is not possible to detect a count rate higher than the repetition rate of the laser (200 kHz in our case). This effect introduces a non-linearity in the response of the detector to incident photons. This is a well known effect in single photon counting detectors and is referred to as the "pile-up" effect.[233, 234] This effect is illustrated in Figure 3.15.

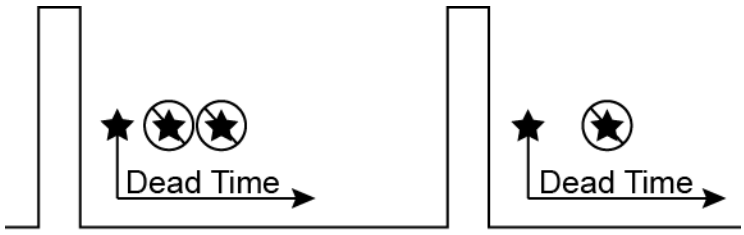

Figure 3.15: Pile-up effect in single photon counting detectors. The square wave indicates the excitation pulse train and the stars are photons incident on the detector. The first photon is detected while photons reaching the detector during the resulting dead time are not.

3.4.2 Derivation of the Pile-up Correction

In order to correct for the pile-up effect, we need to understand the probability that multiple photons reach the detector from a given excitation pulse. This probability is governed by Poisson statistics, which say that if on average μ uncorrelated events are observed per time period, then the probability that n events are observed in a given time period is described by the Poisson distribution,[233]

$$P(n, \mu) = \frac{\mu^n}{n!} e^{-\mu}. \tag{3.23}$$

The single photon counting detector gives a binary response: either $n = 0$ or $n > 0$. We can therefore construct the probability that no photons are detected ($n = 0$) as one minus the

ratio of the actually detected count rate to the repetition rate,

$$P(0,\mu) = 1 - \frac{\text{raw count rate}}{\text{repetition rate}} = e^{-\mu}. \tag{3.24}$$

Then we can solve for the average,

$$\mu = -\ln\left(1 - \frac{\text{raw count rate}}{\text{repetition rate}}\right). \tag{3.25}$$

This is the average number of photons incident on the detector from a single excitation pulse, so to convert back to a corrected count rate that describes the rate at which photons actually hit the detector even if they weren't detected, we just multiply by the repetition rate.

$$\text{Corrected Count Rate} = -\ln\left(1 - \frac{\text{raw count rate}}{\text{repetition rate}}\right) \times (\text{repetition rate}). \tag{3.26}$$

This simple correction can be used to dramatically extend the linear response of the detector. An example of an actual correction we performed is shown in Figure 3.16a.

3.4.3 Modulation and Pile-up Correction to Remove the 2PA Background

The fluorescence that is induced by the STED pulse through 2PA needs to be removed so that the pump fluorescence can be isolated.[216] Typically this kind of process of isolating a signal from a background level can be achieved by modulated the signal and only looking at the component that changes with the correct frequency. This is often achieved with a lock-in amplifier. In this case, however, lock-in amplification fails to isolate the pump induced fluorescence due to the pile-up effect on the detector. This is essentially due to the non-linearity that the pile-up effect creates, but it can be understood statistically as well. Consider a constant pump signal where one pump-induced photon reaches the detector in each duty cycle. If there is an increasing STED induced fluorescent background then as the number of STED induced photons reaching the detector increases, the probability that the one photon that is detected is the pump induced photon is diminishing. So the lock-in signal will decrease as the amplitude of the STED induced fluorescence background increases.

This effect can be overcome by incorporating the pile-up correction with the pump modulation scheme. The problem is that the pile-up correction needs to be performed independently for both chopper phases (open and closed) to return both to a linear response regime before a subtraction can be performed to remove the background. This is achieved by sending the chopper phase reference to the computer so that photon detection events can be binned appropriately in software analysis. The pile-up correction can then be applied, according to Equation 3.26, to both channels, excitation pulse on and off. To yield the isolated count rate of pump-induced fluorescence we compute the difference between the two. This method is not truly analogous to lock-in amplification as it does not use a true frequency filter, but it works well to remove the STED-induced background due to 2PA (Figure 3.16b).

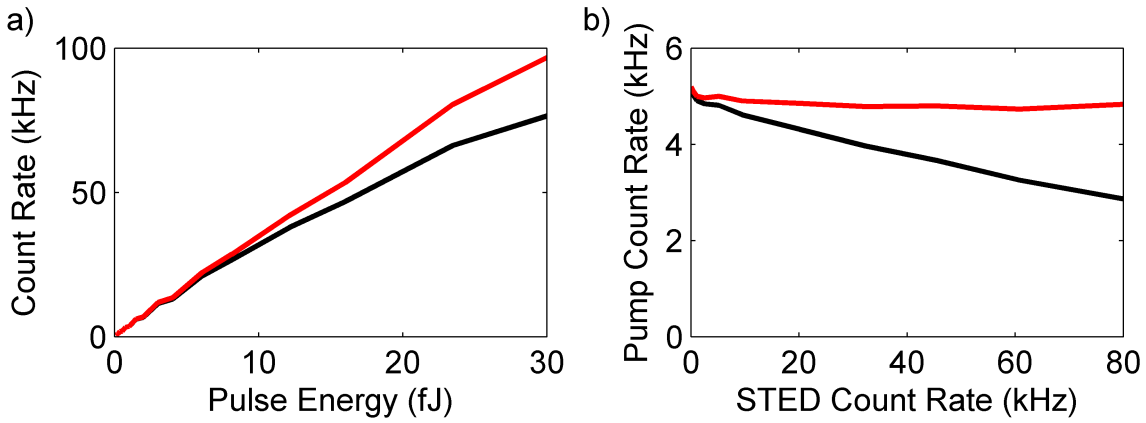

Figure 3.16: Demonstration of the performance of the pile-up correction and modulation. a) Linearity of the detector response. Measured count rate, collected from the reflection of the pump pulse off a coverslip in the sample plane, vs the pulse energy with (red) and without (black) the pile-up correction. b) Isolation of pump-induced fluorescence. The variation in the measured pump-induced count rate, for a constant pump pulse energy, as a function of the count rate of the STED-induced background with (red) and without (black) the pile-up correction.

3.5 STED Microscopy Experimental Setup

A schematic of the experimental setup for STED imaging is shown in Figure 3.17, with a list of part numbers provided in Table A.1. We use a PHAROS laser from Light Conversion, which is a yitterbium-doped potassium gadolinium tungstate (Yb:KGd(WO4)2) regeneratively amplified laser, which produces 230 fs pulses at 200 kHz with 50 μJ/pulse and 10 W average power. The PHAROS is used to pump two ORPHEPUS-N non-colinear optical parametric amplifiers (NOPAs), also from Light Conversion. The NOPA that produces the pump beam uses the third harmonic (3H) of the fundamental and has a tuning range between 440 and 960 nm. The NOPA that produces our STED pulse uses the second harmonic (2H) of the fundamental and has a tuning range between 650 and 900 nm, with an optional second harmonic of the signal stage to reach 325 to 450 nm as well. The 2H NOPA also has glass wedges that can be translated in and out of the white light beam to control the dispersion in the white light before amplification, which allow the amplified bandwidth to be tuned. For the experiments presented here, the 3H NOPA generated our pump pulse at 540 nm with 20 nm bandwidth. Typical powers out of the NOPA were around 50 mW or 250 nJ/pulse. The 2H NOPA generated our STED pulse at 740 nm with 14 nm bandwidth. Typical powers out of the NOPA were 190 mW or 950 nJ/pulse. Both beams are greatly attenuated before reaching the sample.

The pump pulse is collimated and then fiber coupled into a single mode polarization maintaining fiber with a 10 mm focal length achromatic lens. The fiber output is collimated with a 10×/0.3NA objective. The power of the beam is then controlled by focusing through a liquid crystal noise eater, which attenuates the power and reduces power fluctuations. The power out of the noise eater is further reduced by a waveplate/polarizer pair and an absorptive neutral density filter. The transmitted beam is then optically chopped with a Newport chopper, then telescoped by a factor of 2 with 75 and 150 mm achromatic lenses to increase the beam diameter in order to overfill the back aperture of the microscope objective. The beam is then coupled into the microscope with a dichroic mirror from Chroma.

The STED pulse is collimated out of the 2H-NOPA and then passed through a grating stretcher (Clark-MXR, Inc.) in order to extend the duration of the pulse. We use this grating stretcher in place of the long (∼75-100 m) fibers found in other STED setups because our excitation and STED beams originate from a single source, and the required path length in the pump line to match the time delay to the sample would be impractical in this configuration. The polarization is then rotated to 45° with a waveplate/polarizer pair, which also allows for power adjustment if needed. The beam is then split with a polarizing beam splitter cube into two lines. One of these lines is passed through a folded delay stage with a retroreflector, while the other is passed through matching stationary optics. Both lines pass through motorized waveplates and shutters before being recombined in a second polarization beam splitting cube. Note that only the beam on the stationary optics was used in the work presented here; the need for the second STED line will become apparent in Chapter 4. The beam is then coupled into a single mode polarization maintaining fiber with a 10 mm achromatic lens. For maximum coupling efficiency, it is important to match the beam diameter and focusing lens to the mode field diameter in the optical fiber. There will be losses if the NA of the lens is either too high or low. The fiber output is collimated with a 10×/0.3NA objective, which is necessary to minimize the induced wavefront error. Achromatic lenses in this position were found to induce spherical aberrations, and parabolic reflectors of sufficient wavefront flatness could not be sourced. The beam is then passed through a vortex phase mask and waveplate/polarizer pair to control the beam power. The phase mask is mounted in a 6" kinematic mirror mount, with (x, y) linear stages, to allow the phase mask to be properly centered on the beam mode, and the back reflection aligned upstream to ensure a 0° angle of incidence. The beam is then expanded by a factor of 2.14 with 35 and 75 mm achromatic lenses. Note that this telescope was not present for data collection for the work in this chapter, but was added to the setup for the work in Chapter 4. The beam is then coupled into the microscope with a dichroic mirror from Chroma. Finally, just before the objective, the beams are sent through a $\frac{\lambda}{4}$ waveplate (Tower Optics 4505-0190 A-25.4-B-.250-N4) which makes the STED pulse circularly polarized with handedness matched to the phase mask. This waveplate is held in a kinematic rotation stage so that the angle of incidence can be adjusted to optimize the circularity of the STED field.

The microscope has two routing mirrors and a 45° vertical mirror to direct the beams up into the 63×1.4NA Plan Apo Leica objective (HC PL APO 63x/1.40 oil CS2, Leica Material #11506350). The objective is held in a custom mount (see Figure A.1) on a

Newport XYZ stage. The sample is held in a PI Nano scanning piezo stage (P-545.3C7), supported by four adjustable height pedestals and custom brackets (see Figure A.2). There is also a 20×/0.7NA top objective held on a custom mount (see Figure A.3) with a spacer (see Figure A.4) on a Newport linear translation stage. Above the top objective is a white light LED for widefield illumination, to aid in focusing and to image the sample region of interest. Images, reflections, or fluorescence are collected through the bottom objective and transmitted through the dichroic routing mirrors for the pump and STED pulses, then either imaged on a camera for widefield, or focused onto a single photon counting avalanche photodiode (SPAD) (Prof. Alberto Tosi, SPAD lab, Politecnico di Milano; PicoQuant)[235, 236] through optional filters.

The motion of the Newport motorized stages is controlled with a Newport motion controller (XPS-Q8). The SPAD is gated with a Picosecond Delayer (MPD) and has a $\sim$ 200 ps rise time. The gate delay, "on time", and subsequent hold off period can all be controlled through computer interfaces. For imaging, the gate delay is set to gate on just after the STED pulse interacts with the sample. Typical values for the gate duration and hold off time are 20 ns and 300 ns, respectively. The counts from the SPAD can either be sent to a PicoQuant PicoHarp 300 for time correlated single photon counting (TCSPC) or sent through a home built inverting amplification circuit (see Section A.3) to a counting card on our data acquisition card (DAQ) (National Instruments PCIe-6321 with BNC-2090A breakout board). The DAQ is also sent a reference signal from the chopper at twice the modulation frequency, which is used to trigger acquisitions of the SPAD counts and bin them according to the chopper phase. This enables the pile-up correction and background subtraction discussed in Section 3.4.

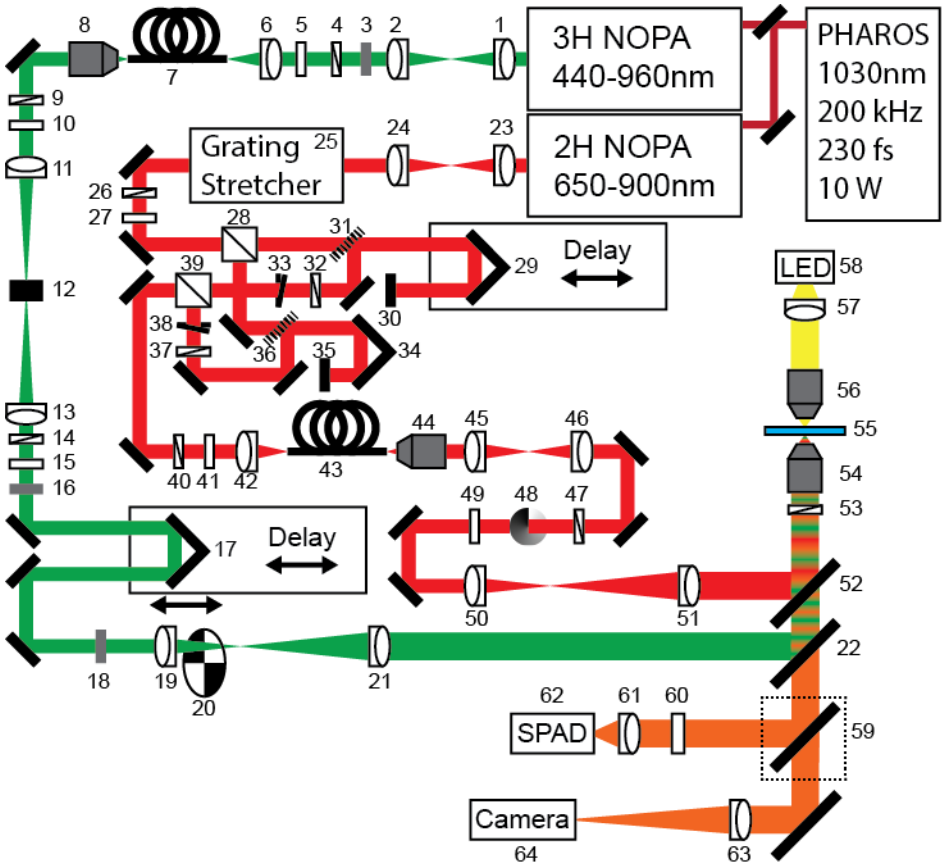

Figure 3.17: Schematic of the experimental setup. A reference table of part numbers is shown in Table A.1

3.6 Imaging CN-PPV Nanoparticles with STED Microscopy

3.6.1 Results for CN-PPV Nanoparticles

In spite of the challenges discussed in Section 3.3, we demonstrate that subdiffraction resolution in STED microscopy can be achieved on materials with endogenous, electronically coupled chromophores.[205] We image luminescent conjugated polymer nanoparticles of the polyphenylenevinylene derivative poly(2,5-di(hexyloxy)cyanoterephthalylidene) (CN-PPV) with 90 nm resolution. This work is enabled by the important adaption that we employ to circumvent 2PA-induced fluorescence from the STED laser pulse, discussed in Section 3.4. We envision that this advance will open up the possibility to employ previously discarded labels in bioimaging. It will also importantly enable direct imaging of solution processed luminescent optoelectronic materials on the subdiffraction scales characteristic of

their structural heterogeneities, which can disproportionately determine the limits on their functionality.

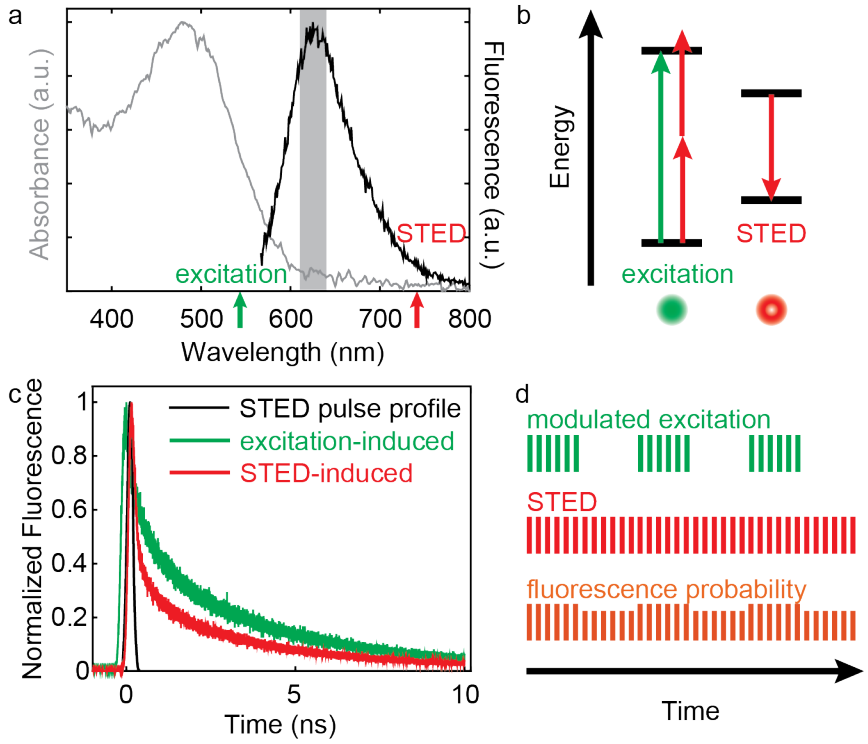

Figure 3.18: a) Absorption (gray) and emission (black) spectra for CN-PPV solids with the excitation wavelength (green), STED wavelength (red), and collection band-pass (gray). b) Schematic of direct excitation by the pump pulse (green) and 2PA and stimulated emission for the STED pulse (red). c) Normalized time correlated single photon counting (TCSPC) fluorescent lifetime of CN-PPV solids when excited directly by the pump (green) or through 2PA by the STED pulse (red), with an overlay of the approximate STED pulse duration (black). The unique shape of the lifetime when excited by the STED pulse is due to the balance between 2PA and stimulated emission. d) Schematic of the modulation scheme used to isolate the pump-induced signal.

In this study, we focus on CN-PPV solids prepared as nanoparticles.[237] Each CN-PPV particle is composed of one or more aggregated polymer chains. As shown in Figure 3.18a, in the solid phase CN-PPV has a broad absorption spectrum, extending from the ultraviolet to a peak absorption wavelength at 480 nm, and tailing off around 600 nm. Its fluorescence is peaked around 625 nm. We therefore use wavelengths of 540 nm for the excitation laser pulse and 740 nm for STED depletion pulse. We find that 2PA at the STED laser pulse wavelength indeed occurs, as evidenced by a super-linear power dependence in the low power limit

(Figure 3.19). Furthermore, we measure 2PA-induced fluorescence in our 610-640 nm imaging detection window, approximately 300 meV higher in energy than the STED laser photons (Figure 3.18a). The material's electronic energy levels and corresponding transitions that are relevant to performing STED microscopy are presented in Figure 3.18b. The excitation laser (green) couples the ground and excited states in a diffraction-limited spot; the STED laser (red) drives an electronic transition on the Stokes-shifted line to deplete the excited state in a spatially dependent manner to achieve super-resolution.[137] Also illustrated is the 2PA of the STED photons whose excitations presumably thermalize to the same excited state as those generated through linear resonant absorption of the excitation laser.

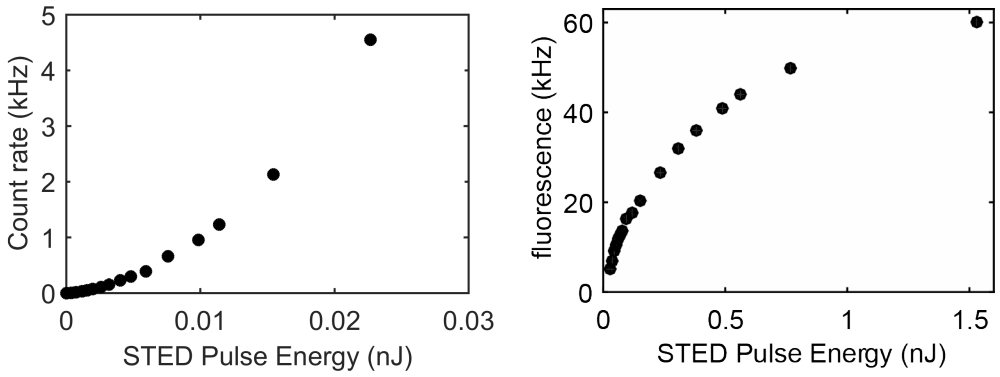

Figure 3.19: Power dependence of the STED-induced fluorescence, showing the characteristic super-linear dependence of 2PA for very low and moderate STED intensities.

The time resolved fluorescence of the CN-PPV is depicted in Figure 3.18c, along with the STED laser pulse temporal profile (black curve). When induced by the excitation laser at 540 nm (green), the transient follows a typical biexponential fluorescence decay.[238] More unusually, when induced by the STED laser pulse at 740 nm (red), the fluorescence intensity rises abruptly with the onset of the nonlinear 2PA and then also falls abruptly with the onset of stimulated emission. The shape of this decay curve primarily depends on the time-dependent competition between 2PA and stimulated emission,[231] as mirrored in simulations of the system (Figure 3.20).

To prepare the CN-PPV nanoparticles, a $\sim 0.005\%$ (w/v) solution of CN-PPV in tetrahydrofuran (THF) was made in a nitrogen glovebox. A 0.2 mL aliquot of the 0.005% CN-PPV in THF solution was quickly added to 0.8 mL of ultrapure water while the water was ultrasonicated. This solution was drop cast onto microscope coverslips and allowed to dry overnight in air. Once dry, residual oxygen and water were removed from the sample in the antechamber of a nitrogen glovebox and the samples were then encapsulated in the glovebox using UV cure epoxy (EPO-TEK, OG159-2). A representative absorbance spectrum of a CN-PPV film was acquired with a UVvis spectrophotometer (Agilent Cary 100); fluorescence spectra of CN-PPV nanoparticles encapsulated on a glass slide were obtained with a Horiba

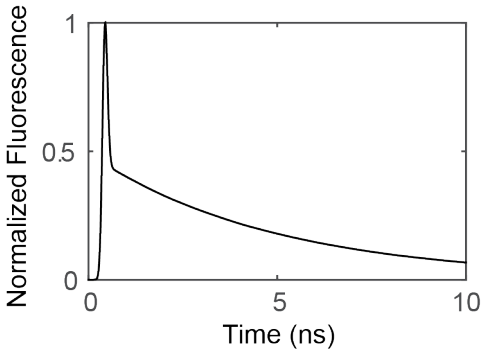

Figure 3.20: Simulation of the competition between 2PA and stimulated emission yielding an approximation of the observed fluorescence liftime lineshape in Figure 3.18c.

Fluoromax-4 fluorimeter at an excitation wavelength of 540 nm. Images were obtained in a home-built epifluorescence microscope described in Section 3.5. The sample was rastered in steps of 10 nm over a 2 μm x 2 μm area with a dwell time of 50 ms/pixel to form an image. At each pixel, epifluorescence is collected between 610 and 640 nm through our dichroics (Chroma T650spxr and T600lpxr-UF2) and two emission filters (ChromaET625/30m) and focused onto our fast gated SPAD detector to eliminate prompt fluorescence. We phase lock the detection to the optical chopper cycle and separately accumulate the photon count rates during the corresponding "excitation-on" and "excitation-off" phases for multiple cycles. The count rates obtained during the open and closed cycles of the chopper are each corrected for the classic pile-up effect with a simple Poisson correction factor before we take the difference of the two to isolate the count rate that is attributed to the modulated excitation pulse only (see Section 3.4). Fluorescence lifetime measurements were performed in the microscope with the fast-gated SPAD with a HydraHarp 400 (PicoQuant) using an excitation pulse energy of 0.22 pJ or a STED pulse energy of 370 pJ.

To image solids of CN-PPV, we modify traditional STED microscopy in the apparatus discussed in Section 3.5. We excite the samples with a pulse energy of 0.16 pJ at 540 nm and we follow this few-picosecond, diffraction-limited excitation with a 120 ps duration, 570 pJ, annular Laguerre-Gauss mode STED pulse (Figure 3.18b) tuned to the red edge of the CN-PPV fluorescence emission peak, 740 nm, in order to stimulate emission everywhere but in the subdiffraction center of the original excitation spot via nonlinear saturation. Because we operate the microscope with NOPAs pumped with a 200 kHz repetition rate PHAROS ultrafast regenerative amplified laser, we are able to carefully tune, control, and optimize many experimental parameters, including pulse wavelengths, bandwidths, duration, and relative delays. Also, in contrast with common STED microscopes, to eliminate the effects of absorption of the STED laser, we modulate the excitation pulse intensity at 500 Hz and separately record on a single photon avalanche diode (SPAD) the fluorescence counts during the "excitation-on" and "excitation-off" phases of the modulation cycle (Figure 3.18d), as

discussed in Section 3.4. This modulation scheme enables us to specifically select for fluorescence induced by the modulated excitation pulse when forming an image in order to obtain superior contrast. Lastly, time-gated detection has been used to improve spatial resolution by eliminating fluorescence collection from the diffraction-limited excitation volume prior to the onset of stimulated emission.[239, 240] Here, our time-gated detection, with an extremely rapid 200 ps turn-on time,[235, 236] furthermore, eliminates early time fluorescence induced by the diffraction-limited excitation and STED pulses.

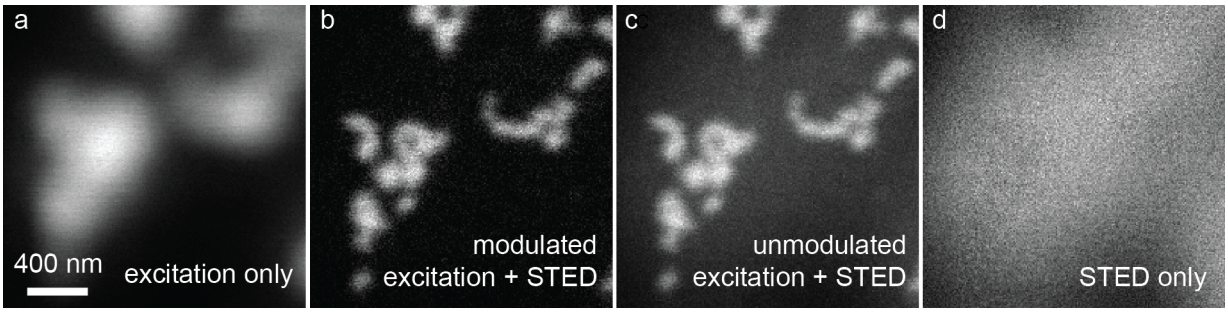

Figure 3.21: Images of CN-PPV nanoparticle clusters with a) excitation only, b) modulated excitation with STED, c) unmodulated excitation with STED, d) STED only.

Using the above scheme, we image clusters of nanoparticles composed of solution-processed CN-PPV. The images in Figure 3.21 reveal that our adaptation of STED microscopy successfully addresses the challenges of 2PA of the STED laser. Using the excitation pulse only (Figure 3.21a), the particles within individual clusters are not at all resolved, whereas the addition of the time-gated STED pulse, along with excitation modulation, reveals multiple features within each cluster with an approximately 3-fold improvement in resolution (Figure 3.21b). Even with time gating, without the excitation modulation, the background intensity is both higher and nonuniform (Figure 3.21c). This deficiency occurs because 2PA-induced fluorescence due to the roughly micron-sized STED laser spot (Figure 3.21d) cannot be distinguished from the desired unquenched excitation-pulse-induced fluorescence originating in the subdiffraction volume centered on the null of the STED lasers Laguerre-Gauss mode. The problem is more clearly visualized in the line scans presented in Figure 3.23.

We also established the dependence of the spatial resolution on the STED pulse intensity (Figure 3.22c) by imaging the individual bead boxed in the bottom left corner of Figure 3.22b at multiple STED laser intensities and by measuring and plotting the width of the nanoparticle feature in these successive measurements. Similar to typical STED experiments,[241] the feature size drops and then saturates at approximately 90 nm.

To analyze the impact that modulating the excitation pulse has on image formation and quality, we present in Figure 3.23 line scans across the STED image of the nanoparticles in Figure 3.22b (black) and compare them to the corresponding line scans obtained without modulation (gray). The locations of these line scans are indicated with dashed lines enumerated i and ii in Figure 3.22b. Because, at the 500 Hz modulation frequency, we separately

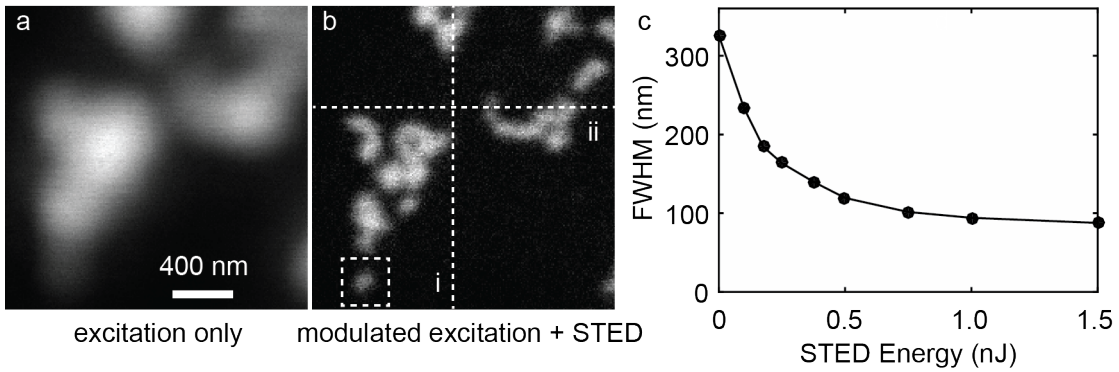

Figure 3.22: Images of CN-PPV nanoparticle clusters with a) excitation only and b) modulated excitation with STED. c) Resolution of the image as a function of STED intensity, measured as the full width half max of the boxed feature in b).

record the fluorescence counts at a given pixel while the excitation pulse illuminates the sample and while it does not, the gray traces in Figure 3.23 are straightforward to extract from the data set that generates a modulated STED image (Figure 3.21). The unmodulated gray trace in Figure 3.23a (section along i in Figure 3.22b) shows an apparent rise to a plateau around 200 nm, whereas only the modulated (black) trace shows that there is an isolated feature centered at approximately ∼300 nm. Overall, the unmodulated "baseline" of detected STED-induced fluorescence is not uniform, making it impossible to quantitatively compare features to one another. Figure 3.23b (section along ii in Figure 3.22b) reveals an unmodulated baseline amplitude greater than the size of the feature at ∼1100 nm riding on top of it. Furthermore, the relative extent of the dip between the two features at the far right appears significantly deeper in the unmodulated gray trace than in the modulated trace. In both cases, the nonuniform unmodulated background levels represent imaging artifacts that, without the ability to compare to the modulated line scans, can be mistaken for features themselves or can distort the relative size of real features. These imaging artifacts arise because the unmodulated, STED-induced fluorescence background level at any given pixel is proportional to the density of other nanoparticles illuminated by the off-axis portion of the large (>1 μm diameter) transverse mode of the STED laser pulse[216] (Figure 3.24). Clearly, without excitation modulation the ability to resolve small features is also heavily compromised.

3.6.2 Discussion on STED Imaging of CN-PPV Nanoparticles

The modulated STED image in Figure 3.22b illustrates the ability to perform super-resolved far-field fluorescence imaging on materials with densely packed endogenous chromophores that have not previously been accessible in this way. Furthermore, when imaging a material that is able to fluoresce as a result of STED illumination alone, modulating the

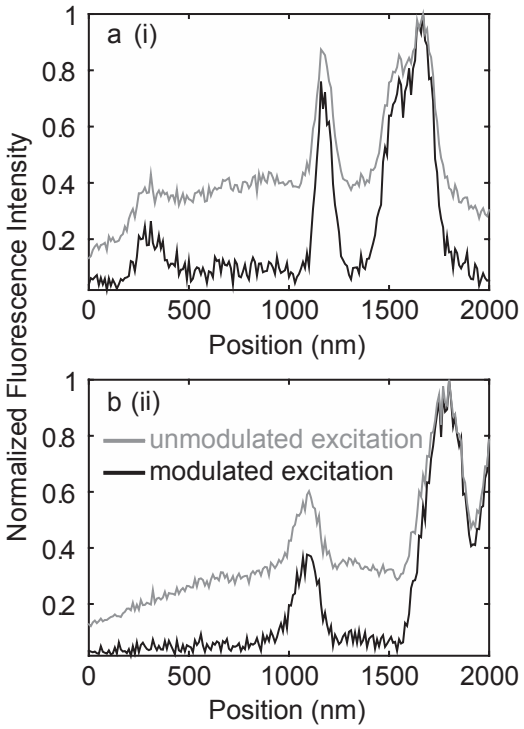

Figure 3.23: Normalized linescans from the modulated (black) and unmodulated (gray) images. Locations of the linescans are shown if Figure 3.22b.

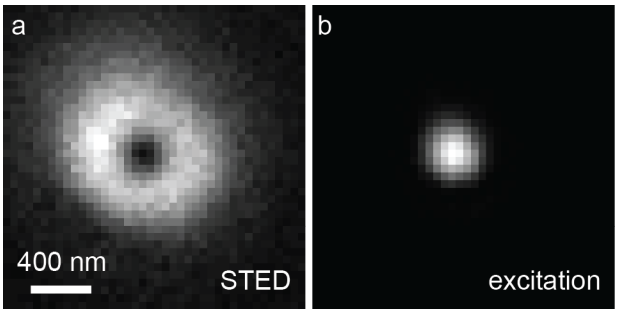

Figure 3.24: Experimentally observed point spread functions of the a) STED pulse and b) pump pulse.

excitation pulse significantly improves the image contrast. To explain how and why we have successfully super-resolved materials with photophysical properties that are generally considered to be nonideal for STED microscopy, we discuss the physics underlying the contrast and resolution that we have achieved. First, we consider the increased complexity of STED imaging specifically using organic chromophores for which nonlinear 2PA competes with linear stimulated emission at the STED laser pulse wavelength. Our results reveal that the time

dependence of the competition of these two processes with different intensity dependences can limit the effects of 2PA. In other words, the STED pulse temporal profile ensures that stimulated emission can persist at intensities at which 2PA is waning in order to quench a significant fraction of the 2PA-induced fluorescence, as illustrated in Figures 3.18c and 3.20. The monotonically decreasing and saturating behavior of the resolution curve obtained in Figure 3.22c also demonstrates that stimulated emission still dominates 2PA even at the highest peak pulse intensities. Because this quenching of 2PA-induced fluorescence occurs over and is limited to the course of the ∼120 ps STED pulse duration, fast gated detection on a similar time scale[235, 236] enables us to suppress a significant fraction of 2PA-induced fluorescent photons from being detected. Although the line scans in Figure 3.23 illustrate that even gated detection is imperfect, our straightforward excitation pulse modulation further selects for fluorescence induced by the excitation pulse only, in order to significantly improve image contrast.

The minimum CN-PPV nanoparticle feature size of 90 nm that we have observed at a maximum STED intensity in Figure 3.22c could be limited by the feature size, excitation modulation rate, sample heating, possible exciton annihilation effects,[242] an imperfect null in the Laguerre-Gauss mode of the STED pulse, or by the inherent spatial resolution of the microscope. For nanoparticles larger than the typical exciton diffusion lengths of several nanometers measured in related PPV materials[101, 243, 244] it is possible that the electronic coupling in the material also limits the ultimate resolution. Additional temporal stretching of the STED pulse to decrease its peak intensity could further mitigate 2PA and enable higher fluences and potentially higher spatial resolution to be achieved. Note that in Chapter 4 we demonstrate an improved resolution of 70 nm after expanding the STED beam diameter to over fill the back aperture of the objective. Nevertheless, the ability to image heterogeneities in solution-cast, functional optoelectronic materials using their endogenous chromophores even at the scale of ∼100 nm will be of significant utility because many of their features that are smeared out at the diffraction limit are able to be resolved on this subdiffraction scale.

3.7 Conclusions for Extending STED Microscopy to Conjugated Polymer Solids

In summary, we have demonstrated that it is possible to perform subdiffraction STED fluorescence imaging of electronically coupled materials as a result of and in spite of their densely packed endogenous chromophores. We have shown that excitation modulation aids in eliminating the challenges of STED laser 2PA, and we anticipate that our findings can be generalized to the large class of organic chromophores that exhibit 2PA so that STED imaging may be performed on a much wider range of materials than originally demonstrated or anticipated. These materials could include dyes not currently considered to be compatible with STED or other super-resolution fluorescence approaches, photosynthetic membranes,

or other autofluorescent biomaterials. In fact, the extremely bright conjugated polymer nanoparticles employed in this study could even be used as labels in super-resolution imaging applications. Moreover, our findings open up the possibility to image the subdiffraction heterogeneities in solution-processed solid optoelectronic materials composed of π-conjugated molecules or even of colloidal nanocrystals. This avenue could reveal directly how these heterogeneities not only affect such a materials local optical properties but also how they affect the materials macroscopic electronic properties that determine its functional potential. Lastly, although 2PA could be reduced by increasing the duration of the STED laser pulse, our shorter pulse duration and similarly fast gated detection will be shown in Chapter 4 to enable a scheme to resolve ultrafast energy transport[59, 60] in similar electronically coupled materials on the nanometer scales that no longer average over their heterogeneities. Such a scheme should be a significant improvement over bulk approaches used to measure exciton migration[14, 75, 85, 245, 246] that cannot currently explain which trajectories an excitation might favor as a function of specific features of the film morphology.

Chapter 4

Time Resolved Ultrafast Stimulated Emission Depletion: Exciton Migration in Conjugated Polymers

4.1 Introduction

The successful adaptation of STED microscopy to the conjugated polymer CN-PPV, as demonstrated in the previous chapter, has the potential to enable super-resolved studies of exciton migration in conjugated polymers on length scales near to the characteristic scale of heterogeneity. Exciton migration is an important process in many opto-electronic systems, especially in natural and artificial light harvesting, where the transfer of optical excitations to reaction centers or p-n junctions is a critical step in energy conversion.[28, 52] In photosynthetic systems, the migration of excitations to reaction centers may be nearly 100% efficient, but the design principles enabling efficient transport in these complex and disordered systems have remained elusive.[247–250] Conversely, the performance of organic photovoltaics has been limited by the short range, 5-20 nm,[14] of exciton migration in organic semiconducting polymers.[14, 52] There has been considerable effort to understand the origin of these limited migration lengths, but the development of a complete physical picture of the migration process has been limited by the difficulty of measuring exciton migration and making correlations to the local material substructure. Representative measures of exciton migration in organic semiconductors, have been challenging because of the mismatch between exciton diffusion lengths (5-20 nm)[14] and the optical diffraction limit. Common methods aim to address this challenge by growing thin films that abruptly terminate at quenching substrates, then studying the photoluminescence quenching as a function of film thickness.[65–79] These physical boundaries, however, inevitably alter the spatioenergetic landscape for migration[80] and the experiments average over large areas, precluding any correlation to the local substructure that determines the diffusion length. Recently, an elegant new approach was demonstrated that removes the need for a quenching boundary by utilizing high

precision time dependent measurements of the emission volume to enable detection of small changes in the exciton distribution, with diffraction limited focal volumes.[59, 60] Here, we present a method to surmount both the diffraction limit and the need for physical quenching boundaries by instead defining quenching boundaries all-optically with sub-diffraction resolution. This approach allows us to characterize spatiotemporal exciton migration on its native nanometer and picosecond scales, without disturbing the semiconductor morphology.

This chapter presents a new method for exciton migration measurements in organic semiconducting polymers, based on an adaptation of STED microscopy, and its successful application to CN-PPV thin films. This method of time-resolved ultrafast stimulated emission depletion (TRUSTED) utilizes the enhanced spatial confinement of the excited state population to more directly track the spatial and temporal evolution of the exciton distribution over its lifetime. The motivation for this method and the conceptual framework for its operation will be introduced (Section 4.2), followed by a discussion of the appropriate normalization conditions to isolate the contribution of migration in the signal, and practical considerations regarding the experimental implementation (Section 4.3). Kinetic simulations are also presented, verifying that the outlined normalization conditions isolate the migration component in the signal (Section 4.4). Experimental results are presented for the application of this new method to thin films of CN-PPV, and a fitting routine is then constructed to extract the exciton diffusion length (L_d) from the data, which is found to be $L_d = 16 \pm 2$ nm (Sections 4.5 and 4.6). Finally, Monte Carlo simulations of incoherent exciton hopping between lattice sites are performed as a model of the migration process in conjugated polymers, to elucidate the nature of the spatioenergetic landscape that underlies the relatively long migration length in CN-PPV (Section 4.7). Based of our analysis of the results and simulations, we determine the exciton migration in CN-PPV to be approximately diffusive because site-specific broadening is comparable to inhomogeneous broadening, thereby leveraging a long, 5-ns, exciton lifetime to yield a relatively long migration length.[251] We also draw general conclusions, beyond CN-PPV, about how energetic and spectral parameters determine the extent and character of migration in the incoherent hopping regime.

The sub-diffraction spatial resolution of our new approach will enable previously unattainable correlations of local material microstructure and the resulting nature and extent of exciton migration, providing an additional level of insight into structure/function relationships in electronically-coupled materials used for energy transport and transduction, applicable not only to organic semiconductors used in photovoltaics or light-emitting devices but also to explaining why natural photosynthesis exhibits the most exemplary exciton migration.

4.2 The TRUSTED Concept

4.2.1 Traditional Exciton Migration Measurements

To measure the migration of excitons, their initial and final positions over the course of their lifetime must be determined. In an ideal case, a single exciton would be created in a

well-defined initial position, and then its change in position would be recorded over time. There are, however, several challenges with realizing this experimentally. First, excitons are optical excitations so their initial position can only be dictated down to the diffraction limit ($\sim$ 200 nm). Second, it is not clear how to read out the position of the exciton at a given time. The primary optical signature of excitons is their fluorescence, which again can not be localized below the diffraction limit. This is problematic since the length scale of migration is typically on the order of 5-20 nm.[14] Therefore, with diffraction limited optics, migration appears as a small perturbation to the population distribution. The most prominent method for addressing this issue has been the use of bilayer photoluminescence quenching (PLQ),[65–79] although there are alternative approaches, such as spectrally resolved photoluminescence quenching,[85–90] fluorescence volume quenching,[91–97] microwave conductivity,[81–84] exciton annihilation,[71, 87, 98–107] and the direct imaging of the photoluminescence distribution[59, 60], as discussed in Section 1.2.6.1. Bilayer PLQ experiments, the most commonly used method of measuring exciton migration in conjugated polymers, measure the degree of quenching achieved in films of varying thickness grown over a quenching substrate, and all but one of the alternative methods depend on the dynamics of exciton quenching. For a thin film in a bilayer PLQ experiment, all excitons are able to migrate to the interface and are quenched, but as the thickness of the film is increased there are some excitons that fail to reach the interface, due to the limited migration length, and survive to generate fluorescence signals. A length scale for migration can then be derived by carefully studying the photoluminescence quenching as a function of film thickness. The disadvantage of this technique is that it averages over a large area of a film, and it uses information from multiple films prepared under different conditions for different thicknesses, which can perturb the structure.[14] The result thus represents an average over many types of possible morphologies. Additionally, there can be issues with excitons being quenched by the interface even when they have not yet reached the boundary, which complicates the analysis.[80] The alternative techniques also have challenges for application to conjugated polymer films: spectrally resolved PLQ is typically only compatible with materials with long diffusion lengths like molecular crystals, in fluorescence volume quenching the embedded dopants may phase separate or alter the electronic structure of the material, microwave conductivity measurements use the same sample geometry as bilayer PLQ and faces the same challenges, exciton annihilation requires high intensity resonant fields that may damage samples, and direct imaging of the photoluminescence distribution lacks the spatial resolution to identify heterogeneity in conjugated polymers, as do the other techniques.

4.2.2 The STED Pulse as an Optical Quenching Boundary

Our experiments replace the physical quenching boundary in previous work with an optical quenching boundary generated by the STED pulse. This technique has the distinct advantage of making the boundary tunable and transient. Since the quenching boundary is generated by an optical field, its location, shape, intensity, duration, and timing can be controlled. Additionally, the field may be blocked to perform a normalization in the absence

of a boundary. Furthermore, all this can be done at a single location within a single film, near the characteristic scales of exciton migration and structural heterogeneity.

4.2.3 Schematic for the Adaption of STED Microscopy for TRUSTED

As demonstrated in Chapter 3, STED microscopy can be successfully adapted to create sub-diffraction excitation volumes in conjugated polymer solids. This method creates a sub-diffraction initial condition, but this pulse sequence (pump pulse plus STED pulse), is insufficient to measure migration. Determining the length and time scale of migration also requires knowledge of the position of the excitons as a function of the migration time. To achieve this, a second STED pulse (STED2) is added to the pulse sequence at a controlled time delay after the initial STED pulse (STED1). This second STED pulse generates the optical quenching boundary for migration measurements. The length and time scale of exciton migration can then be determined by observing the degree of fluorescence quenching achieved by the second STED pulse as a function of the delay time between the initial condition (STED1) and the application of the quenching boundary (STED2). The amount of quenching should increase as a function of the delay time as excitons migrate further away from the initially prepared excitation volume. This technique can therefore determine the exciton migration length in a well-defined location in a single film of a conjugated polymer, with sensitivity to the in-plane component of migration, as opposed to the out of plane component of migration that is measured in traditional PLQ. A schematic of the pulse sequence and the expected response of the exciton population distribution is shown in Figure 4.1.

4.2.4 Origin of the Sensitivity to Migration

To better illustrate the origin of the sensitivity to migration enabled by the pulse sequence described above, consider the processes outlined in Figure 4.1 in more detail. The initial excited state population, frame 1 of Figure 4.1, is a diffraction limited Gaussian distribution determined by the focal volume of the pump pulse. The action of the STED1 pulse is to quench the excitons in regions where the STED field is sufficiently intense to drive the stimulated emission depletion process, as described in Section 3.2. As a result, the excitons around the periphery of the initial distribution are quenched, while those near the central null of the STED pulse survive. This pulse sequence creates a sub-diffraction limited distribution of excitons, which defines the excitation volume, frame 2 of Figure 4.1. This confined exciton distribution then expands over the delay time due to the action of migration, frame 3 of Figure 4.1. For example, under diffusive migration, the variance of the distribution expands linearly in time, as shown in Section 1.2.6.1. The second STED pulse (STED2) acts on the exciton distribution in the same way as the STED1 pulse, applying a radially dependent quenching probability, where excitons at radial positions with higher

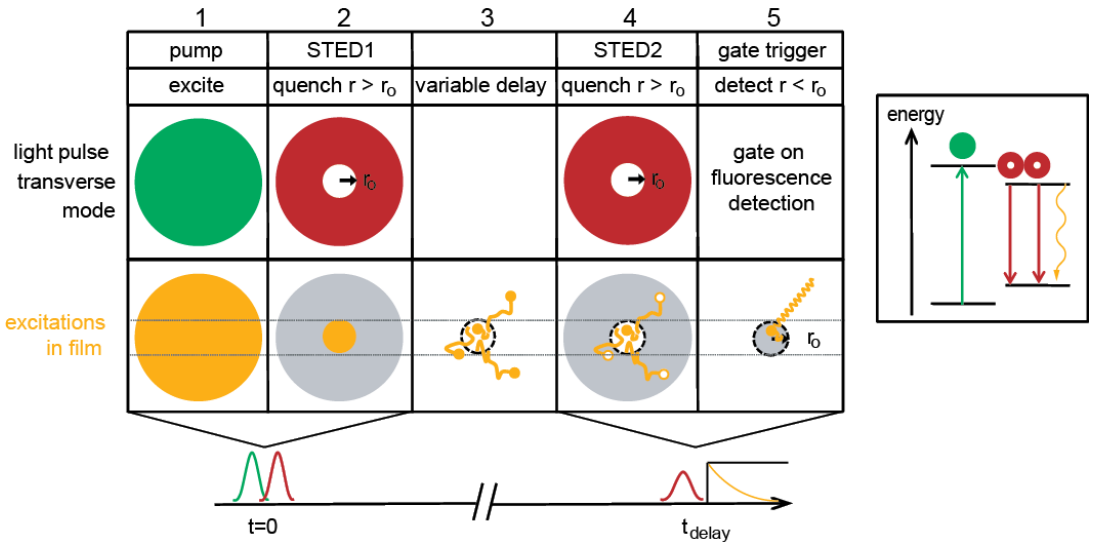

Figure 4.1: Schematic of the TRUSTED pulse sequence and the anticipated evolution of the excited state population, with 1) excitation, 2) STED1 confines the excitation volume, 3) variable time delay for migration, 4) STED2 preferentially quenches exciton at larger radii and defines the detection volume, the interior region that remains unquenched, 5) fluorescence is detected from the remaining population.

STED intensities are preferentially quenched, defining the detection volume from which fluorescence will be collected, frame 4 of Figure 4.1. Thus, the fraction of the population that is quenched by STED2 depends on the physical extent of the excitation distribution at the time the STED2 pulse is applied, and its overlap with the STED2 pulse PSF. The fraction of excitons quenched by STED2 will thus increase with increasing delay time between the STED1 and STED2 pulses as the exciton distribution progressively expands due to the action of migration (see Figure 4.2). The time dependence of the standard deviation of the exciton distribution can then be extracted by building a fitting algorithm to model this trend, and it can be related to the diffusion length L_d as described in Section 1.2.6.1.

4.3 Isolation of the Migration Signal: Experimental Concerns and Normalization Conditions

As discussed in the previous section, the TRUSTED pulse sequence provides a local measurement of the extent of migration, where the extent of migration determines the fraction of the population quenched by the STED2 pulse at each delay time, however, before presenting the experimental results we must find the proper normalization conditions to isolate the migration signal in the data and consider how to eliminate the effects of any additional

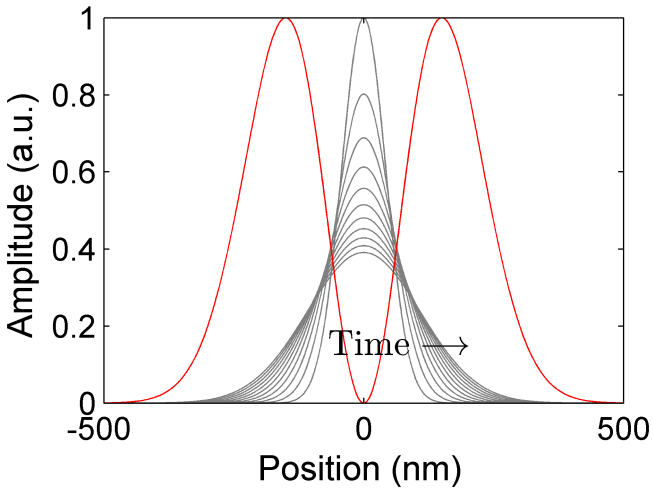

Figure 4.2: An illustration of how the overlap of STED2 cross-section profile (red) and the exciton distribution cross-section profile (grey) changes over the time delay, due to diffusive migration.

processes that could mimic the anticipated effects of migration.

The quantity that underlies the sensitivity to migration is the variation in the fraction of the exciton population distribution quenched by the STED2 pulse for various delay times. The detected raw signal, however, is the fluorescence of the excitons, so a detection scheme and normalization condition are required to isolate the desired quantity. We determined that the best method to extract the fraction of the exciton population quenched by the STED2 pulse from the detected fluorescence involves two main factors. The first is to gate the detector on just after the action of the STED2 pulse for each delay time, removing sensitivity to any prior fluorescence. The second is to modulate the STED2 pulse, so that the fluorescence intensity with and without the application of the the STED2 pulse, which generates the optical quenching boundary, may be recorded. The respective detected fluorescence levels are then proportional to the population of excitons in the sample with and without the action of the optical quenching boundary, so that the fraction quenched by the boundary can be extracted. This normalization eliminates the effects of fluorescence decay due to exciton relaxation. Finally, rather than plotting the fraction of the exciton population that is quenched, we instead choose to consider the fraction that survives, as we feel it is better to plot the data in terms of the normalized detected fluorescence level. This ratio is referred to as the "normalized detection volume fluorescence".

$$\text{normalized detection volume fluorescence} = \frac{\text{detected fluorescence with STED2 on}}{\text{detected fluorescence with STED2 off}} \quad (4.1)$$

This quantity represents the fraction of the population that survives the action of the STED2 pulse at a given delay time, which is directly related to the spatial overlap of the STED2

pulse PSF with the exciton population spatial distribution. Since the population distribution expands as migration proceeds, the spatial overlap with the STED2 pulse PSF increases with the extent of migration (see Figure 4.2). Thus, as migration proceeds, a smaller fraction of the population distribution will survive the action of the STED2 pulse, causing the normalized detection volume fluorescence to decrease for longer delay times.

Determining that the normalized detection volume fluorescence is the quantity that encodes the signatures of migration, and identifying the correct detection scheme and normalization condition to isolate this quantity, was not trivial. There are several complicating effects that had to be accounted for, and several simpler detection schemes were tested before arriving at the method outlined above. For example, the time dependence of the fluorescence decay due to increased overlap of the exciton distribution with the STED2 pulse PSF, caused by migration, needs to be distinguished from the fluorescence decay due to the lifetime of the excitons. The detection scheme outlined above was found to most successfully isolate these signals. We will, however, discuss a few simpler detection schemes in Section 4.3.1 that were initially considered, and why they failed, in order to highlight the need for the complexity of the final detection scheme.

In addition to choosing the correct detection scheme and normalization, it is also important to consider any processes that could produce a trend in the normalized detection volume fluorescence that could be mistaken as a signature of migration. If for instance, the STED2 pulse quenching is more or less efficient at longer delay times, due to excited state dynamics transferring excitons to an excited state energy level with a different Einstein coefficient for stimulated emission, for example a triplet or charge transfer state, then this variation in the effectiveness of the STED2 pulse would generate a trend in the normalized detection volume fluorescence, obscuring the signal produced by migration. This effect is discussed in Section 4.3.2. It is also important that the exciton density be low enough to avoid exciton-exciton annihilation, as this additional source of time dependent exciton quenching would also produce a trend in the normalized detection volume fluorescence that could be mistaken for migration. This effect is addressed in more detail in Section 4.3.3, followed by an overview of the experimental pulse modulation scheme that is required in order to isolate the signatures of migration in Section 4.3.4.

4.3.1 Detection Scheme to Normalize to the Fluorescence Lifetime

The best detection scheme to isolate the desired normalized detection volume fluorescence signal from the background fluorescence lifetime decay requires modulating the STED2 pulse and scanning the detection gate trigger with the STED2 delay time. A time-gated detector turns on just after the action of the STED2 pulse is complete, and it is scanned with the delay time to maintain its timing relative to the STED2 pulse. Modulating the STED2 pulse at each delay time then provides a robust normalization for calculating the normalized detection volume fluorescence. To illustrate the need for, and benefits of, this configuration,

consider how the simpler options fail to fully normalize for the fluorescence lifetime.

One simpler detection scheme would be to integrate all of the fluorescence from the sample, without any time-gate on the detector or with the gate trigger arriving before the pump pulse, for each STED2 pulse delay time (see Figure 4.3), and to modulate the STED2 pulse on/off (unblocked/blocked) and divide the observed fluorescence intensities. In this

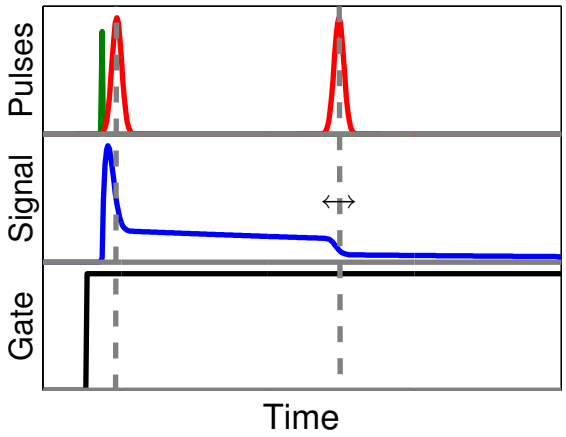

Figure 4.3: Schematic of a simpler detection scheme that integrates the full fluorescence emitted by the sample, but fails to normalize to the fluorescence lifetime. The top panel is the pulse sequence with pump (green) and STED pulses (red). The middle panel shows the excited state population, which is proportional to the instantaneous emission rate. The bottom panel is the gate, triggered on at a fixed time before the pump/STED1 pulses and integrating over the entire fluorescence lifetime.

case, the ratio of the detected fluorescence intensities with and without the STED2 pulse would tend to be smallest at short STED2 pulse delay times. For these short delay times, the excited state population would be smaller over the majority of the integration time, whereas the population would remain greater for longer delay times. This effect of increased relative fluorescence with increasing delay time would compete with the effect of migration, which would tend to decrease this ratio at longer delay times at which the exciton population distribution has greater spatial overlap with the STED2 pulse PSF. The origin of this problem is the detection of fluorescence from times before the action of the STED2 pulse. The origin of this problems is the detection of fluorescence from times before the action of the STED2 pulse. The options to resolve this issue are to either time resolve the entire fluorescence trace with time correlated single photon counting (TCSPC), where the arrival time of individual photons, relative the time of excitation, is recorded with a single photon counting detector and binned to build a histogram of arrival times that recreates the emission profile, or to use a very fast time-gated detector to isolate the fluorescence emitted after the STED2 pulse delay time.

Unfortunately, the pile-up correction discussed in section 3.4, which we use to remove the STED-induced fluorescent signal, is not compatible with TCSPC, since it only corrects for the number of photons missed due to pile-up and can not assign arrival time values for these photons. When using TCSPC the count rate must therefore be kept below 5% (ideally $< 2\%$) of the repetition rate to avoid pile-up, and successive traces must be taken with and without the pump so that the STED-induced contribution can be subtracted off. This severely limits the dynamic range available on the detector and the signal to noise ratio is not sufficient to extract the small changes due to migration. These measurements, however, are still useful for building an intuitive understanding of the experiment. Figure 4.4 shows the results of such experiments, which clearly indicate the action of the first and second STED pulses as sudden drops in the count rate. These traces are also very helpful in identifying the proper

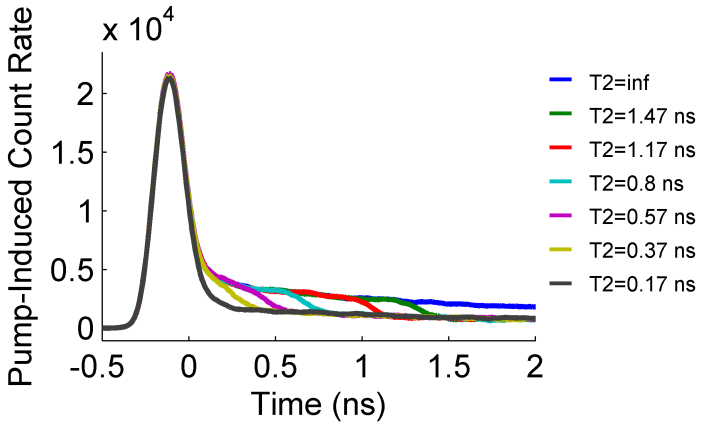

Figure 4.4: Experimental data collected with TCSPC. The data for pump on and off was subtracted to isolate the pump induced fluorescence. The different curves correspond to different STED2 delay times (T2), and the T2 = inf curve corresponds STED2 off (blocked).

normalization conditions to isolate the form of normalized detection volume fluorescence desired, which would correspond to the fraction of the exciton population at a given delay time that survives the action of the STED2 pulse. From Figure 4.4 it is clear that the proper normalization condition would be to measure the fluorescence with a time-gated detection selecting for emission events that occur after the STED2 pulse delay time, and to measure the signal with and without the action of the STED2 pulse to find the percentage of the population that survived the quenching of the STED2 pulse. In principle this could be achieved with a fixed time-gate at long times (longer than the maximum STED2 pulse delay time, $\sim$3 ns in this case), where the detector is always gated on at the same delay after the excitation and where the STED2 pulse delay is scanned within the window between the excitation and detection gate trigger (see Figure 4.5).

This would work well if the fluorescence decay were purely single exponential. Then the cases with and without STED2 would be equivalent for times before the STED2 pulse

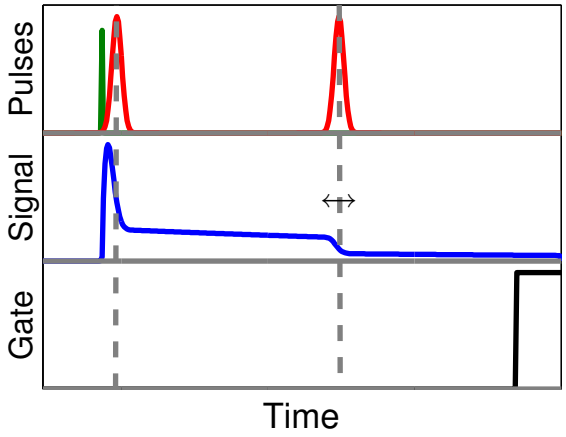

Figure 4.5: Schematic of a possible experiment and detection scheme for a time-gated detection at a constant delay after excitation. The colors indicate the same traces as in Figure 4.3.

arrival (as always), and after the arrival of the STED2 pulse these two cases would lead to a constant ratio between their respective signals. To illustrate this effect, suppose that $A(t)$ and $B(t)$ are two exponential decays

$$A(t) = A_o \exp^{-kt} \quad \text{and} \quad B(t) = B_o \exp^{-kt}, \tag{4.2}$$

with the same rate constant k, but with different initial amplitudes, A_o and B_o respectively, representing the fluorescence decay after the delay time with (A) and without (B) the action of the STED2 pulse. The ratio

$$\frac{A(t)}{B(t)} = \frac{A_o}{B_o} \tag{4.3}$$

is constant over the lifetime of the decay. This results in the normalized detection volume fluorescence being preserved over the course of the additional time delay between the STED2 pulse and the detection gate when the STED2 pulse delay time is small. If the decay is not a simple single exponential, however, then this relation breaks down. For this reason, it is best to scan the delay of the detection gate trigger to maintain a constant delay beyond the STED2 pulse, rather than a constant delay relative to the excitation, so that the gate trigger occurs just after the action of the STED2 pulse is complete for all STED2 delay times, and to integrate the fluorescence from that point onward (see Figure 4.6). This minimizes the effect of any difference in decay characteristics between the cases with and without the STED2 pulse. Scanning the gate trigger delay in sync with the STED2 pulse delay time also requires that the STED2 pulse be modulated on and off for each delay in order to obtain all the information needed to normalize for the fluorescence decay. In contrast to having a fixed detection gate trigger, relative to the excitation, at long times, where a single measurement without the STED2 pulse could be used to normalize the data for all the STED2 pulse delays. For these reasons we converged upon using the detection scheme in Figure 4.6.

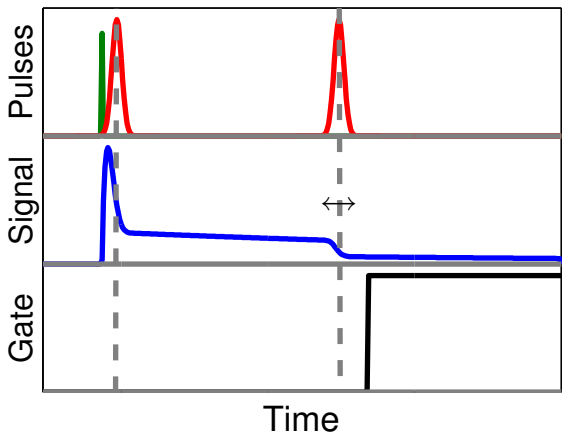

Figure 4.6: Schematic of the implemented experiment and detection scheme for a time-gated detection which is scanned insync with STED2 in delay. The colors indicate the same traces as in Figure 4.3.

Now we will move on to discuss how any variations in the efficiency of stimulated emission depletion over the exciton lifetime and any exciton-exciton annihilation, could produce trends in the normalized detection volume fluorescence that could be mistaken for migration, and how we nevertheless control for these effects.

4.3.2 Time Dependence of the Stimulated Emission Depletion Efficiency

Even with the correct detection scheme and normalization, it is also in principle possible for there to be excited state dynamics that could transfer excitons to an excited state energy level with a different Einstein coefficient for stimulated emission, for example a triplet or charge transfer state, which would alter the efficiency of the stimulated emission depletion process. This variation in the effectiveness of the STED2 pulse over the delay time would generate a trend in the normalized detection volume fluorescence, obscuring the signal produced by migration. If the STED pulse is sufficiently intense, however, operating in a saturation regime, and if its duration is long compared to the vibrational relaxation, then the degree of quenching should be relatively robust to small changes in the Einstein coefficient for stimulated emission. Since the rate constant for stimulated emission and absorption induced by the STED2 pulse is given by the product of the Einstein coefficient and the spectral energy density in the field, this effect would appear similar to a variation in the STED2 pulse energy over the delay time, and would most likely produce a slight change in the degree of confinement. This effect is very hard to fully remove by normalization, but we can monitor the contribution of this effect by performing the experiment with the STED1 pulse blocked, as shown in Figure 4.22. In this case, the population is not confined to a small volume but is dispersed over a large area, with a dramatically reduced gradient in its spatial

distribution. Since the gradient of the distribution drives the observable change produced by exciton migration, there is a negligible change in the extent of the distribution and any change in the normalized detection volume fluorescence can be attributed to either some small residual sensitivity to migration or to a change in the efficiency of the STED2 pulse with delay time. To facilitate this comparison we therefore also modulate the STED1 pulse in the experiment, so that this data can be simultaneously extracted. Fortunately, the result (Figure 4.22) shows no dependence of the normalized detection volume fluorescence over the delay time when the STED1 pulse is blocked. This confirms that the contribution from time dependence in the stimulated emission depletion efficiency is negligible and highlights the need for the confinement provided by the STED1 pulse in order to reveal the effects of migration.

4.3.3 Exciton-Exciton Annihilation

Additionally, if the excitation density is too high, excitons can annihilate with each other via singlet exciton annihilation.[71, 87, 98–107] In this process the energy of two S_1 excitons combines such that one occupies a higher energy state, S_n, and the other returns to the ground state, S_0. The high energy exciton then quickly thermalizes to the S_1 state, so that the net result is a density dependent quenching pathway whereby two excitons collide and one is quenched. Since annihilation is a density dependent process, it has the most dramatic effect near the center of the population distribution where the density is highest. Thus as annihilation proceeds the spatial profile of the exciton distribution changes. This effect is simple to model with the kinetic equation for annihilation,

$$\frac{dN}{dt} = -\gamma N^2, \tag{4.4}$$

where N represents the exciton population distribution as a function of both spatial position and time and γ is the annihilation coefficient. Numerically or analytically solving this kinetic equation for an initial Gaussian spatial population distribution yields the curves shown in Figure 4.7. As time evolves, the peak of the distribution is flattened by the action of annihilation, while the periphery of the distribution, where the density is lower, remains comparatively unaffected. Therefore, even though the distribution is not expanding spatially, the fraction of the population quenched by the STED2 pulse will increase in time as the percentage overlap with the STED2 pulse PSF increases, as shown in Figure 4.7, causing a corresponding decrease in the "normalized detection volume fluorescence." Thus, annihilation can mimic the effects of migration, and we therefore take great care to ensure the experiment is run at densities where annihilation is negligible (see Figure 4.23).

4.3.4 Modulation Scheme to Isolate Migration Signals

In order to implement the detection scheme and controls discussed above, we modulate both of the STED pulses. The STED2 pulse modulation facilitates the normalization scheme

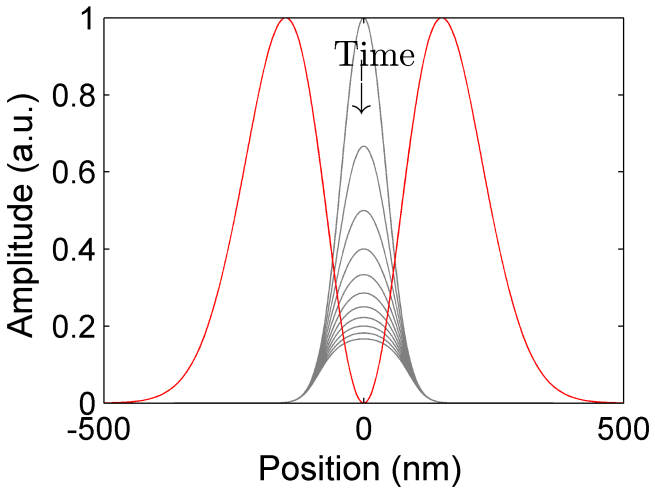

Figure 4.7: An illustration of how the overlap of STED2 (red) and the excited state population (grey) changes over time due to exciton annihilation.

to remove the contribution of the fluorescence lifetime and the calculation of the normalized detection volume fluorescence. The STED1 pulse modulation facilitates the control to identify any variation in the efficiency of stimulated emission over the exciton lifetime. In addition, as discussed in Section 3.4, the pump pulse must be modulated with an optical chopper to remove the background signal from STED-induced fluorescence. This results in 3 modulations with 8 possible beam combinations, outlined in Table 4.1 and illustrated in Figure 4.8, all of which are collected for each STED2 pulse delay time.

Name	Pump	STED1	STED2	Use	
All	1	1	1	Data	Migration
STED1 + STED2	0	1	1		
Pump + STED1	1	1	0	Normalization	
STED1 only	0	1	0		
Pump + STED2	1	0	1	Data	Control
STED2 only	0	0	1		
pump only	1	0	0	Normalization	
background	0	0	0		

Table 4.1: Schematic of the modulation scheme for simultaneous acquisition of the normalization and control conditions, a 1 means the pulse is incident on the sample and a 0 means the pulse is blocked.

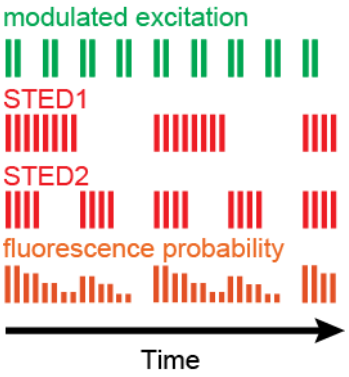

Figure 4.8: Illustration of the modulation scheme.

4.4 Kinetic Simulations of TRUSTED: Verification of Sensitivity to Migration

In order to verify that the normalization condition and modulation scheme presented above do in fact isolate the signature of migration from the detected raw fluorescence, a kinetic simulation of the experiment has been performed and analyzed. The experiment can be simulated starting from the kinetics outlined in Equation 3.1, however, the populations and optical fields must now be functions of both radial position and time. The STED field must also now include the combined temporal dependence of both STED pulses. Additional terms are also added to account for the migration and any other effects to be included, such as fluorescence, annihilation, or 2PA. The resulting equations are,

$$\begin{aligned}
\frac{dN_{ev}}{dt} &= B_{pump}\,\rho_{pump}\,(N_{gg} - N_{ev}) + \beta\,\rho_{sted}^2 N_{gg} - k_{vib}^* N_{ev} \\
\frac{dN_{eg}}{dt} &= B_{sted}\,\rho_{sted}\,(N_{gv} - N_{eg}) + k_{vib}^* N_{ev} - k_f N_{eg} - \gamma N_{eg}^2 + D(t)\nabla^2 N_{eg} \\
\frac{dN_{gv}}{dt} &= B_{sted}\,\rho_{sted}\,(N_{eg} - N_{gv}) - k_{vib} N_{gv} + k_f N_{eg} + \gamma N_{eg}^2 - D(t)\nabla^2 N_{eg} \\
\frac{dN_{gg}}{dt} &= B_{pump}\,\rho_{pump}\,(N_{ev} - N_{gg}) - \beta\,\rho_{sted}^2 N_{gg} - k_{vib} N_{gv}
\end{aligned} \tag{4.5}$$

where B_{pump} is the Einstein coefficient of the transition driven by the pump field with spectral energy density ρ_{pump}, B_{sted} is the Einstein coefficient of the transition driven by the STED field with spectral energy density ρ_{sted}, k_f is the rate constant for fluorescence, k_{vib}^* is the excited state vibrational relaxation rate, k_{vib} is the ground state vibrational relaxation rate, β is the 2PA coefficient, γ is the annihilation coefficient, $D(t)$ is the time dependent diffusivity, N_{ev}, N_{eg}, N_{gv}, and N_{gg} represent the spatially and time-dependent exciton populations in the corresponding levels in Figure 3.2a, and ∇^2 is the second derivative with respect to the spatial coordinates, as in the diffusion equation.

These equations must then be numerically propagated for all eight beam combinations to be used in the experiment (pump, STED1, and STED2) each in both the blocked (off) and unblocked (on) states. The excited state (N_{eg}) population is then integrated over the spatial coordinates for times after the detection gate is triggered, to calculate an analog of the raw fluorescence signal on the detector. These signals are then analyzed, in analogy to the experimentally collected data, as indicated in Table 4.1. The pump-induced fluorescence is first isolated by subtracting the pump-off case from the pump-on case for each combination of STED1 on/off and STED2 on/off. This should eliminate the contribution of the STED-induced fluorescence. Then the normalized detection volume fluorescence is calculated from the ratio of the case with the STED2 pulse on to the case with the STED2 pulse off, both with the STED1 pulse on, to recover the normalized detection volume fluorescence,

$$\text{normalized detection volume fluorescence} = \frac{\text{[Pump, STED1, STED2]-[STED1, STED2]}}{\text{[Pump, STED1]-[STED1]}} \tag{4.6}$$

where the pulses used in each case are indicated in the square brackets. The advantage of the simulation is that each process may be independently controlled, isolated, or removed to verify its effect on the calculated data.

To illustrate the kinetics in the simulation and experiment, an example of the calculated evolution of the exciton population distribution over time is shown in Figure 4.9 for two STED2 pulse delay times, and for the STED2 pulse on and off conditions. For the purposes of this visualization, we simplified the kinetics by assuming the pump and excited state vibrational relaxation are impulsive, so that the initial condition is a Gaussian spatial distribution in level eg. The other parameters were set as follows: The Einstein coefficient of the transition driven by the STED field was set to $B_{sted} = 10$ nm^2/((energy a.u.) ps^2) by trial in combination with the amplitude A of the STED spectral energy density to produce a reasonable degree of confinement, the 2PA coefficient was set to $\beta = 0.1$ nm^6/((energy a.u.)^{2}ps^3) and is not a sensitive parameter since the contribution of 2PA is removed in the analysis, the annihilation coefficient was set to $\gamma = 0$ ps^{-1} to avoid the potential complication of annihilation and visually highlight the effect of migration, the diffusivity was set to $D(t) = 1$ nm^2/ps, which is likely a slight over estimate, but allows for a clear visualization of the effects of migration, the rate constant for fluorescence was set to $k_f = 0.0002$ ps^{-1} based on the lifetime of CN-PPV,[251] the ground state vibrational relaxation was set to $k_{vib} = 0.05$ ps^{-1}, and is not a sensitive parameter as long as it is a fast process compared to the duration of the STED pulse (~ 120 ps). The STED1 field spectral energy density was defined as

$$\rho_{sted1}(r,t) = A_1 r^2 \exp\left(-\frac{r^2}{2\sigma_r^2}\right) \exp\left(-\frac{t^2}{2\sigma_t^2}\right), \tag{4.7}$$

where r is the radius, $\sigma_r = 209.5$ nm is the standard deviation in the radial dimension and was set by comparison to the STED PSF, t is time, $\sigma_t = 33$ ps is the standard deviation in time and was set to reproduce the ~ 120 ps FWHM of the STED pulse, and $A = 10$ (energy a.u.) ps/nm^3 is the amplitude and was chosen by trial, in combination with B_{sted} to produce

a reasonable degree of confinement. The STED2 field spectral energy density was

$$\rho_{sted2}(r,t) = Ar^2 \exp\left(-\frac{r^2}{2\sigma_r^2}\right) \exp\left(-\frac{(t-t_2)^2}{2\sigma_t^2}\right), \tag{4.8}$$

where t_2 is the delay time of the STED2 pulse, and all other variable are the same as in Equation 4.7. The total spectral energy density is

$$\rho_{sted}(r,t) = \rho_{sted1}(r,t) + \rho_{sted2}(r,t). \tag{4.9}$$

Figures 4.9a,b show a short delay time (1 ns), while Figures 4.9c,d, have a longer delay time (2 ns). The initial distribution (blue) is first acted on by the STED1 pulse, creating a confined distribution. Migration is then allowed to proceed over the delay time (green), during which the initially confined distribution expands. The STED2 pulse is then applied (parts a,c) or not (parts b,d), and the detector is triggered to integrate the remaining signal (red). The normalized detection volume fluorescence is the ratio of the area under the red curves in Figure 4.9 a and b, for the short delay, and Figure 4.9 c and d, for the long delay.

These kinetic simulations were also used to determine whether the proposed detection scheme and normalization should isolate the signatures of migration. First, as shown in Figure 4.10a, when fluorescence is the only active process there is no observed change in the calculated normalized detection volume fluorescence, however if diffusion is the only active process, a change in the normalized detection volume fluorescence is observed, Figure 4.10b. Additionally, if both fluorescence and diffusion are active, the observed normalized detection volume fluorescence trend is identical to the diffusion only case, Figure 4.10c. These results indicate that the fluorescence decay due to the the exciton lifetime does not contribute to the normalized detection volume fluorescence trend. Finally, the potential challenge posed by exciton-exciton annihilation is illustrated in Figure 4.10d, where annihilation is the only active process and a change in the normalized detection volume fluorescence is observed, which appears very similar to the trend created by migration, as predicted. This result highlights the importance of verifying that the excitation densities used in the experiment are in the linear regime, where annihilation is negligible. Note that we do not expect these calculations to perfectly match any experimental results, in slope or intercept, as they were not run with a degree of confinement matched to the experimental data and the parameters are not identical to those found in a real material. They primarily serve to illustrate which processes the experiment should be sensitive to by allowing the reader to visualize it.

4.5 Experimental Setup and Scan Operations

Before presenting the experimental results for CN-PPV, we will discuss the experimental setup used to perform the measurements and some of the experimental details and hurdles that were overcome. Specifically, in this section, we will discuss updates to the experimental setup that were implemented after STED imaging work presented in Chapter 3, the method used to stabilize the pump and STED pulse energies over the course of the experiment, and the order in which the parameters are varied during data collection.

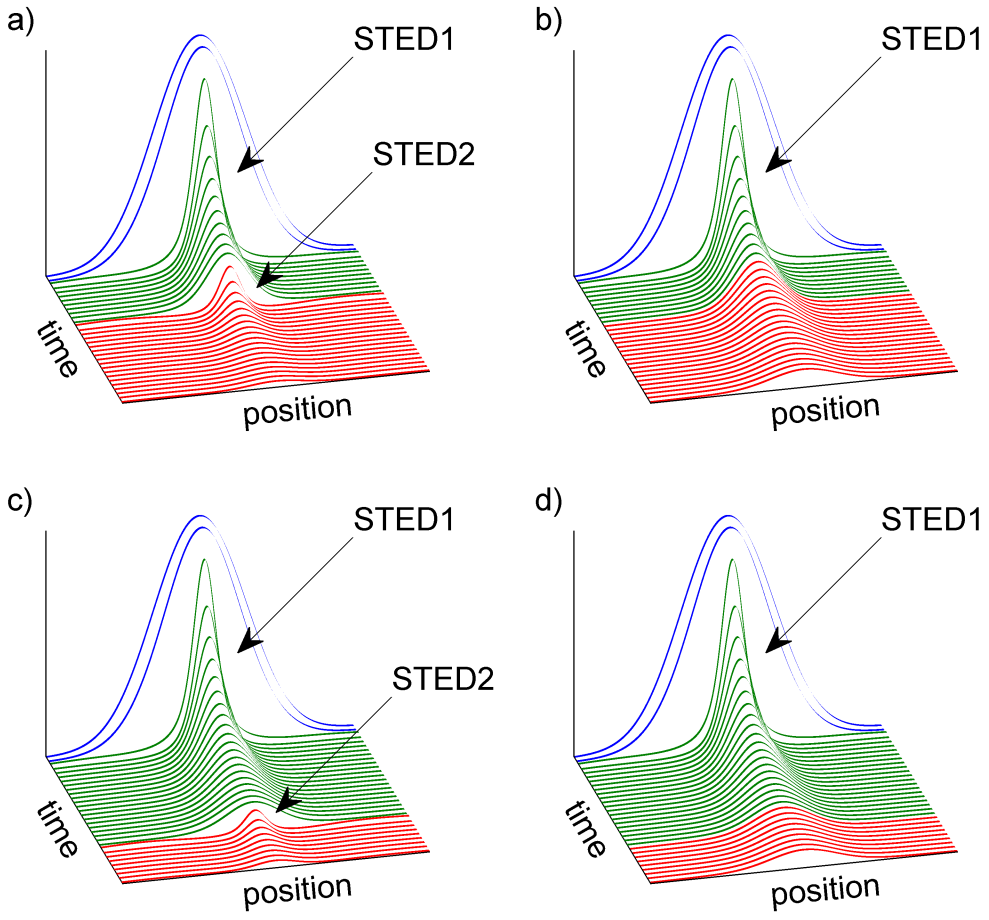

Figure 4.9: Simulations of the exciton population distribution over the course of the experiment. The initial population is shown in blue, the population over the delay time is shown in green, and the population during the detection gate is shown in red. a) short delay with STED2 on, b) short delay time with STED2 off, c) long delay with STED2 on, d) long delay with STED2 off. In each case the range on the position axis is 1 μm and the range on the time axis is 3 ns.

4.5.1 Updates to the Experimental Setup

This experiment utilizes the same experimental setup as the STED imaging project presented in Chapter 3 and is illustrated in Figure 3.17. The interferometer in the STED line, which wasn't used in the imaging project, is designed to allow for the creation of the second STED pulse with a controlled delay time. The STED1 pulse follows the arm of the STED interferometer that has stationary optics, while the arm with the optical delay line is for the STED2 pulse. It is important that the STED1 path optics are the same as those in

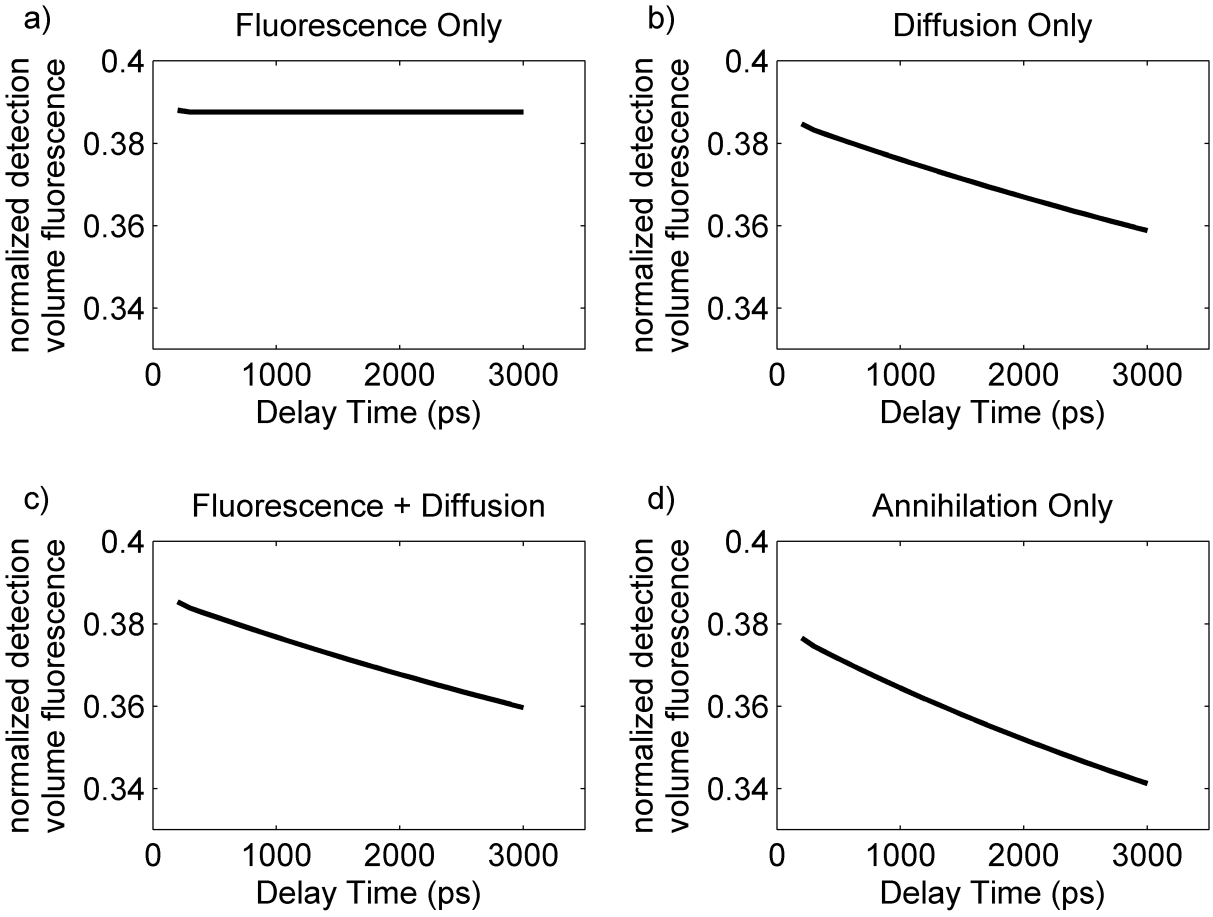

Figure 4.10: Simulated normalized detection volume fluorescence, including only the process of a) k_f=1/5000 ps^{-1}, b) D=0.08 nm^2/ps, c) D=0.08 nm^2/ps and k_f=1/5000 ps^{-1}, d) $\gamma = 0.001$.

the STED2 path so that when the beams are recombined they are in the same orientation and can be overlapped to maintain the same transverse mode profile as found in the original beam. If the optics are not matched, one of the beams may be a mirror image or inversion of the other. This would result in different downstream fiber coupling conditions for the two STED pulses (through the same fiber) and any upstream pointing fluctuations would cause the spatially recombined beams to separate. Both of these effects are minimized by matching the optics in the two lines. Additionally, a telescope was added to the STED line for these experiments, just before the dichroic coupling mirror, which expands the STED beam diameter to more completely fill the back aperture of the objective. The resulting experimental point spread functions for the pump and the STED pulses are shown in Figure 4.11. Note that the size of the STED PSF in Figure 4.11 is approximately 2/3 the size of the one in Figure 3.24.

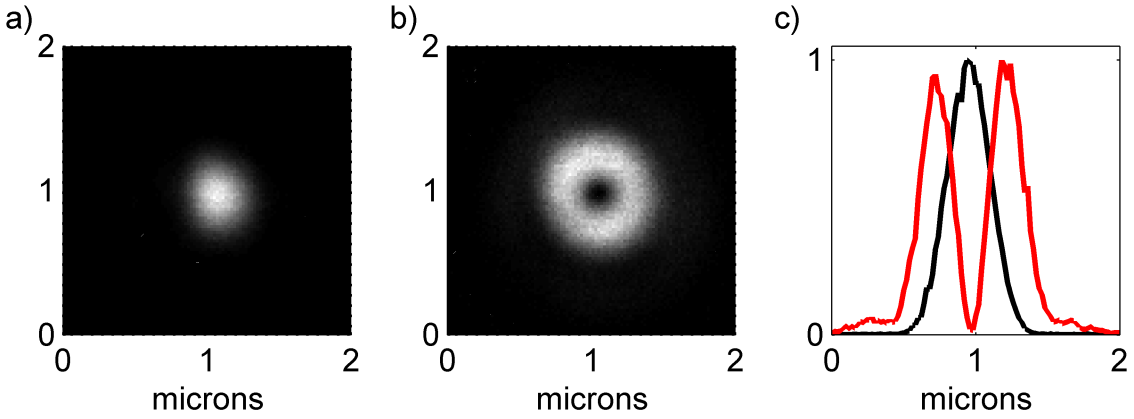

Figure 4.11: The point spread function of a) the pump, b) the STED pulses, and c) an overlay of normalized cross-sections through the pump and STED pulses.

The resolution of the microscope with these updated point spread functions was measured by imaging a CN-PPV nanoparticle, as in the previous chapter. The resulting resolution curve is shown in Figure 4.12. The best resolution yielded a FWHM of 67 nm, while a typical STED energy used in our work of 240 pJ produced an excitation spot size of 85 nm FWHM.

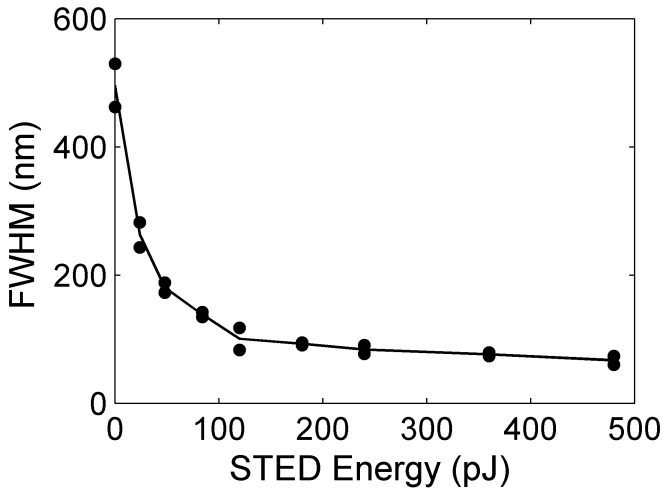

Figure 4.12: Measured resolution as a function of STED pulse energy.

4.5.2 Power Stabilization

The data collection for a single data set can take up to 24-48 hours, and over this time there can be some fluctuations in the output power of the NOPAs used to create the pump and STED pulses, or some drift in the beam pointing, which impacts the fiber coupling efficiency and thus the power incident on the sample. These effects must be monitored and corrected for. As in the imaging work in Chapter 3, the noise eater in the pump line acts to control and stabilize the pump pulse power. In addition, both arms of the STED interferometer paths include motorized waveplates just before the polarizing beam splitting cube that recombines the STED1 and STED2 pulses, which act to independently control their transmitted powers and facilitate corrections for power fluctuations. During the data collection, the LabView code stops periodically to check the powers of the STED1 and STED2 pulses and makes corrections to the motorized waveplates to adjust accordingly. For the STED2 pulse, this process is more complicated. The STED2 beam is difficult to perfectly collimate over the range of the delay stage positions, so the beam size at the fiber changes with the delay setting unless some calibrated path-dependent compensation is performed. This impacts the coupling efficiency of STED2 through the fiber, and thus the fiber output power varies with the delay setting. This effect is mitigated by setting a waveplate calibration curve for the STED2 line that adjusts the waveplate angle for each delay setting, changing the beam power to compensate for the change in the coupling efficiency. This calibration curve is also reset periodically during the data collection to correct for any variations in the calibration over the duration of the experiment.

4.5.3 Order of Events During Data Collection

The order of operations during data collection is also important to consider, as it impacts the duration of the experiment and the fidelity of the data. Our multi-variable data acquisition process can be conceptualized as a set of nested for-loops, defining and iterating over the values of each parameter. The variable in the inner-most loop is changed for every data point collected, while the variable in the outer most loop is only iterated through the values along its range once. The data acquisition will therefore run fastest if the fastest variable to change is placed in the inner-most loop and the slowest variable to change is places in the outer-most loop. When two data points are collected for comparative purposes, however, such as our normalization condition, it is generally advantageous to collect these data as close to simultaneously as possible. The order of operations used is illustrated in Figure 4.13. The inner-most level is the pump modulation. This modulation is driven by an optical chopper at 500 Hz and is the fastest variable. The next level is the position of the sample stage in XYZ, which is driven by piezos. We alternate between a set of spatial positions to eliminate heating effects that otherwise occur, see Section 3.3.1. We then modulate the STED1 and STED2 shutters (labeled S1 shutter and S2 shutter in Figure 4.13). These shutters have response times of $\sim$ 20 ms and $\sim$ 200 ms respectively. This gives the eight possible beam combinations for all spatial locations. Next, we change the STED2 pulse delay stage

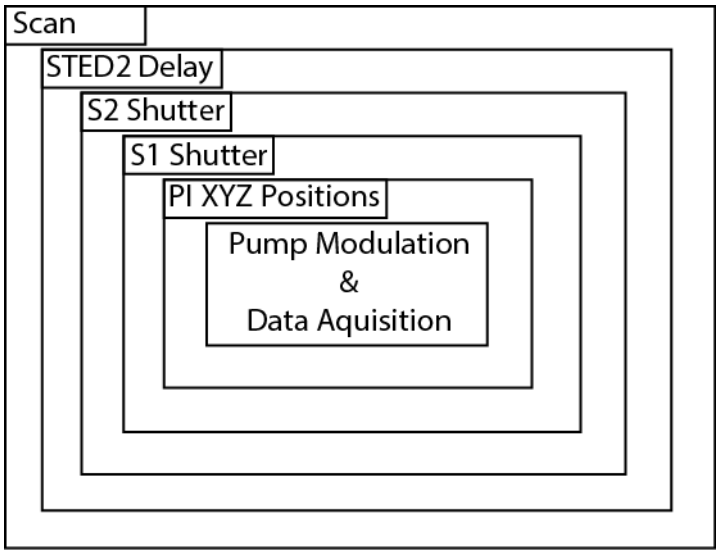

Figure 4.13: Illustration of the order in which variables are changed during our data collection.

position, which is our slowest stage. For this reason we vary the delay linearly, instead of randomizing the delay points, which would provide better fidelity at the cost of increased duration of data collection. Finally, we iterate this entire process, which we refer to as a "scan", to average the data and gather statistics for error analysis. We also pause after every 3-10 scans to refocus the light on the sample and reset the waveplate angles in the STED1 and STED2 lines to set the powers of each beam and compensate for any fluctuations in the STED2 waveplate calibration (caused, for example, by drift in the beam pointing with changes in the room temperature), both of which are automated procedures.

4.6 Results and Data Analysis for TRUSTED on CN-PPV Thin Films

Here we present the experimental results and analysis for the application of TRUSTED to CN-PPV thin films. We will discuss the sample preparation in Section 4.6.1 and the method of data collection and processing in Section 4.6.2. The experimental data is presented in Section 4.6.3. A fitting routine to extract the length scale of migration from the experimental results is then discussed in Section 4.6.4, and the results of the fit shown in Section 4.6.5. We then discuss the results of two control experiments. In Section 4.6.6 we show the data collected with the STED1 pulse blocked to demonstrate that the efficiency of STED2 pulse does not change over the delay time due to excited state dynamics, and in Section 4.6.7 we present an excitation dependence of our experimental result to demonstrate that annihilation does not contribute significantly to our data. These controls verify that the

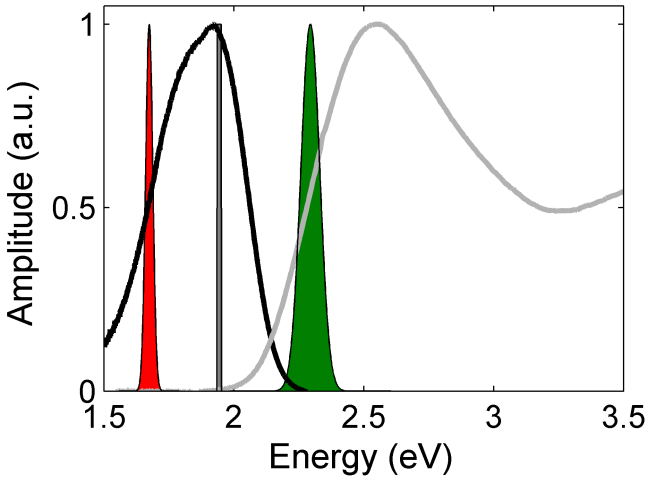

Figure 4.14: The absorption (gray) and emission (black) of a CN-PPV film used for TRUSTED measurements, with the pump (green), STED (red), and fluorescence detection bandpass (gray) spectra overlaid.

observed normalized detection volume fluorescence trend is in fact due to exciton migration.

4.6.1 Sample Preparation

The experimental procedure outlined above was carried out on thin films of CN-PPV prepared by spin-casting a ~ 2.5 mg/mL solution of CN-PPV in chloroform on glass microscope coverslips in a nitrogen glove box, where they were encapsulated to protect them from oxygen during measurement. The solution was prepared by dissolving 9.8 mg CN-PPV in 1 mL chloroform and stirring on a hot plate overnight, then diluting 0.255 mL of this solution with 0.745 mL chloroform. The resulting solution was heated to 50° for ~ 4 hours before spin-casting at 8000 RPM for 1 min with an acceleration of 8000 RPM/sec.

The spectrum of a film thus prepared is shown in Figure 4.14, with our laser pulses and collection bandwidth overlaid.

4.6.2 Data Collection and Processing

Here we discuss the methods used to process the collected experimental data to calculate the normalized detection volume fluorescence and its uncertainty. Experimental data was collected on CN-PPV films using the apparatus described in Section 4.5, where a custom LabView interface was utilized to control all parameters and acquire the data. The pile-up correction and excitation modulation to remove the STED-induced fluorescence is handled in LabView during data collection. This is achieved by sending the second harmonic of the 500 Hz chopping frequency to the DAQ counting card to trigger binning of counts from the

detector. The count rate is then computed for each bin and then sorted, with every other bin corresponding to chopper open and closed phases of the modulation cycle. This process yields two raw count rate data stream channels (Figure 4.15c,d): one for each chopper state. These channels are averaged over multiple chopper modulation cycles to improve signal to noise, and then corrected for the pileup effect (see Section 3.4) and subtracted to isolate the pump-induced fluorescence signal for each particular spatial pixel and delay time (Figure 4.15a,b). This data is collected for all prescribed spatial locations and combinations of STED1 on/off, STED2 on/off, and delay times, and then this process is repeated for the prescribed number of scan iterations for averaging purposes. For reference, an example of these signals is shown in Figure 4.15, where all spatial locations and iterations have been averaged.

After data collection, the resulting multidimensional data set is imported to a custom MatLab analysis code for processing to calculate the normalized detection volume fluorescence and its uncertainty. The essential steps in the data analysis are the averaging of the scans and the calculation of the normalized detection volume fluorescence and its error. The normalized detection volume fluorescence is simply the ratio of the detected, pump-induced, fluorescence at each delay time with the STED2 pulse on and off, and can be quickly calculated from the data set. There is, however, a question as to the appropriate order of operations of the data averaging and the calculation of the normalized detection volume fluorescence. In this case, the choice has an effect on the calculated uncertainty. This problem stems from the difference in correlated and uncorrelated changes in the detected fluorescence levels. The data collection takes up to 48 hrs to complete, and over that time there are some laser power fluctuations and refocusing, which change the overall fluorescence level from the sample. If the average of the pump-induced fluorescence is first calculated for the STED2 pulse on and the STED2 pulse off cases (an is Figure 4.15b), there will be a large standard error of the mean due to these effects that will then propagate through the normalized detection volume fluorescence calculation. These long term effects, however, produce correlated changes in the pump-induced fluorescence level for both the STED2 pulse on and the STED2 pulse off cases, and they can thus be better controlled for by first calculating the ratio of the STED2 pulse on to the STED2 pulse off cases (normalized detection volume fluorescence) for a given scan, spatial pixel, and delay time, and then averaging the normalized detection volume fluorescence and and finding the standard error of the mean of this data set. The result is a smaller standard error of the mean that better reflects the uncertainty in the normalized detection volume fluorescence. To illustrate the issue, Figure 4.16 shows the variation in the pump-induced fluorescence count rates for the STED2 pulse on and the STED2 pulse off cases compared to the variation in the normalized detection volume fluorescence over the course of experiment, for a particular data point (spatial pixel and delay time). The data can then be averaged over the spatial coordinates visited to further improve signal to noise, or it can be analyzed as a function of space to search for heterogeneity in the samples response. Because we found that in CN-PPV there were no statistically significant differences observed at different locations (see Figure B.1), we typically aggregated the data from these spots to improve the signal-to-noise ratio.

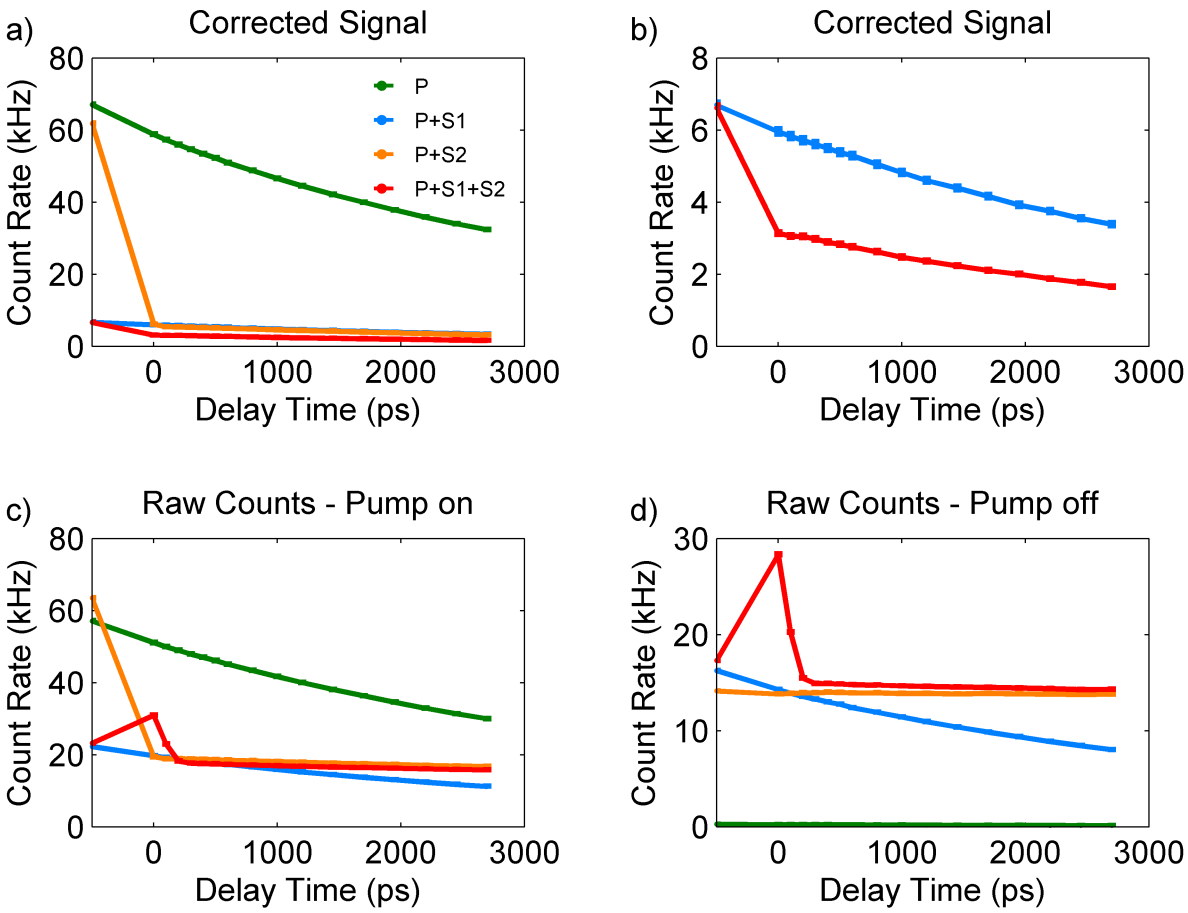

Figure 4.15: Examples of the isolated pile-up corrected modulated signal and the underlying raw data. The graphs include the overlaid data for the 4 possible STED shutter combination (S1 and S2, on or off), the pump only (S1off/S2off) in green, pump+STED1 (S1on/S2off) in cyan, pump+STED2 (S1off/S2on) in orange, and pump+STED1+STED2 (S1on/S2on) in red. a) The isolated and pile-up corrected pump-induced fluorescence calculated from the raw data for the pump on and pump off chopper phases. b) same as part (a) but only showing data for pump+STED1 (S1on/S2off) and pump+STED1+STED2 (S1on/S2on), which go into the determination of the normalized detection volume fluorescence. c) The raw count rates when the pump is on (chopper open). d) The raw count rates when the pump is off (chopper closed).

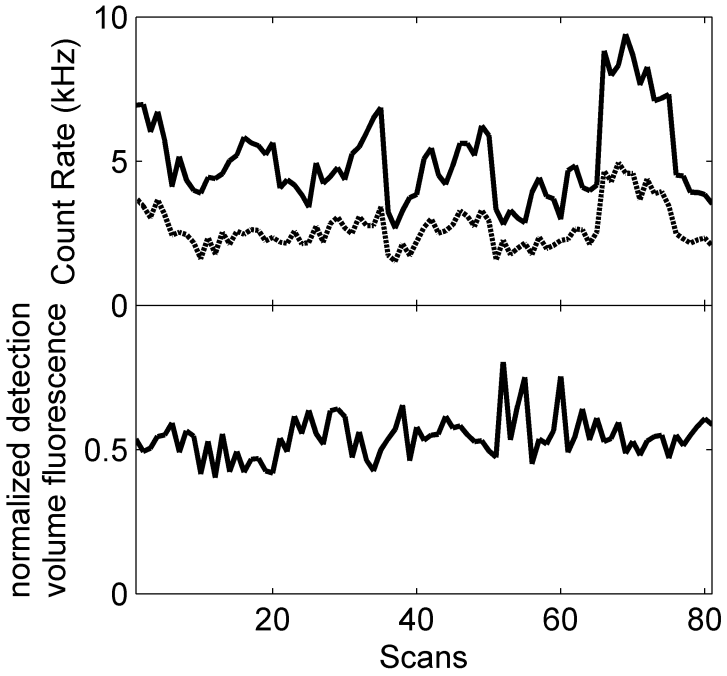

Figure 4.16: Top: Pump induced fluorescence for the STED2 pulse off (solid) and the STED2 pulse on (dashed) cases. Bottom: The ratio the STED2 pulse on/off, or normalized detection volume fluorescence. Notice that the ratio does not reflect the systematic changes in the raw fluorescence values.

4.6.3 Experimental Data for CN-PPV

The resulting normalized detection volume fluorescence for a thin film of CN-PPV, calculated using the procedure discussed above, is shown in Figure 4.17. The data shown represents the average over nine spatial locations in a 60×60 μm area, with 30 μm spacing between points, in order to mitigate sample heating by iterating between spatial locations to allow for any thermal buildup to dissipate. The data from these nine individual locations are shown in Figure B.1, where the consistence of the results within the error of the measurement indicates that the sample is likely amorphous on the scale of the measurement. The pump energy was 3 fJ/pulse and the STED energy was 240 pJ/pulse. The data for delay times <100 ps has been cut out due to STED pulse overlap in this region. The initial value indicates that roughly 50% of the initially confined distribution survives the action of the STED2 pulse at early delay times. If the STED pulse PSF cross section had sharp edges, with zero intensity for $r < r_1$ and $r > r_2$ and a finite value between r_1 and r_2, then the initial value would be 100%, however, since the STED pulse actually has a Laguerre-Gaussian mode there is some quenching of the initially confined distribution, even in the absence of

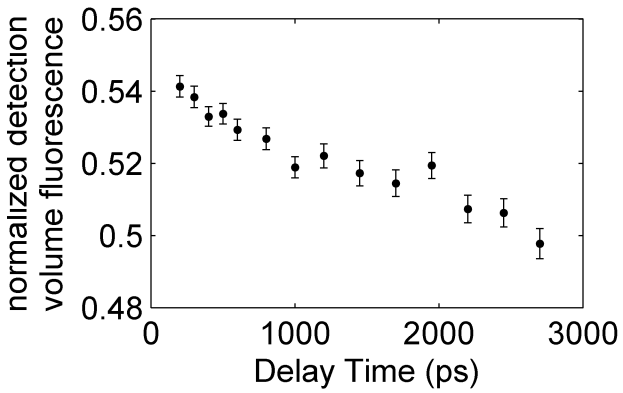

Figure 4.17: Experimental normalized detection volume fluorescence vs delay time for the CN-PPV film.

migration, due to the non-zero overlap of the exciton population distribution and the STED pulse PSF at and near the central axis of both distributions. For longer delay times, migration causes the exciton population distribution to expand, resulting in a larger overlap with the STED2 pulse PSF and a reduction in the percentage of the population that survives to contribute to the normalized detection volume fluorescence. Due to the limited length scales of exciton migration, this effect produces a small but measurable change. Additional data sets are presented in Figure B.2 for reference, which do not show significant deviations from the presented results over multiple days and macroscopic sample locations.

4.6.4 Fitting Algorithm to Extract the Characteristic Migration Length

The next challenge is to identify the length scale of exciton migration that would produce the observed trend in the normalized detection volume fluorescence in Figure 4.17. We extract this length scale for exciton migration from the experimental data using a custom fitting function with Matlab's "lsqcurvefit()" function. The fit function is based on a simplified model of the experiment and is illustrated in Figure 4.18. The model represents the initial population in the excited state as a 2D-Gaussian with a standard deviation obtained from fitting the PSF of the pump pulse (see Figure 4.11a), under the assumptions of impulsive excitation and excited state vibrational relaxation. The kinetics of the STED1 pulse interacting with the exciton population distribution are then treated analytically as described in Equation 3.8, where the rate constant, $k_{sted} = B_{sted}\rho_{sted}$, is proportional to the intensity of the STED pulse and since the intensity is in arbitrary units in the simulation the intensity of the pulse, I_{sted}, is used in place of the rate constant. The STED1 pulse PSF radial dependence is assumed to have the functional form described by Equation 3.16, and its width is obtained from a fit to the experimental STED pulse PSF (see Figure 4.11b). The

ground state vibrational relaxation rate is assumed to be 0.05 ps^{-1}. The model is insensitive to this parameter as long as it is fast compared to the STED pulse duration (∼120 ps). The intensity of the STED1 pulse in the model is then set by performing a separate fit to find the STED1 pulse intensity (Figure 4.18a) that produces a confined distribution (excitation volume) of the desired FWHM, which is an input parameter. This value is chosen by measuring the resolution of a STED image of a CN-PPV nanoparticle with a STED pulse of the same energy as used in the migration measurement. This STED resolution curve is shown in Figure 4.12. This procedure allows the model to account for the pump and STED1 pulses and to treat a confined distribution of the correct size. To proceed, the model must account for migration and the action of the STED2 pulse (Figure 4.18b). The excitation distribution from the previous step is assumed to be a Gaussian, which is a good assumption when the STED pulse duration is long compared to the ground state vibrational relaxation. We have also used numerical models that do not make this assumption and the results were similar. The migration of this Gaussian distribution is then propagated over the time delay with a generalized diffusion model, allowing for time dependent diffusivity (see Section 1.2.6.1), where the the evolution of the Gaussian is described by $\sigma(t)^2 = \sigma_o^2 + 2\int_0^t D(t')dt'$. The STED2 pulse is assumed have an identical intensity and radial distribution as the STED1 pulse and its action is again applied analytically using Equation 3.8. The normalized detection volume fluorescence is then calculated as the ratio of the excited state population after to before the action of STED2.

This model represents a simplified analytical simulation of the experiment which can then be fit to experimental data, using matlab's "lnsqcurvefit()" function. The free parameters in the fit are the parameters that define the time dependence of the diffusivity in the model. For diffusive migration, $D(t) = D_o$, and the diffusivity is the only free parameter, besides an offset to correct the initial value to account for deviations of the real STED pulse PSF from the ideal beam mode assumed in the fit. The diffusivity can be more generally described as a power law, $D(t) = D_o t^{\alpha-1}$, where D_o and α are the free parameters, along with an offset. In the power law model, $\alpha = 1$ corresponds to diffusive migration, $\alpha < 1$ is subdiffusive, and $\alpha > 1$ is superdiffusive.

This fitting procedure yields the parameters that define the time dependence of the diffusivity. The characteristic length for migration can then be calculated by noting that in the diffusive model

$$L_d^2 = \frac{\int_0^\infty D_o t e^{-t/\tau}}{\int_0^\infty e^{-t/\tau}}, \tag{4.10}$$

such that

$$L_d = \sqrt{D_o \tau}, \tag{4.11}$$

or in the power law diffusivity model

$$L_d^2 = \frac{\int_0^\infty \left(\frac{D_o}{\alpha}\right) t^\alpha e^{-t/\tau}}{\int_0^\infty e^{-t/\tau}}, \tag{4.12}$$

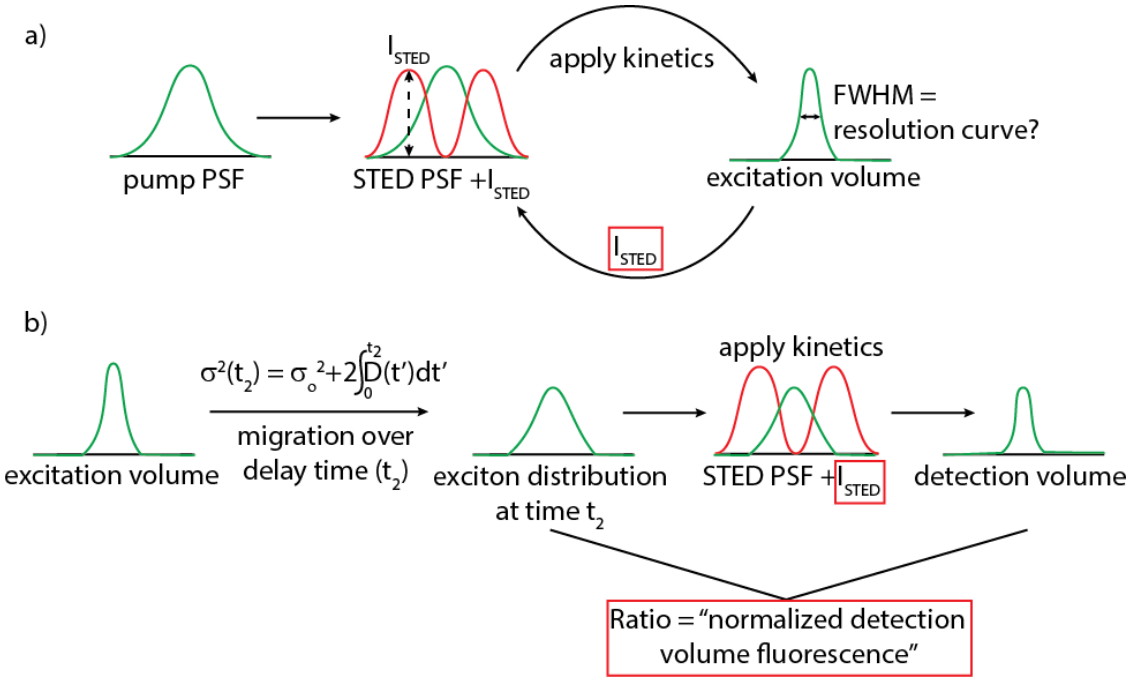

Figure 4.18: A schematic of the model used in the fitting routine. a) The first step starts with a Gaussian distribution of excitons based on the pump pulse PSF, the kinetics of stimulated emission depletion from Equation 3.8 are then applied to account for the STED1 pulse, where the radial dependence of the STED field is taken from Equation 3.16 fit to the STED pulse PSF, and the intensity, I_{STED} is variable. The appropriate value of I_{STED} is found by fitting the FWHM of the resulting excitation volume to the observed value from the resolution curve in Figure 4.12. b) The excitation volume found in the previous step is then propagated under migration over the delay time, t_2, with the expression derived in section 1.2.6.1. The action of the STED2 pulse is then applied, again using Equation 3.16, with the same radial dependence and intensity as found for the STED1 pulse in the previous step. The normalized detection volume fluorescence is then the ratio for the excited state population after to before the action of STED2.

such that

$$L_d = \sqrt{\left(\frac{D_o}{\alpha}\right)\tau^{\alpha}}. \tag{4.13}$$

See Section 1.2.6.1 for the derivation of these expressions. The uncertainty in these "diffusion lengths" is calculated from the uncertainty in the free parameters from the fit, which can be calculated based on the Jacobian of the fit, the experimental error, and the residuals, following an established procedure.[118] The goal of this procedure is to transform the covariance

matrix of the data (C^d) into a convariance matrix for the fit parameters (C^p), which can be expressed as,

$$C^p_{ij} = \frac{dp_i}{dy_k} C^d_{ks} \frac{dp_s}{dy_j} \tag{4.14}$$

or in matrix form as,

$$\mathbf{C^p} = \left[\frac{\mathbf{dp}}{\mathbf{dy}}\right] \mathbf{C^d} \left[\frac{\mathbf{dp}}{\mathbf{dy}}\right]^T \tag{4.15}$$

where $\mathbf{p}$ is a vector of the parameters and $\mathbf{y}$ is a vector of the data points. It can be shown that,

$$\frac{\mathbf{dp}}{\mathbf{dy}} = (\mathbf{J}\mathbf{J}^T)^{-1}\mathbf{J} \tag{4.16}$$

where $\mathbf{J}$ is the Jacobian of the fit,

$$J_{ij} = \frac{df(x_j, \vec{p})}{dp_i}, \tag{4.17}$$

and $f(x_j, \vec{p})$ is the value of the fit for the j^{th} data point. To see this result, consider the equation that is solved in least squares analysis, for each parameter p_i,

$$\frac{d}{dp_i}\left[\sum_j \left[y_j - f(x_j, \vec{p})\right]^2\right] = 0. \tag{4.18}$$

If we apply a small perturbation to the $\vec{y}$ values, such that $\vec{y} = \vec{y_o} + \delta\vec{y}$, there will be a corresponding perturbation in the fit parameters, such that $\vec{p} = \vec{p_o} + \delta\vec{p}$. Plugging this in to equation 4.18 gives,

$$\frac{d}{d(p_i + \delta p_i)}\left[\sum_j \left[y_j + \delta y_j - f(x_j, \vec{p_o} + \delta\vec{p})\right]^2\right] = 0 \tag{4.19}$$

and since p_i is a constant, $\frac{d}{d(p_i+\delta p_i)} \rightarrow \frac{d}{d(\delta p_i)}$. The function $f(x_j, \vec{p_o} + \delta\vec{p})$ can also be expanded as,

$$\begin{aligned} f(x_j, \vec{p_o} + \delta\vec{p}) &= f(x_j, \vec{p_o}) + \left.\frac{f(x_j, \vec{p})}{d\vec{p}}\right|_{\vec{p}_o} \cdot \delta\vec{p} \\ &= f(x_j, \vec{p_o}) + \sum_k \left.\frac{f(x_j, \vec{p})}{dp_k}\right|_{\vec{p}_o} \delta p_k \end{aligned} \tag{4.20}$$

and then using the definition of the Jacobian in equation 4.17 we find,

$$f(x_j, \vec{p_o} + \delta\vec{p}) = f(x_j, \vec{p_o}) + \sum_k J_{kj}\delta p_k. \tag{4.21}$$

Plugging this expression back in to equation 4.19 yields,

$$0 = \frac{d}{d(\delta p_i)} \left[\sum_j \left[y_j + \delta y_j - f(x_j, \vec{p}_o) - \sum_k J_{kj} \delta p_k \right]^2 \right] \tag{4.22}$$

and the derivative can then be applied to obtain

$$0 = -2 \sum_j \left[y_j + \delta y_j - f(x_j, \vec{p}_o) - \sum_k J_{kj} \delta p_k \right] \left[\sum_k J_{kj} \frac{d(\delta p_k)}{d(\delta p_i)} \right], \tag{4.23}$$

where the term $\frac{d(\delta p_k)}{d(\delta p_i)} = \delta_{ik}$ is the Kronecker delta. Also, if we let $f(x_j, \vec{p}_o) = F_j$, then

$$\begin{aligned} 0 &= \sum_j \left[J_{ij} y_j + J_{ij} \delta y_j - J_{ij} F_j - \sum_k J_{ij} J_{kj} \delta p_k \right] \\ &= \sum_j J_{ij} y_j + \sum_j J_{ij} \delta y_j - \sum_j J_{ij} F_j - \sum_k \sum_j J_{ij} J_{kj} \delta p_k, \end{aligned} \tag{4.24}$$

where the sums can now be recognized as matrix and vector products. Note that $(\mathbf{J}\mathbf{J}^T)_{ik} = \sum_j J_{ij} J_{kj}$, such that Equation 4.24 can be recast as

$$\begin{aligned} 0 &= (\mathbf{J}\vec{y})_i + (\mathbf{J}\delta\vec{y})_i - (\mathbf{J}\vec{F})_i - \sum_k (\mathbf{J}\mathbf{J}^T)_{ik} \delta p_k \\ &= (\mathbf{J}\vec{y})_i + (\mathbf{J}\delta\vec{y})_i - (\mathbf{J}\vec{F})_i - ((\mathbf{J}\mathbf{J}^T)\delta\vec{p})_i. \end{aligned} \tag{4.25}$$

This expression should hold for all i, such that

$$0 = \mathbf{J}\vec{y} + \mathbf{J}\delta\vec{y} - \mathbf{J}\vec{F} - (\mathbf{J}\mathbf{J}^T)\delta\vec{p}, \tag{4.26}$$

or rearranging to find $\delta\vec{p}$,

$$\delta\vec{p} = (\mathbf{J}\mathbf{J}^T)^{-1}\mathbf{J}\vec{y} + (\mathbf{J}\mathbf{J}^T)^{-1}\mathbf{J}\delta\vec{y} - (\mathbf{J}\mathbf{J}^T)^{-1}\mathbf{J}\vec{F}. \tag{4.27}$$

Then using the definition of the derivative we find,

$$\frac{\mathbf{dp}}{\mathbf{dy}} = \frac{\delta p(\delta y) - \delta p(-\delta y)}{2\delta y} \tag{4.28}$$

$$= (\mathbf{J}\mathbf{J}^T)^{-1}\mathbf{J}. \tag{4.29}$$

Equation 4.15 can then be used to convert the covariance matrix of the data points to the covariance matrix of the fit parameters, where the data covariance is taken to be a diagonal matrix, with elements equal to the larger of either the square of the standard deviation or the square of the residual from the fit for each point. The resulting uncertainties on the

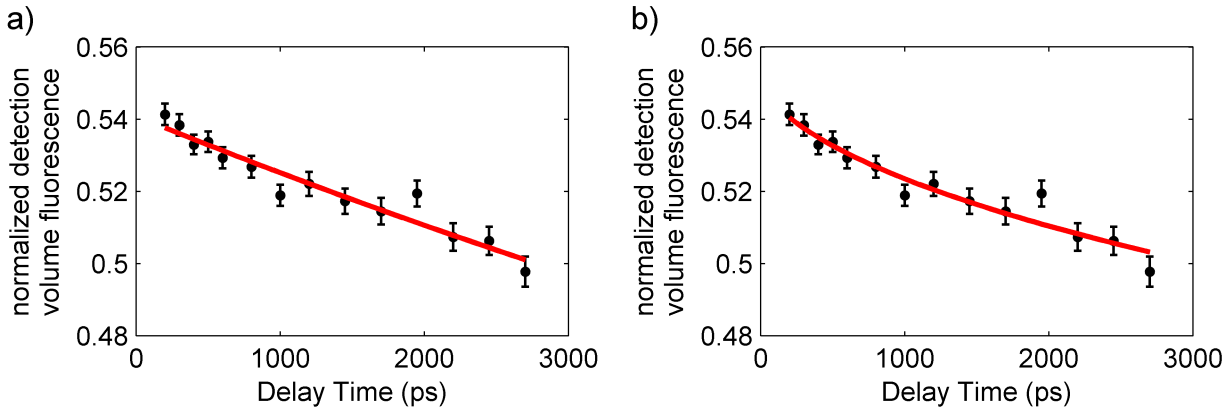

Figure 4.19: Results of the fitting routine for a) the diffusive model and b) the power law model. In both, the fits are shown as red curves overlaid on the data.

parameters may then be propagated through the calculation of the diffusion length in the usual way. This procedure will account for both the error on the data points and the ability of the model to fit the data, however there is one additional factor that is not yet included, which is the error in selecting the degree of confinement for the FWHM of the excitation volume, which enters into the fit as a fixed parameter. This effect with be discussed, along with the results of the fit to the data, in the next section.

4.6.5 Fits to the Experimental Data for CN-PPV

The fitting procedure outlined above was performed on the experimental data in Figure 4.17 for both a diffusive and power law (subdiffusive) model. The diffusive model returned a value of $L_d = 15.5 \pm 0.8$ nm, with $D_o = 0.05 \pm 0.01$ nm^2/ps. The fit is shown in Figure 4.19a, overlaying the experimental data. The sub-diffusive model returned a value of $L_d = 14.7 \pm 0.8$ nm, with $D_o = 0.9 \pm 1.7$ nm^2/ps and $\alpha = 0.6 \pm 0.3$. This fit is shown in Figure 4.19b. The uncertainties in the L_d's reported here include the error on the data and the ability of the model to fit the data, but do not yet include the uncertainty in the selection of the degree of confinement (FWHM) of the excitation volume, see Figure 4.18a.

Interestingly, both models appear to fit the data well, and they return similar values for the diffusion length and error. The sub-diffusive model, however, has very large error bars on its parameters, while the L_d value is more tightly fit. This is due to a trade off between the values of D_o and α in this model, which can combine to produce a given diffusion length. This effect is illustrated in Figure 4.20a, which shows the χ^2 of the fit for different combinations of D_o and α, with the corresponding value of L_d shown in Figure 4.20b. The χ^2 plot show a minimum value for multiple combinations of D_o and α, where the D_o value for the minimum χ^2 increases and becomes more uncertain for decreasing values of α. The calculated value

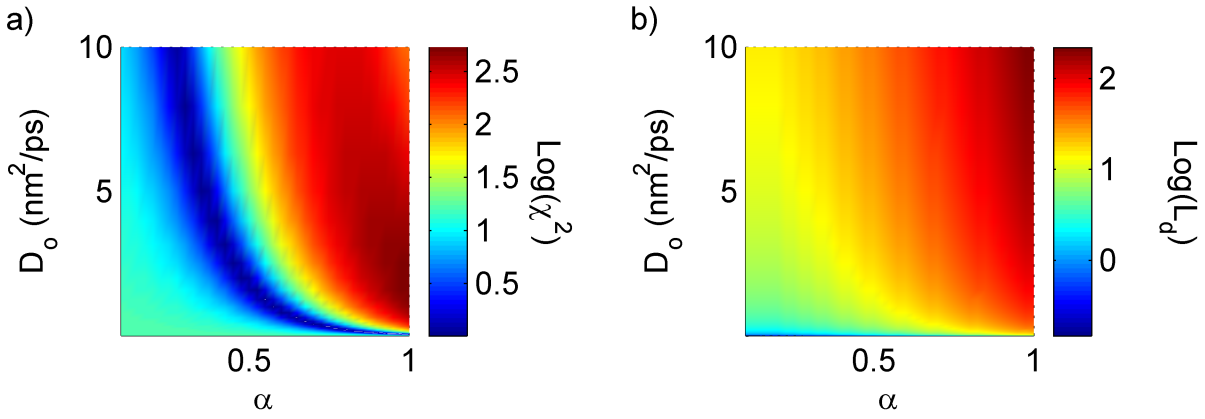

Figure 4.20: a) The χ^2 of the power law fit for various combinations of D_o and α, illustrating the trade off in parameters that leads to the large uncertainty in their values. b) The L_d produced by the corresponding set of parameters. Note that the calculated value does not change along the minimum of the plot in (a), leading to a smaller error in L_d than in the parameters themselves.

of L_d, however, does not change significantly along the minimum of the χ^2 plot, leading to a smaller error in L_d than in the parameters themselves.

The additional error in the diffusion length, introduced by the selection of the FWHM of the confined excitation volume in the fit, can be determined by considering the reasonable range of possible confinements, as shown in Figure 4.21. As discussed in Section 4.6.4, the resolution curve in Figure 4.12 and 4.21a is used to determine the value of the FWHM of the excitation volume in the fitting routine. On this resolution curve the experimental STED pulse energy of 240 pJ (shown in gray in Figure 4.21a) corresponds to a FWHM of 85 nm. The red lines overlaying the resolution curve in Figure 4.21a indicate values for the FWHM of 70 and 100 nm, which we take to be a 95% confidence interval. Note that this range is determined by the uncertainty in the resolution curve at the energy of the STED pulse (gray line), not the uncertainty in the energy of the STED pulse, which is well known. The uncertainty in the calculated value of L_d, due to this effect, is then determined by performing the fit to the experimental data for a range of values of the FWHM of the excitation volume, as shown in Figure 4.21b. The result of the fit for the selected value of FWHM = 85 nm is indicated with a black line. The red lines indicate the results of the fit at the FWHM = 70 and 100 nm extremes of the 95% confidence interval, as in Figure 4.21a. The blue lines indicate the result of the fit at the corresponding ± 1 σ values for the FWHM. The result indicates that the additional uncertainty in the reported L_d value is $\sigma = 1.4$ nm. Combining, in quadrature, this value with the $\sigma = 0.8$ nm reported above, due to the error in the data and the quality of the fit, yields $\sigma = 1.6$ nm, which we round to 2 nm to be conservative.

This fitting procedure allows us to extract a length scale of migration and its uncertainty

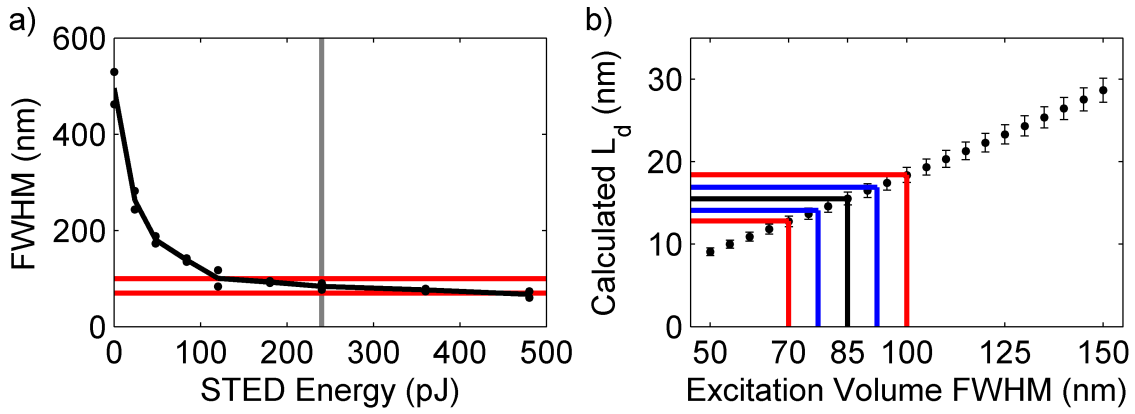

Figure 4.21: Illustration of method used to determine the additional uncertainty in the L_d value from the fit, due to the degree of confinement of the excitation volume. a) Same as Figure 4.12, the resolution (FWHM of the excitation volume) vs STED energy from imaging a CN-PPV nanoparticle. This figure is used in the fitting analysis to select the FWHM of the excitation volume at the STED energy used in the experiment (240 pJ as indicated in gray). The value of the FWHM at this STED energy is 85 nm. The red lines indicate FWHM values of 70 and 100 nm, which we take as a 95% confidence interval. b) The calculated L_d that results results from running the fitting analysis on the experimental data for various values of the FWHM of the excitation volume. The error bars on the L_d values account for the error in the data the quality of the fit, as reported above. The black line indicates the result for our selected value of 85 nm. The red lines correspond to the 95% confidence range of 70 to 100 nm, or $\pm 2\,\sigma$, and the blue lines indicate the corresponding results for $\pm 1\,\sigma$.

from the experimental TRUSTED data. To verify that the observed trend in the experimental data is in fact due to migration, however, we also perform two control experiments, as outlined in Section 4.3, the results of which are discussed below.

4.6.6 Control for Time Dependence of the Stimulated Emission Depletion Efficiency

To verify that the observed trend in the normalized detection volume fluorescence is due to migration and not cause by a variation in the efficiency of the stimulated emission depletion process as a function of the delay time, we perform a control measurement by blocking the STED1 pulse and observing the change in the normalized detection volume fluorescence for a diffraction limited population distribution. The result of this control experiment is shown in Figure 4.22. Any excited state population dynamics that change the Einstein coefficient

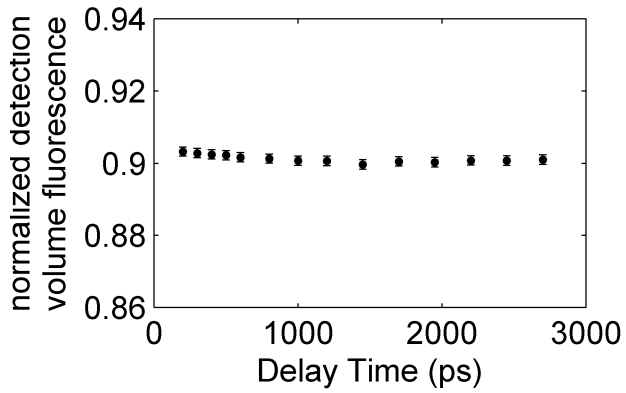

Figure 4.22: Control experiment with the STED1 pulse blocked. Any variation in the ability of the STED2 pulse to stimulated emission, due to excited state population dynamics, would result in a non-constant trend in the normalized detection volume fluorescence. Note that the y-axis has been set to display an eight percentage point range, as in Figure 4.17. The fact that this control data shows no dependence on the delay time confirms that the observed change in the normalized detection volume fluorescence in Figure 4.17 is due to migration. This data also highlights the benefits of confining the initial exciton population for migration measurements, by showing that the diffraction limited initial distribution does not produce a comparable signal.

for stimulated emission over the lifetime of the exciton, such as the formation of a charge transfer or triplet state, would cause the normalized detection volume fluorescence to change over the delay time, which we do not observe. This experiment also highlights the benefit of creating a confined initial condition for migration. When the STED1 pulse is used (Figure 4.17) the initial distribution is tightly confined with steep gradients, so the effect of migration is more pronounced in the data. In contrast, when the STED1 pulse is not applied, as here, the effects of migration on the large, diffraction limited, exciton distribution is negligible, even though there should be net migration away from the center of the diffraction-limited distribution as a function of time.

4.6.7 Excitation Density Control

As previously discussed, exciton annihilation could also produce a normalized detection volume fluorescence trend very similar to those produced by exciton migration. Annihilation, however, has an exciton density dependence, and migration does not. To determine the contribution of annihilation to the observed normalized detection volume fluorescence trend, we therefore performed a series of migration measurements at several excitation densities.

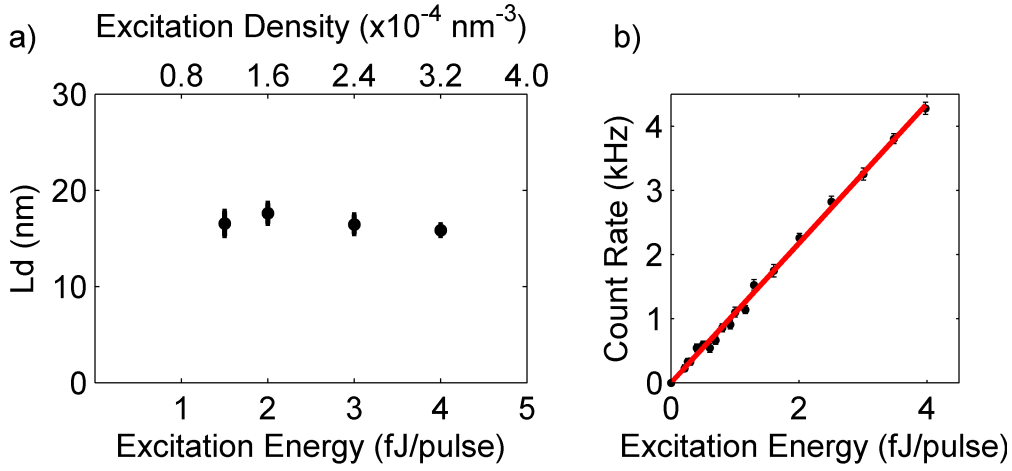

Figure 4.23: Summary of the power dependence of the measurement. a) The excitation density dependence of the calculated diffusion length. The bottom axis shows the pump energy used, while the top axis shows an estimation of the corresponding excitation density after STED1. The errorbars on the L_d's include the error from the fit, but not the error in the selection of the degree of confinement, which would likely be systematic in these successively collected results, for comparative purposes. b) The variation of the observed count rate when gating the detector on after the action of the pump+STED1 pluses vs the excitation energy.

The results are summarized in Figure 4.23a, which shows no dependence of our calculated diffusion length over the range of excitation densities explored. Additionally, Figure 4.23b shows the excitation density dependence of the fluorescence after the STED1 pulse (during migration), which is very linear over this range. In the absence of STED1, which quenches a significant fraction ($\sim 90\%$) of the initially excited exciton population, the observed count rate is much higher and begins to saturate over this range of excitation energy, likely due to annihilation. The quenching effect of STED1, however, reduces the exciton density to a linear regime and the saturation in the count rate is no longer observed. These results illustrate that the experiments are run in a linear regime where annihilation is negligible.

Based on these controls and the simulations presented in Section 4.4, we are confident that the observed trend in the normalized detection volume fluorescence in Figure 4.17 is caused by exciton migration. We have thus shown that TRUSTED can be used to successfully extract the exciton migration length for films of the conjugated polymer CN-PPV and have found that the best fit, with fewest parameters, is to a diffusive migration model with a diffusivity of $D_o = 0.05 \pm 0.01$ nm^2/ps and a diffusion length of $L_d = 16 \pm 2$ nm. Next we will consider the implications of this result on the spatioenegetic landscape in CN-PPV films, and we will discuss how the spectral and energetic parameters of a material, more generally, combine to determine the extent and character of exciton migration.

4.7 TRUSTED Data Interpretation

Having established the theoretical framework of the experiment and demonstrated its successful application to CN-PPV thin films, we now consider what kind of microscopic spatioenergetic landscape and spectral factors could give rise to the relatively long observed migration length, and more generally how these factors determine the extent and character (diffusive vs subdiffusive) of exciton migration in the incoherent hopping regime. Microscopically, the spatioenergetic landscape is composed of closely spaced chromophore sites whose transition energies vary due to statistical fluctuations in the persistence length of the polymer backbone, the chain packing conformations, the local electrostatic environment, and interactions with neighboring chromophores, all of which contribute to the inhomogeneous broadening (σ_{IHB}) of the site energies.[51, 54] The degree of site energy dispersity implied by σ_{IHB} must be considered in relation to the site specific broadening (σ_{SSB}), the spectral width of a single site due to the Franck-Condon progression and fast thermal fluctuations, to determine the effective distinguishability of one site energy from another. Additionally, the intrinsic reorganization energy of a chromophore determines its Stokes shift (Δ_{SS}), which biases excitons to hop to lower energy sites and limits the spectral overlap for isoenergetic hops. Δ_{SS} must also, however, be considered in relation to σ_{SSB} to determine the magnitude of these effects.[61] Thus, we consider the nature and extent of migration as a function of σ_{IHB} and Δ_{SS}, normalized to σ_{SSB}, where $\sigma_{IHB}/\sigma_{SSB}$ is related to the inter-chromophore properties, the distinguishability of sites, and Δ_{SS}/σ_{SSB} is related to the intra-chromophore properties, the spectral overlap of isoenergetic sites. These factors combine to determine the extent and character of migration, where the character of migration is summarized by the time dependence of the mean squared displacement (MSD), or the parameter α from the fitting routine in Section 4.6.4. To determine the spatioenergetic landscape and corresponding nature of exciton migration that is most likely to underlie our $L_d \sim 16$ nm result, we perform Monte Carlo simulations of excitons hopping over spatioenergetic landscapes at multiple points in the $\sigma_{IHB}/\sigma_{SSB}$ vs Δ_{SS}/σ_{SSB} phase space.

4.7.1 Monte Carlo Random Walk Simulations

To aid in the interpretation of our experimental results we have constructed a Monte Carlo simulation of incoherent exciton hopping.[60, 61] The goal of this simulation is to elucidate how the spatioenergetic and spectral parameters combine to determine the extent and character, diffusive or sub-diffusive, of migration. The simulation assumes discrete hops between sites on a $\sim$ 80 x 80 nm 2D hexagonal lattice with periodic boundary conditions and a density of ρ=1.4 sites/nm^2. A 2D lattice is used for simplicity and computational efficiency, as there is no gradient in the z-axis in out experiments and the value of L_d, in the form commonly reported in literature, does not depend on dimensionality, see Section 1.2.6.1. For each random walk trajectory, the sites are randomly assigned absorptive transition energies from a Gaussian distribution, described by the inhomogeneous broadening, σ_{IHB}, centered

at the mean transition energy $\bar{\epsilon}$. The density of sites at a given energy is then,

$$\rho(\epsilon)d\epsilon = \frac{\rho}{\sqrt{2\pi}\sigma_{IHB}} e^{-\frac{(\epsilon-\bar{\epsilon})^2}{2\sigma_{IHB}^2}} d\epsilon. \tag{4.30}$$

The absorption and emission profile for each site are also assumed to be Gaussian, with widths determined by the site specific broadening, σ_{SSB}, due to the Franck-Condon progression and fast thermal fluctuations. The normalized emission spectrum of a donor site of mean energy ϵ_d is,

$$D_{ems}(\epsilon, \epsilon_d) = \frac{1}{\sqrt{2\pi}\sigma_{SSB}} e^{-\frac{(\epsilon-(\epsilon_d-\Delta_{SS}))^2}{2\sigma_{SSB}^2}} \tag{4.31}$$

where the Stokes shift, Δ_{SS}, accounts for the reorganization energy of an individual site (note that this quantity is not the same as the total observed Stokes shift from the film, which also includes the exciton energy relaxation due to migration to lower energy sites). While the absorption spectrum of an acceptor site of mean energy ϵ_a is

$$A_{abs}(\epsilon, \epsilon_a) = S(\epsilon_a) e^{-\frac{(\epsilon-\epsilon_a)^2}{2\sigma_{SSB}^2}}, \tag{4.32}$$

where $S(\epsilon_a)$ is the oscillator strength at ϵ_a. The rate of hopping between a donor and acceptor site is governed by Förster Resonant Energy Transfer (FRET), for point dipoles (see Section 1.2.6), given by[26, 61]

$$k_{FRET}(r, \epsilon_d, \epsilon_a) = \frac{1}{\tau}\left(\frac{R_o(\epsilon_d, \epsilon_a)}{r}\right)^6, \tag{4.33}$$

for

$$R_o(\epsilon_d, \epsilon_a) = \left[\frac{9c^4\hbar^4\eta\kappa^2}{8\pi n^4}\int \frac{A_{abs}(\epsilon, \epsilon_a)D_{ems}(\epsilon, \epsilon_d)}{\epsilon^4} d\epsilon\right]^{1/6}, \tag{4.34}$$

where r is the distance between the sites, τ is the fluorescence lifetime, R_o is the "FRET radius", c is the speed of light, $\hbar$ is the reduced Planck's constant, η is the quantum yield of fluorescence, κ is a dipole orientation factor ($\kappa = 2/3$ for isotropic orientational averaging), n is the index of refraction, and ϵ is energy.

This holds for long hops, however, short hops, over distances comparable to the chromophore size, are not described well by this equation, so our simulation switches from a the radial dependence of r^{-6} to a Dexter-like exponential radial dependence for hops <2 nm, while constraining the overall radial dependence of the rate to be both continuous and smooth. To derive this radial dependence, we find the amplitude, A, and the radial decay constant, c of an exponential function, $A\,e^{-cr}$ that matches the FRET rate and its derivative at $r = r_o$, where r_o is set to 2 nm in our simulations. The constraints are,

$$A\,e^{-c\,r_o} = \frac{R_o(\epsilon_d, \epsilon_a)^6}{\tau} r_o^{-6} \tag{4.35}$$

$$\text{and} \quad -c\,Ae^{-c\,r_o} = -6\frac{R_o(\epsilon_d, \epsilon_a)^6}{\tau} r_o^{-7}, \tag{4.36}$$

which can be solved for A and c, as

$$A = \frac{R_o(\epsilon_d, \epsilon_a)^6}{\tau} r_o^{-6} e^6 \tag{4.37}$$

$$\text{and} \quad c = 6/ro. \tag{4.38}$$

By combining these expressions for A and c with the FRET rate, we can construct the overall radial dependence of the rates as,

$$k(r, \epsilon_d, \epsilon_a) = \begin{cases} \frac{1}{\tau}\left(\frac{R_o(\epsilon_d,\epsilon_a)}{r}\right)^6 & r > r_o \\ \frac{1}{\tau}\left(\frac{R_o(\epsilon_d,\epsilon_a)}{r_o}\right)^6 e^{-6\left(\frac{r}{r_o}-1\right)} & r \leq r_o \end{cases}. \tag{4.39}$$

For each trajectory that is run, the site energies are randomized and the excitation is placed on a site at the center of the density of states. The simulation then steps through a series of hops until the total elapsed time exceeds the lifetime of the trajectory, τ', which is selected for each trajectory from the probability distribution described by the observed lifetime, $\tau = 5000$ ps,

$$\tau' = -\tau \ln[\text{rand}()]. \tag{4.40}$$

The result of a given hop is calculated by first determining the transfer rates from the current donor site, to all other sites (acceptors) on the lattice,

$$\mathbf{K} = k(\mathbf{R}, \epsilon_d, \mathbf{E_a}) \tag{4.41}$$

where $\mathbf{R}$ is a vector of the distances to each site and $\mathbf{E_a}$ is a the vector of the corresponding the site energies. The site to hop to is selected by using the transfer rate vector, $\mathbf{K}$, as a probability distribution function

$$PDF = \frac{\mathbf{K}}{\text{sum}\,(\mathbf{K})}, \tag{4.42}$$

calculating the corresponding cumulative distribution function,

$$CDF = \text{cumsum}(PDF), \tag{4.43}$$

and selecting a value from this distribution as

$$ind = \text{find}(CDF >= \text{rand}(), 1, \text{'first'}), \tag{4.44}$$

where "find()" is the matlab function that returns one value that corresponds to the index *ind* of the first site that is greater than or equal to the random value "rand()". The time for the hop to occur, Δt, is calculated from the total rate of transfer to all sites,

$$\Delta t = \frac{1}{\text{sum}\,(\mathbf{K})}. \tag{4.45}$$

The lattice is then re-centered around the selected location, using the periodic boundary conditions, effectively moving the lattice under the exciton instead of moving the exciton over the lattice.

The simulation tracks many parameters over the trajectory, such as the net displacement, the site energy, and the size and duration of each hop. Many trajectories (typically ∼1000) are then combined to determine the average behavior of an exciton for a given set of site-specific and inhomogeneous broadening parameters and Stokes shift, producing graphs of the mean squared displacement (MSD or $\langle \Delta r^2 \rangle$) vs time and the average energy lost over the course of a trajectory (ΔE). The migration length can be extracted from the average final MSD of all trajectories,

$$L_d^2 = \frac{\langle \Delta r^2 \rangle}{2n}. \tag{4.46}$$

The factor of $2n$, where n is the dimensionality ($n = 2$ in the simulations here), has been divided out so that the reported L_d value is consistent with the common practice in the literature of reporting migration lengths as $L_d = \sqrt{D\tau}$ rather than actual root mean squared displacement, RMSD $= \sqrt{2nD\tau}$. See Section 1.2.6.1 for more discussion on this.

Alternatively, the time dependence of the MSD can be fit to a functional form. For diffusive migration the MSD is linear in time,

$$\left\langle \Delta r^2 \right\rangle (t) = 2nDt, \tag{4.47}$$

where the slope is related to the diffusivity, D.

In real systems, however, the MSD often deviates from this trend. In these case, the additional time dependence is assigned to the diffusivity,[17, 60, 252] such that

$$\left\langle \Delta r^2 \right\rangle (t) = 2n \int_0^t D(t')dt', \tag{4.48}$$

where the derivation of time dependence of the MSD in these cases is presented in Section 1.2.6.1. Note that if $D(t)$ is constant, the diffusive equation is recovered. The most common functional form assumed for the diffusivity is a power law in time,

$$D(t) = D_o t^{\alpha - 1} \tag{4.49}$$

so that the equation for the MSD becomes

$$\left\langle \Delta r^2 \right\rangle (t) = 2n \left(\frac{D_o}{\alpha} \right) t^{\alpha}, \tag{4.50}$$

where $\alpha = 1$ corresponds to the diffusive case, $\alpha < 1$ indicates subdiffusive behavior, and $\alpha > 1$ indicates superdiffusive behavior. The average MSD over the exciton lifetime is then,

$$\begin{aligned} \left\langle \Delta r^2 \right\rangle &= \frac{\int_0^\infty 2n \left(\frac{D_o}{\alpha} \right) t^{\alpha} \, e^{-t/\tau} dt}{\int_0^\infty e^{-t/\tau} dt} \\ &= 2n \left(\frac{D_o}{\alpha} \right) \tau^{\alpha} \end{aligned} \tag{4.51}$$

and the L_d can then be calculated from Equation 4.46.

The result of the simulation is the final calculated migration length, and the nature of the migration, as characterized by the power α. The simulation can then be repeated for multiple combinations of the σ_{IHB}, σ_{SSB}, and Δ_{SS}, to examine how these parameters determine the observed extent and character of migration.

4.7.2 Monte Carlo Simulation Results and Interpretation

To determine the nature of the spatioenergetic landscape that underlies our experimental result for CN-PPV, and more generally how the spectral and energetic parameters of a material combine to determine the extent and nature of migration, the simulations described above were run at 213 points in the phase space defined by the ratios $\sigma_{IHB}/\sigma_{SSB}$ and Δ_{SS}/σ_{SSB}. The results of these simulations are summarized by the L_d and α contours shown in Figure 4.24. Contours of the calculated energy relaxation during migration (due to migration to lower energy sites), reported as $(-\Delta E/\Delta_{SS})$, are shown in Figure 4.25, also overlaid with the L_d contours for reference. Finally the contours of D_o and α are plotted together in Figure 4.26. All contours were calculated using "gridfit()" from the mathworks file exchange,[253] which returns an interpolated and smoothed surface from scattered data points, and Matlab's "contour()" function. The yellow region on these plots represents the range of total broadening (assuming $\Delta_{SS} = 0.45$ eV, from previous measurements[254]) we take to be consistent with our observed absorption spectrum (Figure 4.14). The plotted yellow region spans from $\sigma_{tot} = 0.22$ eV on the bottom right edge to $\sigma_{tot} = 0.25$ eV on the top left. The lower bound of 0.22 eV was taken from a fit of the red edge of the observed absorption profile in Figure 4.14 to a Gaussian, while the upper limit is a guess of the reasonable range that could account for the broader absorption on the blue edge. The blue dot indicates our assignment of the location of CN-PPV in the phase space.

The placement of CN-PPV in this phase space was determined by plotting the intersection of a $L_d = 15.5 \pm 0.8$ nm contour, which we take from our experimental result from the fit assuming a known degree of confinement, and the $-\Delta E/\Delta_{SS}$ contour that best matches the following parameters for CN-PPV: This contour was determined from the value of $\Delta_{SS} = 0.45$ eV, which has been previously reported from site selective fluorescence measurements,[254] and the value of $\Delta E = -0.2$, which was taken as the difference between the 'single site' Stokes shift in the site selective fluorescence measurements and the observed Stokes shift of our film (~ 0.65 eV) that includes the effect of downhill energy transfer among sites. These values put CN-PPV on the $-\Delta E/\Delta_{SS} = 0.44$ contour. These contours are plotted in Figure 4.27. Their intersection determines the location of the blue spot in Figures 4.24-4.26 as well.

This analysis places CN-PPV at $\sigma_{IHB}/\sigma_{SSB} = 0.68$ and $\Delta_{SS}/\sigma_{SSB} = 2.43$, as indicated by the blue dot in Figure 4.27. Since we know the value of $\Delta_{SS} = 0.45$ eV,[254] we determine that $\sigma_{IHB} = 0.13$ and $\sigma_{SSB} = 0.19$. The resulting predicted total broadening, $\sigma_{tot} = \sqrt{\sigma_{IHB}^2 + \sigma_{SSB}^2} = 0.23$ eV is in good agreement with the observed width of the absorption profile in Figure 4.14, where the red edge of the absorption profile can be fit to a Gaussian

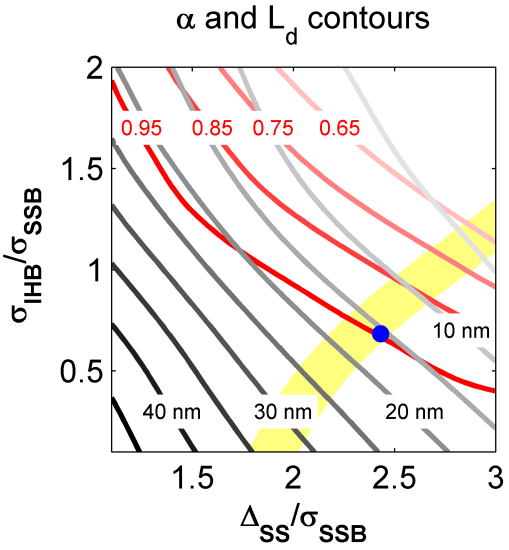

Figure 4.24: An overlay of the contours of L_d (gray) and α (red) plotted against $\sigma_{IHB}/\sigma_{SSB}$ and Δ_{SS}/σ_{SSB}. The yellow region represents the range of total broadening that is consistent with the observed absorption spectral and the blue dot indicates the location of CN-PPV in the phase space.

with $\sigma = 0.22$ eV, which serves as a lower bound for the total broadening. This consistency between the reported (Δ_{SS}), measured (spectra and L_d), and calculated (σ_{IHB} and σ_{SSB}) parameters for CN-PPV gives us confidence in our results. We conclude from the location of CN-PPV in the phase space that exciton migration is approximately diffusive, falling on the boarder of the diffuisve and subdiffusive regions, and that the relatively large reported L_d of ~16 nm is the result of the combination of the approximately diffusive migration and the long (5 ns) exciton lifetime.[251] This approximately diffusive regime is enabled, despite the presence of inhomogeneous broadening, due the large contribution of σ_{SSB} compared to σ_{IHB}. The relatively large value of Δ_{SS}, compared to the σ_{SSB}, is likely a limiting factor in the extent of migration. These results also highlight that the relative quantities that we identified are more fundamentally relevant than the 3 individual values.

Beyond this particular result for CN-PPV, our framework enables more general predictions of how the nature and extent of exciton migration vary as a function the energy relationships that we have identified. The L_d contours in Figure 4.24 roughly fall along the antidiagonal with the highest L_d values in the bottom right corner, where sites are essentially energetically indistinguishable (σ_{SSB} dominates both σ_{IHB} and Δ_{SS}, and $\alpha = 1$). Interestingly, L_d depends additively on $\sigma_{IHB}/\sigma_{SSB}$ and Δ_{SS}/σ_{SSB} with approximately equal weighting, such that their individual contributions are able to trade off to achieve the same extent of migration. If the appropriate weighting is found, corresponding to the direction of the steepest gradient in the L_d contours in Figure 4.24, the L_d trend can be further simplified, as shown in Figure 4.28, where the calculated L_d's have been plotted against the

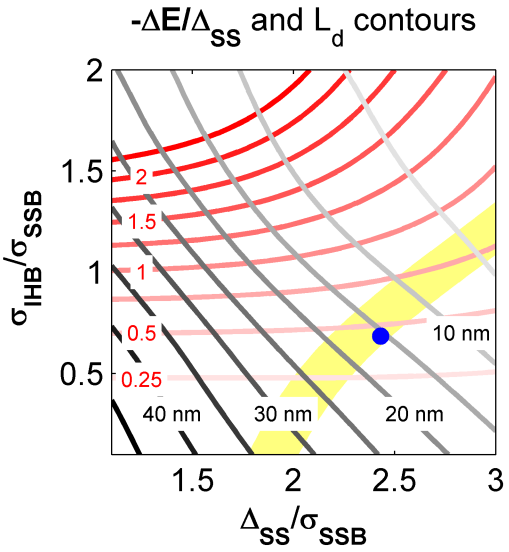

Figure 4.25: An overlay of the contours of L_d (gray) and $-\Delta E/\Delta_{SS}$ (red) plotted against $\sigma_{IHB}/\sigma_{SSB}$ and Δ_{SS}/σ_{SSB}. The yellow region represents the range of total broadening that is consistent with the observed absorption spectral and the blue dot indicates the location of CN-PPV in the phase space.

weighted sum $(\sqrt{2}\frac{\Delta_{SS}}{\sigma_{SSB}} + \frac{\sigma_{IHB}}{\sigma_{SSB}})/(\sqrt{2}+1)$. The overlaid red curve in Figure 4.28 is a fit to a Gaussian with $\sigma = 1$ and amplitude = 61 nm. It is curious that the dependence of the migration length on σ_{IHB}, σ_{SSB}, and Δ_{SS} can be so concisely summarized with these particular weighting factors, and that the resulting trend fits to a Gaussian with a standard deviation of one unit, but the underlying physical reason for this particular relationship is unclear.

The α contours depend most strongly on the distinguishability of sites, $\sigma_{IHB}/\sigma_{SSB}$ and generally start becoming subdiffusive ($\alpha < 1$) near $\sigma_{IHB}/\sigma_{SSB} = 1$, but also generally decrease with decreasing L_d. Another key feature of Figure 4.24 is that the L_d contours intersect multiple α contours. At the trajectory scale, the same L_d can be achieved for multiple values of α, because the same net displacement over the lifetime can be realized for either a constant diffusivity or an initially large diffusivity that decays over time, Figure 4.29. Correspondingly, the value of D_o (Figure 4.26) decreases with decreasing L_d in the region where $\alpha \sim 1$ and shows an increased variability, with respect to the α and L_d contours (Figure 4.24), in the region that corresponds to $\alpha < 1$. This variability in possible values of α and D_o for a given L_d is pronounced for small L_d but decreases as the L_d increases, since there is a maximum allowed diffusivity (when $\sigma_{SSB} >> (\sigma_{IHB}+\Delta_{SS})$). Similarly, the same α can result in multiple L_d values if the diffusivity is scaled, for instance by changing Δ_{SS}/σ_{SSB}.

To further understand the importance of $\sigma_{IHB}/\sigma_{SSB}$ and Δ_{SS}/σ_{SSB}, as well as the mi-

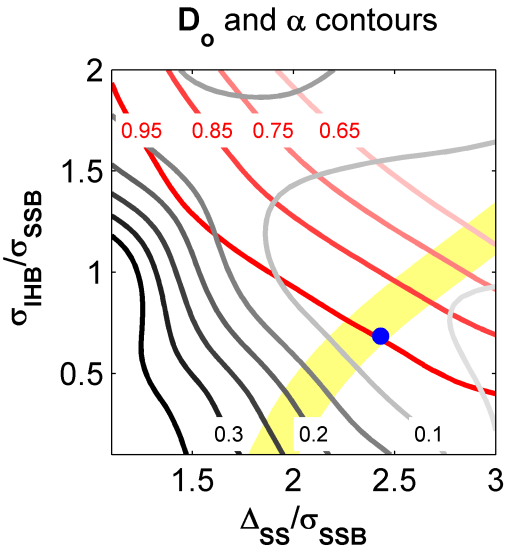

Figure 4.26: An overlay of the contours of D_o (gray) in units of nm^2/ps and α (red) plotted against $\sigma_{IHB}/\sigma_{SSB}$ and Δ_{SS}/σ_{SSB}. The yellow region represents the range of total broadening that is consistent with the observed absorption spectral and the blue dot indicates the location of CN-PPV in the phase space.

croscopic origin of subdiffusive migration, consider the behavior of individual trajectories initiated at the center of the density of states at the level of individual hops. Broadly speaking there are four distinct cases, illustrated in Figure 4.30, corresponding to the four quadrants in Figure 4.24:

Case 1 (Figure 4.30b): If both Δ_{SS}/σ_{SSB} and $\sigma_{IHB}/\sigma_{SSB}$ are large, there will be a large bias for hopping to acceptor sites lower in energy than the donor, and the sites will be distributed over a broad range of energies. In this case, the exciton will rapidly hop to spatially isolated states at the band edge and become trapped, due to the low density of accessible acceptor states at this energy and the very small isoenergetic spectral overlap that a large Δ_{SS} value produces. Therefore, there is little to no migration ($L_d \sim 0$), there is a significant loss of energy (ΔE), and the migration is subdiffusive $\alpha < 1$ since each step reduces the exciton energy, thereby reducing the density of available acceptors for the subsequent hop.

Case 2 (Figure 4.30d): When Δ_{SS}/σ_{SSB} is large and $\sigma_{IHB}/\sigma_{SSB}$ is small, there is still a large bias for hopping to acceptor sites lower in energy than the donor, but now the entire collection of sites are confined to a narrow range of energies. The exciton will thus hop directly to the band edge (in $\sim$1 hop), but the narrow distribution of acceptor site energies, relative the spectral width of each site, results in a relatively large density of available acceptors at this energy. The resulting migration will be diffusive ($\alpha = 1$) since all hops (after the first) are effectively equivalent, however, the diffusivity will be small due

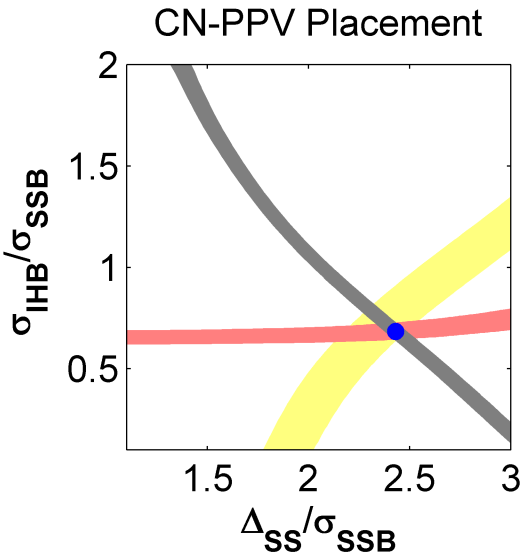

Figure 4.27: The intersection of the $L_d = 15.5$ nm (gray) and $-\Delta E/\Delta_{SS} = 0.44$ contour (red) plotted against $\sigma_{IHB}/\sigma_{SSB}$ and Δ_{SS}/σ_{SSB}. The yellow region represents the range of total broadening that is consistent with the observed absorption spectral and the blue dot indicates the location of CN-PPV in the phase space, which results from this analysis.

to the poor isoenergetic spectral overlap, so L_d will be small but non-zero, and ΔE will be limited by the narrowness of the accessible band of states.

Case 3 (Figure 4.30a): If Δ_{SS}/σ_{SSB} is small and $\sigma_{IHB}/\sigma_{SSB}$ is large, there will be only a slight bias for hopping to acceptor sites lower in energy than the donor and the sites will be distributed over a broad range of energies. In this case, the exciton loses a little energy with each hop, slowly approaching the band edge. Each hop also slightly reduces the density of accessible acceptor sites for subsequent hops, resulting in subdiffusive migration ($\alpha < 1$). An equilibrium is eventually reached where the large density of sites at higher energies balances the slight bias to move to lower energy sites or the exciton is trapped at a spatially and energetically isolated site. The overall energy lost in the trajectory will again be substantial, and the migration length will be moderate.

Case 4 (Figure 4.30c): When both Δ_{SS}/σ_{SSB} and $\sigma_{IHB}/\sigma_{SSB}$ are small, there will be only a slight bias for hopping to acceptor sites lower in energy than the donor and the sites will be confined to a narrow range of energies. This narrow distribution of site energies, combined with the large degree of spectral overlap of isoenergetic sites (implied by the small value of Δ_{SS}/σ_{SSB}), results in a high density of accessible acceptor states. The exciton will, thus, quickly ($\sim$1 hop) reach an equilibrium between the effects of the small bias to lower energies and the steep gradient in the density of states, and the corresponding energy loss with be small. Further hops will then be isoenergetic on average, resulting in diffusive migration ($\alpha = 1$), and the diffusivity will be high due to large spectral overlap of isoenergetic

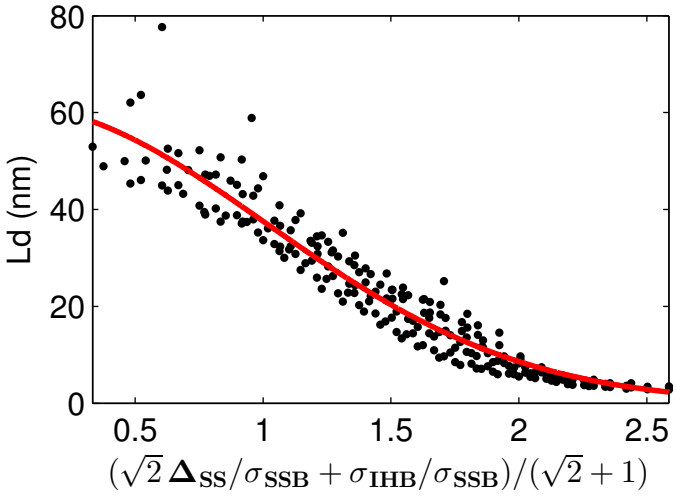

Figure 4.28: The calculated values of L_d (black) from the MC simulations plotted along the axis which corresponds to the steepest gradient in the L_d contours in Figure 4.24, and a fit (red) of this data to a Gaussian with $\sigma = 1$.

sites, resulting in a large migration length.

In each of the four cases, the exciton loses some energy as the effect of bias towards lower energy sites achieves a balance with effect of the gradient in the density of states. This ΔE (Figure 4.25) depends primarily on $\sigma_{IHB}/\sigma_{SSB}$. This is expected as the observed spectral shift in electronically coupled systems is typically considered to be[54]

$$\Delta E = -\frac{\sigma_{IHB}^2}{k_B T}, \tag{4.52}$$

where k_B is the Boltzmann constant and T is temperature. Our Monte Carlo simulations do not explicitly include temperature, but σ_{SSB} should capture analogous behavior to $k_B T$. To check this assumption, we plot $-\Delta E$ vs $\sigma_{IHB}^2/\sigma_{SSB}$ from the simulation data in Figure 4.31. We indeed find a linear trend and the slope is roughly in agreement with the expected value of 1 (red curve), but there a large spread due to the bending of the contours in the upper right corner of Figure 4.25.

The general trends from the microscopic hopping analysis indicate that $\sigma_{IHB}/\sigma_{SSB}$ primarily determines the final energy of the exciton (although Δ_{SS}/σ_{SSB} does play a role) and the density of sites at that energy, while Δ_{SS}/σ_{SSB} determines the energy lost per hop (although this does change depending on the gradient in the density of states) and the spectral overlap for isoenergetic hopping. Both diffusive and subdiffusive trajectories exhibit energy loss, although this loss occurs in $\sim$1 hop in the diffusive regime, where the subsequent diffusivity depends on the isoenergetic hopping rate between sites at the final energy. In the subdiffusive regime the energy loss is gradual and the diffusivity evolves as the relaxation

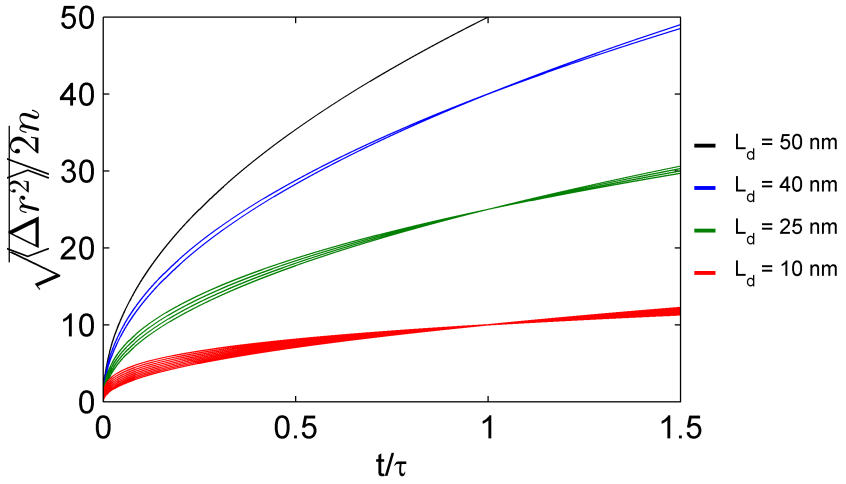

Figure 4.29: Illustration of how multiple trajectories with different values of α can produce the same net displacement over the lifetime of the exciton and why this effect diminishes for large L_d values. This plot assumes a maximum diffusivity that corresponds to $L_d = 50$ nm (black). Also plotted are some example trajectories that achieve $L_d = 40$ nm (blue), $L_d = 25$ nm (green), and $L_d = 10$ nm (red). As the target L_d decreases, relative to the maximum value of 50 nm, a larger number of subdiffusive traces, with smaller values of α, are possible.

in energy reduces the density of available hopping partners. Since $\sigma_{IHB}/\sigma_{SSB}$ determines the density of states available for hopping at a given energy and Δ_{SS}/σ_{SSB} determines the spectral overlap of those states, they can trade off to produce the same migration length.

As an overall prescription for long range exciton hopping trajectories, minimizing the effective distinguishability of sites and maximizing the isoenergetic hopping rate within the lifetime of the exciton appears to be critical. Therefore, one should seek to minimize the Stokes shift and inhomogeneous spectral linewidths of an electronically-coupled material relative to the site specific broadening. As a corollary, substantial site specific broadening should be able to compensate for comparable site energy dispersity and reorganization energy.

Although the migration length values on Figure 4.24 are specific to CN-PPV, these contour trends should hold for other materials, modulated primarily in value by the fluorescence lifetime, chromophore density, oscillator strength, and any orientational anisotropies. We therefore hypothesize the locations in the phase space where other electronically-coupled systems are situated within the above framework. Other conjugated polymer solids should fall into a similar part of the generalized phase space as CN-PPV because site specific broadening is able to compensate the other energies in the problem. These other semiconductors generally suffer from shorter migration lengths (∼5-20 nm),[14] which we attribute primarily to their shorter fluorescence lifetimes, restricting the trajectory duration without compen-

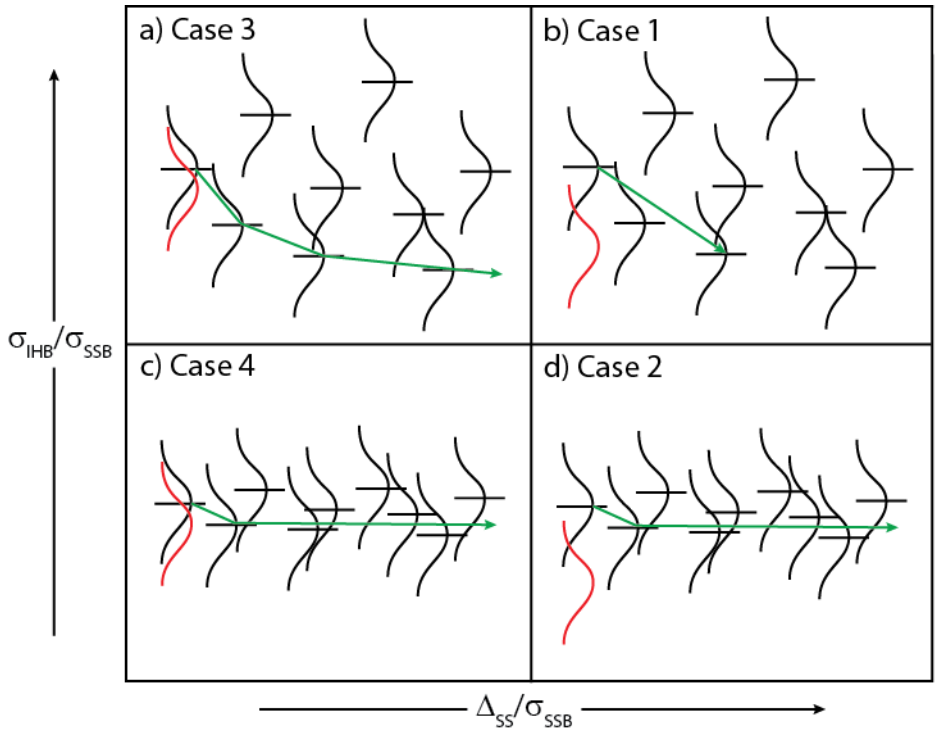

Figure 4.30: Illustration of the microscopic trajectories for, a) case 3, b) case 1, c) case 4, and d) case 2 discussed in the text. The black curves indicate the absorption width of each site, the red curve is the emission profile of the first site to illustrate the size of the Stokes shift, the green arrow indicates the average progression of the trajectory. Note that while (c) and (d) appear similar, the time scales for migration will differ due to the difference in spectral overlap.

sating with faster hopping rates. Nanocrystal arrays generally generate subdiffusive exciton trajectories located further from the phase space origin, albeit with longer migration lengths (tens of nm).[60] We attribute this difference to the much longer nanocrystal excited state lifetimes. In spite of very narrow intrinsic linewidths that generate subdiffusion from polydispersity in size and energy, the slower hopping rates that accompany larger site spacings still enable a compensating number of hops within the lifetime.

4.8 Conclusions of TRUSTED Measurements on CN-PPV

In sum, we have devised and executed an original all-optical scheme to measure exciton migration within sub-diffraction excitation volumes on its native nanometer and picosecond

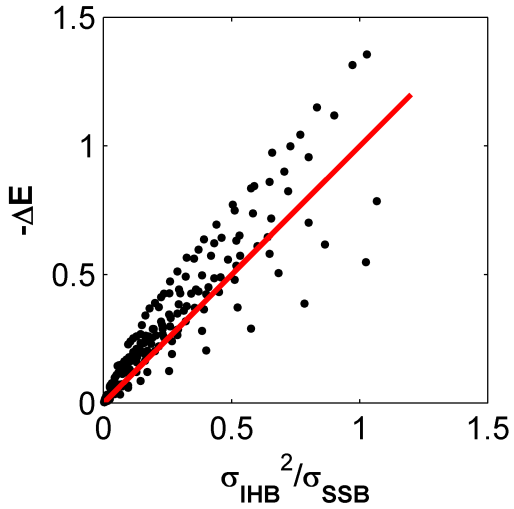

Figure 4.31: The variation of the energy lost during a trajectory (black) with the predicted dependence (red).

scales. Through a combination of our measurements and simulations, we determined that the disordered CN-PPV films that we interrogated exhibit a considerable exciton migration extent of 16 ± 2 nm in the approximately diffusive regime, largely thanks to a relatively long fluorescence lifetime and to the intrinsic site specific broadening of the chromophore site energy. In addition to our measurement and analysis of exciton migration in CN-PPV films, we developed a more general framework in which to contextualize our results by distinguishing between the inter- and intramolecular energy scales that influence the character and extent of exciton migration. We emphasize the significance of assessing inhomogeneous broadening and intrinsic chromophore Stokes shift effects on migration relative to intrinsic variations in chromophore site energies. As such, intrinsic site energy fluctuations are partially able to, or could be designed to, compensate for the latter effects in disordered electronically-coupled molecular systems. For example, deliberately enhancing intrinsic chromophore energy fluctuations on molecular (or even material) scales by design could become an important strategy to extend exciton migration in photovoltaics, while suppressing it could prevent degradation in modern organic displays. We also posit that the additional levels of multiscale hierarchy in photosynthetic light harvesting, namely intra- versus inter-protein exciton transfer and a potentially-active protein scaffold with complementary physical properties to those of the pigment chromophores, could explain their exemplary transport efficiencies, which should be amenable to TRUSTED investigation in the future. Furthermore, although the measured CN-PPV films appear to be amorphous on the scale of our measurement (see Figures B.1 and B.2), TRUSTED is also inherently amenable to resolving spatial heterogeneity in exciton migration. Comparing migration heterogeneity maps to those of the physical heterogeneities observed in complex material microstructure should be a powerful approach to elucidate

correlations between advantageous physical and functional intermolecular configurations in many electronically-coupled molecular materials.

Chapter 5

Conclusion for Spatially and Temporally Resolving Exciton Dynamics in Organic Semiconductors

This thesis has presented new methods and applications of spatially and temporally resolving exciton dynamics in heterogeneous organic semiconducting materials, in order to elucidate the fundamental photophysics and underlying structure/function relation which ultimately determines the performance of an organic electronic device.

In Chapter 2, the benefits of transient absorption microscopy in the context of polycrystalline thin films of small molecule organic semiconductors were demonstrated. The enhanced spatial resolution of this method enabled domain specific studies of exciton population dynamics in TIPS-Pn. The strong probe polarization dependence revealed by single domain studies significantly aids in the assignment of the observed dynamics. A full kinetic model of population dynamics, as a function of both polarization and time, was developed and fit to the experimental data, where the polarization dependence provides a several fold increase in the number of constraints for the fitting routine. The global fitting analysis successfully reproduces the experimental data, and the observed dynamics were determined to include ultrafast thermalization of the initially hot exciton in $\sim$ 50 fs, followed by singlet fission in the first few picoseconds, and then internal conversion over several hundred picoseconds. The success of the kinetic model and the assignment of the dynamics was a direct result of the polarization dependence, which is only revealed at the single domain level. These results clearly illustrate the utility of spatially resolving exciton dynamics on their native length scales. Many organic semiconductors, however, have much smaller length scales of heterogeneity, requiring sub-diffraction limited excitation volumes.

The preparation of such sub-diffraction excitation volumes in naturally luminescent material, however, poses significant challenges. Chapter 3 illustrated one method of achieving the required super-resolution in conjugated polymers, by adapting stimulated emission depletion (STED) microscopy for use with their endogenous chromophores. Notably, the challenge posed by the strong two photon absorption of the STED pulse in conjugated polymers was

successfully mitigated through a combination of the pile-up correction and excitation modulation. This technique was then demonstrated on nanoparticles of the conjugated polymer CN-PPV, where an imaging resolution of better than 90 nm was achieved. This work establishes the ability to define sub-diffraction excitation volumes neat to the scale of the material heterogeneity in conjugated polymers. This advance will enable future correlative studies of exciton dynamics with their underlying microstructure, providing valuable insight into the structure/function relation in conjugated polymers. In addition to opening the door for such correlative measurements, these sub-diffraction excitation volumes are also better matched to the native length scale of exciton migration.

Finally, in Chapter 4, a new method to measure exciton migration on its native nm and ps scales was presented. This new approach is based on a further adaptation of STED microscopy, which provides ultrafast time resolution of spatial migration dynamics. This technique of time resolved ultrafast stimulated emission depletion (TRUSTED) is achieved by adding a second STED pulse, with a controlled time delay, to define an optical quenching boundary (detection volume) that preferentially quenches excitons that have migrated beyond a critical radius. The theoretical and experimental sensitivity of this technique to the migration process was demonstrated, through kinetic simulations and experimental studies. The application of TRUSTED to CN-PPV thin films, in combination with a custom fitting routine, revealed the exciton migration length to be $L_d = 16 \pm 2$ nm. Additionally, Monte Carlo simulations of incoherent exciton hopping were performed for a variety of possible spatioenergetic landscapes, revealing the the migration process in CN-PPV is approximately diffusive in nature, where the 5 ns lifetime capitalizes on the diffusive motion, resulting in the relatively long observed migration length. The simulations also revealed, more generally, how the energetic and spectral parameters of a material combine to determine the extent and nature of exciton migration.

These results reveal the importance of matching the spatial resolution of measurements to the native length scale of the processes and heterogeneity in complex materials. The sub-diffraction limited spatial resolution and ultrafast time resolution of the techniques presented here will enable future correlative studies of exciton dynamic and migration with the underlying substructure. The insights that stand to be gained by such correlative measurements will elucidate the nature of the structure/function relationship in organic semiconductors, thereby informing the rational design of the next generation of semiconducting materials for applications in displays, computing, lighting, and light harvesting.

Bibliography

(1) Anthony, J. E. *Angew. Chem. Int. Ed.* **2008**, *47*, 452–483.

(2) Katz, H. E.; Lovinger, A. J.; Johnson, J.; Kloc, C.; Siegrist, T.; Li, W.; Lin, Y.-Y.; Dodabalapur, A. *Nature* **2000**, *404*, 478–481.

(3) Brütting, W.; Adachi, C., *Physics of Organic Semiconductors*; John Wiley & Sons: 2012.

(4) Pope, M.; Swenberg, C. E., *Electronic Processes in Organic Crystals and Polymers*; Oxford University Press: New York, 1999.

(5) Anthony, J. E. *Chem. Rev.* **2006**, *106*, 5028–5048.

(6) Yi, H. T.; Payne, M. M.; Anthony, J. E.; Podzorov, V. *Nat. Commun.* **2012**, *3*, 1259.

(7) Forrest, S. R. *Nature* **2004**, *428*, 911–918.

(8) Facchetti, A. *Mater. Today* **2007**, *10*, 28–37.

(9) Friend, R. H.; Gymer, R. W.; Holmes, A. B.; Burroughes, J. H.; Marks, R. N.; Taliani, C.; Bradley, D. D. C.; Santos, D. A. D.; Brédas, J. L.; Lögdlund, M.; Salaneck, W. R. *Nature* **1999**, *397*, 121–128.

(10) Kippelen, B.; Brédas, J.-L. *Energy Environ. Sci.* **2009**, *2*, 251–261.

(11) Schwartz, B. J. *Annu. Rev. Phys. Chem.* **2003**, *54*, 141–172.

(12) Thorsmølle, V. K.; Averitt, R. D.; Demsar, J.; Smith, D. L.; Tretiak, S.; Martin, R. L.; Chi, X.; Crone, B. K.; Ramirez, A. P.; Taylor, A. J. *Physica B Condens. Matter.* **2009**, *404*, 3127–3130.

(13) James, D. T.; Frost, J. M.; Wade, J.; Nelson, J.; Kim, J.-S. *ACS Nano* **2013**, *7(9)*, 7983–7991.

(14) Mikhnenko, O.; Blom, P.; Nguyen, T.-Q. T. *Energy Environ. Sci.* **2015**, *8*, 1867–1888.

(15) Pankove, J. I., *Optical Processes in Semiconductors*; Courier Corporation: 1971.

(16) Fox, A. M., *Optical Properties of Solids*; Oxford University Press: 2001.

(17) Bardeen, C. J. *Annu. Rev. Phys. Chem.* **2014**, *65*, 127–148.

(18) Amerongen, H. v.; Valkūnas, L.; Grondelle, R. v., *Photosynthetic Excitons*; World Scientific: 2000.

(19) Moliton, A.; Hiorns, R. C. *Polym. Int.* **2004**, *53*, 1397–1412.

(20) Sirringhaus, H.; Brown, P. J.; Friend, R. H.; Nielsen, M. M.; Bechgaard, K.; Langeveld-Voss, B. M. W.; Spiering, A. J. H.; Janssen, R. a. J.; Meijer, E. W.; Herwig, P.; de Leeuw, D. M. *Nature* **1999**, *401*, 685–688.

(21) Skotheim, T. A., *Handbook of Conducting Polymers, Second Edition,* CRC Press: 1997.

(22) Demtröder, W., *Laser Spectroscopy*; Springer Berlin Heidelberg: Berlin, Heidelberg, 2008.

(23) Cao, J.; Bardeen, C. J.; Wilson, K. R. *Phys. Rev. Lett.* **1998**, *80*, 1406–1409.

(24) Hilborn, R. C. *Am. J. Phys.* **2002**, *50*, 982–986.

(25) Nitzan, A., *Chemical Dynamics in Condensed Phases: Relaxation, Transfer and Reactions in Condensed Molecular Systems*; OUP Oxford: 2006.

(26) Lakowicz, J. R., *Principles of Fluorescence Spectroscopy*; Springer Science & Business Media: 2007.

(27) McQuarrie, D. A.; Simon, J. D., *Physical Chemistry: A Molecular Approach*; University Science Books: 1997.

(28) Nelson, J., *The Physics of Solar Cells*; Imperial College Press: 2003.

(29) Grancini, G.; Maiuri, M.; Fazzi, D.; Petrozza, A.; Egelhaaf, H.-J.; Brida, D.; Cerullo, G.; Lanzani, G. *Nat. Mater.* **2013**, *12*, 29–33.

(30) Arkhipov, V. I.; Emelianova, E. V.; Bässler, H. *Phys. Rev. Lett.* **1999**, *82*, 1321–1324.

(31) Katoh, R.; Suzuki, K.; Furube, A.; Kotani, M.; Tokumaru, K. *J. Phys. Chem. C* **2009**, *113*, 2961–2965.

(32) Platt, A. D.; Day, J.; Subramanian, S.; Anthony, J. E.; Ostroverkhova, O. *J. Phys. Chem. C* **2009**, *113*, 14006–14014.

(33) Jakubiak, R.; Bao, Z.; Rothberg, L. *Synth. Met.* **2000**, *114*, 61–64.

(34) Schäfer, F. P., *Dye Lasers*; Springer Science & Business Media: 2013.

(35) Yost, S. R.; Hontz, E.; Yeganeh, S.; Van Voorhis, T. *J. Phys. Chem. C* **2012**, *116*, 17369–17377.

(36) Tang, K.-C.; Liu, K. L.; Chen, I.-C. *Chem.l Phys. Lett.* **2004**, *386*, 437–441.

(37) Zhang, Q.; Li, J.; Shizu, K.; Huang, S.; Hirata, S.; Miyazaki, H.; Adachi, C. *J. Am. Chem. Soc.* **2012**, *134*, 14706–14709.

(38) Goushi, K.; Yoshida, K.; Sato, K.; Adachi, C. *Nat. Photon.* **2012**, *6*, 253–258.

(39) Johnson, J. C.; Nozik, A. J.; Michl, J. *Acc. Chem. Res.* **2013**, *46*, 1290–1299.

(40) Reusswig, P. D.; Congreve, D. N.; Thompson, N. J.; Baldo, M. A. *Appl. Phys. Lett.* **2012**, *101*, 113304.

(41) Wilson, M. W. B.; Rao, A.; Clark, J.; Kumar, R. S. S.; Brida, D.; Cerullo, G.; Friend, R. H. *J. Am. Chem. Soc.* **2011**, *133*, 11830–11833.

(42) Wilson, M. W. B.; Rao, A.; Ehrler, B.; Friend, R. H. *Acc. Chem. Res.* **2013**, *46*, 1330–1338.

(43) Sternlicht, H.; Nieman, G. C.; Robinson, G. W. *J. Chem. Phys.* **1963**, *38*, 1326–1335.

(44) Scholes, G. D. *J. Phys. Chem. A* **2015**, *119*, 12699–12705.

(45) West, B. A.; Womick, J. M.; McNeil, L. E.; Tan, K. J.; Moran, A. M. *J. Phys. Chem. C* **2010**, *114*, 10580–10591.

(46) Ostroverkhova, O.; Cooke, D. G.; Hegmann, F. A.; Anthony, J. E.; Podzorov, V.; Gershenson, M. E.; Jurchescu, O. D.; Palstra, T. T. M. *Appl. Phys. Lett.* **2006**, *88*, 162101.

(47) Megerle, U.; Pugliesi, I.; Schriever, C.; Sailer, C. F.; Riedle, E. *Appl. Phys. B* **2009**, *96*, 215–231.

(48) Cabanillas-Gonzalez, J.; Grancini, G.; Lanzani, G. *Adv. Mater.* **2011**, *23*, 5468–5485.

(49) Mukamel, S., *Principles of nonlinear optical spectroscopy*; Oxford University Press: 1995.

(50) Makhov, D. V.; Barford, W. *Phys. Rev. B* **2010**, *81*, 165201.

(51) Hoffmann, S. T.; Bässler, H.; Köhler, A. *J. Phys. Chem. B* **2010**, *114*, 17037–17048.

(52) Kirchartz, T.; Taretto, K.; Rau, U. *J. Phys. Chem. C* **2009**, *113*, 17958–17966.

(53) Scholes, G. D. *Annu. Rev. Phys. Chem.* **2003**, *54*, 57–87.

(54) Tamai, Y.; Ohkita, H.; Benten, H.; Ito, S. *J. Phys. Chem. Lett.* **2015**, *6*, 3417–3428.

(55) Dexter, D. L. *J. Chem. Phys.* **1953**, *21*, 836–850.

(56) Grover, M.; Silbey, R. *J. Chem. Phys.* **1971**, *54*, 4843–4851.

(57) Hwang, I.; Scholes, G. D. *Chem. Mater.* **2011**, *23*, 610–620.

(58) Aragó, J.; Troisi, A. *Adv. Funct. Mater.* **2016**, *26*, 2316–2325.

(59) Akselrod, G. M.; Deotare, P. B.; Thompson, N. J.; Lee, J.; Tisdale, W. A.; Baldo, M. A.; Menon, V. M.; Bulović, V. *Nat. Commun.* **2014**, *5*, 3646.

(60) Akselrod, G. M.; Prins, F.; Poulikakos, L. V.; Lee, E. M. Y.; Weidman, M. C.; Mork, A. J.; Willard, A. P.; Bulović, V.; Tisdale, W. A. *Nano Lett.* **2014**, *14*, 3556–3562.

(61) Lee, E. M. Y.; Tisdale, W. A.; Willard, A. P. *J. Phys. Chem. B* **2015**, *119*, 9501–9509.

(62) Cussler, E. L., *Diffusion: Mass Transfer in Fluid Systems*; Cambridge University Press: 2009.

(63) Junping, S. Derivation of the Reaction-Diffusion Equations., Math 480-01 Partial Differential Equations and Mathematical Biology, `http://www.resnet.wm.edu/~jxshix/math490/` (accessed 07/08/2016).

(64) Weitsman, Y. *J. Compos. Mater.* **1976**, *10*, 193–204.

(65) Luhman, W. A.; Holmes, R. J. *Adv. Funct. Mater.* **2011**, *21*, 764–771.

(66) Terao, Y.; Sasabe, H.; Adachi, C. *Appl. Phys. Lett.* **2007**, *90*, 103515.

(67) Mikhnenko, O. V.; Cordella, F.; Sieval, A. B.; Hummelen, J. C.; Blom, P. W. M.; Loi, M. A. *J. Phys. Chem. B* **2008**, *112*, 11601–11604.

(68) Haugeneder, A.; Neges, M.; Kallinger, C.; Spirkl, W.; Lemmer, U.; Feldmann, J.; Scherf, U.; Harth, E.; Gügel, A.; Müllen, K. *Phys. Rev. B* **1999**, *59*, 15346–15351.

(69) Mikhnenko, O. V.; Cordella, F.; Sieval, A. B.; Hummelen, J. C.; Blom, P. W. M.; Loi, M. A. *J. Phys. Chem. B* **2009**, *113*, 9104–9109.

(70) Masuda, K.; Ikeda, Y.; Ogawa, M.; Benten, H.; Ohkita, H.; Ito, S. *ACS Appl. Mater. Interfaces* **2010**, *2*, 236–245.

(71) Shaw, P. E.; Ruseckas, A.; Samuel, I. D. W. *Adv. Mater.* **2008**, *20*, 3516–3520.

(72) Goh, C.; Scully, S. R.; McGehee, M. D. *J. Appl. Phys.* **2007**, *101*, 114503.

(73) Scully, S. R.; McGehee, M. D. *J. Appl. Phys.* **2006**, *100*, 034907.

(74) Wu, Y.; Zhou, Y. C.; Wu, H. R.; Zhan, Y. Q.; Zhou, J.; Zhang, S. T.; Zhao, J. M.; Wang, Z. J.; Ding, X. M.; Hou, X. Y. *Appl. Phys. Lett.* **2005**, *87*, 044104.

(75) Markov, D. E.; Amsterdam, E.; Blom, P. W. M.; Sieval, A. B.; Hummelen, J. C. *J. Phys. Chem. A* **2005**, *109*, 5266–5274.

(76) Theander, M.; Yartsev, A.; Zigmantas, D.; Sundström, V.; Mammo, W.; Andersson, M. R.; Inganäs, O. *Phys. Rev. B* **2000**, *61*, 12957–12963.

(77) Leow, C.; Ohnishi, T.; Matsumura, M. *J. Phys. Chem. C* **2014**, *118*, 71–76.

(78) Köse, M. E.; Graf, P.; Kopidakis, N.; Shaheen, S. E.; Kim, K.; Rumbles, G. *Phys. Chem. Chem. Phys.* **2009**, *10*, 3285–3294.

(79) Rim, S.-B.; Fink, R. F.; Schneboom, J. C.; Erk, P.; Peumans, P. *Appl. Phys. Lett.* **2007**, *91*, 173504.

(80) Becker, H.; Burns, S. E.; Friend, R. H. *Phys. Rev. B* **1997**, *56*, 1893–1905.

(81) Kroeze, J. E.; Savenije, T. J.; Vermeulen, M. J. W.; Warman, J. M. *J. Phys. Chem. B* **2003**, *107*, 7696–7705.

(82) Fravventura, M. C.; Hwang, J.; Suijkerbuijk, J. W. A.; Erk, P.; Siebbeles, L. D. A.; Savenije, T. J. *J. Phys. Chem. Lett.* **2012**, *3*, 2367–2373.

(83) Huijser, A.; Savenije, T. J.; Kroeze, J. E.; Siebbeles, L. D. A. *J. Phys. Chem. B* **2005**, *109*, 20166–20173.

(84) Huijser, A.; Suijkerbuijk, B. M. J. M.; Klein Gebbink, R. J. M.; Savenije, T. J.; Siebbeles *J. Am. Chem. Soc.* **2008**, *130*, 2485–2492.

(85) Lunt, R. R.; Giebink, N. C.; Belak, A. A.; Benziger, J. B.; Forrest, S. R. *J. Appl. Phys.* **2009**, *105*, 053711.

(86) Lunt, R. R.; Benziger, J. B.; Forrest, S. R. *Adv. Mater.* **2010**, *22*, 1233–1236.

(87) Cook, S.; Furube, A.; Katoh, R.; Han, L. *Chem.l Phys. Lett.* **2009**, *478*, 33–36.

(88) Gregg, B. A.; Sprague, J.; Peterson, M. W. *J. Phys. Chem. B* **1997**, *101*, 5362–5369.

(89) Najafov, H.; Lee, B.; Zhou, Q.; Feldman, L. C.; Podzorov, V. *Nat. Mater.* **2010**, *9*, 938–943.

(90) Wei, G.; Lunt, R. R.; Sun, K.; Wang, S.; Thompson, M. E.; Forrest, S. R. *Nano Lett.* **2010**, *10*, 3555–3559.

(91) Raisys, S.; Kazlauskas, K.; Daskeviciene, M.; Malinauskas, T.; Getautis, V.; Jursenas, S. *J. Mater. Chem. C* **2014**, *2*, 4792–4798.

(92) Ward, A. J.; Ruseckas, A.; Samuel, I. D. W. *J. Phys. Chem. C* **2012**, *116*, 23931–23937.

(93) Hedley, G. J.; Ward, A. J.; Alekseev, A.; Howells, C. T.; Martins, E. R.; Serrano, L. A.; Cooke, G.; Ruseckas, A.; Samuel, I. D. W. *Nat. Commun.* **2013**, *4*, 2867.

(94) Markov, D. E.; Blom, P. W. M. *Phys. Rev. B* **2006**, *74*, 085206.

(95) Mikhnenko, O. V.; Azimi, H.; Scharber, M.; Morana, M.; Blom, P. W. M.; Loi, M. A. *Energy Environ. Sci.* **2012**, *5*, 6960–6965.

(96) Groff, L. C.; Wang, X.; McNeill, J. D. *J. Phys. Chem. C* **2013**, *117*, 25748–25755.

(97) Bruno, A.; Reynolds, L. X.; Dyer-Smith, C.; Nelson, J.; Haque, S. A. *J. Phys. Chem. C* **2013**, *117*, 19832–19838.

(98) Suna, A. *Phys. Rev. B* **1970**, *1*, 1716–1739.

(99) Wang, H.; Wang, H.-Y.; Gao, B.-R.; Wang, L.; Yang, Z.-Y.; Du, X.-B.; Chen, Q.-D.; Song, J.-F.; Sun, H.-B. *Nanoscale* **2011**, *3*, 2280–2285.

(100) Cook, S.; Liyuan, H.; Furube, A.; Katoh, R. *J. Phys. Chem. C* **2010**, *114*, 10962–10968.

(101) Lewis, A.; Ruseckas, A.; Gaudin, O.; Webster, G.; Burn, P.; Samuel, I. *Org. Electron.* **2006**, *7*, 452–456.

(102) Tamai, Y.; Matsuura, Y.; Ohkita, H.; Benten, H.; Ito, S. *J. Phys. Chem. Lett.* **2014**, *5*, 399–403.

(103) Shin, H.-Y.; Woo, J. H.; Gwon, M. J.; Barthelemy, M.; Vomir, M.; Muto, T.; Takaishi, K.; Uchiyama, M.; Hashizume, D.; Aoyama, T.; Kim, D.-W.; Yoon, S.; Bigot, J.-Y.; Wu, J. W.; Ribierre, J. C. *Phys. Chem. Chem. Phys.* **2013**, *15*, 2867–2872.

(104) Marciniak, H.; Li, X.-Q.; Würthner, F.; Lochbrunner, S. *J. Phys. Chem. A* **2011**, *115*, 648–654.

(105) Shaw, P. E.; Ruseckas, A.; Peet, J.; Bazan, G. C.; Samuel, I. D. W. *Adv. Funct. Mater.* **2010**, *20*, 155–161.

(106) Ruseckas, A.; Ribierre, J. C.; Shaw, P. E.; Staton, S. V.; Burn, P. L.; Samuel, I. D. W. *Appl. Phys. Lett.* **2009**, *95*, 183305.

(107) Engel, E.; Leo, K.; Hoffmann, M. *Chem. Phys.* **2006**, *325*, 170–177.

(108) Chen, J.; Tee, C. K.; Shtein, M.; Anthony, J.; Martin, D. C. *J. Appl. Phys.* **2008**, *103*, 114513.

(109) Rivnay, J.; Jimison, L. H.; Northrup, J. E.; Toney, M. F.; Noriega, R.; Lu, S.; Marks, T. J.; Facchetti, A.; Salleo, A. *Nat. Mater.* **2009**, *8*, 952–958.

(110) Marsh, R. A.; Groves, C.; Greenham, N. C. *J. Appl. Phys.* **2007**, *101*, 083509.

(111) Chen, J.; Martin, D. C.; Anthony, J. E. *J. Mater. Res.* **2007**, *22*, 1701–1709.

(112) Dickey, K. C.; Anthony, J. E.; Loo, Y.-L. *Adv. Mater.* **2006**, *18*, 1721–1726.

(113) Shi, Y.; Liu, J.; Yang, Y. *J. Appl. Phys.* **2000**, *87*, 4254–4263.

(114) Yin, W.; Dadmun, M. *ACS Nano* **2011**, *5*, 4756–4768.

(115) Chen, D.; Nakahara, A.; Wei, D.; Nordlund, D.; Russell, T. P. *Nano Lett.* **2011**, *11*, 561–567.

(116) Verploegen, E.; Miller, C. E.; Schmidt, K.; Bao, Z.; Toney, M. F. *Chem. Mater.* **2012**, *24*, 3923–3931.

(117) Ruderer, M. A.; Müller-Buschbaum, P. *Soft Matter* **2011**, *7*, 5482–5493.

(118) Rivnay, J.; Noriega, R.; Kline, R. J.; Salleo, A.; Toney, M. F. *Phys. Rev. B* **2011**, *84*, 045203.

(119) Hoppe, H.; Sariciftci, N. S. *J. Mater. Chem.* **2006**, *16*, 45–61.

(120) Giri, G.; Verploegen, E.; Mannsfeld, S. C. B.; Atahan-Evrenk, S.; Kim, D. H.; Lee, S. Y.; Becerril, H. A.; Aspuru-Guzik, A.; Toney, M. F.; Bao, Z. *Nature* **2011**, *480*, 504–508.

(121) Stingelin-Stutzmann, N.; Smits, E.; Wondergem, H.; Tanase, C.; Blom, P.; Smith, P.; de Leeuw, D. *Nat. Mater.* **2005**, *4*, 601–606.

(122) Minari, T.; Kano, M.; Miyadera, T.; Wang, S.-D.; Aoyagi, Y.; Seto, M.; Nemoto, T.; Isoda, S.; Tsukagoshi, K. *Appl. Phys. Lett.* **2008**, *92*, 173301.

(123) Sun, Y.; Liu, Y.; Zhu, D. *J. Mater. Chem.* **2005**, *15*, 53.

(124) Born, M.; Wolf, E.; Bhatia, A. B., *Principles of Optics: Electromagnetic Theory of Propagation, Interference and Diffraction of Light*; Cambridge University Press: 1999.

(125) Pedrotti, F. L.; Pedrotti, L. S., *Introduction to Optics*; Prentice Hall: 1993.

(126) Hecht, E., *Optics*; Pearson Education: 2015.

(127) Abbe, E. *Archiv f. mikrosk. Anatomie* **1873**, *9*, 413–418.

(128) Köhler, H. *Optica Acta: Int. J. Opt.* **1981**, *28*, 1691–1701.

(129) The Nobel Prize in Chemistry 2014., `http://www.nobelprize.org/nobel_prizes/chemistry/laureates/2014/` (accessed 06/11/2016).

(130) Möckl, L.; Lamb, D. C.; Bräuchle, C. *Angew. Chem. Int. Ed.* **2014**, *53*, 13972–13977.

(131) Rust, M. J.; Bates, M.; Zhuang, X. *Nat. Methods* **2006**, *3*, 793–796.

(132) Betzig, E.; Patterson, G. H.; Sougrat, R.; Lindwasser, O. W.; Olenych, S.; Bonifacino, J. S.; Davidson, M. W.; Lippincott-Schwartz, J.; Hess, H. F. *Science* **2006**, *313*, 1642–1645.

(133) Hess, S. T.; Girirajan, T. P. K.; Mason, M. D. *Biophys. J.* **2006**, *91*, 4258–4272.

(134) Gustafsson, M. G. L. *PNAS* **2005**, *102*, 13081–13086.

(135) Hell, S. W.; Wichmann, J. *Opt. Lett.* **1994**, *19*, 780–782.

(136) Klar, T. A.; Hell, S. W. *Opt. Lett.* **1999**, *24*, 954.

(137) Hell, S. W. *Science* **2007**, *316*, 1153–1158.

(138) Birks, J., *Photophysics of Aromatic Molecules*; Wiley: New York, 1970.

(139) McGlynn, S.; Azumi, T., *Molecular Spectroscopy of the Triplet State*; Prentice-Hall Inc.: New Jersey, 1969.

(140) Klevens, H. B.; Platt, J. R. *J. Chem. Phys.* **1949**, *17*, 470–481.

(141) Platt, J. R. *J. Chem. Phys.* **1949**, *17*, 484–495.

(142) Ramanan, C.; Smeigh, A. L.; Anthony, J. E.; Marks, T. J.; Wasielewski, M. R. *J. Am. Chem. Soc.* **2012**, *134*, 386–397.

(143) Lloyd, M. T.; Anthony, J. E.; Malliaras, G. G. *Mater. Today* **2007**, *10*, 34–41.

(144) Roberts, S. T.; McAnally, R. E.; Mastron, J. N.; Webber, D. H.; Whited, M. T.; Brutchey, R. L.; Thompson, M. E.; Bradforth, S. E. *J. Am. Chem. Soc.* **2012**, *134*, 6388–6400.

(145) Bardeen, C. J. *MRS Bulletin* **2013**, *38*, 65–71.

(146) Congreve, D. N.; Lee, J.; Thompson, N. J.; Hontz, E.; Yost, S. R.; Reusswig, P. D.; Bahlke, M. E.; Reineke, S.; Voorhis, T. V.; Baldo, M. A. *Science* **2013**, *340*, 334–337.

(147) Lee, J.; Jadhav, P.; Reusswig, P. D.; Yost, S. R.; Thompson, N. J.; Congreve, D. N.; Hontz, E.; Van Voorhis, T.; Baldo, M. A. *Acc. Chem. Res.* **2013**, *46*, 1300–1311.

(148) Fu, D.; Ye, T.; Yurtsever, G.; Warren, W. S.; Matthews, T. E. *J. Biomed. Opt* **2007**, *12*, 054004–054004.

(149) Furube, A.; Tamaki, Y.; Katoh, R. *J. Photochem. Photobiol. A* **2006**, *183*, 253–260.

(150) Gabriel, M. M.; Kirschbrown, J. R.; Christesen, J. D.; Pinion, C. W.; Zigler, D. F.; Grumstrup, E. M.; Mehl, B. P.; Cating, E. E. M.; Cahoon, J. F.; Papanikolas, J. M. *Nano Lett.* **2013**, *13*, 1336–1340.

(151) Gao, B.; Hartland, G.; Fang, T.; Kelly, M.; Jena, D.; Xing, H. G.; Huang, L. *Nano Lett.* **2011**, *11*, 3184–3189.

(152) Grancini, G.; Polli, D.; Fazzi, D.; Cabanillas-Gonzalez, J.; Cerullo, G.; Lanzani, G. *J. Phys. Chem. Lett.* **2011**, *2*, 1099–1105.

(153) Hartland, G. V. *Chem. Sci.* **2010**, *1*, 303–309.

(154) Huang, L.; Cheng, J.-X. *Annu. Rev. Mater. Res.* **2013**, *43*, 213–236.

(155) Huang, L.; Hartland, G. V.; Chu, L.-Q.; Luxmi; Feenstra, R. M.; Lian, C.; Tahy, K.; Xing, H. *Nano Lett.* **2010**, *10*, 1308–1313.

(156) Jung, Y.; Slipchenko, M. N.; Liu, C. H.; Ribbe, A. E.; Zhong, Z.; Yang, C.; Cheng, J.-X. *Phys. Rev. Lett.* **2010**, *105*, 217401.

(157) Matthews, T. E.; Piletic, I. R.; Selim, M. A.; Simpson, M. J.; Warren, W. S. *Sci. Transl. Med.* **2011**, *3*, 71ra15.

(158) Min, W.; Freudiger, C. W.; Lu, S.; Xie, X. S. *Annu. Rev. Phys. Chem.* **2011**, *62*, 507–530.

(159) Min, W.; Lu, S.; Chong, S.; Roy, R.; Holtom, G. R.; Xie, X. S. *Nature* **2009**, *461*, 1105–1109.

(160) Murphy, S.; Huang, L. *J. Phys.: Condens. Matter* **2013**, *25*, 144203.

(161) Polli, D.; Grancini, G.; Clark, J.; Celebrano, M.; Virgili, T.; Cerullo, G.; Lanzani, G. *Adv. Mater.* **2010**, *22*, 3048–3051.

(162) Rösner, B.; Zeilmann, N.; Schmidt, U.; Fink, R. H. *Org. Electron.* **2014**, *15*, 435–440.

(163) Ruzicka, B. A.; Wang, S.; Liu, J.; Loh, K.-P.; Wu, J. Z.; Zhao, H. *Opt. Mater. Express* **2012**, *2*, 708–716.

(164) Seo, M.; Boubanga-Tombet, S.; Yoo, J.; Ku, Z.; Gin, A. V.; Picraux, S. T.; Brueck, S. R. J.; Taylor, A. J.; Prasankumar, R. P. *Opt. Express* **2013**, *21*, 8763–8772.

(165) Simpson, M. J.; Glass, K. E.; Wilson, J. W.; Wilby, P. R.; Simon, J. D.; Warren, W. S. *J. Phys. Chem. Lett.* **2013**, *4*, 1924–1927.

(166) Tamai, N.; Porter, C. F.; Masuhara, H. *Chem. Phys. Lett.* **1993**, *211*, 364–370.

(167) Virgili, T.; Grancini, G.; Molotokaite, E.; Suarez-Lopez, I.; Rajendran, S. K.; Liscio, A.; Palermo, V.; Lanzani, G.; Polli, D.; Cerullo, G. *Nanoscale* **2012**, *4*, 2219–2226.

(168) Wong, C. T. O.; Lo, S. S.; Huang, L. *J. Phys. Chem. Lett.* **2012**, *3*, 879–884.

(169) Ye, T.; Fu, D.; Warren, W. S. *Photochem. Photobiol.* **2009**, *85*, 631–645.

(170) Wong, C. Y.; Penwell, S. B.; Cotts, B. L.; Noriega, R.; Wu, H.; Ginsberg, N. S. *J. Phys. Chem. C* **2013**, *117*, 22111–22122.

(171) Carey, C. R.; LeBel, T.; Crisostomo, D.; Giblin, J.; Kuno, M.; Hartland, G. V. *J. Phys. Chem. C* **2010**, *114*, 16029–16036.

(172) Staleva, H.; Hartland, G. V. *Adv. Funct. Mater.* **2008**, *18*, 3809–3817.

(173) Staleva, H.; Skrabalak, S. E.; Carey, C. R.; Kosel, T.; Xia, Y.; Hartland, G. V. *Phys. Chem. Chem. Phys.* **2009**, *11*, 5889–5896.

(174) Mehl, B. P.; Kirschbrown, J. R.; House, R. L.; Papanikolas, J. M. *J. Phys. Chem. Lett.* **2011**, *2*, 1777–1781.

(175) Wang, P.; Slipchenko, M. N.; Mitchell, J.; Yang, C.; Potma, E. O.; Xu, X.; Cheng, J.-X. *Nat. Photon.* **2013**, *7*, 449–453.

(176) Grancini, G.; Martino, N.; Bianchi, M.; Rizzi, L. G.; Russo, V.; Li Bassi, A.; Casari, C. S.; Petrozza, A.; Sordan, R.; Lanzani, G. *Phys. Status Solidi B* **2012**, *249*, 2497–2499.

(177) Yago, T.; Tamaki, Y.; Furube, A.; Katoh, R. *Phys. Chem. Chem. Phys.* **2008**, *10*, 4435–4441.

(178) Matsuda, H.; Fujimoto, Y.; Ito, S.; Nagasawa, Y.; Miyasaka, H.; Asahi, T.; Masuhara, H. *J. Phys. Chem. B* **2006**, *110*, 1091–1094.

(179) Anthony, J. E.; Brooks, J. S.; Eaton, D. L.; Parkin, S. R. *J. Am. Chem. Soc.* **2001**, *123*, 9482–9483.

(180) Lloyd, M.; Mayer, A.; Tayi, A.; Bowen, A.; Kasen, T.; Herman, D.; Mourey, D.; Anthony, J.; Malliaras, G. *Org. Electron.* **2006**, *7*, 243–248.

(181) Palilis, L. C.; Lane, P. A.; Kushto, G. P.; Purushothaman, B.; Anthony, J. E.; Kafafi, Z. H. *Org. Electron.* **2008**, *9*, 747–752.

(182) Wu, Y.; Liu, K.; Liu, H.; Zhang, Y.; Zhang, H.; Yao, J.; Fu, H. *J. Phys. Chem. Lett.* **2014**, *5*, 3451–3455.

(183) Mannsfeld, S. C. B.; Tang, M. L.; Bao, Z. *Adv. Mater.* **2011**, *23*, 127–131.

(184) Maliakal, A.; Raghavachari, K.; Katz, H.; Chandross, E.; Siegrist, T. *Chem. Mater.* **2004**, *16*, 4980–4986.

(185) Ostroverkhova, O.; Shcherbyna, S.; Cooke, D. G.; Egerton, R. F.; Hegmann, F. A.; Tykwinski, R. R.; Parkin, S. R.; Anthony, J. E. *J. Appl. Phys.* **2005**, *98*, 033701.

(186) Ostroverkhova, O.; Cooke, D. G.; Shcherbyna, S.; Egerton, R. F.; Hegmann, F. A.; Tykwinski, R. R.; Anthony, J. E. *Phys. Rev. B* **2005**, *71*, 035204.

(187) Gélinas, S.; Kirkpatrick, J.; Howard, I. A.; Johnson, K.; Wilson, M. W. B.; Pace, G.; Friend, R. H.; Silva, C. *J. Phys. Chem. B* **2013**, *117*, 4649–4653.

(188) Xu, Q.-H.; Moses, D.; Heeger, A. J. *Phys. Rev. B* **2003**, *68*, 174303.

(189) Folie, B. D.; Ginsberg, N. S. *unpublished* **2016**.

(190) Steinfeld, J. I.; Francisco, J. S.; Hase, W. L., *Chemical Kinetics and Dynamics*, 2 edition; Pearson: Upper Saddle River, N.J, 1998.

(191) Wong, C. Y.; Cotts, B. L.; Wu, H.; Ginsberg, N. S. *Nat. Commun.* **2015**, *6*, 5946.

(192) Wong, C. Y.; Folie, B. D.; Cotts, B. L.; Ginsberg, N. S. *J. Phys. Chem. Lett.* **2015**, *6*, 3155–3162.

(193) Brédas, J.-L.; Beljonne, D.; Coropceanu, V.; Cornil, J. *Chem. Rev.* **2004**, *104*, 4971–5004.

(194) Scholes, G. D.; Rumbles, G. *Nat. Mater.* **2006**, *5*, 683–696.

(195) Spano, F. C. *Annu. Rev. Phys. Chem.* **2006**, *57*, 217–243.

(196) Clark, J.; Silva, C.; Friend, R. H.; Spano, F. C. *Phys. Rev. Lett.* **2007**, *98*, 206406.

(197) Arias, A. C.; MacKenzie, J. D.; Stevenson, R.; Halls, J. J. M.; Inbasekaran, M.; Woo, E. P.; Richards, D.; Friend, R. H. *Macromolecules* **2001**, *34*, 6005–6013.

(198) Kline, R. J.; McGehee, M. D.; Kadnikova, E. N.; Liu, J.; Fréchet, J. M. J.; Toney, M. F. *Macromolecules* **2005**, *38*, 3312–3319.

(199) Salleo, A.; Kline, R. J.; DeLongchamp, D. M.; Chabinyc, M. L. *Adv. Mater.* **2010**, *22*, 3812–3838.

(200) Groves, C.; Reid, O. G.; Ginger, D. S. *Acc. Chem. Res.* **2010**, *43*, 612–620.

(201) Noriega, R.; Rivnay, J.; Vandewal, K.; Koch, F. P. V.; Stingelin, N.; Smith, P.; Toney, M. F.; Salleo, A. *Nat. Mater.* **2013**, *12*, 1038–1044.

(202) Bierwagen, J.; Testa, I.; Flling, J.; Wenzel, D.; Jakobs, S.; Eggeling, C.; Hell, S. W. *Nano Lett.* **2010**, *10*, 4249–4252.

(203) Welsh, D. K.; Yoo, S.-H.; Liu, A. C.; Takahashi, J. S.; Kay, S. A. *Curr. Biol.* **2004**, *14*, 2289–2295.

(204) Contag, C. H.; Bachmann, M. H. *Annu. Rev. Biomed.l Eng.* **2002**, *4*, 235–260.

(205) Penwell, S. B.; Ginsberg, L. D. S.; Ginsberg, N. S. *J. Phys. Chem. Lett.* **2015**, *6*, 2767–2772.

(206) List of dyes used in STED microscopy., Fluorescent Dyes Used in STED Microscopy, `http://nanobiophotonics.mpibpc.mpg.de/old/dyes/` (accessed 04/11/2016).

(207) Leung, B. O.; Chou, K. C. *Appl. Spectrosc.* **2011**, *65*, 967–980.

(208) Sednev, M. V.; Belov, V. N.; Hell, S. W. *Methods Appl. Fluoresc.* **2015**, *3*, 042004.

(209) Török, P.; Munro, P. *Opt. Express* **2004**, *12*, 3605.

(210) Bokor, N.; Iketaki, Y.; Watanabe, T.; Fujii, M. *Opt. Express* **2005**, *13*, 10440–10447.

(211) Pavani, S. R. P.; Thompson, M. A.; Biteen, J. S.; Lord, S. J.; Liu, N.; Twieg, R. J.; Piestun, R.; Moerner, W. E. *PNAS* **2009**, *106*, 2995–2999.

(212) Irvine, S. E.; Staudt, T.; Rittweger, E.; Engelhardt, J.; Hell, S. W. *Angew. Chem. Int. Ed.* **2008**, *47*, 2685–2688.

(213) Rittweger, E.; Han, K. Y.; Irvine, S. E.; Eggeling, C.; Hell, S. W. *Nat. Photon.* **2009**, *3*, 144–147.

(214) Maurer, P. C.; Maze, J. R.; Stanwix, P. L.; Jiang, L.; Gorshkov, A. V.; Zibrov, A. A.; Harke, B.; Hodges, J. S.; Zibrov, A. S.; Yacoby, A.; Twitchen, D.; Hell, S. W.; Walsworth, R. L.; Lukin, M. D. *Nat. Phys.* **2010**, *6*, 912–918.

(215) Lesoine, M. D.; Bhattacharjee, U.; Guo, Y.; Vela, J.; Petrich, J. W.; Smith, E. A. *J. Phys. Chem. C* **2013**, *117*, 3662–3667.

(216) Hanne, J.; Falk, H. J.; Görlitz, F.; Hoyer, P.; Engelhardt, J.; Sahl, S. J.; Hell, S. W. *Nat. Commun.* **2015**, *6*, 7127.

(217) Vogelsang, J.; Steinhauer, C.; Forthmann, C.; Stein, I. H.; Person-Skegro, B.; Cordes, T.; Tinnefeld, P. *Phys. Chem. Chem. Phys.* **2010**, *11*, 2475–2490.

(218) Denk, W.; Strickler, J. H.; Webb, W. W. *Science* **1990**, *248*, 73–76.

(219) Albota, M. et al. *Science* **1998**, *281*, 1653–1656.

(220) Chemla, D. S., *Nonlinear Optical Properties of Organic Molecules and Crystals*; Elsevier: 2012.

(221) Wildanger, D.; Patton, B. R.; Schill, H.; Marseglia, L.; Hadden, J. P.; Knauer, S.; Schnle, A.; Rarity, J. G.; O'Brien, J. L.; Hell, S. W.; Smith, J. M. *Adv. Mater.* **2012**, *24*, OP309–OP313.

(222) Encyclopedia of Laser Physics and Technology - laser-induced damage, optical intensity, fluence, specification of laser damage threshold, measurements, ISO 21254., Laser-induced Damage, `https://www.rp-photonics.com/laser_induced_damage.html` (accessed 04/11/2016).

(223) Scurlock, R. D.; Wang, B.; Ogilby, P. R.; Sheats, J. R.; Clough, R. L. *J. Am. Chem. Soc.* **1995**, *117*, 10194–10202.

(224) Gill, R. K.; Smith, Z. J.; Lee, C.; Wachsmann-Hogiu, S. *J. Biophotonics* **2016**, *9*, 171–180.

(225) Kumagai, H.; Midorikawa, K.; Toyoda, K.; Nakamura, S.; Okamoto, T.; Obara, M. *Appl. Phys. Lett.* **1994**, *65*, 1850–1852.

(226) Tien, A.-C.; Backus, S.; Kapteyn, H.; Murnane, M.; Mourou, G. *Phys. Rev. Lett.* **1999**, *82*, 3883–3886.

(227) Correa, D.; Cardoso, M.; Tribuzi, V.; Misoguti, L.; Mendonca, C. *IEEE J. Sel. Top. Quantum Electron.* **2012**, *18*, 176–186.

(228) Perry, M. D.; Stuart, B. C.; Banks, P. S.; Feit, M. D.; Yanovsky, V.; Rubenchik, A. M. *J. Appl. Phys.* **1999**, *85*, 6803–6810.

(229) Hell, S. W. In *Topics in Fluorescence Spectroscopy*, Lakowicz, J. R., Ed.; Topics in Fluorescence Spectroscopy 5; Springer US: 2002, pp 23–24.

(230) Donnert, G.; Keller, J.; Medda, R.; Andrei, M. A.; Rizzoli, S. O.; Lührmann, R.; Jahn, R.; Eggeling, C.; Hell, S. W. *PNAS* **2006**, *103*, 11440–11445.

(231) Scheul, T.; DAmico, C.; Wang, I.; Vial, J.-C. *Opt. Express* **2011**, *19*, 18036.

(232) Bianchini, P.; Harke, B.; Galiani, S.; Vicidomini, G.; Diaspro, A. *PNAS* **2012**, *109*, 6390–6393.

(233) Harris, C.; Selinger, B. *Aust. J. Chem.* **1979**, *32*, 2111–2129.

(234) Holzapfel, C. *Rev. Sci. Instrum.* **1974**, *45*, 894–896.

(235) Buttafava, M.; Boso, G.; Ruggeri, A.; Mora, A. D.; Tosi, A. *Rev. Sci. Instrum.* **2014**, *85*, 083114.

(236) Dalla Mora, A.; Tosi, A.; Zappa, F.; Cova, S.; Contini, D.; Pifferi, A.; Spinelli, L.; Torricelli, A.; Cubeddu, R. *IEEE J. Sel. Top. Quantum Electron.* **2010**, *16*, 1023–1030.

(237) Szymanski, C.; Wu, C.; Hooper, J.; Salazar, M. A.; Perdomo, A.; Dukes, A.; McNeill, J. *J. Phys. Chem. B* **2005**, *109*, 8543–8546.

(238) Dogariu, A.; Vacar, D.; Heeger, A. J. *Phys. Rev. B* **1998**, *58*, 10218–10224.

(239) Moffitt, J. R.; Osseforth, C.; Michaelis, J. *Opt. Express* **2011**, *19*, 4242.

(240) Vicidomini, G.; Moneron, G.; Han, K. Y.; Westphal, V.; Ta, H.; Reuss, M.; Engelhardt, J.; Eggeling, C.; Hell, S. W. *Nat. Meth.* **2011**, *8*, 571–573.

(241) Harke, B.; Keller, J.; Ullal, C. K.; Westphal, V.; Schonle, A.; Hell, S. W. *Opt. Express* **2008**, *16*, 4154–4162.

(242) Martini, I. B.; Smith, A. D.; Schwartz, B. J. *Phys. Rev. B* **2004**, *69*, 035204.

(243) Gaab, K. M.; Bardeen, C. J. *J. Phys. Chem. A* **2004**, *108*, 10801–10806.

(244) Markov, D. E.; Tanase, C.; Blom, P. W. M.; Wildeman, J. *Phys. Rev. B* **2005**, *72*, 045217.

(245) Menke, S. M.; Holmes, R. J. *Energy Environ. Sci.* **2014**, *7*, 499–512.

(246) Lin, J. D. A.; Mikhnenko, O. V.; Chen, J.; Masri, Z.; Ruseckas, A.; Mikhailovsky, A.; Raab, R. P.; Liu, J.; Blom, P. W. M.; Loi, M. A.; García-Cervera, C. J.; Samuel, I. D. W.; Nguyen, T.-Q. *Mater. Horiz.* **2014**, *1*, 280.

(247) Caruso, F.; Chin, A. W.; Datta, A.; Huelga, S. F.; Plenio, M. B. *J. Chem. Phys.* **2009**, *131*, 105106.

(248) Lee, H.; Cheng, Y.-C.; Fleming, G. R. *Science* **2007**, *316*, 1462–1465.

(249) Nagy, A.; Prokhorenko, V.; Miller, R. D. *Curr. Opin. Struct. Biol.* **2006**, *16*, 654–663.

(250) Gilmore, J.; McKenzie, R. H. *J. Phys. Chem. A* **2008**, *112*, 2162–2176.

(251) Samuel, I. D. W.; Rumbles, G.; Collison, C. J. *Phys. Rev. B* **1995**, *52*, R11573–R11576.

(252) Ahn, T.-S.; Wright, N.; Bardeen, C. J. *Chem. Phys. Lett.* **2007**, *446*, 43–48.

(253) Surface Fitting using gridfit - File Exchange - MATLAB Central., `http://www.mathworks.com/matlabcentral/fileexchange/8998-surface-fitting-using-gridfit` (accessed 07/11/2016).

(254) Harrison, N. T.; Baigent, D. R.; Samuel, I. D. W.; Friend, R. H.; Grimsdale, A. C.; Moratti, S. C.; Holmes, A. B. *Phys. Rev. B* **1996**, *53*, 15815–15822.

Appendix A

Experimental Setup Details For STED and TRUSTED

A.1 Part Numbers

Ref	Description	Company	Part
1	achromatic doublet f = 150 mm	ThorLabs	AC254-150-A-ML
2	achromatic doublet f = 100 mm	ThorLabs	AC254-100-A-ML
3	reflective neutral density OD = 1	ThorLabs	ND10A
4	half wave plate	ThorLabs	AHWP10M-600
5	Glan-Thompson polarizer	Thorlabs	GTH5M
6	achromatic doublet f = 10 mm	ThorLabs	AC080-010-A-ML
7	polarization maintaining single mode fiber 5 m	ThorLabs	PM105953
8	Olympus UPlanFL N 10x0.3 objective	Thorlabs	RMS10x-PF
9	half wave plate	ThorLabs	AHWP10M-600
10	polarizer	ThorLabs	LPVISA100-MP
11	achromatic doublet f = 125 mm	ThorLabs	AC254-125-A-ML
12	liquid crystal noise eater	ThorLabs	LCC3111L
13	achromatic doublet f = 100 mm	ThorLabs	AC254-100-A-ML
14	half waveplate	ThorLabs	AHWP10M-600
15	polarizer	ThorLabs	LPVIS100-MP2
16	absorptive neutral density OD = 1	NA	NA
17	retro-reflector	PLX	OW-25-1E
	mounted on delay stage	Newport	LS250CC
18	absorptive neutral density OD = 2	NA	NA
19	achromatic doublet f = 75 mm	ThorLabs	AC254-075-A-ML
20	optical chopper	Newport	3501
21	achromatic doublet f = 150 mm	ThorLabs	AC254-150-A-ML

22	dichroic mirror	Chroma	T600lpxr-UF2
23	achromatic doublet f = 100 mm	ThorLabs	AC254-100-B-ML
24	achromatic doublet f = 45 mm	ThorLabs	AC254-045-B-ML
25	grating stretcher	Clark-MXR, Inc	NA
26	half waveplate	ThorLabs	AHWP10M-980
27	polarizer	ThorLabs	LPVIS100-MP
28	polarizing beam splitting cube	Newport	10FC16PB.5
29	retro-reflector	PLX	OW-25-1E
	mounted on delay stage	Newport	LS250CC
30	90° roof mirror	PLX	RM-10-2E
31	silver pick-off mirror	NA	NA
32	half waveplate	ThorLabs	AHWP10M-600
	mounted on rotation stage	Newport	PR50CC
33	home built optical shutter	NA	NA
34	retro-reflector	PLX	OW-25-1E
35	90° roof mirror	PLX	RM-10-2E
36	silver pick-off mirror	NA	NA
37	half waveplate	ThorLabs	AHWP10M-980
	mounted on rotation stage	Newport	PR50CC
38	optical shutter	ThorLabs	SHB1T
39	polarizing beam splitting cube	Newport	10FC16PB.5
40	half waveplate	ThorLabs	AHWP10M-600
41	polarizer	ThorLabs	LPVIS100-MP
42	achromatic doublet f = 10 mm	ThorLabs	AC080-10-B-ML
43	single mode polarization maintaining fibber	ThorLabs	PM105-605
44	Olympus UPlanFL N 10x0.3 objective	Thorlabs	RMS10x-PF
45	achromatic doublet f = 75 mm	ThorLabs	AC254-075-B-ML
46	achromatic doublet f = 100 mm	ThorLabs	AC254-100-B-ML
47	half waveplate	ThorLabs	AHWP10M-600
48	vortex phase mask	RPC Photonics	VPP-1a
49	Glan-Laser polarizer	ThorLabs	GL15-B
50	achromatic doublet f = 35 mm	ThorLabs	AC254-035-B-ML
51	achromatic doublet f = 75 mm	ThorLabs	AC254-075-B-ML
52	dichroic mirror	Chroma	T650spxr
53	quarter waveplate	Tower Optics	A-25.4-B-.250-N4
54	63×/1.4NA HC PL APO CS2 oil objective	Leica	NA
	mounted on XYZ positioner	Newport	VP-25XL-XYZL
55	Nano mover piezo positioning sample stage	PI	P-545.3C7
56	20×/0.7NA HC PL APO air objective	Leica	NA

	mounted on a linear positioner	Newport	VP-25XL
57	plano-convex lens f = 25.4 mm	ThorLabs	LA1951-A-ML
58	white light LED	ThorLabs	MWWHL3
59	silver mirror on kinematic mount	Newport	BK-3A
60	emission filter set		
61	achromatic doublet f = 50 mm	ThorLabs	AC250-050-B-ML
62	fast-gated SPAD (see Section 3.5 for details)		
63	plano-convex lens f = 200 mm	ThorLabsv	LA1708-A-ML
64	CMOS camera	ThorLabs	DCC1545M

Table A.1: Table of part numbers, referenced to the schematic of the experimental setup in Figure 3.17.

A.2 Custom Parts

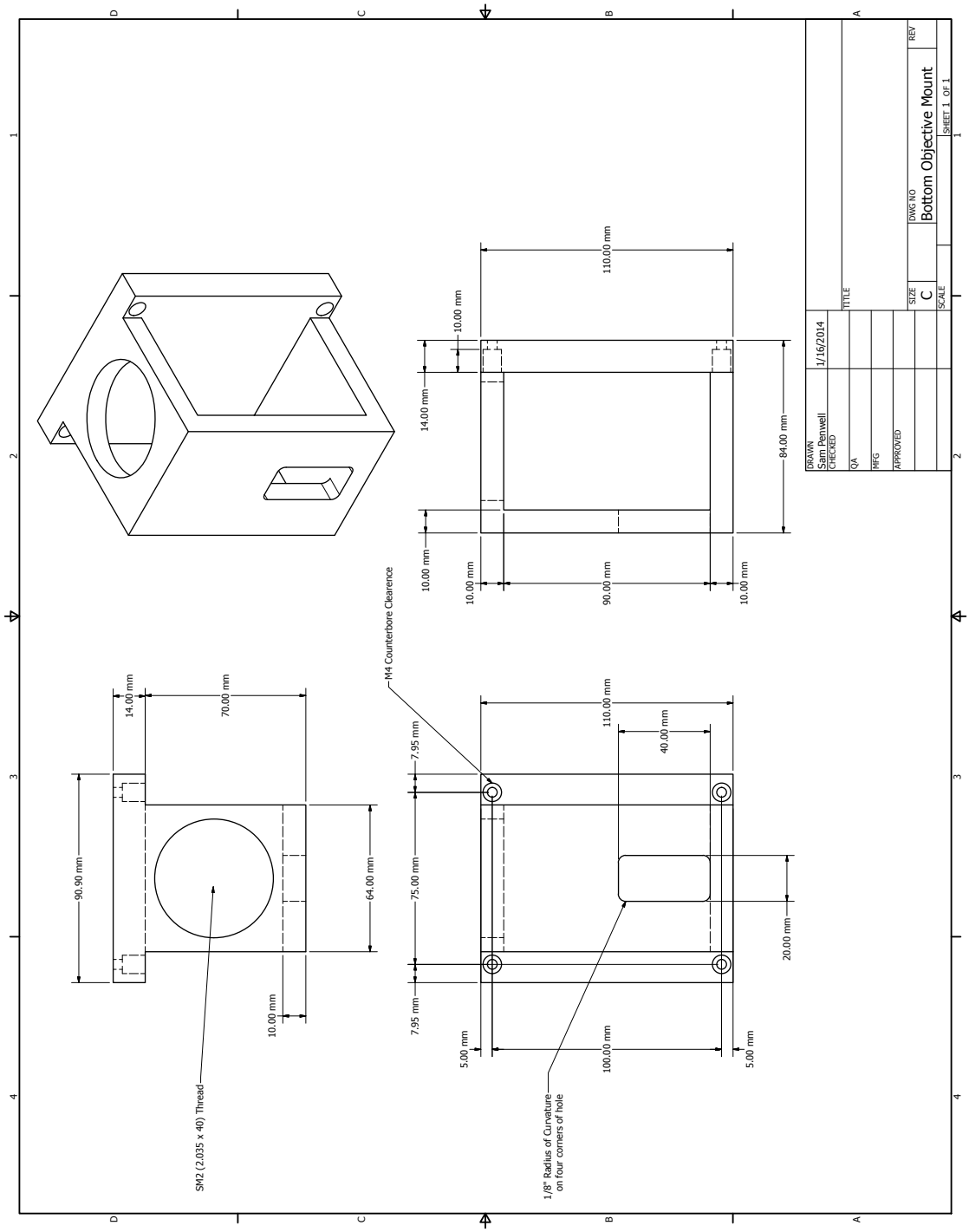

Figure A.1: Custom mount for the bottom objective in the STED/TRUSTED Microscope.

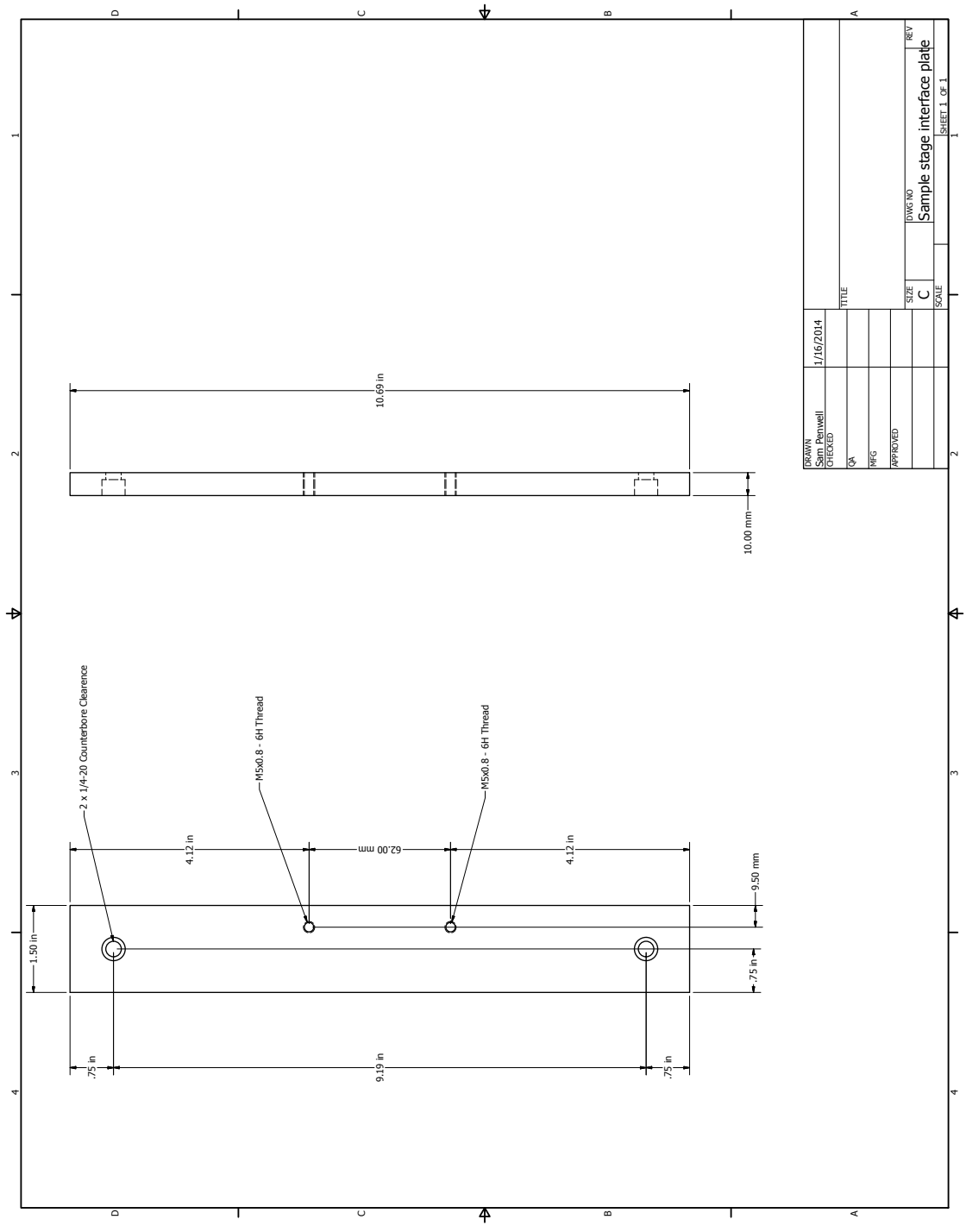

Figure A.2: Custom mount that interfaces the PI sample stage with Thor-Lab Pedestals in the STED/TRUSTED Microscope.

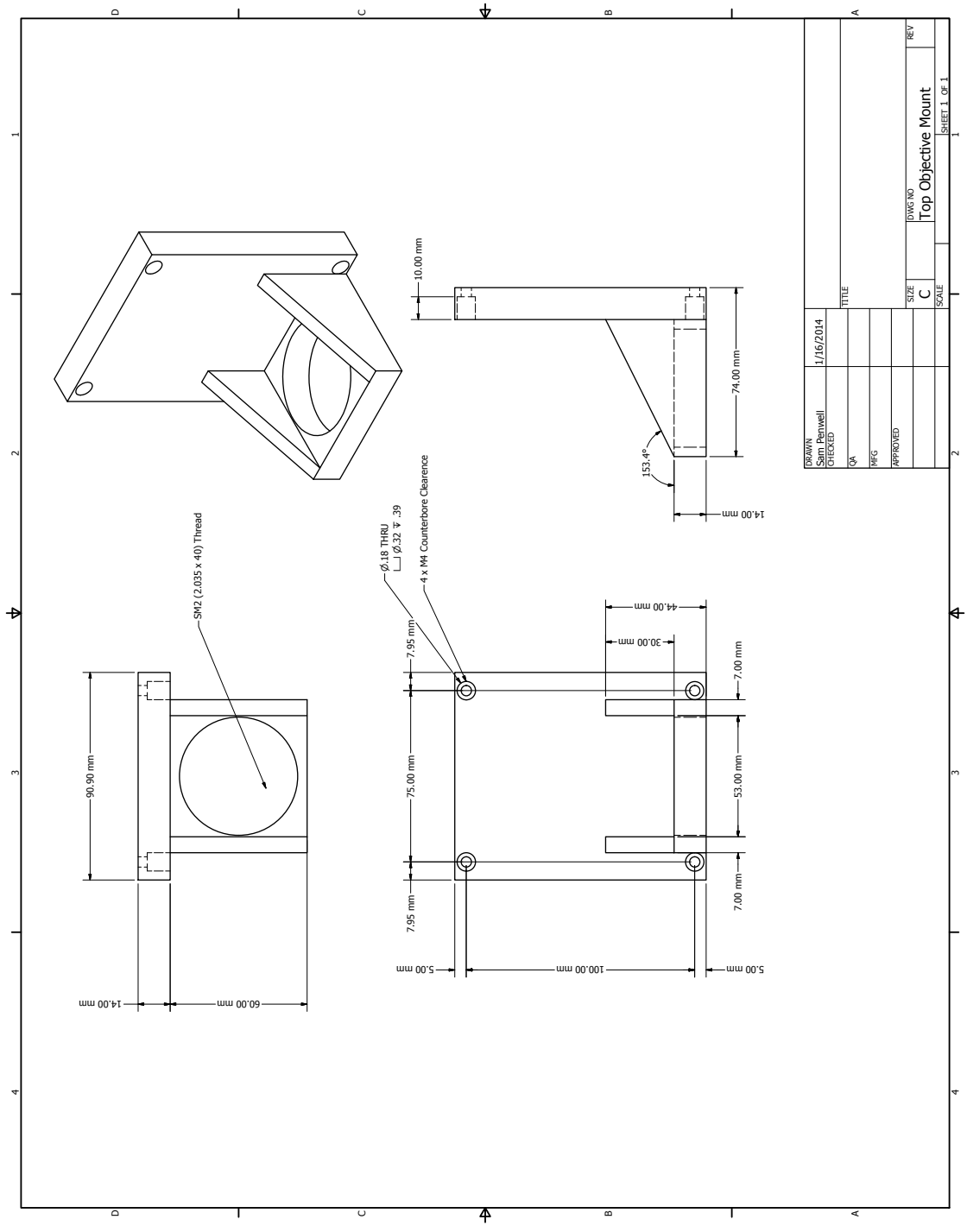

Figure A.3: Custom mount for the top objective in the STED/TRUSTED Microscope.

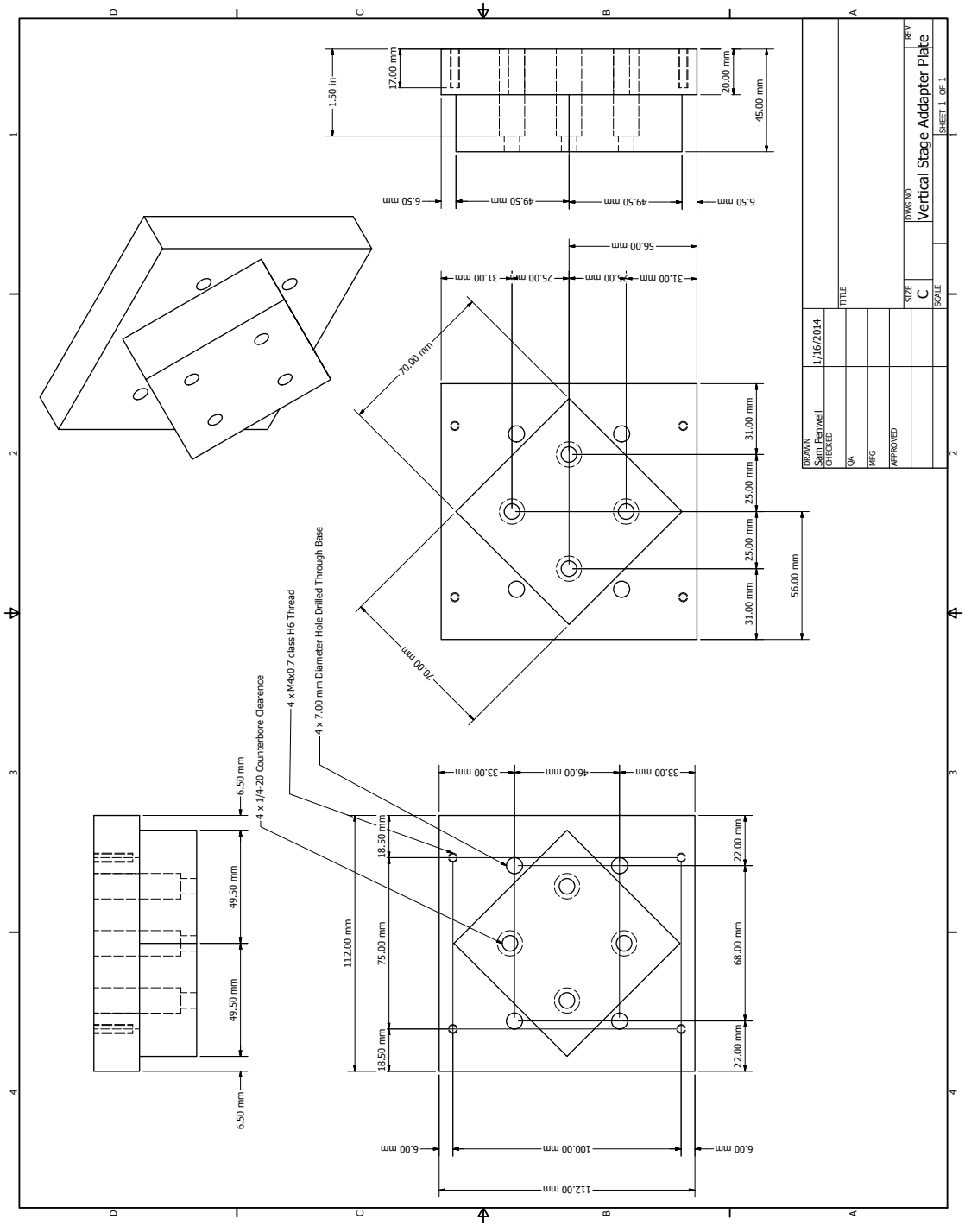

Figure A.4: Custom interface plate to add space between the top objective mount and the newport translation stage it is mounted on in the STED/TRUSTED Microscope.

A.3 Detection Amplification Circuit

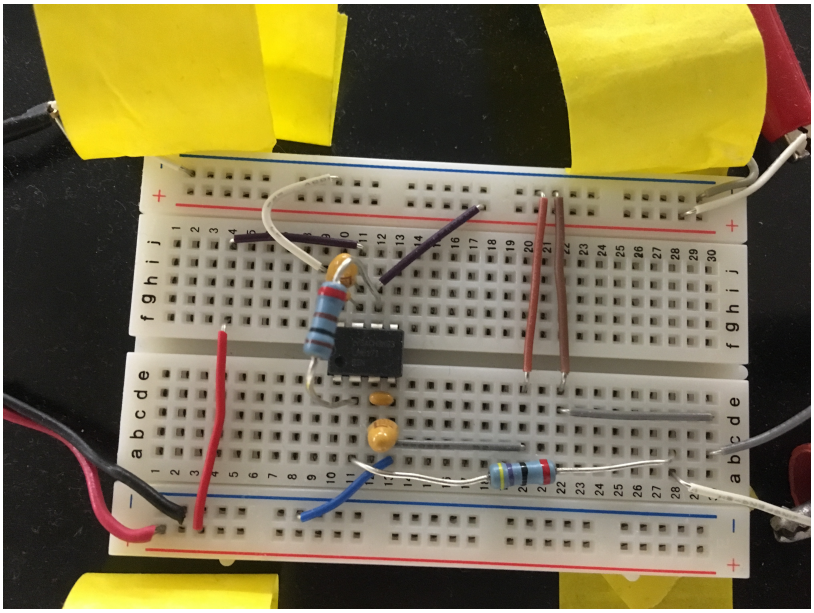

Figure A.5: Picture of the detection circuit.

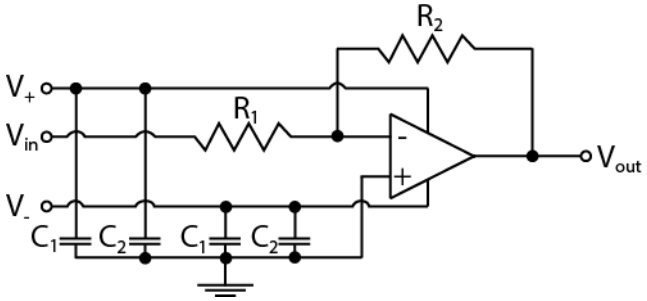

Figure A.6: Diagram of the detection circuit, where $V_+ = 15$ V, $V_- = -15$ V, $R_1 = 47\,\Omega$, $R_2 = 100\,\Omega$, $C_1 = 10$ nF, $C_2 = 2.2$ μF. The operational amplifier is a National Semiconductor model LM6171. The capacitors bridging the power supply (V_+, V_-) to ground reduce noise.

Appendix B

Additional TRUSTED Data Sets

Comparing spatial averaging to unaveraged results: The data for the nine individual sample locations, spaced by 30 μm over a 60×60 μm area and collected as part of a single scan, which are averaged in the data reported in Figure 4.17, are shown in Figure B.1a-i with overlaid fits in red. Note, that the error on each data point from individual sample locations is increased relative to Figure 4.17 due to the reduced averaging, however, the same general trend is seen. The variation in the calculated value of L_d over these sample locations is shown in Figure B.1j with the error from the fit, but not the error due to the selection of the degree of confinement, which is a systematic effect in these simultaneously collected data sets, see Section 4.6.5. There does not appear to be any significant heterogeneity in the reported values of L_d over the spatial locations, at least with the current degree of error in the data, implying that the sample is likely amorphous at the spatial resolution given by our single point measurements. It is possible, however, that further improvements to the experiment to increase the signal-to-noise ratio could reveal some underlying heterogeneity in this or other samples.

Measurement of reproducibility: Additional measurements of the exciton migration length in CN-PPV thin films are shown in Figure B.2a-e. The presented data were taken over a series of days, one set per day, at different positions on the sample. Note that each scan is an average over nine spatial locations spaced by 30 μm over a 60×60 μm area, as in Figure 4.17. Also shown, in Figure B.2f, is a summary of the value of L_d returned by the fit for each location, shown with the error from the fit, but not the error from the selection of the degree of confinement, which would likely be systematic in these successively collected results, for comparative purposes. The consistency in the reported value of L_d over different days of data collection and different sample locations indicates that the measurement is reproducible.

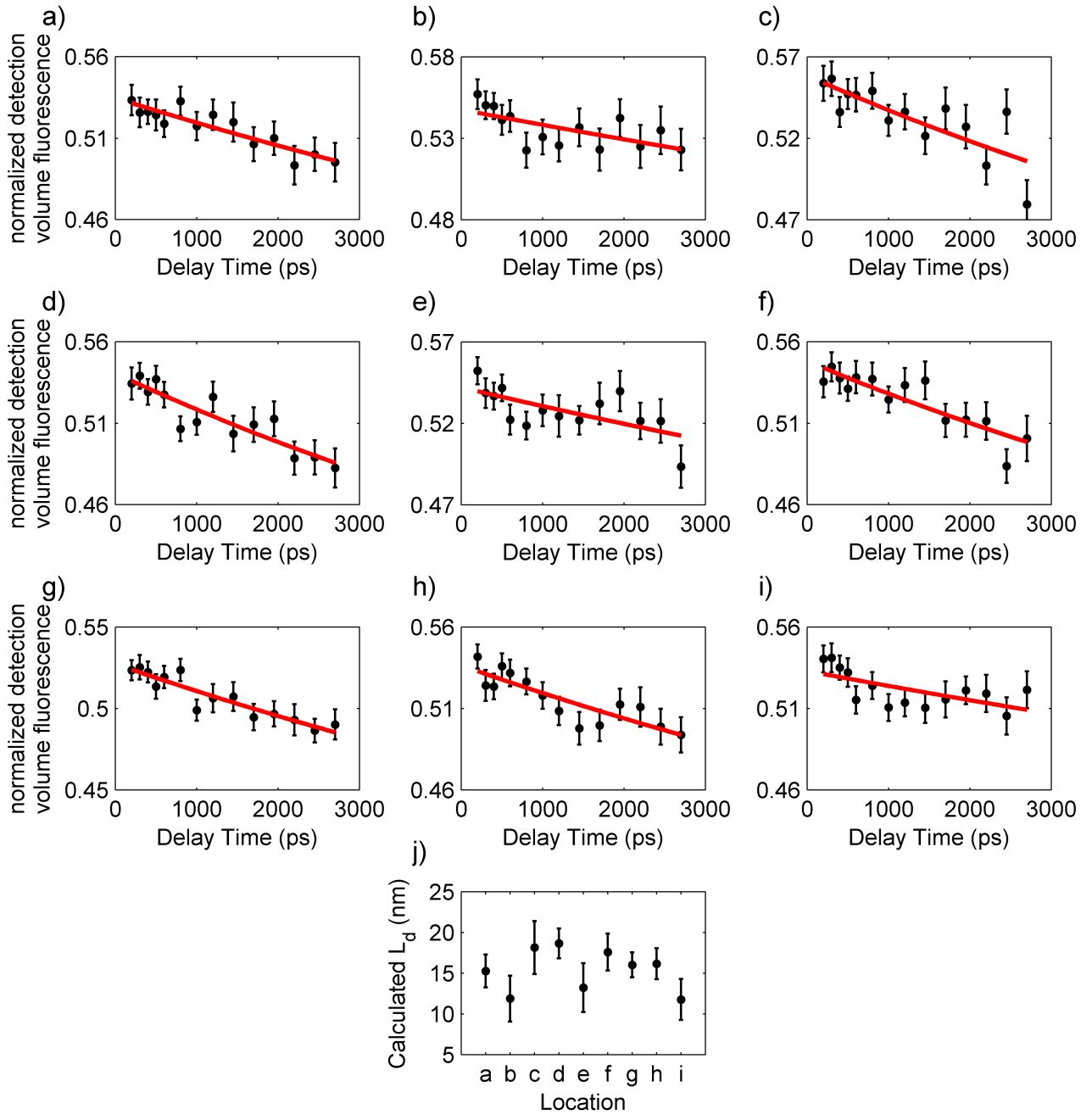

Figure B.1: The data from nine individual sample locations (parts a-i) collected as part of a single scan, which were averaged to produce the results shown in Figure 4.17. Fits to the data are overlaid in red. Part (j) shows the variation in the calculated L_d over these sample locations.

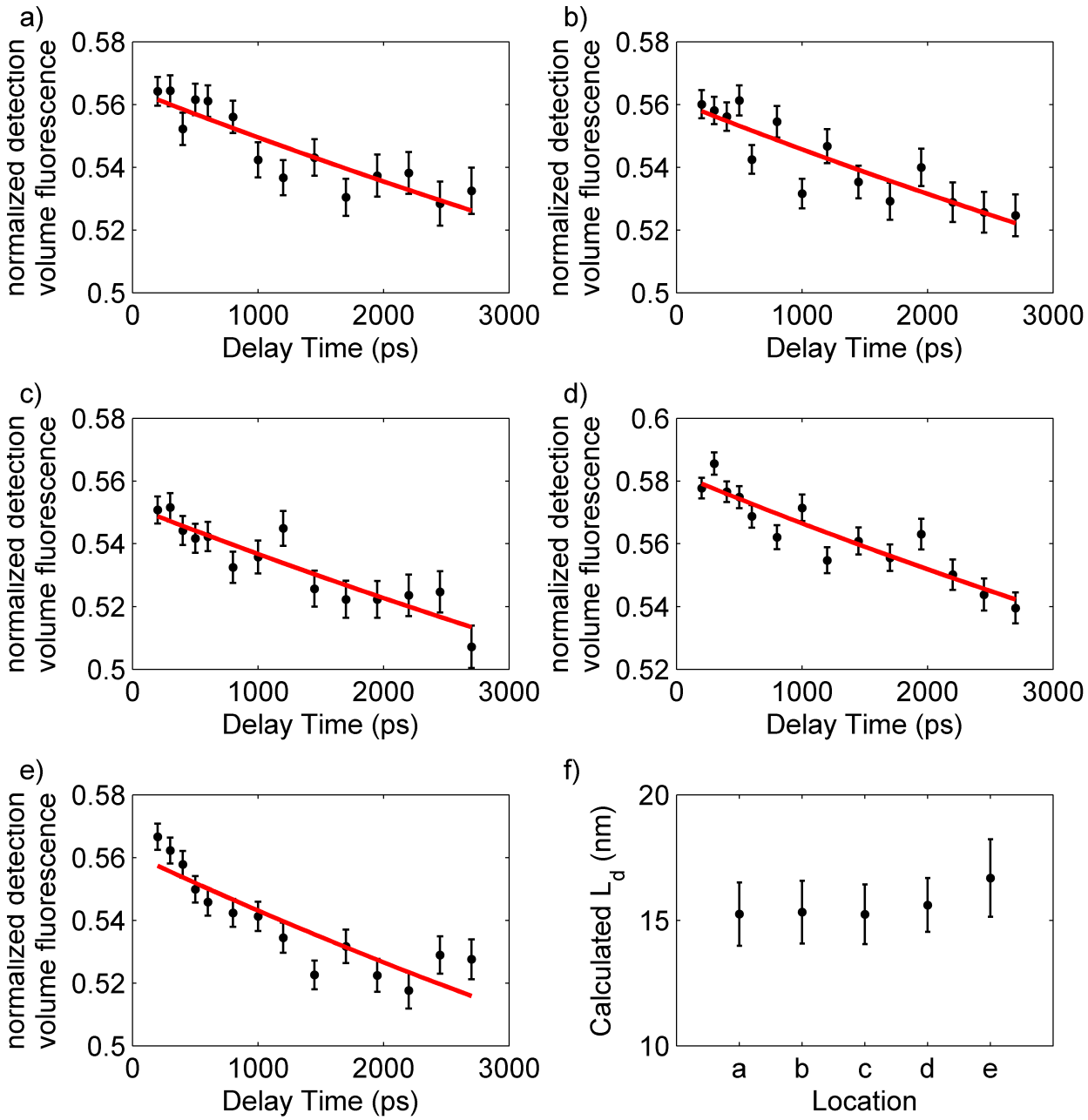

Figure B.2: Additional measurements of the exciton migration length in CN-PPV thin films, at sample coordinates relative to the center of the sample of: a) X = 2.72 mm Y = 2.80 mm, b) X = 3 mm Y = 2.88 mm, c) X = 2 mm Y = 1.88 mm, d) X = 1 mm Y = 0.88 mm, e) X=0 mm Y = 0.13 mm. f) A summary of the value of L_d returned by the fit for each location.